Johannes Tieber BSc

Aeroacoustic sound sources in internal turbulent flows computed from Large-Eddy Simulation

Master's Thesis
to achieve the university degree of
Diplom-Ingenieur
Masters degree programme: Mechanical Engineering

submitted to
Graz University of Technology

Supervisors:

Ao.Univ.-Prof. Dipl.-Ing. Dr.techn. Helfried Steiner
Institut of Fluid Mechanics and Heat Transfer
Graz University of Technology

DI Alexander Machold
AVL LIST GmbH

Graz, September 2018

For my daughter *Klara*.

AFFIDAVIT

EIDESSTATTLICHE ERKLÄRUNG

Ich erkläre an Eides statt, dass ich die vorliegende Arbeit selbstständig verfasst, andere als die angegebenen Quellen/Hilfsmittel nicht benutzt, und die den benutzten Quellen wörtlich und inhaltlich entnommenen Stellen als solche kenntlich gemacht habe. Das in TUGRAZonline hochgeladene Textdokument ist mit der vorliegenden Masterarbeit identisch.

STATUTORY DECLARATION

I declare that I have authored this thesis independently, that I have not used other than the declared sources/resources, and that I have explicitly indicated all material which has been quoted either literally or by content from the sources used. The text document uploaded to TUGRAZonline is identical to the present Master's Thesis.

Datum / Date

Unterschrift / Signature

Preface

The Master's Thesis at hand was performed during my masters program mechanical engineering at the Graz University of Technology. During the bachelors program, I already became interested in fluid mechanics, working as a student assistant at the Institute of Fluid Mechanics and Heat Transfer of the Graz University of Technology. This is why I finished my bachelors program with a bachelor project on subcooled boiling flow at the Institute of Fluid Mechanics and Heat Transfer. During my studies and internships at AVL LIST GmbH I had the chance to get more acquainted with computational fluid dynamics. This led to the opportunity of doing a Master's Thesis in cooperation with the DAC department of AVL LIST GmbH and the Institute of Fluid Mechanics and Heat Transfer, which gave me some insight into the field of study of aeroacoustics. During this period of time, I could improve my programing skills and got more detailed insight into AVL FIRE™, the computational fluid dynamics software of AVL LIST GmbH. I also had the opportunity to visit the *4. Workshop „Strömungsschall in Luftfahrt-, Fahrzeug- und Anlagentechnik“* and got some interesting input on the current topics in aeroacoustics.

I would like to express my gratitude to all those supporting me. First, I would like to thank DI Andreas Ennemoser, head of the department DAC at AVL LIST GmbH for granting me the opportunity of writing this Master's Thesis. Second, many thanks to my two supervisors Ao.Univ.-Prof. Dipl.-Ing. Dr.techn. Helfried Steiner of the Institute of Fluid Mechanics and Heat Transfer at the Graz University of Technology and DI Alexander Machold of AVL LIST GmbH. Both contributed greatly to the success and quality of this Master's Thesis by many interesting discussions we had and their support. Third, I would like to thank my colleagues at the Graz University of Technology and AVL LIST GmbH for the great working and social environment. I also thank my family for standing by my side during the last couple of years. Finally, I would like to mention my wife Miriam and my daughter Klara for the great support during this exceptional period of my life.

Abstract

The purpose of this Master's Thesis was to numerically investigate the aeroacoustic sources produced by an orifice inside a straight cylindrical pipe. The flow through the orifice was investigated using computational fluid dynamics (CFD) based on the numerical solution of the Reynolds averaged Navier-Stokes (RANS) equations and Large-Eddy Simulation (LES).

In the CFD software AVL FIRE™ a computational aeroacoustics (CAA) tool is included, which is based on a hybrid CAA approach, where linearized Euler equations (LEE) are solved. In this Master's Thesis, the acoustic analogy based on the LEE, and the accordingly appearing aeroacoustic source terms were derived.

The primary aim of this Master's Thesis was to compute aeroacoustic source terms, as input into the LEE, from LES and to compare them to the modeled aeroacoustic source terms obtained from the unstructured kinematic source generator (UKSG), which is already implemented in FIRE™. This alternative RANS-based concept computationally models an isotropic turbulence spectrum using a stochastic random based algorithm, which faces severe limitations in highly sheared flow fields with anisotropic turbulence, as considered in this Master's Thesis. Additionally, the aeroacoustic source terms obtained from the LES solution are supposed to be more realistic, because they are computed directly from a resolved turbulent fluctuating velocity field, which is better predicted by LES in comparison to RANS simulations, since less turbulence modeling is involved.

In most previous related work, it has become a standard procedure to center the obtained aeroacoustic source terms by subtracting their temporal averages, to avoid the generation of unphysical acoustic noise induced by large vortical structures. A further aim of this Master's Thesis was therefore to investigate the influence of large low-frequency vortical structures on the aeroacoustic source terms by applying temporal filters based on different turbulence time-scales.

Furthermore, this Master's Thesis investigated the possible contribution of the, often neglected, cross-terms, which arise from the linearization of the Euler equations, and are constituted by contributions from the mean and turbulent flow field. These cross-terms appeared as similarly intense as the other generally included aeroacoustic source terms.

Kurzfassung

Der Zweck dieser Masterarbeit war die numerische Untersuchung von aeroakustischen Quelltermen, welche von einer durchströmten Blende in einem zylindrischem Rohr erzeugt werden. Der mathematischen Beschreibung der Quellterme wurden dabei alternativ auf Basis der Reynolds gemittelten Navier-Stokes (RANS) Gleichungen und Large-Eddy Simulationen (LES) berechnete Strömungsfelder zu Grunde gelegt.

In der Strömungssimulationssoftware AVL FIRE™ ist ein Aeroakustikmodul (CAA) implementiert, welches auf Basis eines hybriden Ansatzes linearisierte Euler Gleichungen löst. In dieser Masterarbeit wurde die akustische Analogie für die linearisierten Euler Gleichungen und die entsprechenden aeroakustischen Quellterme hergeleitet.

Das primäre Ziel dieser Masterarbeit war die direkte Berechnung der aeroakustischen Quellterme unter Verwendung des instationären turbulenten Geschwindigkeitsfeldes einer LES Lösung, sowie deren Vergleich mit den entsprechenden aeroakustischen Quelltermen, welche mittels des im Aeroakustikmodul von FIRE™ implementierten „Unstrukturierten Kinematischen Qelltermgenerators"(UKSG) modelliert wurden. Dieses auf RANS basierende alternative Konzept modelliert die aeroakustischen Quellterme mit einem Zufallsgenerator unter Annahme eines isotropen Turbulenzspektrums. Die aus LES erhaltenen aeroakustischen Quellterme sind deshalb grundsätzlich realistischer, weil einerseits das turbulente Strömungsfeld im Vergleich zur RANS Lösung, vor allem bei anisotroper turbulenter Strömung, besser beschrieben wird, und andererseits bei einer gut aufgelösten LES generell weniger Modellierungsunsicherheit besteht.

Oftmals werden die aeroakustischen Quellterme durch Abzug ihres zeitlichen Mittelwerts statistisch zentriert, was die Vorhersage des akustischen Schallfeldes durch die Elimination nicht akustisch relevanter großen turbulenter Wirbelstrukturen verbessern soll. In diesem Zusammenhang wurde in dieser Masterarbeit überdies der konkrete Einfluss von großen niederfrequenten wirbelnden Strukturen, welche durch Anwendung von speziellen zeitlichen Filterungsmethoden basierend auf bestimmten turbulenten Zeitskalen determiniert wurden, auf die resultierenden aeroakustischen Quellterme, untersucht.

Ein weiteres Ziel dieser Masterarbeit war es, den Anteil der sehr oft vernachläs-

sigten, gemischten aeroakustischen Quellterme, nicht-linear zusammengesetzt aus einer statistisch gemittelten und einer turbulenten Komponente zu untersuchen. Die aus der LES-Lösung berechneten gemischten aeroakustischen Quellterme wiesen generell eine ähnliche Intensität auf wie jene aus der Interaktion turbulent-turbulent hervorgerufenen, als alleinige Schallquelle berücksichtigte, Terme.

Nomenclature

List of Symbols

Latin symbols

Symbol	Unit	Description
A	$[\mathrm{m}^2]$	area
$\mathcal{AR}$	$[-]$	Aspect Ratio of a computational cell
c_p	[J/kgK]	specific heat capacity at constant pressure
c_v	[J/kgK]	specific heat capacity at constant volume
$\mathscr{c}$	[m/s]	speed of sound
C_{ij}	$[\mathrm{m}^2/\mathrm{s}^2]$	Cross stresses
$C_{\mathrm{SGS},\mu}$	$[-]$	SGS model parameter
$C_{\mathscr{k}\zeta f}$	$[-]$	$\mathscr{k}$-ζ-f model parameter
$\mathscr{d}$	[m]	hydraulic diameter
D_{I}	[m]	inner diameter of cylindrical pipe
e	[J/kg]	internal energy per unit of mass
e_{tot}	[J/kg]	total energy per unit of mass
$\mathcal{E}_{\mathrm{VKS}}$	$[\mathrm{m}^2/\mathrm{s}^2]$	Von Kármán spectrum
$\mathscr{f}$	[Hz]	frequency
f	[1/s]	elliptic relaxation function of the $\mathscr{k}$-ζ-f turbulence model
F_{CSM}	$[-]$	SGS modelling function for CSM
h_{O}	[m]	orifice gap height
h	[J/kg]	specific enthalpy
H	[J]	total enthalpy
k	[W/mK]	heat conductivity of the fluid
$\mathscr{k}$	$[\mathrm{m}^2/\mathrm{s}^2]$	turbulence kinetic energy

Symbol	Unit	Description
ℓ	[m]	length-scale
L_{ij}	$[\mathrm{m}^2/\mathrm{s}^2]$	Leonard stresses
L_p	[dB]	sound pressure level
$\dot{m}$	[kg/s]	mass flow rate
n	$[-]$	time-step iteration counter
N	$[-]$	number of sth.
N_{poly}	$[-]$	degree of polynomial base-function
p	[Pa]	pressure
$\mathcal{P}$	$[-]$	logarithmic pressure
P_{ji}	[Pa]	fluid stress tensor
$P_{\mathscr{k}}$	$[\mathrm{m}^2/\mathrm{s}^3]$	production term of $\mathscr{k}$
q_j	[W]	conductive heat flux, described by Fourier's law
r	[m]	radial coordinate in a cylindrical coordinate system
$\mathcal{R}$	[J/kgK]	specific gas constant
R_{I}	[m]	inner radius of a cylindrical pipe
R_{ij}	$[\mathrm{m}^2/\mathrm{s}^2]$	Reynolds stresses
s	[J/kgK]	specific entropy
S_{ij}	[1/s]	symmetric rate of strain tensor
$S_{f,i}$	$[\mathrm{N}/\mathrm{m}^3]$	external force source term per unit of volume
$S_{\dot{m}}$	$[\mathrm{kg}/\mathrm{m}^3\mathrm{s}]$	mass source term per unit of volume
S_p	$[\mathrm{Pa}/\mathrm{s}^2]$	acoustic source term for the wave equation dependent on the acoustic pressure
S_θ	$[\mathrm{W}/\mathrm{m}^3]$	heat source term per unit of volume
S_ρ	$[\mathrm{kg}/\mathrm{m}^3\mathrm{s}^2]$	acoustic source term for the wave equation dependent on the acoustic density
$\mathcal{S}$	$[\mathrm{m}/\mathrm{s}^2]$	aeroacoustic turbulent momentum source term
t	[s]	time
Δt	[s]	time-step
$\mathscr{t}$	[s]	time-scale
$\mathscr{t}_{\mathscr{k}\varepsilon}$	[s]	integral time-scale, eddy turnover time

Symbol	Unit	Description
$\boldsymbol{t}_{\mathrm{ST}}$	[s]	time-scale based on the temporal averaged rate of strain tensor $\| \langle S \rangle \|^{-1}$
$\boldsymbol{t}_{\mathrm{SW}}$	[s]	sweeping time-scale
T	[s]	time-frame, time-period
T_{ij}	[kg/ms^2]	Lighthill stress tensor
U	[m]	circumference
v	[m/s]	velocity
$\boldsymbol{v}$	[m/s]	velocity-scale
V	[m^3]	volume
$\dot{V}$	[m^3/s]	volume flow rate
W_{ij}	[1/s]	asymmetric vorticity tensor
x, y, z	[m]	Cartesian coordinates
$\Delta\boldsymbol{x}$	[m]	characteristic length of the computational cell
y^+	[−]	dimensionless normal wall distance
Δy_{BL}	[m]	normal thickness of the boundary layer cell

Greek symbols

Symbol	Unit	Description
α_{B}	[−]	blending factor between temporal and spatial discretization schemes
α_{UR}	[−]	under-relaxation factor
$\beta_{c,\theta,\mathrm{water}}$	[m/sK]	parameter for calculating the speed of sound in water
$\beta_{c,p,\mathrm{water}}$	[m/sPa]	parameter for calculating the speed of sound in water
β_{SK}	[−]	skewness of a computational cell
γ	[−]	isentropic coefficient
δ_{ij}	[−]	Kronecker delta
ε	[m^2/s^3]	turbulence dissipation rate
ζ	[−]	model parameter of the $\boldsymbol{k}$-ζ-f turbulence model
κ	[1/m]	wave-number

Symbol	Unit	Description
λ	$[-]$	parameter
Λ	$[\mathrm{m/s^2}]$	aeroacoustic momentum source cross-term
μ	$[\mathrm{Pas}]$	molecular viscosity of the fluid
ν	$[\mathrm{m^2/s}]$	kinematic viscosity of the fluid
ν_{SGS}	$[\mathrm{m^2/s}]$	SGS viscosity
ν_{t}	$[\mathrm{m^2/s}]$	eddy viscosity
Ξ	$[\mathrm{rad}]$	random phase
ρ	$[\mathrm{kg/m^3}]$	density
σ	$[\mathrm{kgK/J}]$	inverse of c_p
$\vec{\sigma}_\kappa$	$[-]$	direction of turbulence velocity vector per wave-number κ
$\sigma_{\mathscr{k}\zeta f}$	$[-]$	$\mathscr{k}$-ζ-f model parameter
θ	$[\mathrm{K}]$	temperature
θ_{S}	$[\mathrm{K}]$	Sutherland's temperature
τ_{ij}	$[\mathrm{kg/ms^2}]$	viscous shear stress tensor
Π	$[\mathrm{Pa/s}]$	aeroacoustic pressure source cross-term
ϕ	$[-]$	arbitrary quantity
ψ	$[-]$	arbitrary quantity
Ψ	$[-]$	complex amplitude of an arbitrary quantity
$\vec{\omega}$	$[\mathrm{1/s}]$	vorticity vector
Ω	$[\mathrm{m/s^2}]$	centered aeroacoustic source term

Superscript symbols

Superscript	Description
$'$	fluctuating variable based on temporal average
$'^{\mathrm{ea}}$	fluctuating variable based on ensemble average
$'^{\mathrm{fa}}$	fluctuating variable based on Fourier average
$'^{\mathrm{ma}}$	fluctuating variable based on moving average
$''$	unresolved by LES
$+$	dimensionless quantity normalized with the wall friction velocity

Superscript	Description
*	dimensionless quantity normalized with characteristic scale of the geometry (inner pipe radius R_I)

Subscript symbols

Subscript	Description
0	mean base flow
ax	axial direction
a	acoustic contribution
conv	convective
C	computational cell
Cyl	cylindrical
diff	diffusive
ea	ensemble average
E	computational cell edge
fluct	fluctuating
F	computational cell face
G	geometry
high	upper limit
h_5	orifice with $h_\mathrm{O} = 5\,\mathrm{mm}$
h_{10}	orifice with $h_\mathrm{O} = 10\,\mathrm{mm}$
i	directional index x, y and z
init	initialization
I	inner pipe radius
j	directional index x, y and z
k	directional index x, y and z
K	Von Kármán constant
$\mathcal{K}$	Kolmogorov scale
κ	wave-number
$k\zeta f$	k-ζ-f turbulence model
low	lower limit
L	large (integral) scale

Subscript	Description
max	maximum
mean	mean base flow
min	minimum
ma	moving average
N	computational cell nodes
O	orifice
pert	perturbation function
PL	power law
ramp	ramping function
ref	reference quantity
t	turbulent
tg	tangential direction
tot	total
TF	temporal filter
τ_{W}	wall friction
W	wall

Acronyms

Acronym	Description
AP	acoustic pipe
BC	boundary condition
BL	boundary layer
CAA	computational aeroacoustics
CFD	computational fluid dynamics
CV	control volumes
DES	detached eddy simulation
DNS	direct numerical simulation
FEM	finite element method
FFT	fast Fourier transformation
FTT	flow-through time

Acronym	Description
FVM	finite volume method
G	grid
GP	grid positions
LEE	linearized Euler equations
LES	Large-Eddy Simulation
LHS	left hand side
PANS	partial averaged Navier-Stokes
PP	periodic pipe
RANS	Reynolds averaged Navier-Stokes
RHS	right hand side
SGM	subgrid-scale model
SGS	subgrid-scale
SNGR	stochastic noise generation and radiation
UKSG	unstructured kinematic source generator
URANS	unsteady Reynolds averaged Navier-Stokes
VKS	Von Kármán spectrum

Dimensionless Numbers

Dimensionless Number	Definition
Courant Friedrichs Lewy number in case of incompressible CFD:	$CFL_{\text{CFD}} = \frac{\lvert v \rvert \Delta t}{\Delta x}$
Courant Friedrichs Lewy number in case of CAA:	$CFL_{\text{CAA}} = \frac{(\lvert v \rvert + c)\,\Delta t}{\Delta x}$
Mach number:	$\mathcal{Ma} = \frac{\lvert v \rvert}{c}$
Reynolds number:	$\mathcal{Re} = \frac{v \ell}{\nu}$

Mathematical expressions

Most equations are written in the Cartesian tensor notation, also known as *Einstein* notation. Thus, a simple rule of summation applies, indicating a summation over all three components 1,2 and 3 (which correspond to the three Cartesian coordinates x,y and z) is required whenever the same indices appear repeatedly in a given term, e.g.,

$$\sum_{i=1}^{3} \phi_i \psi_i = \phi_1 \psi_1 + \phi_2 \psi_2 + \phi_3 \psi_3 = \phi_i \psi_i$$

Definition	Description
$\langle \ \rangle$	temporal average
$\langle \ \rangle_{\mathrm{ea}}$	ensemble average
$\langle \ \rangle_{\mathrm{fa}}$	Fourier average
$\langle \ \rangle_{\mathrm{ma}}$	moving average
$\tilde{}$	from LES resolved (filtered) quantity
$\bar{}$	mean flow configuration
$\vec{}$	column vector
$\vert \ \vert$	absolute of quantity
$\vert\vert \ \vert\vert$	norm of quantity
δ	change
$\frac{\partial}{\partial x_i}$	partial derivative in i direction
$\frac{D}{Dt}$	material derivative
$\mathcal{F}$	Fourier transformation
$\mathcal{F}^{-1}$	inverse Fourier transformation

Contents

1 Introduction

1.1 Background

One important goal of research and development in industry is to shorten and simultaneously improve product development processes. This can be achieved by introducing novel enhanced methods into the product development process or by improving already existing ones. One of these methods is numerical simulation, which is now standard in various product development processes in many branches of industry, e.g. the automotive industry. Basically, all simulation methods have the advantage that they can be applied at a relatively early phase of the product development process, as compared to measurements, when there is no physical model available yet. Therefore, simulation can strongly support the whole product development process from the very beginning. Of course, the reliability of simulations significantly depends on the quality of the input data (boundary conditions, geometry data, etc.) which has to be available. The rapid increase and cost reduction of computational power has led to a large increase of simulation tools and models.

The automotive industry currently experiences a shift from combustion engines to electric engines which is driven by climate change and political decisions. As a consequence, new issues arise, which essentially come from the change of the engine. This Master's Thesis is particularly motivated by the fact that combustion engines are basically much louder than electric engines, and hence drown all additional low-intensity noise coming from other sources (e.g. from valves in the coolant system). Due to the much lower sound emissions of electric engines, this additional noise generated from other sources might become more and more relevant. Therefore, the automotive industry is supposed to put more effort into interior and exterior sound design, which requires a better description, understanding, and finally control of the acoustics of the individual components.

1.2 Acoustics and aeroacoustics

The main aim of acoustics is to assess (both numerically and experimentally) the noise which is radiated from an object at an arbitrary point that can be detected by the human ear. The major difficulty in acoustics lies with the wide range of acoustic energy which has to be resolved. For example, the human ear can detect sound in the range from the threshold of hearing at $p_{\mathrm{RMS,min}} = 10^{-5}\,\mathrm{Pa}$ to the threshold of pain at $p_{\mathrm{RMS,max}} = 10^{2}\,\mathrm{Pa}$, within the frequency range of $\not{f}_{\mathrm{low}} = 20\,\mathrm{Hz}$ to $\not{f}_{\mathrm{high}} = 20\,\mathrm{kHz}$. Acoustics is a very broad field of study, which can be divided into multiple subfields. The numerous subfields focus on different effects of acoustics. E.g., psychoacoustics studies the perception of noise by humans and its influence on health, whereas elastoacoustics studies the noise emission of vibrating objects.

In classical acoustics non-linear effects are often negligible and the generation of sound is often defined in terms of a specific boundary condition (e.g. the unsteady movement (vibration) of a solid plate: loudspeakers).

This Master's Thesis can be assigned to the subfield of aeroacoustics. Aeroacoustics focuses on the radiation of noise from turbulent flow. Turbulence is a non-linear partly chaotic motion of the fluid, where a rigorous deterministic description is not available. Basically, the governing equations of fluid dynamics, the Navier-Stokes equations together with the conservation equation of energy, describe all flow (turbulence, etc.) and acoustic (wave propagation, scattering, refraction, etc.) effects. Therefore, aeroacoustics involves a large part of fluid dynamics, as it is dealing with turbulent flow structures as sound sources.

Aeroacoustics is typically based on the famous *Lighthill's acoustic analogy* [36, 37]. Lighthill used the Navier-Stokes equations, which are the governing equations of fluid mechanics, to derive an exact formulation of the wave equation for the density (and pressure) fluctuations ρ_{a}

$$\frac{\partial^2 \rho_{\mathrm{a}}}{\partial t^2} - \frac{1}{c_0^2} \frac{\partial^2 \rho_{\mathrm{a}}}{\partial x_i^2} = \frac{\partial^2 T_{ij}}{\partial x_i \partial x_j}, \tag{1.1}$$

where c_0 is the speed of sound. The left hand side (LHS) represents a simple wave operator, which can be solved numerically but also analytically, as long as the aeroacoustic sources on the right hand side (RHS) are known. The wave operator, on the LHS, of Lighthill's equation is equal to the wave operator used in classical acoustics. Therefore, Lighthill's theory is called an acoustic analogy.

The aeroacoustic source term, on the RHS, is represented by the well-known *Lighthill stress tensor*:

$$T_{ij} = \rho v_i v_j - \tau_{ij} + (p_\mathrm{a} - c_0^2 \rho_\mathrm{a})\delta_{ij}, \tag{1.2}$$

where v_i is the flow velocity, τ_{ij} are the viscous shear stresses and p_a are the pressure fluctuations, which are related to the density fluctuations through $p_\mathrm{a} = c_0^2 \rho_\mathrm{a}$. Aeroacoustics might also include the generation of sound due to heat transfer and chemical reactions within the flow (e.g. in a combustion engine).

The main problem with Lighthill's acoustic analogy is that all interactions between the acoustic field and the aeroacoustic sources are neglected and all sound propagation phenomena, like refraction or scattering at flow uniformities appear as sound sources, although they are only kinematic effects. Lighthill's acoustic analogy was repeatedly improved by including additional effects into the aeroacoustic source term. E.g., Curle [20] introduced the impact of solid boundaries. Powell [44] and Howe [30] included the feedback phenomenon from the acoustic field to the sound sources based on the vortex-sound theory. Ffowcs-Williams & Hawkings [57] introduced the noise from arbitrarily moving objects.

Goldstein [25, 26] derived a more general acoustic analogy based on Phillips' [42] convected wave equation and Lilley's [38, 39] idea to split the aeroacoustic source terms into its isentropic and anisentropic parts. This acoustic analogy includes sound propagation phenomena into the wave operator. Thus, it becomes better applicable in non-uniform flows (at least for some simple applications), but it has to be solved numerically due to the complex wave operator. This advanced acoustic analogy is often referred to as *Lilley's acoustic analogy.*

1.3 Computational aeroacoustics

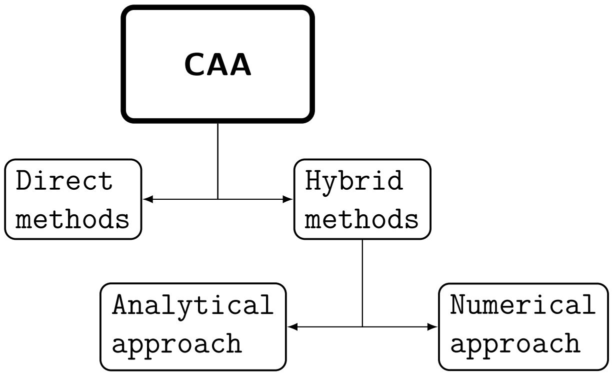

Figure 1.1: Overview of CAA methods.

In computational aeroacoustics (CAA) generally two different approaches (see figure 1.1) for solving the acoustic field exist [10, 56].

The first approach is to solve directly the Navier-Stokes equations and therefore, to resolve all flow and acoustic effects, which is computationally very demanding and costly. Subsonic flow configurations with high turbulence, which this Master's Thesis is focused on, require a high spatial resolution to capture all relevant turbulent structures. Acoustics additionally requires a significantly higher temporal resolution to resolve all frequencies of interest. In combination this enormously increases the computational demand. This is the reason why direct approaches are often not feasible for most technically relevant applications. Additionally, the energy contained in the aerodynamic forces is usually some orders of magnitude greater than the acoustic energy [35]. Therefore, CAA solvers need to be as numerically accurate as possible so that even the smallest acoustic waves are still resolved.

One possible alternative approach to direct simulations is to use a *hybrid approach*, which seperates the flow and acoustic fields and therefore calculates the flow field using (incompressible) computational fluid dynamics (CFD), and acoustic field separately. These hybrid approaches are based on the *aeroacoustic decompositions*, which is for an arbitrary field variable ϕ defined as

$$\phi = \langle\phi\rangle + \phi' + \phi_{\mathrm{a}}, \tag{1.3}$$

where, $\langle\phi\rangle$ represents the mean value, ϕ' the turbulent fluctuating and ϕ_{a} the acoustic contribution. Hybrid approaches are based on acoustic analogies (e.g. Lighhill, Lilley, etc.) which introduce a wave operator describing the wave propagation and associated aeroacoustic sources. The latter are required as closure for solving the acoustic field and are extracted from the CFD solution. CAA methods distinguish between analytical and numerical approaches. Analytical techniques are based on integral methods (e.g. Kirchhoff's surface integral, Ffowcs Williams-Hawkings (FW-H) equations, etc.), where the sound pressure, at a specific point, is calculated by integrating over the region containing the aeroacoustic sources. Numerical techniques are similar to the CFD approach, in that both solve numerically the governing partial differential equations in the entire domain of interest. Thus, in contrast to analytical techniques the numerical approach computes the flow field and the sound pressure simultaneously in the whole computational domain.

One typical feature of hybrid approaches is that different computational grids and temporal resolution are possible. On the one hand, this is disadvantageous, because additional temporal and spatial interpolation is required, which might introduce additional numerical uncertainties and instabilities. On the other hand, it is advantageous, since the temporal and spatial discretization schemes can easily be fine-tuned to meet the different requirements of CFD and CAA, seperately. In general, CFD solvers are often more diffusive than CAA solvers, which helps them to quickly damp numerical instabilities so that a converged solution is reached faster. In contrast, CAA solvers, which describe the propagation of sound waves have to transport also the weakest sound waves, therefore, need to be as less diffusive as possible.

The main drawback, of hybrid CAA approaches is that acoustic and flow effects are decoupled, because the turbulent flow and acoustic fields are computed separately. Therefore, the aeroacoustic sources obtained from the incompressible flow field being fully decoupled from acoustic phenomena cannot account for effects, which originate from the interactions between the turbulent flow and acoustic field.

In the numerical approach the acoustic field is often computed solving *linearized Euler equations* (LEE) [10, 11], which are much simpler compared to the full set of the compressible conservation equations, since non-linear terms do not occur in the wave operator. It can be further shown that the acoustic analogy based on the LEE is equivalent to Lilley's acoustic analogy [17, 18, 26], if both are applied to sheared flows.

The dominant aeroacoustic source term appearing in the momentum equation of the LEE, which originates from turbulence-turbulence interaction, is

$$\Omega'_i = v'_j \frac{\partial v'_i}{\partial x_j} - \left\langle v'_j \frac{\partial v'_i}{\partial x_j} \right\rangle , \tag{1.4}$$

where v'_i are the turbulent velocity fluctuations. This formulation for the aeroacoustic source term is often applied when solving the acoustic field based on the LEE [1, 8, 17, 19]. Bogey et al. [17] argued that centering achieved by the subtraction of the temporal average of the source term in equation (1.4) stabilizes the numerical solution process of the LEE and leads to better prediction of the acoustic field near the source region.

Carrying out the linearization of the Euler equations, based on the aeroacoustic decomposition, additional cross-terms, representing interaction between the mean flow field and the turbulence fluctuations, appear in the momentum and energy equation. If these cross-terms are included into the source term the equation stays formally exact. Bechara et al. [13] considered the dominant aeroacoustic source terms (1.4) together with the cross-terms, whereas Colonius et al. [18] and Goldstein [26] argued that these additional cross-terms are often negligible.

1.4 Motivation and aims

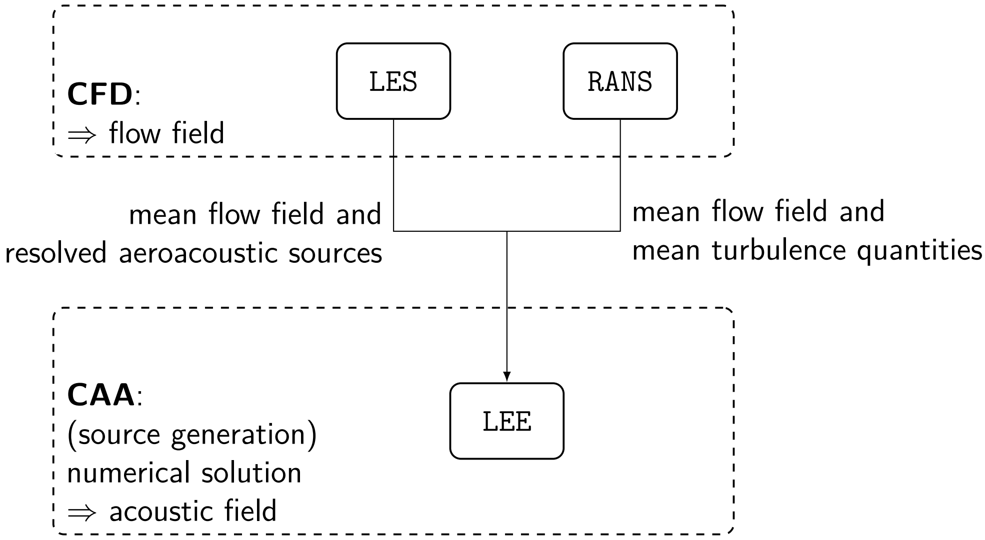

Figure 1.2: Discussed hybrid CAA methods.

This Master's Thesis was done in cooperation with AVL LIST GmbH[1](AVL) and the Institute of Fluid Mechanics and Heat Transfer (ISW) of Graz University of Technology (TU Graz). Because of the cooperation with AVL, the CFD software AVL FIRE™ [7] was used. A CAA tool is already implemented into FIRE™ [6], which follows a hybrid approach, where the source terms are calculated from a prior RANS-type CFD simulation, and the acoustic radiation (CAA) is based on numerical solution of the LEE (see figure 1.2), which is a widespread standard approach [8, 9, 11, 14]. In the current version the aeroacoustic sources are artificially generated by using the *unstructured kinematic source generator* (UKSG), which is part of the CAA tool implemented in FIRE™. This aeroacoustic source generation module relies on a stochastic approach reflecting the stochastic nature of turbulence.

The alternative to a RANS based CFD in combination with a modeling of the aeroacoustic source terms is to use a CFD method, which is capable of computing directly the aeroacoustic source terms, which requires the direct simulation of turbulent motion. The method of *Large-Eddy Simulation* (LES) [23, 54] is by definition capable of resolving directly most parts of the turbulent motion down to the limit of the unresolved small structures (*subgrid-scale*, SGS). Therefore, the aeroacoustic sources calculated from a LES are expected to better describe the physics of sound generation induced by the turbulent eddy motion, especially in complex flow configurations. This higher level of description comes of course

---

[1] https://www.avl.com/home

with much higher computational costs, which is the main advantage of the RANS based method.

The primary goal of this Master's Thesis is to calculate the sound sources for the LEE directly from LES and compare them with the aeroacoustic sources computed with the existing sound generation module of FIRE™. As a secondary goal it shall be further analyzed to which extent the source terms obtained from the LES contain contributions from large low-frequency vortical structures. It shall be investigated, how to assess and quantify the possible contribution of these large low-frequency vortical structures to the aeroacoustic source term. An additional goal is the investigation of the possible contributions of the cross-terms, arising from the linearization of the Euler equations. Aside from the computation and analysis of the aeroacoustic source terms, the results of the underlying LES and RANS-type CFD solutions of the flow field shall be discussed and validated against data from direct numerical simulation (DNS) as well [32].

The geometry considered in this Master's Thesis is a straight pipe containing a sharp contraction/orifice. This geometry was particularly chosen because AVL launched a project in parallel to this Master's Thesis, where this particular configuration was examined experimentally and numerically. The design of the experimental setup used in this project essentially follows the Ph.D.-thesis of Hofman [29]. Similar geometries were considered in publications of Bailly et al. [8], Longatte et al. [40], Crouzet et al. [19], Gloerfelt & Lafon [24] and Bayati et al. [12]. The computational part of the parallel project was focused on the simulation of the flow using RANS and the acoustic field with the CAA module as implemented in FIRE™. The project was carried out by the VIRTUAL VEHICLE Research Center[2] Graz. The grids for the CAA simulation were generated by the VIRTUAL VEHICLE Research Center, whereas the grids used for all the CFD simulations were generated in the framework of this Master's Thesis.

---

[2] http://www.v2c2.at

1.5 Document structure

The structure of this Master's Thesis can roughly be divided into two parts, the theoretical and the practical part. In the first part, the fundamental theories are introduced. In the second part, the methods for reaching the aims of this Master's Thesis and the obtained results are presented and discussed.

The theoretical part starts with an introduction of the basic principles for describing acoustics, fluid mechanics and the propagation of sound waves in chapter 2. The document continues with a discussion of the phenomenon of turbulence in chapter 3, in particular with the generally applied modeling approaches, and the realization in CFD. An introduction to aeroacoustics is given in chapter 4, where the acoustic analogies and their corresponding aeroacoustic sources are derived. The computation of the aeroacoustic sources from the LES solution and the possible contribution of the unresolved SGS terms is presented and discussed as well. The theoretical part is concluded with a brief introduction of the solution procedure in the CAA tool implemented in FIRE™ and the presentation of the mathematical algorithm of the UKSG.

The practical part starts with a detailed problem definition (geometry, flow configuration, etc.) and the applied methods for handling the individual tasks of this Master's Thesis in chapter 5. The results of the CFD simulations, which are the basis of the aeroacoustic sources, are presented in chapter 6. In the following chapter 7 the resulting aeroacoustic source terms from the CFD simulation are presented and compared to the aeroacoustic sources from the source generation module implemented in FIRE™. The possible influence of the large low-frequency vortical structures on the aeroacoustic source terms is also discussed and presented in this chapter. Additionally, the LES results for the cross-terms, arising from the linearization of the Euler equations, are presented and discussed. The document concludes in chapter 8 with a summary of the most important results and conclusions as well as an outlook on possible further investigations. Additional tabulated results are appended (see appendix A).

2 Fundamentals

This chapter introduces and discusses the fundamentals which are required for describing the acoustics in a stagnant fluid in section 2.1. The sound pressure, one of the target quantities of acoustics, is explained at first. It follows a presentation of the governing equations of fluid mechanics in section 2.2, which are derived in various different formulations. The focus is on a most complete derivation of these governing equations so that all applied assumptions and simplifications are clearly seen. In section 2.3 the propagation of sound waves is discussed by deriving the simplest wave equation, introducing the speed of sound as the characteristic velocity.

2.1 Acoustics

Hearing is the sensation of sound due to small mechanical stimulations of certain parts of the ear. These oscillatory stimulations are essentially caused by the unsteady *sound pressure*, which is defined as

$$p'(t) := p(t) - \langle p \rangle \qquad [\mathrm{Pa}], \tag{2.1}$$

where $\langle p \rangle$ is the temporal average (steady or mean part) of the instantaneous pressure $p(t)$. The *temporal average pressure* $\langle p \rangle$ is defined as:

$$\langle p \rangle := \lim_{T \to \infty} \frac{1}{T} \int_{T_0}^{T} p(t) dt. \tag{2.2}$$

This steady base pressure has no influence on the sensation of sound. The strength of the sound pressure is quantified in terms of the *root mean square* (RMS) of the fluctuation, written as

$$p_{\mathrm{RMS}} = \sqrt{\langle (p'(t))^2 \rangle} \qquad [\mathrm{Pa}]. \tag{2.3}$$

The human ear is capable of resolving a large range of sound pressure strength. It covers a range from the threshold of hearing at $p_{\mathrm{RMS,min}} = 10^{-5}$ Pa to the threshold of pain at $p_{\mathrm{RMS,max}} = 10^{2}$ Pa. Due to this wide range, a logarithmic scale was introduced to define the *sound pressure level* as:

$$L_p := 10 \log_{10} \left(\frac{p_{\mathrm{RMS}}}{p_{\mathrm{ref}}} \right)^2 = 20 \log_{10} \left(\frac{p_{\mathrm{RMS}}}{p_{\mathrm{ref}}} \right) \qquad [\mathrm{dB}]. \tag{2.4}$$

The threshold of hearing at approximately 1 kHz in air is used as the reference pressure $p_{\mathrm{ref,air}} = 20 \times 10^{-6}$ Pa. For other fluids (e.g. water) the reference pressure $p_{\mathrm{ref}} = 10^{-6}$ Pa is used.

The main difficulty of computational acoustics is the strong disparity of the largest and smallest scales of the sound pressure, which need to be resolved for accurate predictions.

The time-period T, over which the temporal averaging is applied, determines the lower limit of frequencies f_{low}, which can be considered, since

$$f_{\mathrm{low}} = \frac{1}{T}. \tag{2.5}$$

The upper limit of the resolvable frequencies is practically determined by the sampling rate in measurements, or the time-step size in numerical simulations used for temporal discretization. Accordingly, the number of time-steps N_T, which are used to discretize the time-period T, define the upper limit of resolved frequencies:

$$\not{f}_{\text{high}} = \frac{1}{2\Delta t}, \quad \text{where} \tag{2.6}$$

$$\Delta t = \frac{T}{N_T}. \tag{2.7}$$

This restriction is based on the Nyquist criterion, which states that the highest resolved frequency $\not{f}_{\text{high}}$ is half of the sampling frequency $1/\Delta t$. Thus, the time-period T and the time-step Δt have to be chosen appropriately to the considered problem, regardless of whether the sound pressure is accessed by simulation or measurement. For example, the human ear responds to frequencies from approximately $\not{f}_{\text{low}} = 20\,\text{Hz}$ to $\not{f}_{\text{high}} = 20\,\text{kHz}$, which requires a time-step of $\Delta t = 2.5\times10^{-5}\,\text{s}$ and a time-period of $T = 0.05\,\text{s}$.

Summing up, it can be stated, that the pressure p represents a key quantity in acoustics. The difficulty to access the sound pressure level is not only due to the typical large disparity of the smallest and the largest relevant pressure scales. It also arises from the energy associated with the acoustic pressure fluctuations, which might be very small compared to the energy contained in the turbulent motion, and thus, is difficult to capture.

2.2 Governing equations

In this section, the governing equations of fluid mechanics are introduced [52]. Starting from the general laws of conservation, several alternative formulations will be derived, which constitute the basis for further definitions and specifications.

2.2.1 Conservation laws

In general, fluid is considered a continuum and its motion can be described by the conservation laws for mass, momentum and energy. The corresponding conservation equations assume a compressible Newtonian fluid and are written in Cartesian coordinates. The conservation law for mass, termed *continuity equation*, reads

$$\frac{\partial \rho}{\partial t} + \frac{\partial}{\partial x_j} \left(\rho v_j \right) = S_{\dot{m}}, \tag{2.8}$$

where ρ is the fluid density, v_j is the velocity component in direction x_j and t is the time. The term $S_{\dot{m}}$ represents a mass source. It is included in the general formulation, because mass sources $S_{\dot{m}}$ can contribute to the generation of sound. They will be excluded for the presently considered sound field though, as will be shown later.

The conservation equation of momentum are also known as the *Navier-Stokes equations*. For the momentum in direction x_i, they are rewritten as

$$\frac{\partial}{\partial t} \left(\rho v_i \right) + \frac{\partial}{\partial x_j} \left(\rho v_j v_i \right) = + \frac{\partial}{\partial x_j} \left(P_{ji} \right) + S_{f,i} + S_{\dot{m}} v_i, \tag{2.9}$$

where P_{ji} is the *fluid stress tensor* and $S_{f,i}$ is an external volumetric body force. The term $S_{\dot{m}} v_i$ is the contribution of the mass source to the momentum, if injected with velocity v_i, when considering the mass source term $S_{\dot{m}}$ in the continuity equation. The fluid stress tensor P_{ji} is composed of the static pressure p and the *viscous stresses* τ_{ji}

$$P_{ji} = -p \delta_{ij} + \tau_{ji}, \tag{2.10}$$

where δ_{ij} is the *Kronecker delta*, which is defined as

$$\delta_{ij} = \begin{cases} 1 & \text{if } i = j \\ 0 & \text{if } i \neq j \end{cases}. \tag{2.11}$$

Fluids in general oppose the rate of deformation and not the deformation itself, as solids do. The stress tensor τ_{ji} is modeled based on *Stokes' hypothesis* for Newtonian fluids, where the relation between stresses and the deformation rate is linear. Using these assumptions the stress tensor τ_{ji} is

$$\tau_{ji} = \eta \left(\frac{\partial v_i}{\partial x_j} + \frac{\partial v_j}{\partial x_i} \right) - \frac{2}{3} \eta \left(\frac{\partial v_k}{\partial x_k} \right) \delta_{ij}. \tag{2.12}$$

The *dynamic viscosity* η is a property of the fluid, which is in general dependent of the temperature θ and the pressure p, and can be experimentally determined for the considered fluid.

The velocity gradient $\partial v_i / \partial x_j$ can be decomposed into two parts

$$\frac{\partial v_i}{\partial x_j} = \underbrace{\frac{1}{2} \left(\frac{\partial v_i}{\partial x_j} + \frac{\partial v_j}{\partial x_i} \right)}_{S_{ij}} + \underbrace{\frac{1}{2} \left(\frac{\partial v_i}{\partial x_j} - \frac{\partial v_j}{\partial x_i} \right)}_{W_{ij}}, \tag{2.13}$$

where the symmetric *rate of strain tensor* S_{ij} and the asymmetric *vorticity tensor* W_{ij} appear. Note that the stress tensor τ_{ji} (2.12) only depends on the rate of strain tensor S_{ij}, because a fluid in rigid rotation represented by W_{ij} does not experience viscous stresses.

The conservation equation for the *total energy* e_{tot}, which is composed of the specific *internal energy* e and the specific kinetic energy

$$e_{\mathrm{tot}} = e + \frac{1}{2} |v|^2. \tag{2.14}$$

reads

$$\begin{aligned} \frac{\partial}{\partial t} \left(\rho e_{\mathrm{tot}} \right) + \frac{\partial}{\partial x_j} \left(\rho v_j e_{\mathrm{tot}} \right) = & - \frac{\partial}{\partial x_j} \left(p v_j \right) - \frac{\partial q_j}{\partial x_j} + \frac{\partial}{\partial x_j} \left(\tau_{ji} v_i \right) \\ & + S_{f,i} v_i + S_{\dot{m}} e_t + S_\theta. \end{aligned} \tag{2.15}$$

The heat flux q_j, due to conduction, can be described by *Fourier's law*

$$q_j = -\mathrm{k} \frac{\partial \theta}{\partial x_j}, \tag{2.16}$$

where k is the heat conductivity of the fluid and θ is the local fluid temperature. $S_{f,i} v_i$ is the power due to the action of an external body force, $S_{\dot{m}} e_t$ is the power due to mass injection, if included, and S_θ is an external volumetric heat source.

The non-linear convective terms on the LHS of the conservation equations momentum (2.9) and energy (2.15) are the origin of turbulence. Since turbulence plays a great role for the generation of flow-induced sound sources, two distinct sections 3.1 and 3.2 are devoted to this phenomenon. It is further noted that the acoustic pressure p_a, the key acoustic variable, is included in the presented fully compressible formulation. Thus, if this system of equations is solved directly, all aeroacoustic effects, like wave propagation, refraction and scattering, can be described as well. As already mentioned, the direct numerical solution of this system of equations comes with huge computational costs. This is mainly due to the large wide range of relevant scales of the pressure as well as the turbulence, which need to be resolved.

2.2.2 Primitive form of the conservation laws

In this section, the so called primitive forms of the conservation laws are derived. For this derivation the *material derivative*, defined as:

$$\frac{D}{Dt} := \underbrace{\frac{\partial}{\partial t}}_{I} + \underbrace{v_j \frac{\partial}{\partial x_j}}_{II}, \tag{2.17}$$

is considered. The first term on the RHS (I) represents the local temporal change, while the second therm (II) represents convective change of an arbitrary quantity. Using this material derivative, the conservation equations of mass (2.8), momentum (2.9) and energy (2.15) can be rewritten in primitive formulation as

$$\frac{D\rho}{Dt} = -\rho \frac{\partial v_j}{\partial x_j} + S_{\dot{m}}, \tag{2.18a}$$

$$\rho \frac{Dv_i}{Dt} = -\frac{\partial p}{\partial x_i} + \frac{\partial \tau_{ji}}{\partial x_j} + S_{f,i} \qquad \text{and} \tag{2.18b}$$

$$\rho \frac{De}{Dt} = -p \frac{\partial v_j}{\partial x_j} + \tau_{ji} \frac{\partial v_i}{\partial x_j} - \frac{\partial q_j}{\partial x_j} + S_\theta. \tag{2.18c}$$

The mass source in the momentum and energy equation vanish in this formulation.

2.2.3 The closure of the system of primitive equations

The system of conservation law equations (2.18) involve seven dependent variables: density ρ, pressure p, three velocity components v_i, specific inner energy e and the temperature θ. To close this set of equations, two additional relations are needed. The closure is essentially based on the *fundamental law of thermo-*

dynamics by Gibbs, which reads for a reversible process

$$\theta \delta s = \delta e - \frac{p}{\rho^2} \delta \rho \tag{2.19}$$

Here, the *specific entropy* s is introduced as a new variable, which will replace the internal energy e. The *change* δ can be interpreted as the material based change following a fluid particle. Thus, the fundamental law of thermodynamics can be written in terms of the material derivatives as

$$\theta \frac{Ds}{Dt} = \frac{De}{Dt} - \frac{p}{\rho^2} \frac{D\rho}{Dt}. \tag{2.20}$$

Introducing the material derivative of the internal energy obtained from (2.20) into the primitive form of the energy equation (2.18c) and incorporating the primitive form of the continuity equation (2.18a) yields

$$\rho \frac{Ds}{Dt} = \frac{1}{\theta} \left[\tau_{ji} \frac{\partial v_i}{\partial x_j} - \frac{\partial q_j}{\partial x_j} + S_\theta - \frac{p}{\rho} S_{\dot{m}} \right]. \tag{2.21}$$

Note that the entropy equation (2.21) is just a reformulation of the energy equation (2.18c).

In the next step a thermodynamic relation

$$\rho = \rho(p, s) \tag{2.22}$$

is introduced, which describes in particular the dependence of the density ρ as a function of the pressure p and the entropy s. The total variation of the density can be accordingly written as

$$\delta \rho = \underbrace{\left(\frac{\partial \rho}{\partial p} \right)_s}_{=:\frac{1}{c^2}} \delta p + \underbrace{\left(\frac{\partial \rho}{\partial s} \right)_p}_{=:-\rho\sigma} \delta s, \tag{2.23}$$

involving the two new expressions

$$c^2 := \left(\frac{\partial \rho}{\partial p} \right)_s^{-1}, \qquad \text{and} \tag{2.24a}$$

$$\sigma := \left(\frac{\partial \rho}{\partial s} \right)_p. \tag{2.24b}$$

Later in this chapter it is shown that c is a measure for the isentropic speed of sound. Recalling the equivalence between the total variation and the material derivative, equation (2.23) can be written as

$$\frac{1}{c^2}\frac{Dp}{Dt} = \frac{D\rho}{Dt} + \rho\sigma\frac{Ds}{Dt}. \tag{2.25}$$

Introducing (2.25) into the entropy equation (2.21) and recalling the primitive formulation of the continuity equation (2.18a) finally leads to a formulation of the energy equation yielding the pressure p according to

$$\frac{1}{c^2}\frac{Dp}{Dt} = -\rho\frac{\partial v_j}{\partial x_j} + \frac{\sigma}{\theta}\left[\tau_{ji}\frac{\partial v_i}{\partial x_j} - \frac{\partial q_j}{\partial x_j} + S_\theta\right] + S_{\dot{m}}\left[1 - \frac{\sigma}{\theta}\frac{p}{\rho}\right]. \tag{2.26}$$

The system of equations is finally closed by introducing the *thermal equation of state*, which reads for a *perfect gas*

$$\rho = \frac{p}{\mathcal{R}\theta}, \tag{2.27}$$

where $\mathcal{R}$ is the *specific gas constant.* The perfect gas assumption is applied as well for determining the parameters c^2 and σ. For a perfect gas one can write

$$de = c_v d\theta, \tag{2.28a}$$

$$\mathcal{R} = c_p - c_v \qquad \text{and} \tag{2.28b}$$

$$\gamma = \frac{c_p}{c_v}, \tag{2.28c}$$

where c_p and c_v are the constant *specific heat capacities* at constant pressure and volume, respectively, and γ is the *isentropic coefficient.* Using (2.27), (2.28a), (2.28c) and (2.19) one obtains

$$c^2 = \gamma\mathcal{R}\theta = \gamma\frac{p}{\rho} \qquad \text{and} \tag{2.29a}$$

$$\sigma = \frac{1}{c_p}. \tag{2.29b}$$

Finally, the closed system of equations for a perfect gas in primitive form can be rewritten as

$$\frac{D\rho}{Dt} = -\rho\frac{\partial v_j}{\partial x_j} + S_{\dot{m}}, \tag{2.30a}$$

$$\rho\frac{Dv_i}{Dt} = -\frac{\partial p}{\partial x_i} + \frac{\partial \tau_{ji}}{\partial x_j} + S_{f,i}, \tag{2.30b}$$

$$\frac{Dp}{Dt} = -\gamma p\frac{\partial v_j}{\partial x_j} + \left[\tau_{ji}\frac{\partial v_i}{\partial x_j} - \frac{\partial q_j}{\partial x_j} + S_\theta\right](\gamma - 1) + S_{\dot{m}}\frac{p}{\rho}. \tag{2.30c}$$

2.2.4 Inviscid flows with no conductive/radiative heat transfer

Inviscid flow of non-conducting/radiating fluids is generally described by the so called Euler equations. The *Euler equations* can be directly derived from the full closed system of equations given by (2.30), applying some simplifications. The first simplification excludes the external sources of mass $S_{\dot{m}}$ and chemical heat release S_θ. The second simplification neglects the viscous forces and dissipation, as well as the conductive or radiative heat transfer. These simplifications imply isentropic flow such that

$$\frac{Ds}{Dt} = 0. \tag{2.31}$$

Applying these simplifications, the system of governing equations is reduced to

$$\frac{D\rho}{Dt} = -\rho\frac{\partial v_j}{\partial x_j}, \tag{2.32a}$$

$$\frac{Dv_i}{Dt} = -\frac{1}{\rho}\frac{\partial p}{\partial x_i} + S_{f,i}, \tag{2.32b}$$

$$\frac{1}{c^2}\frac{Dp}{Dt} = -\rho\frac{\partial v_j}{\partial x_j}. \tag{2.32c}$$

It is noted that the pressure equation (2.32c) is equivalent to the isentropy condition (2.31). However, since the pressure p is the target variable in acoustics, the pressure equation is often preferred.

The system of Euler equations, which is solved by the CAA module of FIRE™, additionally neglects all body forces $S_{f,i}$, and uses a different formulation of the pressure equation (2.32c). Since the isentropy condition (2.31) also implies

$$\frac{1}{\rho}\frac{Dp}{Dt} = \gamma\frac{D\rho}{Dt}, \tag{2.33}$$

equation (2.32c) is accordingly rewritten to

$$\frac{Dp}{Dt} = -\,\gamma p \frac{\partial v_j}{\partial x_j}. \tag{2.34}$$

2.2.5 Incompressible flows

Starting from the full system of conservation equations written in conservative form, (2.8), (2.9) and (2.15) and introducing some simplifications, the system of equations for *incompressible* flows is derived. The external source terms $S_{\dot{m}}$ and S_θ are neglected again. Dissipation due to viscous stresses are also neglected. Assuming incompressible flow basically implies that the pressure p is decoupled from the density ρ. Additionally, assuming no heat transfer due to conduction and radiation further implies isothermal flows such that the density is constant and the conservative equations of mass and momentum reduce to

$$\frac{\partial v_j}{\partial x_j} = 0 \quad \text{and} \tag{2.35a}$$

$$\rho_{\text{ref}} \frac{\partial v_i}{\partial t} + \rho_{\text{ref}} \frac{\partial v_j v_i}{\partial x_j} = -\,\frac{\partial p}{\partial x_i} + \mu \frac{\partial^2 v_i}{\partial x_j^2}. \tag{2.35b}$$

where ρ_{ref} is the constant reference density of the fluid.

Note that the pressure p in the momentum equation (2.35b) does not include any acoustic component due to the assumed incompressibility. The shown system of incompressible equations is still the basis for the computations of the acoustic pressure field, when using the hybrid approach. In this approach, the incompressible formulation is solved to obtain the turbulence-induced aeroacoustic source terms, which are used as input to the solution of the acoustic field produced by a separate solver. In the present Master's Thesis the incompressible solution of the turbulent flow field is computed using the method of LES. In the following chapter 3 the phenomenon turbulence, which originates from the non-linear term of the momentum equation, shall be further discussed.

2.3 Propagation of waves and the speed of sound

In this section, a brief introduction to the propagation of (sound-) waves is presented by deriving a simple wave equation from the Navier-Stokes equations. The derivation is based on the *acoustic decomposition*, which is for an arbitrary quantity ϕ defined as:

$$\phi := \langle \phi \rangle + \phi_\mathrm{a}, \tag{2.36}$$

where $\langle \phi \rangle$ is the mean base flow and ϕ_a is the acoustic perturbation. Linearization of an arbitrary non-linear term $\phi\psi$ would lead to the following three terms

$$\begin{aligned} \phi\psi = {} & \langle \phi \rangle \langle \psi \rangle \\ & + \langle \phi \rangle \psi_\mathrm{a} + \phi_\mathrm{a} \langle \phi \rangle \\ & + \cancel{\phi_\mathrm{a}\psi_\mathrm{a}}, \end{aligned} \tag{2.37}$$

since non-linear effects are not considered.

2.3.1 Wave equation for a quiescent fluid

Applying the acoustic decomposition (2.36) to the flow field variables pressure p, velocity v_i and density ρ and introducing these into the Euler equations (2.32) together with the isentropy condition (2.31) yields

$$\frac{\partial}{\partial t}\left(\langle \rho \rangle + \rho_\mathrm{a}\right) + \frac{\partial}{\partial x_j}\left[(\langle \rho \rangle + \rho_\mathrm{a})(\langle v_j \rangle + v_{\mathrm{a},j})\right] = 0, \tag{2.38a}$$

$$\begin{aligned} & \frac{\partial}{\partial t}\left(\langle v_j \rangle + v_{\mathrm{a},j}\right) + (\langle v_j \rangle + v_{\mathrm{a},j})\frac{\partial}{\partial x_j}\left(\langle v_j \rangle + v_{\mathrm{a},j}\right) = \\ & \quad - \frac{1}{\langle \rho \rangle + \rho_\mathrm{a}}\frac{\partial}{\partial x_i}\left(\langle p \rangle + p_\mathrm{a}\right), \quad \text{and} \end{aligned} \tag{2.38b}$$

$$\frac{\partial}{\partial t}\left(\langle s \rangle + s_\mathrm{a}\right) + (\langle v_j \rangle + v_{\mathrm{a},j})\frac{\partial}{\partial x_j}\left(\langle s \rangle + s_\mathrm{a}\right) = 0, \tag{2.38c}$$

respectively. Before continuing, additional assumptions are introduced. First, the fluid is considered as stagnant ($v_{0,i} = 0$) and uniform ($\langle \rho \rangle = \rho_0$, $\langle p \rangle = p_0$ and $\langle s \rangle = s_0$). These fluid conditions are often described as quiescent. Second, acoustic perturbations are assumed as very small ($\phi_\mathrm{a} \ll \langle \phi \rangle$). As a result, all second order terms $\phi_\mathrm{a}\psi_\mathrm{a}$ are neglected as in (2.37). Third, the acoustic perturbations are isentropic $s_\mathrm{a} = 0$. Applying all these assumptions, only the equations for the acoustic perturbations ϕ_a remain:

$$\frac{\partial \rho_\mathrm{a}}{\partial t} + \rho_0 \frac{\partial v_{\mathrm{a},j}}{\partial x_j} = 0 \tag{2.39a}$$

$$\rho_0 \frac{\partial v_{\mathrm{a},i}}{\partial t} + \frac{\partial p_\mathrm{a}}{\partial x_i} = 0. \tag{2.39b}$$

To eliminate $v_{\mathrm{a},i}$ from the equations (2.39a) and (2.39b), the time derivative of the continuity equation (2.39a) was subtracted from the divergence of the momentum equation (2.39b) such that

$$\frac{\partial^2 \rho_\mathrm{a}}{\partial t^2} - \frac{\partial^2 p_\mathrm{a}}{\partial x_j^2} = 0. \tag{2.40a}$$

Rewriting (2.24a) based on the applied assumptions to $c_0^2 = p_\mathrm{a}/\rho_\mathrm{a}$ either p_a or ρ_a can be expressed in terms of the other and the wave equations for a quiescent fluid finally read

$$\frac{\partial^2 p_\mathrm{a}}{\partial t^2} - c_0^2 \frac{\partial^2 p_\mathrm{a}}{\partial x_j^2} = 0 \tag{2.41a}$$

$$\frac{\partial^2 \rho_\mathrm{a}}{\partial t^2} - c_0^2 \frac{\partial^2 \rho_\mathrm{a}}{\partial x_j^2} = 0. \tag{2.41b}$$

This formulation makes evident that c represents the speed of the perturbation traveling through the space, namely the *speed of sound*. No source terms have been considered thus far in this derivation. They are subsequently included as arbitrary sources S_p and S_ρ so that the wave equations for a quiescent fluid become inhomogeneous

$$\frac{\partial^2 p_\mathrm{a}}{\partial t^2} - c_0^2 \frac{\partial^2 p_\mathrm{a}}{\partial x_j^2} = S_p, \tag{2.42a}$$

$$\frac{\partial^2 \rho_\mathrm{a}}{\partial t^2} - c_0^2 \frac{\partial^2 \rho_\mathrm{a}}{\partial x_j^2} = S_\rho. \tag{2.42b}$$

These are the main equations for wave propagation in classical acoustics, which can also be solved analytically, if the sources S_p or S_ρ are known and permit it mathematically.

2.3.2 Speed of sound

Recalling equation (2.24a)

$$c^2 = \left(\frac{\partial \rho}{\partial p}\right)_s^{-1}$$

and assuming a perfect gas, the speed of sound is only dependent of the fluid temperature θ as in (2.29a) such that

$$c^2 = \gamma \mathcal{R} \theta = \gamma \frac{p}{\rho}.$$

Thus, the speed of sound for air, at given atmospheric conditions, is

$$c_{\text{air}} = \sqrt{\gamma \mathcal{R}_{\text{air}} \theta} = 343.48\,\text{m/s}, \tag{2.43}$$

where

$$\begin{aligned} \gamma &= 1.402, \\ \mathcal{R}_{\text{air}} &= 287.06\,\text{J/(kg K)} \quad \text{and} \\ \theta &= 293.15\,\text{K} = 20\,^\circ\text{C}. \end{aligned} \tag{2.44a}$$

When assuming an incompressible fluid, the heat capacities are equal $c_v = c_p$ and the density ρ is only dependent of the fluid temperature θ such that

$$\rho \neq \rho(p), \quad \rho = \rho(\theta) \qquad \Rightarrow \tag{2.45}$$

$$c^{-2} = \left(\frac{\partial \rho}{\partial p}\right)_s^{-1} = 0, \tag{2.46}$$

which implies an infinitely high speed of sound. This explains the very large difference between the propagation speed of sound in compressible gaseous and (nearly) incompressible fluids.

E.g. the speed of sound in water, which can be computed within the temperature range from 273 K to 293 K and the pressure range from 10^5 Pa to 10^7 Pa, from the expression [46]

$$c_{\text{water}} = c_{\text{ref}} + \beta_{c,\theta,\text{water}}(\theta - \theta_{\text{ref}}) + \beta_{c,p,\text{water}} p \tag{2.47}$$

becomes with

$$\begin{aligned} c_{\text{ref}} &= 1447\,\text{m/s}, \\ \beta_{c,\theta,\text{water}} &= 4.0\,\text{m K/s}, \\ \beta_{c,p,\text{water}} &= 1.6{\times}10^{-6}\,\text{m Pa/s}, \\ \theta_{\text{ref}} &= 283.16\,\text{K}, \\ \theta &= 293.15\,\text{K} \quad \text{and} \\ p &= 1.0{\times}10^{6}\,\text{Pa}, \end{aligned} \tag{2.48a}$$

$$c_{\text{water}} = 1487.12\,\text{m/s}. \tag{2.49}$$

Due to the much higher speed of sound in (nearly) incompressible flows, the computational costs for resolving all relevant time-scales increase significantly. Thus, dealing with (nearly) incompressible fluids is numerically even more challenging.

Using the speed of sound c as reference velocity, a non-dimensional characteristic number, the *Mach number* $\mathcal{M}a$, can be defined as

$$\mathcal{M}a = \frac{\bar{v}}{c}, \tag{2.50}$$

where $\bar{v}$ a characteristic velocity of the flow. The Mach number describes the compressibility of the flow configuration. For $\mathcal{M}a < 0.3$ the flow is considered as incompressible, whereas for $\mathcal{M}a > 0.3$ the fluid behaves compressible. Flow configurations with $\mathcal{M}a < 1$ are referred to as subsonic and those with $\mathcal{M}a \geq 1$ are called supersonic. In this Master's Thesis only small Mach numbers $\mathcal{M}a$ are considered so that the flow can be assumed as incompressible.

3 Turbulent flow

In the previous chapter the governing equations of fluid mechanics were introduced. The non-linear terms in the momentum equation are, as already mentioned, the origin of turbulence. The phenomenon of turbulence and its mathematical description shall be discussed in much detail in section 3.1 and section 3.2, because the turbulent fluctuating motion strongly contributes to the aeroacoustic sources. In section 3.3 the CFD solution procedure as implemented in FIRE™ is shortly addressed.

3.1 Turbulence

Turbulence is one of the great still unsolved physical phenomena. It is very complex and therefore difficult to handle. Due to its strong dependence on time and space and its non-linear and multi-dimensional nature, every assumption inherently introduces certain simplifications, which do not universally apply to all types of turbulent flow situations. Therefore, turbulence is very difficult to model. At the same time, it is present in almost every technical application, where it exhibits a great influence on the transport processes of heat, mass and momentum. In this section, a short introduction on the fundamentals of turbulence [21, 41, 52, 54] is given.

3.1.1 Reynolds number

To describe the basic characteristics of turbulence, one can start with the incompressible momentum equation (2.35b) written as

$$\frac{\partial v_i}{\partial t} + \frac{\partial v_j v_i}{\partial x_j} = -\frac{1}{\rho}\frac{\partial^2 p}{\partial x_j^2} + \nu \frac{\partial^2 v_i}{\partial x_j^2}.$$

The momentum equation can be non-dimensionalized by introducing characteristic reference values for the flow quantities and the geometry

$$v_i = v_i^* \boldsymbol{v}, \tag{3.1a}$$

$$x_i = x_i^* \boldsymbol{\ell}, \tag{3.1b}$$

$$t = t^* \frac{\boldsymbol{\ell}}{\boldsymbol{v}} \qquad \text{and} \tag{3.1c}$$

$$p = p^* \rho_{\mathrm{ref}} \boldsymbol{v}^2, \tag{3.1d}$$

where ρ_{ref} is the reference density, $\boldsymbol{v}$ is a typical velocity-scale (e.g. the bulk velocity of a pipe-flow) and $\boldsymbol{\ell}$ a typical length-scale (e.g. the hydraulic diameter of an arbitrary channel) of the application. The hydraulic diameter $\boldsymbol{d}$ of a channel of arbitrary shape is defined as

$$\boldsymbol{d} = \frac{4A}{U}, \tag{3.2}$$

where A is the cross-sectional area and U is the circumference of the channel. For cylindrical pipes the hydraulic diameter becomes the inner diameter $\boldsymbol{d} = D_{\mathrm{I}}$ of the pipe. Using the characteristic reference values as shown in (3.1), one can non-dimensionalize the momentum equation (2.35b) to get

$$\frac{\partial v_i^*}{\partial t^*} + \frac{\partial v_j^* v_i^*}{\partial x_j^*} = -\frac{\partial p^*}{\partial x_j^*} + \frac{1}{\mathcal{R}e} \frac{\partial^2 v_i^*}{\partial x_j^{*2}}. \tag{3.3}$$

In this dimensionless formulation (3.3) the *Reynolds number* $\mathcal{R}e$ appears, which is the characteristic number determining the flow. The Reynolds number can be interpreted as a ratio between inertia and viscous forces and is defined as

$$\mathcal{R}e = \frac{\mathcal{v}\ell}{\nu} = \frac{\text{inertia forces}}{\text{viscous forces}}. \tag{3.4}$$

Note that the Reynolds number is the only free parameter in equation (3.3), and thus, its value determines the solution. For every flow configuration, there exists a critical Reynolds number ($\mathcal{R}e_{\text{crit}}$), which defines the transition from laminar to turbulent flow. This can be illustrated by the well-known Reynolds experiment.

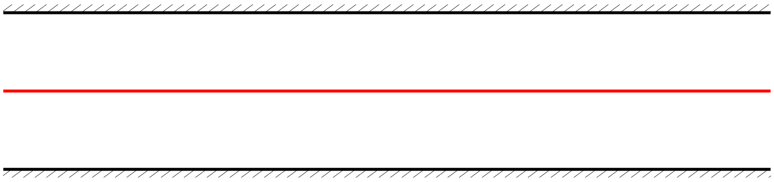

(a) laminar flow: $\mathcal{R}e < \mathcal{R}e_{\text{crit}}$

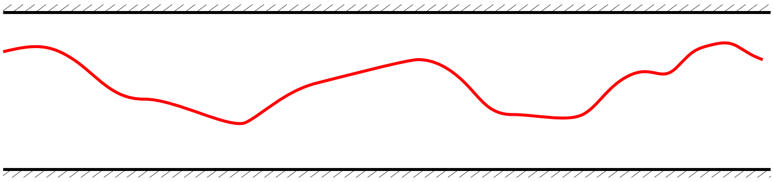

(b) early transitional (but still laminar) flow: $\mathcal{R}e \approx \mathcal{R}e_{\text{crit}}$

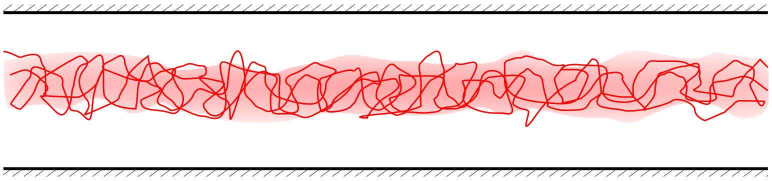

(c) turbulent flow: $\mathcal{R}e > \mathcal{R}e_{\text{crit}}$

FIGURE 3.1: The Reynolds experiment [41].

In figure 3.1 the three different regimes are sketched, which can be displayed by injecting dye into a pipe flow with varied Reynolds numbers. For small Reynolds numbers ($\mathcal{R}e < \mathcal{R}e_{\text{crit}}$) the flow is laminar, thus only molecular diffusion causes the dye to mix with the main flow. When the Reynolds number is slightly increased ($\mathcal{R}e \approx \mathcal{R}e_{\text{crit}}$), the dye streak becomes wavy, but stays laminar. When the Reynolds number is further increased ($\mathcal{R}e > \mathcal{R}e_{\text{crit}}$), the flow might become turbulent, thus the streamlines become irregular and chaotic. As a result, the dye strongly mixes with the main fluid due to the increased convection. In laminar as in turbulent flows the dye will mix with the main fluid, but in turbulent flows the mixing is strongly enhanced. It is noted that, with increasing Reynolds numbers above the critical limit, the flow basically becomes unstable. This instability makes a transition from laminar to turbulent flow possible, because any arbitrarily small perturbation will be further amplified for $\mathcal{Re} > \mathcal{Re}_{\text{crit}}$ and not dampened. The higher the Reynolds number beyond this limit, the more unstable the flow, and thus the transition is more likely. Further note that it is even possible to realize laminar flows at Reynolds numbers larger than the critical Reynolds number, if the configuration is kept free from outer perturbations and disturbances at the flow inlet and boundaries (very smooth walls) as much as possible.

3.1.2 Reynolds decomposition

As indicated in the Reynolds experiment, one can describe turbulence as an irregular and chaotic motion. This led to the definition of the Reynolds decomposition which attempts to separate the mean flow effects and the turbulence. The Reynolds decomposition of an arbitrary flow quantity ϕ is defined as

$$\phi(t) = \langle\phi\rangle + \phi'(t), \tag{3.5}$$

where $\phi'(t)$ are the time dependent fluctuations around the statistical average $\langle\phi\rangle$. For statistically stationary turbulent flows, the average $\langle\phi\rangle$ is calculated as a temporal average of the instantaneous flow quantity $\phi(t)$ according to (2.2). The statistical averaging procedure is associated with the following identities:

$$\langle\phi'\rangle = 0, \tag{3.6a}$$

$$\langle\langle\phi\rangle\rangle = \langle\phi\rangle\,, \tag{3.6b}$$

$$\langle\phi + \psi\rangle = \langle\phi\rangle + \langle\psi\rangle\,, \tag{3.6c}$$

$$\langle\langle\phi\rangle\,\psi\rangle = \langle\phi\rangle\,\langle\psi\rangle\,, \tag{3.6d}$$

$$\left\langle\frac{\partial\phi}{\partial x_i}\right\rangle = \frac{\partial\langle\phi\rangle}{\partial x_i}. \tag{3.6e}$$

The intensity of the fluctuating quantities is quantified by the corresponding RMS-values

$$\phi_{\mathrm{RMS}} = \sqrt{\langle(\phi'(t))^2\rangle}. \tag{3.7}$$

Accordingly, the kinetic energy contained in the turbulence velocity fluctuations v'_i, namely the *turbulence kinetic energy* $\boldsymbol{k}$, is defined as:

$$\boldsymbol{k} = \frac{1}{2}\left(\left\langle(v'_x)^2\right\rangle + \left\langle(v'_y)^2\right\rangle + \left\langle(v'_z)^2\right\rangle\right). \tag{3.8}$$

In the modeling of turbulence, *isotropic turbulence* is often assumed, which implies

$$\left\langle(v'_x)^2\right\rangle = \left\langle(v'_y)^2\right\rangle = \left\langle(v'_z)^2\right\rangle. \tag{3.9}$$

Based on this assumption, the averaged *isotropic velocity fluctuations* are calculated as

$$\langle v'_{\mathrm{iso}}\rangle = \left(\frac{2}{3}\boldsymbol{k}\right)^{1/2}. \tag{3.10}$$

The turbulence kinetic energy will decay due to the action of the viscous forces, if a continuous supply of energy is not available. The rate, at which the turbulent energy decays, is the *dissipation rate* ε, which is defined as:

$$\varepsilon = \nu\left\langle\frac{\partial v'_i}{\partial x_k}\frac{\partial v'_i}{\partial x_k}\right\rangle. \tag{3.11}$$

3.1.3 Energy cascade

As already mentioned, due to the permanent dissipation of turbulence kinetic energy caused by the action of viscous forces, turbulence requires a continuous supply of energy, to sustain a statistically stationary turbulent flow. This kinetic energy is essentially provided by large vortical structures (eddies) of the mean flow and is further transferred to the smaller and smaller scales. At the smallest scales the kinetic energy is dissipated due to the viscous forces. The energy cascade from the large scale eddies to the small scale eddies is presented in figure 3.2.

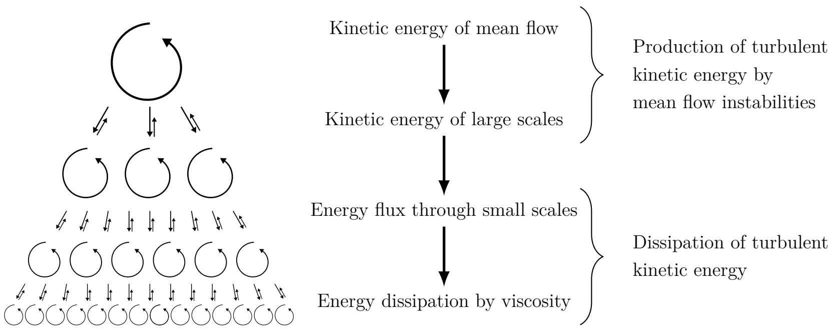

FIGURE 3.2: Energy flux from the large scale to small scale eddies [2].

Richardson [45] clearly described this phenomenon as follows

Big whorls have little whorls,
which feed on their velocity;
And little whorls have lesser whorls,
and so on to viscosity.

3.1.4 Scales of turbulence

The energy cascade describes the transport of energy through the different scales of turbulence. In this paragraph a short description of the turbulence-scales and the energy flux between them is presented [2, 41]. To describe those turbulence-scales, characteristic length-scales ℓ, time-scales t and velocity-scales v are defined.

Geometry related scales

The geometry related scales of turbulence are based on the main characteristic features of the considered configuration. The length-scale is a characteristic length ℓ_G of the geometry (e.g. the hydraulic diameter d) and the characteristic velocity-scale v_G might be the mean velocity of the application (e.g. the bulk velocity for pipe flows). Using the length-scale and the velocity-scale, a so called *convective* time-scale $t_\mathrm{G,conv}$ can be constructed. Using the kinematic viscosity ν of the fluid, a *diffusive* time-scale $t_\mathrm{G,diff}$ can be constructed:

$$t_\mathrm{G,conv} = \frac{\ell_\mathrm{G}}{v_\mathrm{G}}, \tag{3.12a}$$

$$t_\mathrm{G,diff} = \frac{\ell_\mathrm{G}^2}{\nu}. \tag{3.12b}$$

The shown time-scales basically describe the rate at which flow properties are transferred due to convection or diffusion, respectively. Note that these time-scales allow for an alternative interpretation of the Reynolds number $\mathcal{Re}_{\mathrm{G}}$, if it is rewritten as

$$\mathcal{Re}_{\mathrm{G}} = \frac{t_{\mathrm{G,diff}}}{t_{\mathrm{G,conv}}} = \frac{v_{\mathrm{G}} \ell_{\mathrm{G}}}{\nu}. \tag{3.13}$$

If $\mathcal{Re}_{\mathrm{G}}$ is large, the diffusive time-scale is much larger than the convective time-scale, thus diffusive effects are negligible.

Integral scale

The length and time-scales of the largest turbulent structures within the flow are often chosen as a characteristic scale of turbulence. These large scales, which are associated with the so called integral length-scale ℓ_{L}, contain a significant part of the kinetic energy. The rate of the transfer of turbulent energy from the large scales to the small scales is determinded by the turbulence dissipation rate ε. Accordingly, the characteristic length-scale of these large scales ℓ_{L} are estimated using the turbulence kinetic energy k and the turbulence dissipation rate ε as

$$\ell_{\mathrm{L}} = \frac{k^{3/2}}{\varepsilon}. \tag{3.14}$$

The integral time-scale t_{L} is defined as

$$t_{\mathrm{L}} = t_{k\varepsilon} = \frac{k}{\varepsilon}, \tag{3.15}$$

which can be interpreted as the lifetime of the turbulent large scale structures, named the *eddy turnover time.* A characteristic turbulence fluctuation velocity-scale v_{L} can be constructed using the definition of the turbulence kinetic energy k as

$$v_{\mathrm{L}} = \left(\frac{2}{3}k\right)^{1/2}. \tag{3.16}$$

Kolmogorov scale

The *Kolmogorov* length-scale represents the smallest relevant scales of turbulent motion. It was originally derived by Kolmogorov and is also called the *dissipation-scale* due to the assumption that any turbulent eddies associated with this small length-scale are significantly affected by viscous dissipation. Accordingly, the definition of this length-scale is based on the kinematic viscosity ν and the turbulence dissipation rate ε of the turbulence kinetic energy $\boldsymbol{k}$, and is written as

$$\boldsymbol{\ell}_{\mathcal{K}} = \left(\frac{\nu^3}{\varepsilon}\right)^{1/4} . \tag{3.17}$$

The corresponding time- and velocity-scales are defined as:

$$\boldsymbol{t}_{\mathcal{K}} = \left(\frac{\nu}{\varepsilon}\right)^{1/2} , \tag{3.18a}$$

$$\boldsymbol{v}_{\mathcal{K}} = (\nu\varepsilon)^{1/4} , \tag{3.18b}$$

respectively. Using the Kolmogorov length- and velocity-scales, a Reynolds number can be constructed as

$$\mathcal{R}e_{\mathcal{K}} = \frac{\boldsymbol{v}_{\mathcal{K}}\boldsymbol{\ell}_{\mathcal{K}}}{\nu} = 1. \tag{3.19}$$

Being unity by definition implies that viscous dissipation becomes significant. The turbulent structures, whose size is larger than the integral scale ($\boldsymbol{\ell} > \boldsymbol{\ell}_{\mathrm{L}}$) are generally anisotropic and depend on the geometry and the Reynolds number of the flow configuration. A major part of the kinetic energy is contained in these large scales. Kolmogorov stated that in the cascading process from the large scales to the small scales the turbulent motion becomes statistically isotropic. Thus, at scales below $\boldsymbol{\ell}_{\mathrm{L}}$, the turbulent eddies become universal, thus define the so-called universal range, where the turbulent structures are independent of the geometry and the Reynolds number. The production of turbulent energy, its transfer and final dissipation according to the different length-scales, is schematically shown in figure 3.3.

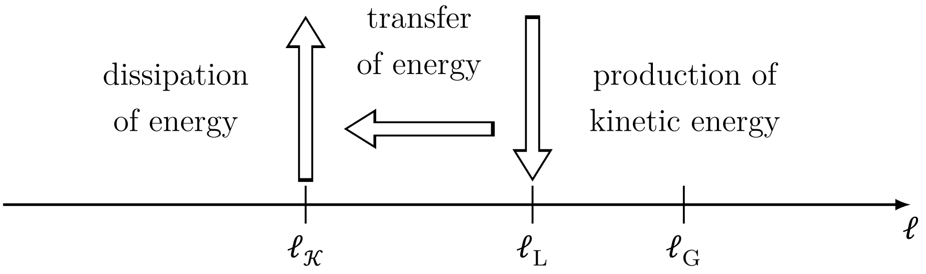

Figure 3.3: The energy transfer between different length-scales [2].

3.1.5 Turbulence energy spectrum

Applying a spectral analysis to the turbulence kinetic energy $\mathcal{F}(\boldsymbol{k})$, the *turbulence energy spectrum* $\mathcal{E}(\kappa)$ can be calculated, where κ is the wave number. A typical energy spectrum of a fully developed homogeneous turbulent flow is shown in figure 3.4. One can observe that the large scale eddies κ_{L} contain the highest turbulence kinetic energy. These large scale eddies, basically generated by the main flow, break into smaller eddies, transferring their energy to these smaller structures. No energy is created nor dissipated but only transferred within the inertial subrange. The higher the Reynolds number of the flow configuration, the wider the inertial subrange. In this inertial subrange the spectral kinetic energy density follows the Kolmogorov spectrum law written as

$$\mathcal{E}(\kappa) = C_{\mathcal{K}} \varepsilon^{2/3} \kappa^{-5/3}, \quad \text{for} \quad \frac{1}{\ell_{\mathrm{L}}} < \kappa < \frac{1}{\ell_{\mathcal{K}}}. \tag{3.20}$$

At higher wave numbers, $\kappa > 1/\ell_{\mathcal{K}}$ the turbulence kinetic energy is dissipated.

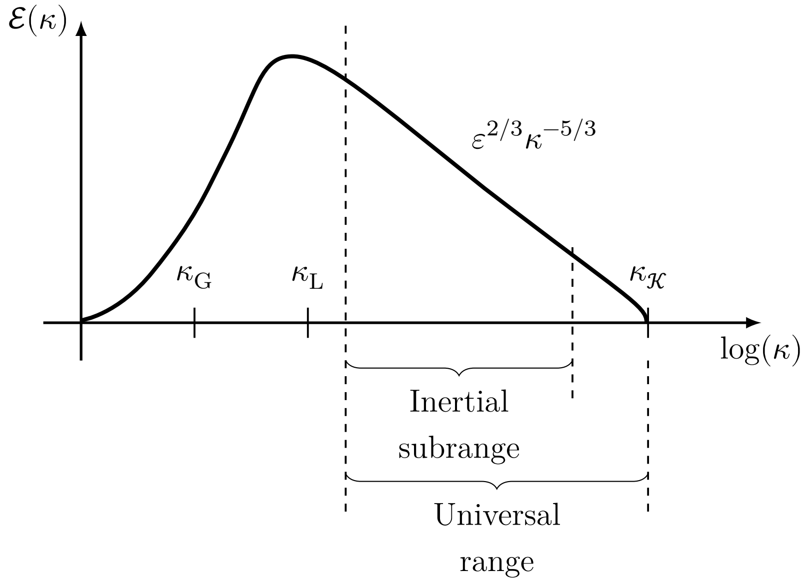

Figure 3.4: The turbulence kinetic energy spectrum [2].

3.1.6 Characteristics of turbulence

Before continuing some important characteristics of turbulence are summarized [2].

Irregularity: Turbulence is random, chaotic and irregular. The flow contains large scale as well as small scale structures within a large range.

Diffusivity: Turbulence enhances all diffusion processes, which add up with the molecular diffusion processes, due to increased convective transport.

Instability: Turbulence is associated with unstable flow configurations at high Reynolds numbers, where the flow is very sensible to perturbations. Due to that turbulent flows are stochastic, although the governing equations are deterministic.

Three-dimensional: Turbulent flow is always an unsteady spatially three-dimensional flow.

Energy cascade: In turbulent flows energy is typically transferred from the large scales to the small scales, mainly carried by inviscid processes. The energy is dissipated at the smallest scales due to viscous stresses.

Continuum: Turbulence is a phenomenon of the continuum. Thus, the smallest scales are larger than the molecular scales and therefore are determined by the conservation laws for continua and influenced by boundary and initial conditions.

State of the flow: Turbulence is a state of the flow and not a state of the fluid.

3.1.7 Coherent structures

In turbulent flow configurations a wide range of scales of turbulent structures appear, which are spatially correlated and thus coherent. These coherent structures appear as vortical structures and can therefore be identified based on the vorticity [31]

$$\vec{\omega} = \begin{bmatrix} \dfrac{\partial v_z}{\partial y} & - & \dfrac{\partial v_y}{\partial z} \\ \dfrac{\partial v_x}{\partial z} & - & \dfrac{\partial v_z}{\partial x} \\ \dfrac{\partial v_y}{\partial x} & - & \dfrac{\partial v_x}{\partial y} \end{bmatrix} . \tag{3.21}$$

In figure 3.5 vortical structures developing from sheared flow are presented.

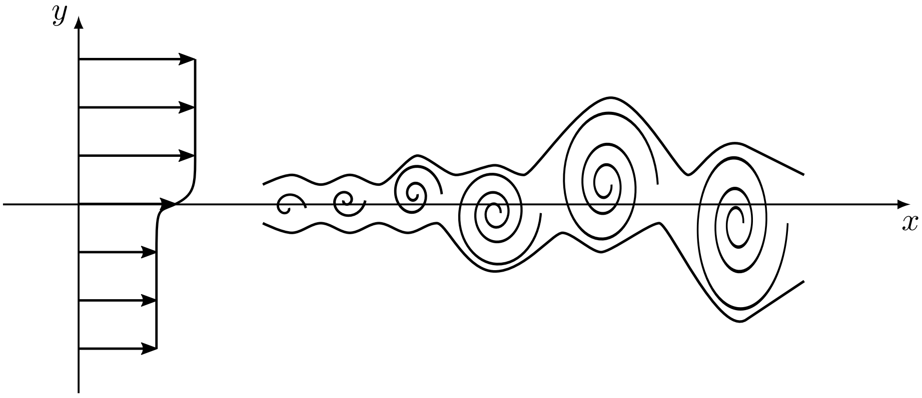

FIGURE 3.5: Vortical structures developing from sheared flow.

One can distinguish between large and small vortical structures based on their length- or time-scales, because large structures are associated with long time-scales. In general, small structures are mainly turbulent, whereas some large vortical structures might be not chaotic and not stochastic and therefore not turbulent. Hussain [31] argues that, not the vortical structures themselves, but rather their breakdown process into smaller and smaller structures is the dominant sound generation process. These large vortical structures might still strongly influence the propagation of sound waves, as they are convected through large regions of the flow field, while small structures are dissipated much quicker. Therefore, the influence of the large vortical structures on the aeroacoustic source terms shall be investigated in the present Master's Thesis as well. To achieve this task a method which excludes vortical structures associated with large time-scales from the aeroacoustic source terms is applied and discussed in this Master's Thesis.

3.1.8 Temporal filtering

As already mentioned, the definition of the Reynolds decomposition (3.5) basically splits the instantaneous flow quantities into a statistical mean value and a relative deviation therefrom. In the hybrid CAA approach, basically the full turbulent content, represented by the fluctuating term in the Reynolds decomposition, is included into the aeroacoustic source terms. In this Master's Thesis the possible contribution of these large turbulent structures to the aeroacoustic sources is investigated. Therefore, alternative methods for calculating acoustically relevant fluctuating contributions, excluding large low-frequency vortical structures, shall be introduced and tested. The foundation of these alternative methods is, similar as in the Reynolds decomposition (3.5), the decomposition of the instantaneous flow quantities into a statistical mean and a fluctuation

$$\phi_{\text{fluct}}(t) = \phi(t) - \phi_{\text{mean}}(t). \tag{3.22}$$

The difference to the standard Reynolds decomposition is that in this case the mean flow quantity $\phi_{\mathrm{mean}}(t)$ is time dependent, as it includes the low-frequency content of the large vortical structures. In turn, the fluctuations $\phi_{\mathrm{fluct}}(t)$ include the remaining high frequency turbulence of the small scale structures. The mean flow quantities $\phi_{\mathrm{mean}}(t)$ are calculated by applying a temporal low-pass filter to the instantaneous flow field $\phi(t)$. In this Master's Thesis two different methods for temporal filtering are used for this purpose.

The first method calculates the mean flow quantities ($\phi_{\mathrm{mean}}(t) = \langle\phi\rangle_{\mathrm{ma}}$) by applying a moving average procedure, which is defined as

$$\phi_{\mathrm{mean}}(t) = \langle\phi\rangle_{\mathrm{ma}} := \frac{1}{T_{\mathrm{TF}}} \int\limits_{t-T_{\mathrm{TF}}/2}^{t+T_{\mathrm{TF}}/2} \phi(t)dt \approx \frac{1}{T_{\mathrm{TF}}} \sum_{t-T_{\mathrm{TF}}/2}^{t+T_{\mathrm{TF}}/2} \phi(t)\Delta t. \tag{3.23}$$

This procedure basically represents a temporal box filter, which has a constant width T_{TF} and moves with time t. Note that the standard temporal averaging method (2.2), used in the Reynolds decomposition (3.5), basically represents a box filter with an infinity long width. The fluctuations are then simply computed by

$$\phi'^{\mathrm{ma}} = \phi - \langle\phi\rangle_{\mathrm{ma}}. \tag{3.24}$$

The second method splits the instantaneous flow field $\phi(t)$ into a high and low frequency part, where the mean flow is defined as the low frequency part. The low frequency part is obtained from an Fourier analysis of the instantaneous flow field $\Psi_{\boldsymbol{\kappa}} = \boldsymbol{\mathcal{F}}(\phi)$, where $\Psi_{\boldsymbol{\kappa}}$ is the complex amplitude corresponding to the wave number κ, and where only the low frequency part below the corresponding cut-off frequency $\boldsymbol{f}_{\mathrm{TF}} = 1/T_{\mathrm{TF}}$ is considered. Finally the mean flow field is computed from the inverse Fourier transformation

$$\begin{aligned} \phi_{\mathrm{mean}}(t) = \langle\phi\rangle_{\mathrm{fa}} &= \boldsymbol{\mathcal{F}}^{-1}\left(\Psi_{\boldsymbol{\kappa}}(\phi)\right) \qquad (3.25) \\ &= \sum_{\kappa=0}^{\kappa_{\mathrm{TF}}} \left(\Psi_{\boldsymbol{\kappa}}(\phi)e^{i\kappa t}\right) \qquad \kappa = 0, 1, \dots, \kappa_{\mathrm{TF}}, \end{aligned}$$

where κ_{TF} is the wave number which corresponds to the cut off frequency of the temporal filter $\boldsymbol{f}_{\mathrm{TF}}$. The fluctuations are then analogously computed as

$$\phi'^{\mathrm{fa}} = \phi - \langle\phi\rangle_{\mathrm{fa}}. \tag{3.26}$$

The difficult part of temporal filtering methods is to find an appropriate temporal filter width T_{TF} (time-scale), which corresponds to the large low-frequency structures to be excluded from the aeroacoustic source terms. Note that these time-scales might vary locally, because different sizes of vortical structures might appear in a turbulent flow field. Strictly speaking, vortical structures represent spatially correlated structures. Applying only temporal filters, without including any spatial structure information, the present approach inherently assumes that the spatial and time-scales of large low-frequency structures are equivalent. In the following paragraph, candidates for the time-scale of the temporal filtering methods are presented and discussed.

3.1.9 Timescales of vortical structures

In general, it is not a trivial task to estimate the time-scales associated with vortical structures in a flow configuration. Several alternatives are possible, which might be differently reliable depending on the application.

Based on the energy cascade theory, the integral time-scale can be determined from the rate at which turbulence kinetic energy k cascades down to smaller and smaller scales, as represented by the turbulence dissipation rate ε. As such, it can be considered as a first candidate, which is often used to estimate the lifetime of large scale eddies, and generally referred to as the *eddy turnover time* (3.15)

$$t_{k\varepsilon} = \frac{k}{\varepsilon}.$$

Another possibility is to define a time-scale, which is based on the reciprocal of the norm of the temporally averaged rate of strain tensor:

$$t_{\mathrm{ST}} = || \left\langle S_{ij} \right\rangle ||^{-1}. \tag{3.27}$$

The time-scale t_{ST} is expected to deliver higher values than the *eddy turnover time*, because it is based on temporally averaged flow quantities and not fluctuating quantities. Therefore, it should deliver some kind of upper limit for the large scale structures. In regions, where the averaged flow quantities significantly change, e.g. near walls or within shear layers, this time-scale might locally drop to very small values, though.

The third option considered in this Master's Thesis, is a time-scale based on the isotropic velocity fluctuations (3.10) computed from the turbulence kinetic energy k

$$\left\langle v'_{\mathrm{iso}} \right\rangle = \left(\frac{2}{3} k \right)^{1/2}, \tag{3.28}$$

and a length-scale ℓ_{E} corresponding to the large vortical structures within the flow configuration, written as

$$\boldsymbol{t}_{\mathrm{SW}} = \frac{\boldsymbol{\ell}_{\mathrm{E}}}{\langle v'_{\mathrm{iso}} \rangle}. \tag{3.29}$$

Since in this Master's Thesis internal flow through a straight pipe locally contracted by a orifice is considered, the gap height of the orifice was presently chosen as the characteristic length-scale, such that $\boldsymbol{\ell}_{\mathrm{E}} = h_{\mathrm{O}}$. The time-scale $\boldsymbol{t}_{\mathrm{SW}}$ is often referred to as the *sweeping time*. Guowei et al. [27] found that the sweeping time $\boldsymbol{t}_{\mathrm{SW}}$ is a more suitable time-scale than the eddy turnover time. Using this time as reference time-scale gave a better time-correlation for the different scales of turbulent structures.

3.2 Turbulence modeling

Turbulence is a very important phenomenon, which strongly influences all convective and diffusive transport processes in various technical applications. In addition, it is often considered as the main aeroacoustic source. Due to its physical complexity, it is very difficult to model. In this section a brief introduction of the different approaches to handle turbulence is presented [2, 23, 54].

Basically, three different most prominent approaches exist. The first, essentially the most generic approach, is to fully resolve the turbulent spectrum down to the smallest turbulence scales. This method is called *direct numerical simulation* (DNS) and has the highest computational costs, which makes this method unfeasible for most technical flow configurations. The second method solves the *Reynolds averaged Navier-Stokes* (RANS) equations derived from the Reynolds decomposition. The solution of the RANS equations for the statistical mean quantities require a turbulence model for closure, which models the whole turbulence spectrum. The third method is the *Large-Eddy Simulation* (LES), which directly resolves the turbulent spectrum down to a certain length-scale ℓ_{LES}, and only the unresolved turbulent spectrum needs to be modeled. Within the last decade, many hybrid approaches have been developed, which attempt to combine the latter two concepts, like detached eddy simulation (DES) or partial averaged Navier-Stokes (PANS) simulation. These approaches however, will not be discussed in this Master's Thesis.

In the present Master's Thesis the resolved aeroacoustic sources obtained from LES as well as the RANS based reconstructed aeroacoustic sources using unstructured kinematic source generator (UKSG), shall be calculated and compared against each other.

3.2.1 Reynolds averaged Navier-Stokes equations

The derivation of the RANS equations recalls the continuity equation (2.35a) and momentum equation (2.35b) for incompressible flows

$$\frac{\partial v_j}{\partial x_j} = 0 \qquad \text{and}$$

$$\frac{\partial v_i}{\partial t} + \frac{\partial v_j v_i}{\partial x_j} = -\frac{1}{\rho_0}\frac{\partial p}{\partial x_i} + \nu \frac{\partial^2 v_i}{\partial x_j^2}.$$

Including the Reynolds decomposition (3.5) for the velocity $v_i = \langle v_i \rangle + v_i'$ and the pressure $p = \langle p \rangle + p'$ leads to

$$\frac{\partial \langle v_j \rangle + v_j'}{\partial x_j} = 0 \qquad \text{and} \tag{3.31a}$$

$$\frac{\partial \langle v_j \rangle + v_j'}{\partial t} + \frac{\partial \big(\langle v_j \rangle + v_j' \big) \left(\langle v_i \rangle + v_i' \right)}{\partial x_j} =$$

$$- \frac{1}{\rho_0} \frac{\partial \langle p \rangle + p'}{\partial x_i} + \nu \frac{\partial^2 \left\langle v_i \right\rangle + v_i'}{\partial x_j^2}. \tag{3.31b}$$

After temporally averaging, using equation (2.2), these equations become

$$\left\langle \frac{\partial \langle v_j \rangle + v_j'}{\partial x_j} \right\rangle = 0 \qquad \text{and} \tag{3.32a}$$

$$\left\langle \frac{\partial \langle v_i \rangle + v_i'}{\partial t} \right\rangle + \left\langle \frac{\partial \big(\langle v_j \rangle + v_j' \big) \left(\langle v_i \rangle + v_i' \right)}{\partial x_j} \right\rangle =$$

$$- \left\langle \frac{1}{\rho} \frac{\partial \langle p \rangle + p'}{\partial x_i} \right\rangle + \left\langle \nu \frac{\partial^2 \left\langle v_i \right\rangle + v_i'}{\partial x_j^2} \right\rangle . \tag{3.32b}$$

Applying the rules of statistical averaging (3.6) the continuity equation reduces to

$$\frac{\partial \langle v_j \rangle}{\partial x_j} = 0, \quad \text{because} \tag{3.33a}$$

$$\frac{\partial \left\langle v_j' \right\rangle}{\partial x_j} = 0. \tag{3.33b}$$

Note that, as indicated by equations (3.31a) and (3.33a), the temporally averaged velocity $\langle v_i \rangle$ and its fluctuation v_i' separately fulfill the continuity equation.

The non-linear term in the momentum equation (3.32b) can be rewritten as

$$\begin{aligned} \left\langle v_i v_j \right\rangle &= \left\langle \left(\langle v_i \rangle + v_i' \right) \left(\left\langle v_j \right\rangle + v_j' \right) \right\rangle = \left\langle \langle v_i \rangle \left\langle v_j \right\rangle + v_i' \left\langle v_j \right\rangle + \langle v_i \rangle v_j' + v_i' v_j' \right\rangle \\ &= \langle v_i \rangle \left\langle v_j \right\rangle + \langle v_i' \rangle \left\langle v_j \right\rangle + \langle v_i \rangle \left\langle v_j' \right\rangle + \left\langle v_i' v_j' \right\rangle \\ &= \langle v_i \rangle \left\langle v_j \right\rangle + \left\langle v_i' v_j' \right\rangle . \end{aligned} \tag{3.34}$$

Substituting the decomposition (3.34) into the momentum equation (3.32b) and using the continuity equation finally leads to the general RANS equations

$$\frac{\partial\langle v_i\rangle}{\partial t} + \frac{\partial\left\langle v_j\right\rangle\langle v_i\rangle}{\partial x_j} = -\frac{1}{\rho_0}\frac{\partial\langle p\rangle}{\partial x_i} + \nu\frac{\partial^2\langle v_i\rangle}{\partial x_j^2} - \frac{\partial\left\langle v_j' v_i'\right\rangle}{\partial x_j}. \tag{3.35}$$

Apart from the non-linear term constituted by the fluctuations, these equations are formally quite similar to the non-averaged Navier-Stokes equations. The additional non-linear term originates from the turbulent convective transport of momentum and is well-known as the *Reynolds stress* term. This term represents a second-order statistical moment of the velocities, which cannot be computed directly from the statistical lower-order moments, and therefore, has to be modeled. Basically, two different approaches exist to close the problem: *Reynolds stress models* (RMS) and *eddy viscosity models* (EVM). Reynolds stress models (RSM) close the RANS equation by solving separately a transport equation for all six Reynolds stresses $\left\langle v_j v_i\right\rangle$ and the turbulence dissipation rate ε. The eddy viscosity models compute the Reynolds stress tensor in analogy to the viscous stresses. They have become a standard approach for most technical flow configurations and are therefore discussed in more detail.

Eddy viscosity models

Eddy viscosity models are based on the *Boussinesq ansatz*. Following this ansatz, the components of the Reynolds stress tensor $\left\langle v_i' v_j'\right\rangle$ are assumed as proportional to the mean velocity gradients analogously to the viscous fluxes of momentum. In other words, Boussinesq proposed to model the convective turbulent transport of momentum in terms of a diffusive transport, written as

$$\frac{\langle\tau_\mathrm{t}\rangle}{\rho} = -\left\langle v_i' v_j'\right\rangle = 2\nu_\mathrm{t}\underbrace{\left(\frac{\partial\langle v_i\rangle}{\partial x_j} + \frac{\partial\left\langle v_j\right\rangle}{\partial x_i}\right)}_{\langle S_{ij}\rangle} - \frac{2}{3}\langle k\rangle\,\delta_{ij}, \tag{3.36}$$

where the *eddy viscosity* ν_t represents a turbulent analogue to the molecular kinematic viscosity ν. Using the ansatz (3.36), the momentum equation used for RANS (3.35) becomes

$$\frac{\partial\langle v_i\rangle}{\partial t} + \frac{\partial\left\langle v_j\right\rangle\langle v_i\rangle}{\partial x_j} = -\frac{1}{\rho_0}\frac{\partial\langle p\rangle}{\partial x_i} + (\nu + \nu_\mathrm{t})\frac{\partial^2\langle v_i\rangle}{\partial x_j^2}. \tag{3.37}$$

Note that the eddy viscosity ν_t is not a fluid property and strongly depends on the turbulence. Therefore, eddy viscosity models generally solve additional transport equations for certain characteristic turbulence parameters, which are used to calculate the local eddy viscosity ν_{t}. As compared to RSM, these models have the advantage that only a small number of additional equations need to be solved so that computational time is saved. For example, the $\mathscr{k}$-ε model solves two extra transport equations, for the turbulence kinetic energy $\mathscr{k}$ and the turbulence dissipation rate ε. In FIRE™ the standard turbulence model is the so called $\mathscr{k}$-ζ-f model, which will be introduced further below in this section.

In statistically stationary flow the solution obtained from RANS are temporally averaged flow quantities $\langle v_i \rangle$ and $\langle p \rangle$, as well as the temporal averaged turbulence kinetic energy $\langle \mathscr{k} \rangle$ and the turbulence dissipation rate $\langle \varepsilon \rangle$. The turbulence kinetic energy is supposed to represent the motion of the whole turbulence energy spectrum. Since RANS solutions are mostly computed as steady-state solutions, they do not capture any unsteady large scale vortical structures.

The $\mathscr{k}$-ζ-f model

The $\mathscr{k}$-ζ-f model [28, 43] is based on a non-linear eddy viscosity approach, where the eddy viscosity ν_{t} is defined as:

$$\nu_{\mathrm{t}} = C_{\mathscr{k}\zeta f,\nu} \zeta \frac{\mathscr{k}^2}{\varepsilon}, \tag{3.38}$$

and three different transport equations for $\mathscr{k}$, ε and ζ written as

$$\rho \frac{D\mathscr{k}}{Dt} = \rho(P_{\mathscr{k}} - \varepsilon) + \frac{\partial}{\partial x_j}\left(\left[\rho\left(\nu + \frac{\nu_{\mathrm{t}}}{\sigma_{\mathscr{k}\zeta f,\mathscr{k}}}\right)\frac{\partial \mathscr{k}}{\partial x_j}\right]\right) \tag{3.39a}$$

$$\rho \frac{D\varepsilon}{Dt} = \rho \frac{(C^*_{\mathscr{k}\zeta f,\varepsilon 1} P_{\mathscr{k}} - C_{\mathscr{k}\zeta f,\varepsilon 2}\varepsilon)}{t_{\mathscr{k}\zeta f}} + \frac{\partial}{\partial x_j}\left(\left[\rho\left(\nu + \frac{\nu_{\mathrm{t}}}{\sigma_{\mathscr{k}\zeta f,\varepsilon}}\right)\frac{\partial \varepsilon}{\partial x_j}\right]\right) \tag{3.39b}$$

$$\rho \frac{D\zeta}{Dt} = \rho f - \rho\frac{\zeta}{\mathscr{k}} P_{\mathscr{k}} + \frac{\partial}{\partial x_j}\left(\left[\rho\left(\nu + \frac{\nu_{\mathrm{t}}}{\sigma_{\mathscr{k}\zeta f,\zeta}}\right)\frac{\partial \zeta}{\partial x_j}\right]\right) \tag{3.39c}$$

are solved. The here appearing production term of the turbulence kinetic energy $P_{\mathscr{k}}$ is defined as:

$$P_{\mathscr{k}} = -\left\langle v_i' v_j' \right\rangle \frac{\partial \langle v_i \rangle}{\partial x_j} \tag{3.40}$$

The function $C^*_{\mathscr{k}\zeta f,\varepsilon 1}$ is used to dampen ε near solid walls by

$$C^*_{\mathscr{k}\zeta f,\varepsilon 1} = C_{\mathscr{k}\zeta f,\varepsilon 1}\left(1 + 0.045\sqrt{1/\zeta}\right). \tag{3.41}$$

The elliptic relaxation function f, occurring in equation (3.39c), is obtained from the solution of equation

$$f - \ell_{k\zeta f}^2 \frac{\partial^2 f}{\partial x_i^2} = \left(C_{k\zeta f,1} + C_{k\zeta f,2} \frac{P_k}{\varepsilon} \right) \frac{(2/3 - \zeta)}{t_{k\zeta f}}, \tag{3.42}$$

where the time-scale $t_{k\zeta f}$ and length-scale $\ell_{k\zeta f}$ are defined as

$$t_{k\zeta f} = \max\left(\min\left(\frac{k}{\varepsilon}, \frac{0.6}{\sqrt{6} C_{k\zeta f,\nu} |S| \zeta} \right), C_{k\zeta f,t} \left(\frac{\nu}{\varepsilon} \right)^{1/2} \right), \tag{3.43a}$$

$$\ell_{k\zeta f} = C_{k\zeta f,\ell} \max\left(\min\left(\frac{k^{3/2}}{\varepsilon}, \frac{k^{1/2}}{\sqrt{6} C_{k\zeta f,\nu} |S| \zeta} \right) C_{k\zeta f,\eta} \frac{\nu^{3/4}}{\varepsilon^{1/4}} \right), \tag{3.43b}$$

respectively. The constants in equations (3.39), (3.41), (3.42) and (3.43) are listed in table 3.1.

TABLE 3.1: The constants appearing in the k-ζ-f model.

symbol	value	symbol	value
$\sigma_{k\zeta f,k}$	1	$\sigma_{k\zeta f,\zeta}$	1.2
$\sigma_{k\zeta f,\varepsilon}$	1.3	$C_{k\zeta f,\varepsilon 1}$	0.012
$C_{k\zeta f,\varepsilon 2}$	1.9	$C_{k\zeta f,1}$	1.4
$C_{k\zeta f,2}$	0.65	$C_{k\zeta f,\nu}$	0.22
$C_{k\zeta f,t}$	6	$C_{k\zeta f,\eta}$	85

3.2.2 Turbulence near solid walls

At solid walls the relative velocity between the fluid and the wall is zero. This is the so called *no-slip* condition. Thus, near a solid wall all the momentum is lost and therefore, a *boundary layer* (BL) is created. Inside this BL the relative velocity increases from zero to the velocity outside the boundary layer (e.g. the velocity of the core region in a pipe). The turbulent motion inside the BL strongly enhances the diffusive transport processes due to the increased shear rates. This turbulent boundary layer can be split into different sublayers [48]. The sublayer next to the wall, the so called *viscous sublayer*, is dominated by the viscous stresses and the sublayer near the mean flow, the so called *turbulent sublayer*, is dominated by the turbulent stresses. Between these two layers there is a transitional sublayer (buffer layer), where both, viscous and turbulent stresses, are equally important. The *total shear stress* τ_{tot} inside the turbulent boundary layer can be expressed as the sum of the viscous and Reynolds stresses

$$\frac{\tau_{\mathrm{tot}}}{\rho} = \nu \frac{\partial \langle v_x \rangle}{\partial y} - \left\langle v_x' v_y' \right\rangle , \tag{3.44}$$

where $\langle v_x \rangle$ is the velocity component in the main flow direction parallel to the wall and y is the normal distance to the wall. At the wall ($y = 0$) the total shear stress is equal to the *wall shear stress* τ_{W}

$$\frac{\tau_{\mathrm{tot}}}{\rho} = \frac{\tau_{\mathrm{W}}}{\rho} = \nu \left. \frac{\partial \langle v_x \rangle}{\partial y} \right|_{y=0} \tag{3.45}$$

The *wall friction velocity* $\boldsymbol{v}_{\tau_{\mathrm{W}}}$ is often chosen as a characteristic velocity-scale for the turbulent boundary layer and is defined as:

$$\boldsymbol{v}_{\tau_{\mathrm{W}}} = \sqrt{\frac{\tau_{\mathrm{W}}}{\rho}}. \tag{3.46}$$

Using the wall friction velocity $\boldsymbol{v}_{\tau_{\mathrm{W}}}$ and the kinematic viscosity ν a characteristic length-scale can be defined as:

$$\boldsymbol{\ell}_{\tau_{\mathrm{W}}} = \frac{\nu}{\boldsymbol{v}_{\tau_{\mathrm{W}}}}. \tag{3.47}$$

Using the wall friction velocity-scale $\boldsymbol{v}_{\tau_{\mathrm{W}}}$ in combination with the hydraulic diameter $\boldsymbol{d}$ of the geometry (3.2), the wall friction based Reynolds number $\mathcal{R}e_{\tau_{\mathrm{W}}}$ can be defined as:

$$\mathcal{R}e_{\tau_{\mathrm{W}}} = \frac{\boldsymbol{v}_{\tau_{\mathrm{W}}} \boldsymbol{d}}{\nu}. \tag{3.48}$$

Based on the superposition (3.44), it is possible to derive wall functions $\langle v_x^+ \rangle = f(y^+)$ for the different sublayers, where $\langle v_x^+ \rangle = \langle v_x \rangle / \boldsymbol{v}_{\tau_{\mathrm{W}}}$ is the dimensionless velocity and $y^+ = y / \boldsymbol{\ell}_{\tau_{\mathrm{W}}}$ is the dimensionless distance from the wall. The thickness of the sublayers of the turbulence boundary layer can be universally classified as follows:

1. *viscous* sublayer: $(0 < y^+ < 5)$,
2. *buffer* sublayer: $(5 < y^+ < 30)$ and
3. fully *turbulent* inner sublayer: $(30 < y^+ < 400)$.

The universal velocity wall functions, valid inside the viscous and fully turbulent inner sublayer, are written as

$$\langle v_x^+\rangle_{\mathrm{lam}} = y^+, \quad 0 < y^+ < 5, \tag{3.49a}$$

$$\langle v_x^+\rangle_{\mathrm{t}} = \frac{1}{A_{\mathrm{K}}} ln(y^+) + B_{\mathrm{K}}, \quad y^+ > 30, \tag{3.49b}$$

where $A_{\mathrm{K}} = 0.42$ and $B_{\mathrm{K}} = 5$ is the Von Kármán constant. For the description of the buffer sublayer different models are available. The universal solutions (3.49a) and (3.49b) are shown in figure 3.6.

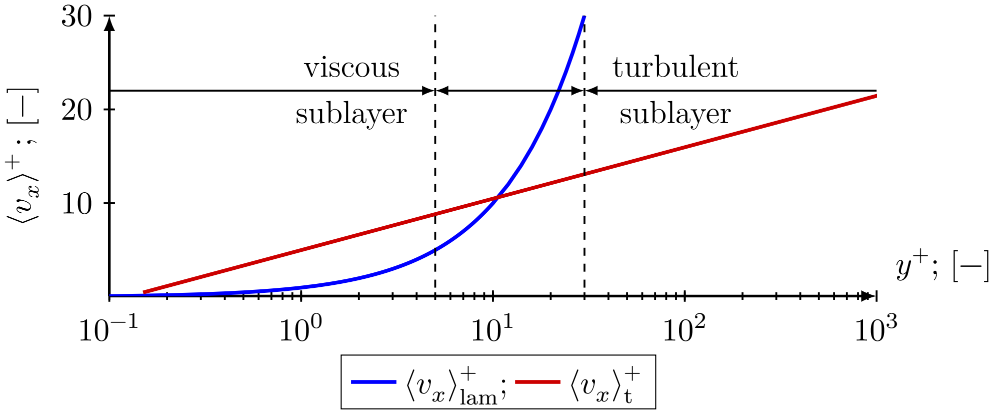

FIGURE 3.6: Logarithmic law of the wall.

If the linear laminar near-wall profile and wall friction based Reynolds number $\mathcal{Re}_{\tau_{\mathrm{W}}}$ of a flow configuration is known, it can be used to estimate the spatial resolution of the near-wall region in terms of the dimensionless wall distance y^+ written as

$$\Delta y^+ = \frac{\Delta y_{\mathrm{BL}}}{2} \frac{\mathcal{Re}_{\tau_{\mathrm{W}}}}{d}, \tag{3.50}$$

where Δy_{BL} is the distance of the first computational grid point to the wall. For LES simulations the boundary layer should be resolved down to the viscous sublayer, which requires $\Delta y^+ < 5$. Depending on the used wall model for RANS simulation $\Delta y^+ \approx 30$ might be sufficient.

3.2.3 Large-Eddy Simulation

The basic idea of LES [23] is to resolve the large scales of turbulence and to model only the small scales. This can be achieved by applying a spatial filter to the governing equations. This filter can be explicit (e.g. Gaussian filter, box filter, etc.) or implicit, where the spatial discretization of the computational grid (as in FIRE™) represents the filter. Using the grid as a filter (see figure 3.7), the resolved scales are greater than the grid size $\Delta\boldsymbol{x}_{\mathrm{C}}$, while the unresolved scales are smaller. The unresolved scales are therefore often referred to as the *subgrid-scales* (SGS). The unresolved scales need to be modeled by a so called *subgrid-scale model* (SGM).

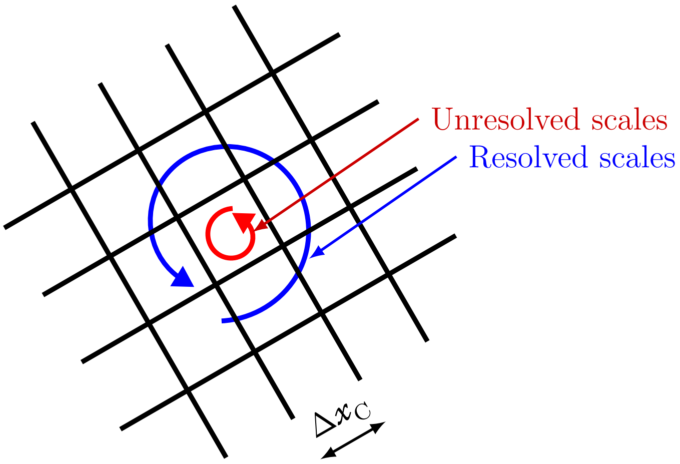

FIGURE 3.7: Resolved and unresolved scales of the computational grid with the local cell size $\Delta\boldsymbol{x}_{\mathrm{C}}$.

Applying an arbitrary filter on an arbitrary quantity ϕ, its instantaneous value can be decomposed into the resolved $\tilde{\phi}$ and unresolved ϕ'' part, which is known as the *Leonard decomposition* and defined as:

$$\phi = \tilde{\phi} + \phi''. \tag{3.51}$$

For different explicit or implicit filters (e.g. due to different computational grids) the filtered quantity $\tilde{\phi}$ varies. In comparison to the statistical averaging used for the Reynolds decomposition (3.6) the filtering exhibits some important different features, such as

$$\tilde{\tilde{\phi}} \neq \tilde{\phi} \quad \text{and} \tag{3.52a}$$

$$\widetilde{\phi''} \neq 0. \tag{3.52b}$$

The governing equations for LES, are derived by filtering the incompressible Navier-Stokes equations, which yields:

$$\frac{\partial \tilde{v}_j}{\partial x_j} = 0, \tag{3.53a}$$

$$\frac{\partial \tilde{v}_i}{\partial t} + \frac{\partial \widetilde{v_j v_i}}{\partial x_j} = -\frac{1}{\rho_0}\frac{\partial \tilde{p}}{\partial x_i} + \frac{1}{\rho_0}\frac{\partial \tilde{\tau}_{ji}}{\partial x_j}. \tag{3.53b}$$

Since the continuity equation (3.53a) is individually satisfied by both, the resolved filtered and the local instantaneous unresolved velocities, the unresolved subgrid-scale fluctuations satisfy the continuity equation as well:

$$\frac{\partial v_j''}{\partial x_j} = 0. \tag{3.54}$$

The non-linear term occurring in the filtered momentum equation (3.53b) cannot be computed directly. Substituting the Leonard decomposition into the non-linear term and subtracting the resolved term $\tilde{v}_j \tilde{v}_i$ yields

$$\begin{aligned} \widetilde{v_j v_i} - \tilde{v}_j \tilde{v}_i &= \widetilde{(\tilde{v}_j + v_j'')(\tilde{v}_i + v_i'')} - \tilde{v}_j \tilde{v}_i \\ &= \widetilde{\tilde{v}_j \tilde{v}_i} - \tilde{v}_j \tilde{v}_i + \widetilde{\tilde{v}_j v_i''} + \widetilde{v_j'' \tilde{v}_i} + \widetilde{v_j'' v_i''}, \end{aligned} \tag{3.55}$$

where three different terms can be distinguished:

$$\text{Leonard stresses:} \qquad L_{ij} = \widetilde{\tilde{v}_j \tilde{v}_i} - \tilde{v}_j \tilde{v}_i, \tag{3.56a}$$

$$\text{Cross stresses:} \qquad C_{ij} = \widetilde{\tilde{v}_j v_i''} + \widetilde{v_j'' \tilde{v}_i} \quad \text{and} \tag{3.56b}$$

$$\text{Reynolds stresses:} \qquad R_{ij} = \widetilde{v_j'' v_i''}. \tag{3.56c}$$

The *Leonard stresses* are resolved, if the explicit function of the LES filter is known, while the other stresses, the *Cross* and *Reynolds stresses*, are unresolved. These three stress tensors are mostly modeled together in terms of one common *SGS-tensor* $\tau_{ij,\mathrm{SGS}}$, which is the sum of the Leonard, Cross and Reynolds stress tensors:

$$\tilde{v}_j \tilde{v}_i + \left[\widetilde{v_j v_i} - \tilde{v}_j \tilde{v}_i\right] = \tilde{v}_j \tilde{v}_i + \left[L_{ij} + C_{ij} + R_{ij}\right] = \tilde{v}_j \tilde{v}_i + \tau_{ij,\mathrm{SGS}}. \tag{3.57}$$

The resulting system of equations, which is solved by the LES reads

$$\frac{\partial \tilde{v}_j}{\partial x_j} = 0 \quad \text{and} \tag{3.58a}$$

$$\frac{\partial \tilde{v}_i}{\partial t} + \frac{\partial \tilde{v}_j \tilde{v}_i}{\partial x_j} = -\frac{1}{\rho_0} \frac{\partial \tilde{p}}{\partial x_i} + \frac{1}{\rho_0} \frac{\partial \tilde{\tau}_{ji}}{\partial x_j} - \frac{1}{\rho_0} \frac{\partial \tau_{ji,\mathrm{SGS}}}{\partial x_j}, \tag{3.58b}$$

where the unresolved SGS stress tensor is computed from a subgrid-scale model to close the system of equations.

Subgrid-scale model

Most subgrid-scale model (SGM), which are required for closure of the filtered equations, are based on an eddy viscosity ansatz, written as

$$\tau_{ij,\mathrm{SGS}} - \frac{1}{3}\tilde{\tau}_{kk}\delta_{ij} = -2\nu_{\mathrm{SGS}}\tilde{S}_{ij}, \tag{3.59}$$

where ν_{SGS} is the SGS viscosity and $\tilde{S}_{ij}$ is the resolved rate of strain tensor. In FIRE™ the *Coherent Structure Model* (CSM) by Kobayashi [33, 34] is implemented, where the SGS viscosity ν_{SGS} is calculated as

$$\nu_{\mathrm{SGS}} = F_{\mathrm{CSM}}\Delta \boldsymbol{x}_{\mathrm{C}}^2|\tilde{S}|. \tag{3.60}$$

$\Delta \boldsymbol{x}_{\mathrm{C}}^2$ is the local filter width, which is calculated by FIRE™ using the local cell volumes V_{C} of the computational grid ($\Delta \boldsymbol{x}_{\mathrm{C}} = V_{\mathrm{C}}^{1/3}$). The function F_{CSM} is calculated from the resolved flow quantities as follows:

$$F_{\mathrm{CSM}} = \frac{1}{22}|F_{\mathrm{CSM,CS}}|^{3/2}F_{\mathrm{CSM},\Omega}, \tag{3.61a}$$

$$\text{with} \quad F_{\mathrm{CSM,CS}} = \frac{-\dfrac{1}{2}\dfrac{\partial \tilde{v}_j}{\partial x_i}\dfrac{\partial \tilde{v}_i}{\partial x_j}}{\dfrac{1}{2}\left(\dfrac{\partial \tilde{v}_j}{\partial x_j}\right)^2} \quad \text{and}$$

$$F_{\mathrm{CSM},\Omega} = 1 - F_{\mathrm{CSM,CS}}.$$

The CSM represents a so called dynamic SGM, where an additional wall damping function to provide a vanishing SGS viscosity ν_{SGS} near the wall is not necessary. Based on the SGS viscosity, the turbulence kinetic energy and the turbulence dissipation rate associated with the unresolved SGS-scale motion can be estimated as

$$k_{\mathrm{SGS}} = \nu_{\mathrm{SGS}}||\tilde{S}||/\sqrt{C_{\mathrm{SGS},\mu}} \quad \text{and} \tag{3.62a}$$

$$\varepsilon_{\mathrm{SGS}} = \nu_{\mathrm{SGS}}||\tilde{S}||^2, \tag{3.62b}$$

respectively, where $C_{\mathrm{SGS},\mu} = 0.09$ is a constant and $||\tilde{S}|| = \sqrt{2\tilde{S}_{ij}\tilde{S}_{ij}}$.

RANS vs. LES

For a comparison with RANS results the resolved flow quantities of the LES have to be temporally averaged using (2.2), such that

$$\phi_{\mathrm{RANS}} = \langle \phi \rangle \Leftrightarrow \left\langle \tilde{\phi} \right\rangle , \tag{3.63}$$

once the LES solution is statistically converged. When comparing the turbulence kinetic energy $\langle \mathcal{k} \rangle$, the resolved as well as the unresolved parts have to be considered in terms of their temporal averages:

$$\mathcal{k}_{\mathrm{RANS}} = \langle \mathcal{k}_{\mathrm{tot}} \rangle \Leftrightarrow \left\langle \widetilde{\mathcal{k}}_{\mathrm{LES}} \right\rangle + \langle \mathcal{k}_{\mathrm{SGS}} \rangle \, . \tag{3.64}$$

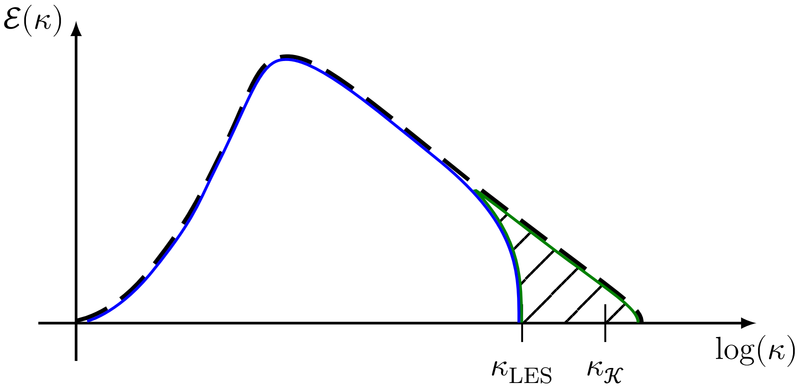

Figure 3.8: The turbulence kinetic energy spectrum of an LES simulation.

In figure 3.8 the energy spectrum of a LES is presented. A DNS simulation resolves the whole spectrum (black dashed line), up to the wave number associated with the Kolmogorov scale $\kappa_{\mathcal{K}} \sim 1/\nu$, whereas the LES only resolves the spectrum up to $\kappa_{\mathrm{LES}} \sim 1/\Delta \boldsymbol{x}_{\mathrm{C}}$ due to the filtering procedure (blue line). The SGS model essentially has the task to extract the right amount of turbulence kinetic energy from the resolved scales at $\kappa = \kappa_{\mathrm{LES}}$ to bridge the gap (hatched area) in dissipation between κ_{LES} and $\kappa_{\mathcal{K}}$. A RANS simulation has to model the whole turbulence kinetic energy spectrum, instead.

3.3 Computational fluid dynamics

In the previous sections, the governing system of equations for incompressible flows (2.35) were derived, which were solved using the CFD-software FIRE™ [7]. In the present section some fundamentals of CFD, some solution techniques applied in FIRE™ and related particular tasks of this Master's Thesis are discussed.

CFD is a numerical method to solve approximately the governing set of equations for the flow field, heat and mass transfer and associated phenomena like chemical reactions [2, 47, 54]. Commercial CFD codes often provide a pre- and post-processor as well, where the latter generally has the task to bring the results of the CFD solution into interpretable form (graphs, figures, ect.).

3.3.1 Pre-processing

The pre-processor translates the required user input into a form suitable for the solver. The required user input consists of several parts [55], which are presented in the following.

Computational domain and grid

The first step is the definition of the *computational domain* and the required time-frame ($T = t_{\text{end}} - t_{\text{start}}$) by the engineer. The result is the geometry of the considered fluid volume, specified by the outer surface of the computational domain. This computational volume is often generated using commercial CAD[1] programs. In the successive grid-generation process the computational domain is subdivided into N_{C} non-overlapping *finite control volumes* (cells) with the cell volume V_{C}. The *computational grid* (or mesh) can be structured or unstructured (see figure 3.9), depending on the chosen geometry of the cells (Tetrahedron (tet), Hexahedron (hex), etc.). Each cell has N_{N} corner nodes, N_{E} edges and N_{F} faces (see figure 3.10).

---

[1] CAD: Computer Aided Design

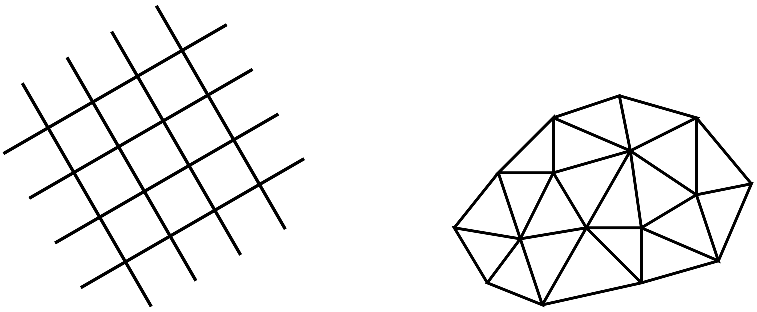

(a) A structured grid. **(b)** An unstructured grid.

Figure 3.9: Different types of grids.

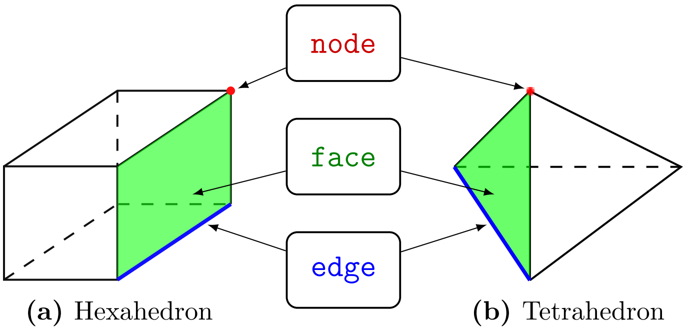

(a) Hexahedron **(b)** Tetrahedron

Figure 3.10: Different grid topologies and their structure.

The quality of the cells (grid) can be quantified by various parameters:

Skewness is a quantity that quantifies the distortion of a cell:

$$\beta_{\mathrm{SK}} = \max\left(\frac{\beta_{\mathrm{max}} - \beta_{\mathrm{opt}}}{\beta_{\mathrm{opt}}}, \frac{\beta_{\mathrm{opt}} - \beta_{\mathrm{min}}}{\beta_{\mathrm{opt}}}\right), \tag{3.65}$$

where β_{opt} is the optimal angle (e.g. 90° for an optimal quadrilateral cell, represented by a rectangle). In figure 3.11 the definition of the skewness for an arbitrary quadrilateral is presented.

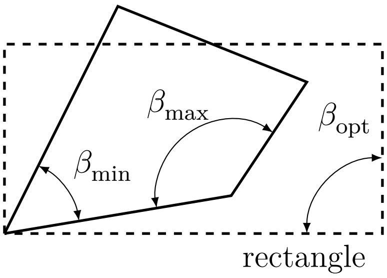

Figure 3.11: The skewness of a quadrilateral cell.

Aspect Ratio quantifies the stretching of a cell:

$$\mathit{AR} = \frac{\text{longest edge}}{\text{shortest edge}} \quad \text{and} \tag{3.66}$$

$$\mathit{AR}_\mathrm{V} = \frac{\text{Volume circumsphere}}{C_{\mathit{AR}}\text{Volume cell}} \qquad \text{(Volume based)}, \tag{3.67}$$

where C_{AR} is a chosen factor so that the volume based *aspect ratio* $\mathit{AR}_\mathrm{V} = 1$ for an optimal cell (e.g. equilateral tetrahedron). Its definition for an arbitrary triangle is presented in figure 3.12.

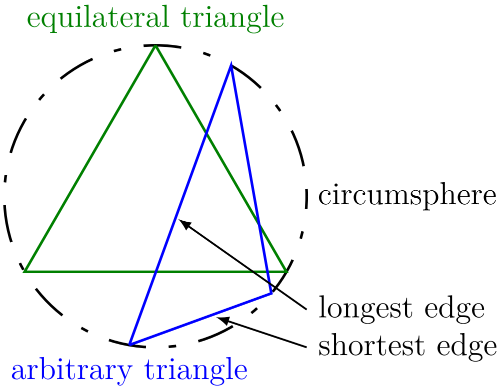

Figure 3.12: The aspect ratio AR of a triangle.

Smoothness of the grid compares the volumes V_C of neighboring cells, which should not differ too much. In figure 3.13 the smoothness between cells is illustrated, where the transition between cells A and B is smooth, while is not between the cells B and C.

Figure 3.13: The smoothness between cells.

Additionally, the computational grid needs to fulfill certain resolution requirements, which might be, e.g. imposed by the actually applied turbulence wall model.

Model definition and numerical setup

The second step is the definition of the required physical models (compressibility, turbulence models, etc.). For the present Master's Thesis the setup for solving the incompressible Navier-Stokes equations (2.35b) is selected.

The numerical setup determines the important settings of the solver, choosing different solution control parameters (under relaxation, blending factors, etc.), differencing schemes (central, upwind, etc.), or different solver-types. A well-chosen numerical setup might accelerate the performed simulation, whereas badly chosen parameters might lead to unphysical results or to the divergence of the simulation.

Fluid definition

The third step is the definition of the fluid and its properties. This Master's Thesis considers *atmospheric air*, which is defined as ideal gas, with the spezific gas constant $\mathcal{R}_{\mathrm{air}}$, where the reference pressure p_{ref} and the reference temperature θ_{ref} need to be specified. The reference density is then calculated from the equation of state for an ideal gas (2.27). The dynamic viscosity of the fluid is specified using *Sutherland's law* [53] for an ideal gas, where the dynamic viscosity μ is dependent on the fluid temperature θ:

$$\mu(\theta) = \mu_{\mathrm{ref}} \left(\frac{\theta}{\theta_{\mathrm{S,ref}}} \right)^{3/2} \frac{\theta_{\mathrm{S,ref}} + \theta_{\mathrm{S}}}{\theta + \theta_{\mathrm{S}}}. \tag{3.68}$$

Therein, $\theta_{\mathrm{S,ref}}$ is the reference temperature of the model, θ_S is the so called Sutherland's temperature, and μ_{ref} is the reference dynamic viscosity. The presently used values of these coefficients are listed in table 3.2.

TABLE 3.2: The coefficients of Sutherland's law.

coefficient	value	[unit]
μ_{ref}	18.27×10^{-6}	[Pa s]
$\theta_{\mathrm{S,ref}}$	291.15	[K]
θ_{S}	120	[K]

Initial conditions

The fourth step is the definition of *initial conditions*, from which the solver will start the solution procedure. Good initial conditions can accelerate the solution process significantly. In case of eddy resolving simulations (LES) at moderate Reynolds numbers, imposing an initial disturbance might be necessary to finally obtain a statistically converged self-sustained turbulent flow (see section 3.1.1).

Boundary conditions

The last step is the definition of appropriate *boundary conditions* (BC), in particular at the inlet, outlet and wall boundary.

For the inlet and the outlet BCs certain combinations of in- and outflow conditions (e.g. mass flow, velocity distribution, pressure etc.) are possible. Additionally, a BC at the inlet, for the turbulence kinetic energy k and turbulence dissipation rate ε are required. In case of RANS-type simulations the BCs are necessary for the temporally averaged field quantities, whereas in case of LES, the BCs are required for the instantaneous field variables. The instantaneous inlet BC, required for the LES simulation, might be modeled or computed from an additional auxiliary LES.

At the outlet a constant pressure level p_{ref} is often specified. In FIRE™ the definition of an *averaged pressure* (averaged over the boundary face) is available for this scope. The averaged pressure BC is advantageous, especially for LES, since it allows for instantaneous pressure fluctuations at the boundary.

Usually, at solid boundaries (walls), the *no-slip* condition ($v_i = 0$) is imposed.

3.3.2 Solution procedure

The CFD-solver implemented in FIRE™ [7] numerically solves the governing set of conservation equations using the finite volume method (FVM) in a Cartesian coordinate system ($i = x, y, z$). This method basically performs the following three steps:

Integration: The integration of the governing conservation equations over all individual cells N_{C}.

Discretization: The spatial and temporal discretization of the integral equations. The result is a system of algebraic equations.

Solution: The iterative numerical solution of the system of algebraic equations. The result is the flow field plus the results for the transported scalars.

Depending on the considered problem, FIRE™ solves the conservation equations of mass ρ, momentum ρv_i, total enthalpy $H = h + v_i v_i / 2$ and the concentration of any number of species c_{species}. Since this Master's Thesis is focused on incompressible isothermal flows, only the conservation laws for mass ρ (2.8) and momentum ρv_i (2.9) are solved. In the integration step FIRE™ transforms the conservation laws into an integral form by integrating over an arbitrary control volume V (FVM) bounded by N_{F} ($l = 1 \dots N_{\mathrm{F}}$) piecewise smooth surfaces. Using the *Gauss theorem*, a volume integral can be converted into surface integrals, which is thus transformed into a sum of surface integrals over all cell faces N_{F}. The required face values are computed from an interpolation between the nodal values of neighboring cells. For calculating gradients different discretization schemes (central differencing, upwind schemes, etc.) are available. A *blending factor* $0 \leq \alpha_{\mathrm{B,s}} \leq 1$ has to be chosen for interpolation between the central differencing $\alpha_{\mathrm{B,s}} = 1$ and the upwind schemes $\alpha_{\mathrm{B,s}} = 0$. In case of LES the blending factor should be as close to $\alpha_{\mathrm{B,s}} = 1$ as possible so that the most accurate discretization scheme is used. The simulation though might become unstable so that smaller values $\alpha_{\mathrm{B,s}} \approx 0.98$ have to be chosen.

For unsteady flow problems the solver requires a time marching method, which integrates the solution step by step over a discrete time-step Δt. For fully explicit schemes a stability criterion

$$\mathit{CFL}_{\mathrm{CFD}} = \frac{|v|\Delta t}{\Delta \boldsymbol{x}_{\mathrm{C}}} \leq 1 \tag{3.69}$$

has to be satisfied, where $\Delta \boldsymbol{x}_{\mathrm{C}} = V_{\mathrm{C}}^{1/3}$ can be estimated for each cell separately. Even though FIRE™ uses implicit time integration schemes, which are also stable for $\mathit{CFL}_{\mathrm{CFD}} > 1$, equation (3.69) can be used to estimate an appropriate time-step for the simulation. First (Euler) or second order implicit schemes are available. A blending factor $0 \leq \alpha_{\mathrm{B},t} \leq 1$ can be used to interpolate between the solutions of the first $\alpha_{\mathrm{B},t} = 0$ and second order $\alpha_{\mathrm{B},t} = 1$. In the implicit solution procedure, the system of algebraic equations is obtained from the spatial and temporal discretization, which is iteratively solved. After each iterative step *under-relaxation* factors α_{UR} are used to limit the temporal change of the field variables. The sum of the under relaxation factors of the continuity equation and of the momentum equation should be one. The iterative procedure within each time-step Δt is continued, until a converged solution is reached.

Pressure correction

Due to the incompressibility of the flow configuration, the density ρ and the pressure p are decoupled. In FIRE™ the SIMPLE[2] algorithm is used to solve for the pressure. This method basically solves a Poisson equation for the pressure, which is further used to correct the predicted velocities, so that they satisfy the continuity equation. For unsteady flows a combination of the SIMPLE and PISO[3] algorithm is used, which is more efficient in these cases [54].

---

[2] SIMPLE: Semi-Implicit-Method for Pressure-Linked Equations

[3] PISO: Pressure Implicit Split Operator

The numerical algorithm

The numerical algorithm (see figure 3.14) in FIRE™ (applied to incompressible flows) based on a SIMPLE/PISO pressure correction approach can be summarized as follows:

1. Calculate all geometric quantities (cell volumes, cell face areas, etc.) of the computational grid.

2. Initialize the field variables ϕ^n at $t = 0$.

3. Start the time stepping loop. Store current field variables as old field variables ($\phi^{n-1} = \phi^n$). Update the BCs for the current time-step.

4. Start the implicit time iteration loop.

5. Compute the predicted flow field by assembling and solving the algebraic system of equations, which represent the conservation equations of momentum.

6. SIMPLE/PISO algorithm:
    a) Assemble and solve the algebraic system of equations to obtain the velocity and pressure corrections.
    b) Compute the corrected values of the flow field v_i and p.

7. Solve the turbulence model and update the eddy viscosity ν_t.

    RANS: Assemble and solve corresponding transport equations depending on the selected eddy viscosity model (e.g. k-ζ-f) and calculate the eddy viscosity ν_t. The turbulence kinetic energy $\langle k \rangle$ and the turbulence dissipation rate $\langle \varepsilon \rangle$ are direct results from the model.

    LES: Calculate the eddy viscosity ν_SGS (3.60) by applying the SGS model. Additionally calculate the turbulence dissipation rate ε_SGS (3.62b) and the SGS turbulence kinetic energy k_SGS (3.62a).

8. Check the convergence criterion and return to step 4 if convergence criterion is not fulfilled, else:

    steady: Simulation is finished.

    transient: Return to step 3 and continue until the required simulation time t_end is reached. In case of an LES, calculate temporal averaged values (3.63) and calculate the total turbulence kinetic energy $\left\langle \widetilde{k}_\mathrm{tot} \right\rangle$ (3.64) from the resulting fluctuations.

Ensemble average

Since transient eddy resolving simulations (DNS, LES, etc.) advance step per step over time, the database available for calculating the temporal average increases with each time-step. For calculating statistically reliable temporal averages (and the fluctuations around these), long simulation times are necessary. For a constant time-step Δt the temporal average of an arbitrary quantity ϕ can be computed as

$$\langle \phi \rangle = \frac{1}{N_T \Delta t} \sum_{N_{\text{start}}+1}^{N_{\text{start}}+N_T} \Delta t \phi^n, \tag{3.70}$$

where N_T denotes the number of time-steps after the start of the averaging process at $N = N_{\text{start}} + 1$.

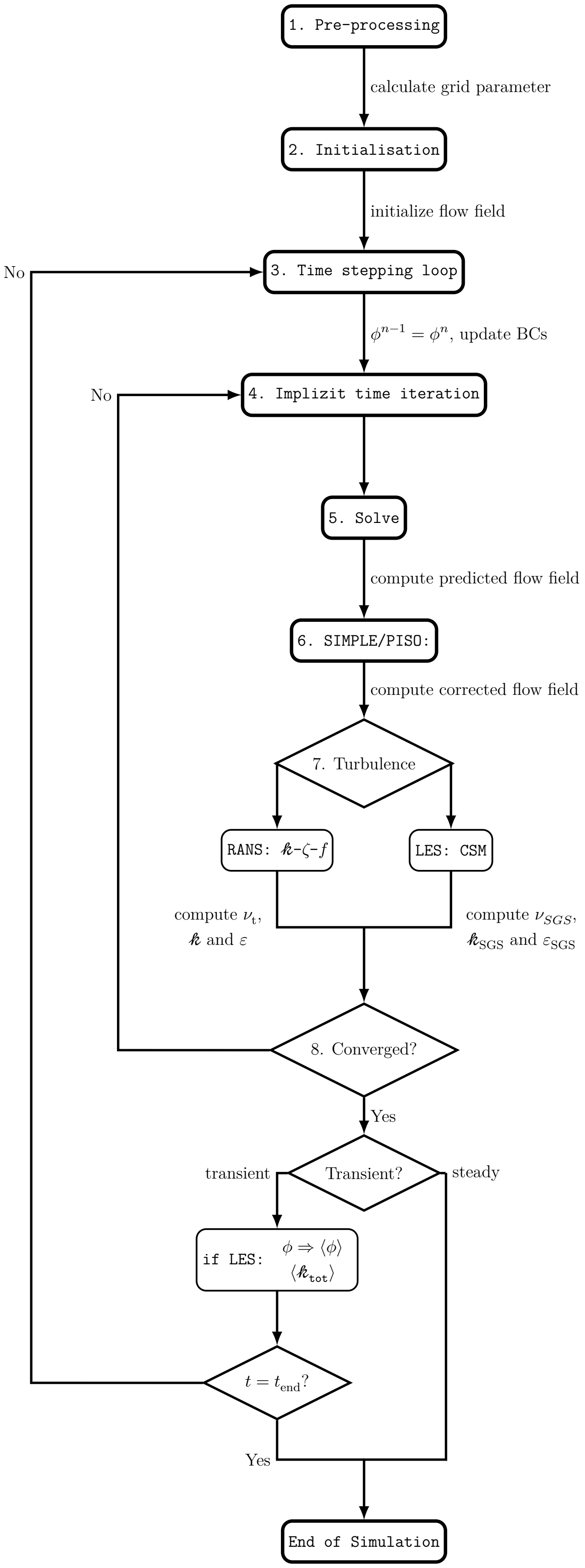

Figure 3.14: The FIRE™ solver algorithm.

4 Aeroacoustics

In the previous chapter, some fundamental features of the presently applied CFD-solver were described, whose solution is used to calculate the targeted aeroacoustic sources. In this chapter, the mathematical derivation of these aeroacoustic sources is presented in detail. First, Lighthill's acoustic analogy is presented in section 4.1, which is the foundation of aeroacoustics, but is very limited in application due to the underlying assumptions. Second, the acoustic analogy of Lilley is derived in section 4.2, which is a more general acoustic analogy, but, due to its mathematical complexity, is difficult to solve. Third, the aeroacoustic decomposition, the foundation of hybrid CAA approaches, is introduced in section 4.3, which further delivers a LEE based acoustic analogy. In section 4.4 it is shown that the main aeroacoustic source term from the LEE is equivalent to the aeroacoustic source term in Lilley's acoustic analogy, by applying both acoustic analogies to a two-dimensional sheared flow. The successive section 4.5 explains the computation of the aeroacoustic source terms from the LES solution. Some additional methods for the centering of the aeroacoustic source term are also proposed, to investigate the influence of large low-frequency vortical structures in incompressible flows. Additionally, the impact of the SGS contributions on the aeroacoustic sources is briefly discussed. In section 4.6 this chapter is concluded by shortly presenting the solution procedure of the CAA module in FIRE™, including a description of the UKSG model used for reconstructing the aeroacoustic source terms from a RANS solution.

4.1 Lighthill's acoustic analogy

In this section *Lighthill's acoustic analogy* is presented and discussed. The basic idea of Lighthill was to derive a wave equation, in which the source term includes all possible sound generation mechanisms driven by the motion of the fluid. To achieve that goal, Lighthill derived a formally exact wave equation, applying no approximations to the Navier-Stokes equations. Accordingly, Lighthill started from the full set of Navier-Stokes equations, as already presented in section 2.2. Originally, Lighthill excluded the mass source term $S_{\dot{m}}$ from the continuity and momentum equations as well as the external force term $S_{f,i}$ from the momentum equation. Since effects like mass injection, can also act as a sound source, these terms are presently not excluded. Thus, the derivation starts with the continuity equation (2.8) and the momentum equation (2.9), rewritten in conservative form as

$$\frac{\partial \rho}{\partial t} + \frac{\partial}{\partial x_j}\left(\rho v_j\right) = S_{\dot{m}},$$

$$\frac{\partial}{\partial t}\left(\rho v_i\right) + \frac{\partial}{\partial x_j}\left(\rho v_j v_i\right) = -\frac{\partial}{\partial x_j}\left(P_{ji}\right) + S_{f,j} + S_{\dot{m}} v_i.$$

Taking the time derivative of the continuity equation and the divergence of the momentum equation, one obtains

$$\frac{\partial^2}{\partial t \partial x_j}\left(\rho v_j\right) = -\frac{\partial^2 \rho}{\partial t^2} + \frac{\partial S_{\dot{m}}}{\partial t} \quad \text{and} \tag{4.2a}$$

$$\frac{\partial^2}{\partial t \partial x_j}\left(\rho v_j\right) = -\frac{\partial^2}{\partial x_i \partial x_j}\left(p\delta_{ij} - \tau_{ji} + \rho v_j v_i\right) + \frac{\partial S_{f,j}}{\partial x_j} + \frac{\partial S_{\dot{m}} v_j}{\partial x_j}. \tag{4.2b}$$

After eliminating the term on the LHS from (4.2), one obtains

$$\frac{\partial^2 \rho}{\partial t^2} = \frac{\partial^2}{\partial x_i \partial x_j}\left(p\delta_{ij} - \tau_{ji} + \rho v_j v_i\right) + \frac{\partial S_{\dot{m}}}{\partial t} - \frac{\partial S_{f,j}}{\partial x_j} - \frac{\partial S_{\dot{m}} v_j}{\partial x_j}. \tag{4.3}$$

Decomposing the pressure p and density ρ into fluid-dynamical (temporally averaged $\langle\phi\rangle$ and turbulent fluctuations ϕ') and acoustic components (acoustic perturbation ϕ_a), written as

$$\rho = \langle\rho\rangle + \rho' + \rho_\mathrm{a}, \tag{4.4a}$$

$$p = \langle p\rangle + p' + p_\mathrm{a}, \tag{4.4b}$$

equation (4.3) can be transformed into

$$\frac{\partial^2 \rho_\mathrm{a}}{\partial t^2} - c_0^2 \frac{\partial^2 \rho_\mathrm{a}}{\partial x_i^2} = \frac{\partial^2 T_{ij}}{\partial x_i \partial x_j} + \frac{\partial S_{\dot{m}}}{\partial t} - \frac{\partial S_{f,j}}{\partial x_j} - \frac{\partial S_{\dot{m}} v_j}{\partial x_j}, \tag{4.5}$$

Equation (4.5) represents the well-known wave equation of Lighthill, whose RHS evidently consists of several different aerodynamic source terms. The first term, involving the *Lighthill stress tensor* T_{ij}:

$$T_{ij} = \rho v_i v_j - \tau_{ij} + (p_\mathrm{a} - c_0^2 \rho_\mathrm{a})\delta_{ij}. \tag{4.6}$$

contains three different terms which originate from different flow effects:

- non-linear convective forces due to the Reynolds stresses: $\rho v_i v_j$,
- viscous forces: τ_{ij}
- entropy perturbations (e.g. due to combustion): $s_\mathrm{a} = p_\mathrm{a} - c_0^2 \rho_\mathrm{a}$.

As already mentioned, the remaining three source terms originate from mass injection ($S_{\dot{m}}$) with the impulse ($S_{\dot{m}} v_i$) and from the external force ($S_{f,i}$), which are now excluded.

Note that the LHS of equation (4.5) is equal to the simple wave operator equation (2.42b) derived in section 2.3. This is the major benefit of Lighthill's acoustic analogy, since methods from classical acoustics are applicable without restrictions if the aeroacoustic source terms on the RHS are known. Since these source terms have still to be calculated or measured, the solution of this wave equation (4.5) is not easier than that of the original set of compressible equations. Therefore, Lighthill made some simplifying assumptions for the Lighthill stress tensor T_{ij}, which essentially limit his analogy. This implies that the observer is standing far away from the source surrounded by a quiescent fluid with the reference speed of sound c_ref at the observers position. Accordingly, only the acoustic components of the flow variables, $\phi_\mathrm{a} = \phi - \langle\phi\rangle$, are varying in space and time in the far field, whereas the turbulent fluctuations are zero ($\phi' = 0$), as the fluid is quiescent. Assuming further isentropic flow, implying $p_\mathrm{a} = c_\mathrm{ref}^2 \rho_\mathrm{a}$ and neglecting viscous forces ($\tau_{ij} = 0$), finally reduces the Lighthill stress tensor to

$$T_{ij} = \langle \rho \rangle \, v_i v_j . \tag{4.7}$$

In hybrid CAA approaches the aeroacoustic sources on the RHS of equation (4.5) are calculated from a CFD solution. One major drawback still remains in that all sound propagation phenomena, like refraction inside shear or boundary layers, appear as aeroacoustic sources, although they are wave propagation effects, as the interaction between the sound sources and the acoustic field is completely neglected. Throughout history numerous extensions were added to Lighthill's acoustic analogy. E.g. Curle [20] introduced the influence of solid boundaries. Powell [44] and Howe [30] included the feedback phenomenon from the acoustic field to the sound sources based on the vortex sound theory. Ffowcs-Williams & Hawkings [57] accounted for the noise from arbitrary moving objects. All these acoustic analogies are based on analytically solving the wave equation of the type (4.5) using so called *Green functions*. Therefore, a more advanced acoustic analogy has to be found, which includes less assumptions and is also applicable in internal flows. In the following section 4.2, the generalization of Lighthill's acoustic analogy to non-uniform flows by Phillips and Lilley is derived.

4.2 Lilley's acoustic analogy

In this section *Lilley acoustic analogy* is derived following the description of Goldstein [26]. The derivation starts with the equation for the material derivative of the entropy s rewritten as

$$\frac{1}{c^2}\frac{Dp}{Dt} - \frac{D\rho}{Dt} = \rho\sigma\frac{Ds}{Dt}. \tag{4.8}$$

Using the continuity equation in primitive form (2.30a), with zero mass source term $\dot{m}$ yields

$$\frac{1}{\rho c^2}\frac{Dp}{Dt} + \frac{\partial v_j}{\partial x_j} = \sigma\frac{Ds}{Dt}. \tag{4.9}$$

Taking the material derivative of equation (4.9) leads to

$$\frac{D}{Dt}\left(\frac{1}{\rho c^2}\frac{Dp}{Dt}\right) + \frac{D}{Dt}\frac{\partial v_j}{\partial x_j} = \frac{D}{Dt}\left(\sigma\frac{Ds}{Dt}\right). \tag{4.10}$$

Recalling the momentum equation in primitive form (2.30b)

$$\frac{Dv_i}{Dt} = -\frac{1}{\rho}\frac{\partial p}{\partial x_i} + \frac{1}{\rho}\frac{\partial \tau_{ji}}{\partial x_j} \tag{4.11}$$

and taking the divergence it gives

$$\frac{\partial}{\partial x_i}\frac{Dv_i}{Dt} = -\frac{\partial}{\partial x_i}\left(\frac{1}{\rho}\frac{\partial p}{\partial x_i}\right) + \frac{\partial}{\partial x_i}\left(\frac{1}{\rho}\frac{\partial \tau_{ji}}{\partial x_j}\right). \tag{4.12}$$

Using the identity

$$\frac{\partial}{\partial x_i}\frac{D}{Dt} \equiv \frac{D}{Dt}\frac{\partial}{\partial x_i} + \frac{\partial v_j}{\partial x_i}\frac{\partial}{\partial x_j} \tag{4.13}$$

and eliminating the term $\partial/\partial x_i(D(v_i)/Dt)$ in equation (4.10) and (4.12), the following wave equation can be derived

$$\begin{aligned}\frac{D}{Dt}\left(\frac{1}{\rho c^2}\frac{Dp}{Dt}\right) - \frac{\partial}{\partial x_i}\left(\frac{1}{\rho}\frac{\partial p}{\partial x_i}\right) = \\ \frac{\partial v_j}{\partial x_i}\frac{\partial v_i}{\partial x_j} - \frac{\partial}{\partial x_i}\left(\frac{1}{\rho}\frac{\partial \tau_{ji}}{\partial x_j}\right) + \frac{D}{Dt}\left(\sigma\frac{Ds}{Dt}\right).\end{aligned} \tag{4.14}$$

Equation (4.14) is the so called *Phillips equation.* It is formally similar to Lighthill's wave equation with the time derivative $\partial/\partial t$ replaced by the material derivative D/Dt. Originally, a logarithmic expression for the pressure p was introduced as

$$\mathcal{P} := \frac{1}{\gamma}\ln\frac{p}{p_{\text{ref}}}, \quad \text{and} \tag{4.15a}$$

$$\gamma = c^2\frac{\rho}{p}, \tag{4.15b}$$

where p_{ref} is a convenient reference pressure. Using the definition (4.15a), the following wave equation for the *logarithmic pressure* $\mathcal{P}$ is obtained as

$$\begin{aligned}\frac{D^2\mathcal{P}}{Dt^2} - \frac{\partial}{\partial x_i}\left(c^2\frac{\partial\mathcal{P}}{\partial x_i}\right) = \\ \frac{\partial v_j}{\partial x_i}\frac{\partial v_i}{\partial x_j} - \frac{\partial}{\partial x_i}\left(\frac{1}{\rho}\frac{\partial\tau_{ji}}{\partial x_j}\right) + \frac{D}{Dt}\left(\sigma\frac{Ds}{Dt}\right).\end{aligned} \tag{4.16}$$

Equation (4.14) can take account of some interaction between the mean flow and the acoustic waves. Lilley and Doak [22] argued that some wave propagation effect are still hidden in the first term on the RHS of the Phillips equation so that this term is not a pure aeroacoustic source term. To obtain a wave equation, where all the wave propagation effects are appearing exclusively on the LHS, included in the wave operator, the further following steps are necessary. First, another material derivative is applied to Phillips equation (4.14) yielding a third order differential equation written as

$$\begin{aligned}\frac{D}{Dt}\left[\frac{D}{Dt}\left(\frac{1}{\rho c^2}\frac{Dp}{Dt}\right) - \frac{\partial}{\partial x_i}\left(\frac{1}{\rho}\frac{\partial p}{\partial x_i}\right)\right] = \\ \frac{D}{Dt}\left[\frac{\partial v_j}{\partial x_i}\frac{\partial v_i}{\partial x_j}\right] - \frac{D}{Dt}\left[\frac{\partial}{\partial x_i}\left(\frac{1}{\rho}\frac{\partial\tau_{ji}}{\partial x_j}\right)\right] + \frac{D}{Dt}\left[\frac{D}{Dt}\left(\sigma\frac{Ds}{Dt}\right)\right].\end{aligned} \tag{4.17}$$

Using the product rule of differentiation, the first term on the RHS can be rewritten as

$$\begin{aligned}\frac{D}{Dt}\left[\frac{\partial v_j}{\partial x_i}\frac{\partial v_i}{\partial x_j}\right] &= \frac{\partial v_j}{\partial x_i}\frac{D}{Dt}\left(\frac{\partial v_i}{\partial x_j}\right) + \frac{\partial v_i}{\partial x_j}\frac{D}{Dt}\left(\frac{\partial v_j}{\partial x_i}\right) \\ &= 2\frac{\partial v_j}{\partial x_i}\frac{D}{Dt}\left(\frac{\partial v_i}{\partial x_j}\right).\end{aligned} \tag{4.18}$$

Introducing (4.18) into (4.17) gives

$$\begin{aligned}&\frac{D}{Dt}\left[\frac{D}{Dt}\left(\frac{1}{\rho c^2}\frac{Dp}{Dt}\right)-\frac{\partial}{\partial x_i}\left(\frac{1}{\rho}\frac{\partial p}{\partial x_i}\right)\right]=\\&\qquad 2\frac{\partial v_j}{\partial x_i}\frac{D}{Dt}\left(\frac{\partial v_i}{\partial x_j}\right)-\frac{D}{Dt}\left[\frac{\partial}{\partial x_i}\left(\frac{1}{\rho}\frac{\partial \tau_{ji}}{\partial x_j}\right)\right]+\frac{D}{Dt}\left[\frac{D}{Dt}\left(\sigma\frac{Ds}{Dt}\right)\right].\end{aligned} \tag{4.19}$$

Applying again the identity (4.13) to the LHS term of equation (4.12), the latter can be rewritten as

$$\frac{D}{Dt}\frac{\partial v_i}{\partial x_j}=-\frac{\partial v_j}{\partial x_i}\frac{\partial v_i}{\partial x_j}-\frac{\partial}{\partial x_j}\left(\frac{1}{\rho}\frac{\partial p}{\partial x_i}\right)+\frac{\partial}{\partial x_j}\left(\frac{1}{\rho}\frac{\partial \tau_{ik}}{\partial x_k}\right). \tag{4.20}$$

Substituting equation (4.20) into equation (4.18) leads to

$$\begin{aligned}2\frac{\partial v_j}{\partial x_i}\frac{D}{Dt}\left(\frac{\partial v_i}{\partial x_j}\right)=&-2\frac{\partial v_j}{\partial x_i}\frac{\partial v_k}{\partial x_j}\frac{\partial v_j}{\partial x_k}-2\frac{\partial v_j}{\partial x_i}\frac{\partial}{\partial x_i}\left(\frac{1}{\rho}\frac{\partial p}{\partial x_i}\right)\\&+2\frac{\partial v_j}{\partial x_i}\frac{\partial}{\partial x_i}\left(\frac{1}{\rho}\frac{\partial \tau_{ik}}{\partial x_k}\right).\end{aligned} \tag{4.21}$$

After substituting equation (4.19) into equation (4.18) and rearranging some terms *Lilley's wave equation* can be written as

$$\begin{aligned}&\frac{D}{Dt}\left[\frac{D}{Dt}\left(\frac{1}{\rho c^2}\frac{Dp}{Dt}\right)-\frac{\partial}{\partial x_i}\left(\frac{1}{\rho}\frac{\partial p}{\partial x_i}\right)\right]+2\frac{\partial v_j}{\partial x_i}\frac{\partial}{\partial x_j}\frac{1}{\rho}\frac{\partial p}{\partial x_i}=\\&-2\frac{\partial v_j}{\partial x_i}\frac{\partial v_k}{\partial x_j}\frac{\partial v_i}{\partial x_k}+\mathcal{S}_{\tau,s},\end{aligned} \tag{4.22}$$

where $\mathcal{S}_{\tau,s}$ represent aeroacoustic sources from viscous and entropy changing effects (e.g. chemical heat release)

$$\mathcal{S}_{\tau,s}=2\frac{\partial v_j}{\partial x_i}\frac{\partial}{\partial x_j}\frac{1}{\rho}\frac{\partial \tau_{ik}}{\partial x_k}-\frac{D}{Dt}\left[\frac{\partial}{\partial x_i}\left(\frac{1}{\rho}\frac{\partial \tau_{ji}}{\partial x_j}\right)\right]+\frac{D}{Dt}\left[\frac{D}{Dt}\left(\sigma\frac{Ds}{Dt}\right)\right]. \tag{4.23}$$

Introducing again the logarithmic pressure $\mathcal{P}$ (4.15a) as the dependent quantity, the following wave equation is finally obtained

$$\begin{aligned} \frac{D}{Dt}\left[\frac{D^2\mathcal{P}}{Dt^2} - \frac{\partial}{\partial x_i}\left(c^2\frac{\partial\mathcal{P}}{\partial x_i}\right)\right] + 2\frac{\partial v_j}{\partial x_i}\frac{\partial}{\partial x_j}c^2\frac{\partial\mathcal{P}}{\partial x_i} = \\ -2\frac{\partial v_j}{\partial x_i}\frac{\partial v_k}{\partial x_j}\frac{\partial v_i}{\partial x_k} + \mathcal{S}_{\tau,s}. \end{aligned} \tag{4.24}$$

In contrast to Lighthill's acoustic analogy, Lilley's acoustic analogy includes refraction and convection effects of sound sources on the LHS into the wave operator. As a consequence, the aeroacoustic source term on the RHS is a pure source of sound without wave propagation effects. However, the advantage of the high order wave operator comes with the great mathematical complexity of the solutions of this equation. To date, only limited solutions are known for Lilley's acoustic analogy.

The CAA Module of FIRE™ is based on linearized Euler equations (LEE) which are solved for the acoustical field. Thus, an acoustic analogy has to be found, which can deliver aeroacoustic sources for the LEE and is applicable in internal flows. Therefore, in the following section, an acoustic analogy based on the LEE is derived.

4.3 Acoustic analogy based on LEE

4.3.1 Aeroacoustic decomposition

The *aeroacoustic decomposition*, the foundation of hybrid CAA approaches, separates the flow variables into the base flow components, represented by the mean values $\langle \phi \rangle$, the turbulence fluctuations ϕ', and the acoustic perturbations ϕ_{a}. It is defined as:

$$\phi = \langle \phi \rangle + \phi' + \phi_{\mathrm{a}}. \tag{4.25}$$

In hybrid CAA approaches the turbulent flow field, represented by the first two components, and the acoustic field are calculated separately. Thus, the CFD solution for the flow is decoupled from the acoustic perturbations.

Applying this decomposition to the flow variables density ρ , pressure p and velocity v_i gives

$$\rho = \langle \rho \rangle \ + \rho' + \rho_{\mathrm{a}}, \tag{4.26a}$$

$$v_i = \langle v_i \rangle + v_i' + v_{\mathrm{a},i}, \tag{4.26b}$$

$$p = \langle p \rangle \ + p' + p_{\mathrm{a}}. \tag{4.26c}$$

4.3.2 Linearized Euler equations

In this section the linearized form of the compressible Euler equations (2.32) are derived based on the aeroacoustic decomposition (4.25). Since the hybrid approach is based on an incompressible simulation, only the turbulent instantaneous fluctuations of the velocity v_i' and the pressure p' are considered, as $\rho' = 0$ and $\rho = \langle \rho \rangle = \rho_{\mathrm{ref}} = \mathrm{const.}$. Thus, the aeroacoustic decomposition only includes the turbulent velocity and pressure fluctuations, which need to be provided by a submodel, while neglecting the turbulent density fluctuation, such that

$$\rho = \rho_{\mathrm{ref}} \qquad + \rho_{\mathrm{a}}, \tag{4.27a}$$

$$v_i = \langle v_i \rangle + v_i' + v_{\mathrm{a},i}, \tag{4.27b}$$

$$p = \langle p \rangle \ + p' + p_{\mathrm{a}}. \tag{4.27c}$$

Substituting the reduced aeroacoustic decomposition (4.27) into the system of Euler equations (2.34) gives

$$\frac{D}{Dt}\left(\rho_{\mathrm{ref}}+\rho_{\mathrm{a}}\right) = -\left(\rho_{\mathrm{ref}}+\rho_{\mathrm{a}}\right)\frac{\partial}{\partial x_j}\left(\left\langle v_j\right\rangle + v'_j + v_{\mathrm{a},j}\right), \tag{4.28a}$$

$$\frac{D}{Dt}\left(\left\langle v_i\right\rangle + v'_i + v_{\mathrm{a},i}\right) = -\frac{1}{\rho_{\mathrm{ref}}+\rho_{\mathrm{a}}}\frac{\partial}{\partial x_i}\left(\langle p\rangle + p' + p_{\mathrm{a}}\right) \quad \text{and} \tag{4.28b}$$

$$\frac{D}{Dt}\left(\langle p\rangle + p' + p_{\mathrm{a}}\right) = -\gamma(\langle p\rangle + p' + p_{\mathrm{a}})\frac{\partial}{\partial x_j}\left(\left\langle v_j\right\rangle + v'_j + v_{\mathrm{a},j}\right). \tag{4.28c}$$

Assuming that the acoustic density perturbations ρ_{a} are small compared to the mean flow density $\langle\rho\rangle = \rho_{\mathrm{ref}}$ the linearization of the inverse of the density can be written as

$$\frac{1}{\rho_{\mathrm{ref}}+\rho_{\mathrm{a}}} \approx \frac{1-\dfrac{\rho_{\mathrm{a}}}{\rho_{\mathrm{ref}}}}{\rho_{\mathrm{ref}}} = \frac{1}{\rho_{\mathrm{ref}}} - \cancelto{\ll}{\frac{\rho_{\mathrm{a}}}{\rho_{\mathrm{ref}}^2}} \approx \frac{1}{\rho_{\mathrm{ref}}}. \tag{4.29}$$

We further rewrite the statistically averaged representation of the Euler equations. The terms, including only temporal averaged flow quantities written as

$$\cancelto{=0}{\frac{\partial\rho_{\mathrm{ref}}}{\partial t}} + \rho_{\mathrm{ref}}\frac{\partial\left\langle v_j\right\rangle}{\partial x_j} + \left\langle v_j\right\rangle \cancelto{=0}{\frac{\partial\rho_{\mathrm{ref}}}{\partial x_j}} = 0, \tag{4.30a}$$

$$\frac{\partial\left\langle v_i\right\rangle}{\partial t} + \left\langle v_j\right\rangle\frac{\partial\left\langle v_i\right\rangle}{\partial x_j} = -\frac{1}{\rho_{\mathrm{ref}}}\frac{\partial\langle p\rangle}{\partial x_i} - \left\langle v'_j\frac{\partial v'_i}{\partial x_j}\right\rangle, \tag{4.30b}$$

$$\frac{\partial\langle p\rangle}{\partial t} + \left\langle v_j\right\rangle\frac{\partial\langle p\rangle}{\partial x_j} = -\gamma\langle p\rangle\frac{\partial\left\langle v_j\right\rangle}{\partial x_i} \tag{4.30c}$$

appear as subsets in the full set of equations (4.28), and hence, cancel out. Incompressible flow behavior also implies divergence-free mean and fluctuating velocity fields, $\partial\left\langle v_i\right\rangle/\partial x_i = 0$ and $\partial v'_i/\partial x_i = 0$, respectively. Additionally neglecting the non-linear cross-terms, constituted by the turbulence fluctuations and acoustic components, the *linearized Euler equations* (LEE) finally become

$$\frac{\partial \rho_\mathrm{a}}{\partial t} + \left\langle v_j \right\rangle \frac{\partial \rho_\mathrm{a}}{\partial x_j} + \langle \rho \rangle \frac{\partial \rho_\mathrm{a}}{\partial x_j} = 0 \tag{4.31a}$$

$$\frac{\partial v_{\mathrm{a},i}}{\partial t} + v_{\mathrm{a},j} \frac{\partial \langle v_i \rangle}{\partial x_j} + \left\langle v_j \right\rangle \frac{\partial v_{\mathrm{a},i}}{\partial x_j} + \frac{1}{\rho_\mathrm{ref}} \frac{\partial p_\mathrm{a}}{\partial x_i} =$$

$$- \frac{\partial v_i'}{\partial t} - v_j' \frac{\partial \langle v_i \rangle}{\partial x_j} - \left\langle v_j \right\rangle \frac{\partial v_i'}{\partial x_j} - v_j' \frac{\partial v_i'}{\partial x_j} + \left\langle v_j' \frac{\partial v_i'}{\partial x_j} \right\rangle - \frac{1}{\rho_\mathrm{ref}} \frac{\partial p'}{\partial x_j} \tag{4.31b}$$

$$\frac{\partial p_\mathrm{a}}{\partial t} + \left\langle v_j \right\rangle \frac{\partial p_\mathrm{a}}{\partial x_j} + v_{\mathrm{a},j} \frac{\partial \langle p \rangle}{\partial x_j} + \gamma \langle p \rangle \frac{\partial v_{\mathrm{a},j}}{\partial x_j} =$$

$$- \frac{\partial p'}{\partial t} - \left\langle v_j \right\rangle \frac{\partial p'}{\partial x_j} - v_j' \frac{\partial \langle p \rangle}{\partial x_j} - v_j' \frac{\partial p'}{\partial x_j} \tag{4.31c}$$

The terms on the LHS of equation (4.31) represent a convective wave operator depending on the mean flow field, whereas terms on the RHS can be considered as aeroacoustic sources similar as in other acoustic analogies. For an accurate prediction of the acoustic field in terms of ρ_a, $v_{\mathrm{a},i}$ and p_a a reliable prescription of the aeroacoustic source terms determined from the underlying turbulent flow field is a standard requirement.

In most previous related work found in various publications [1, 17, 19] only the non-linear terms, constituted by the turbulent velocity fluctuations, written as

$$\Omega_i' = \mathcal{S}_i - \langle \mathcal{S}_i \rangle \,, \quad \text{where} \tag{4.32a}$$

$$\mathcal{S}_i = v_j' \frac{\partial v_i'}{\partial x_j} \quad \text{and} \tag{4.32b}$$

$$\langle \mathcal{S}_i \rangle = \left\langle v_j' \frac{\partial v_i'}{\partial x_j} \right\rangle , \tag{4.32c}$$

are considered, whereas all other aeroacoustic source terms are neglected. Therefore, the aeroacoustic source term Ω_i' occurring in the momentum equation of the LEE is the mainly investigated aeroacoustic source term in the present Master's Thesis.

4.3.3 Linearized Euler equations solved by the CAA tool in FIRE™

The CAA tool, actually implemented in FIRE™, additionally neglects the turbulent pressure fluctuations p' in the aeroacoustic decomposition (4.26), which becomes

$$
\begin{aligned}
\rho &= \rho_{\mathrm{ref}} \qquad + \rho_{\mathrm{a}}, && (4.33\mathrm{a})\\
v_i &= \langle v_i \rangle + v'_i + v_{\mathrm{a},i}, && (4.33\mathrm{b})\\
p &= \langle p \rangle \qquad + p_{\mathrm{a}}. && (4.33\mathrm{c})
\end{aligned}
$$

Accordingly, all aeroacoustic source terms containing the pressure fluctuations p' in the LEE (4.31) vanish. Additionally, the temporal derivative of the velocity fluctuations $\partial v'_i/\partial t$ and the temporally averaged non-linear aeroacoustic source term $\langle \mathcal{S}_i \rangle$ are neglected, as well. The cross-terms, constituted of the mean flow variables and the turbulence fluctuations, are not neglected, though. The obtained LEE, solved by the CAA module in FIRE™, reads

$$
\begin{aligned}
&\frac{\partial \rho_{\mathrm{a}}}{\partial t} + \langle v_j \rangle \frac{\partial \rho_{\mathrm{a}}}{\partial x_j} + \langle \rho \rangle \frac{\partial \rho_{\mathrm{a}}}{\partial x_j} = 0 && (4.34\mathrm{a})\\
&\frac{\partial v_{\mathrm{a},i}}{\partial t} + v_{\mathrm{a},j} \frac{\partial \langle v_i \rangle}{\partial x_j} + \langle v_j \rangle \frac{\partial v_{\mathrm{a},i}}{\partial x_j} + \frac{1}{\rho_{\mathrm{ref}}} \frac{\partial p_{\mathrm{a}}}{\partial x_i} = \\
&\quad - v'_j \frac{\partial \langle v_i \rangle}{\partial x_j} - \langle v_j \rangle \frac{\partial v'_i}{\partial x_j} - v'_j \frac{\partial v'_i}{\partial x_j} && (4.34\mathrm{b})\\
&\frac{\partial p_{\mathrm{a}}}{\partial t} + \langle v_j \rangle \frac{\partial p_{\mathrm{a}}}{\partial x_j} + v_{\mathrm{a},j} \frac{\partial \langle p \rangle}{\partial x_j} - \gamma \langle p \rangle \frac{\partial v_{\mathrm{a},j}}{\partial x_j} = -v'_j \frac{\partial \langle p \rangle}{\partial x_j}. && (4.34\mathrm{c})
\end{aligned}
$$

The aeroacoustic source term appearing in the momentum equation evidently reads

$$
\Lambda_i + \mathcal{S}_i = v'_j \frac{\partial \langle v_i \rangle}{\partial x_j} + \langle v_j \rangle \frac{\partial v'_i}{\partial x_j} + v'_j \frac{\partial v'_i}{\partial x_j}, \tag{4.35}
$$

which is the same aeroacoustic source term used by Bechara et al. [13]. The current version of the CAA tool in FIRE™ generates output only for the cross-terms in the pressure equation of the LEE (4.34c)

$$
\Pi = v'_j \frac{\partial \langle p \rangle}{\partial x_j}, \tag{4.36}
$$

therefore, only this term can be considered, when the aeroacoustic source terms, computed form LES and the UKSG in the CAA tool of FIRE™ are compared.

Nontheless, the possible contribution of the cross-terms, appearing in the momentum equation of the LEE (4.34b) as

$$\Lambda_i = \langle v_j \rangle \frac{\partial v_i'}{\partial x_j} + v_j' \frac{\partial \langle v_i \rangle}{\partial x_j}, \tag{4.37}$$

to the aeroacoustic source terms shall be investigated in this Master's Thesis.

4.4 Aeroacoustic Sources for two-dimensional sheared flows

In the previous section 4.2 the acoustic analogy of Lilley was derived, which is more suitable for non-uniform flows compared to Lighthill's acoustic analogy. In this section it will be shown that the LEE formulation is equivalent to Lilley's acoustic analogy, when considering [17, 18, 26] a two-dimensional sheared mean flow. Considering in particular two-dimensional incompressible transversly sheared mean flow given in a Cartesion coordinate system by

$$\langle v_1 \rangle (x_2), \langle v_2 \rangle = \langle v_3 \rangle = 0, \tag{4.38a}$$

$$\langle p \rangle = \text{const.} = p_{\text{ref}}, \tag{4.38b}$$

$$\langle \rho \rangle = \text{const.} = \rho_{\text{ref}}, \tag{4.38c}$$

the Reynolds decomposition of the instantaneous quantities read

$$v_1 = \langle v_1 \rangle + v_1', \tag{4.39a}$$

$$v_2 = v_2', \tag{4.39b}$$

$$p = \langle p \rangle + p'. \tag{4.39c}$$

We further assume uniform speed of sound $c = c_{\text{ref}}$ and neglect the turbulent velocity fluctuations occuring in the wave operator on the LHS of Phillips (4.14) and Lilley's (4.24) acoustic analogy, so that they read

$$\frac{\bar{D}^2 \mathcal{P}}{\bar{D}^2 t} - c_{\text{ref}}^2 \frac{\partial^2 \mathcal{P}}{\partial x_j^2} = 2 \frac{\partial \langle v_1 \rangle}{\partial x_2} \frac{\partial v_2}{\partial x_1} + \frac{\partial v_j}{\partial x_i} \frac{\partial v_i}{\partial x_j}, \tag{4.40a}$$

$$\frac{\bar{D}}{\bar{D}t} \left[\frac{\bar{D}^2 \mathcal{P}}{\bar{D} t^2} - c_{\text{ref}} \frac{\partial^2 \mathcal{P}}{\partial x_i^2} \right] + 2 c_{\text{ref}}^2 \frac{\partial v_1}{\partial x_2} \frac{\partial}{\partial x_1} \frac{\partial \mathcal{P}}{\partial x_2} = -2 \frac{\partial v_j}{\partial x_i} \frac{\partial v_k}{\partial x_j} \frac{\partial v_i}{\partial x_k}, \tag{4.40b}$$

where the material derivative is simplified to

$$\frac{\bar{D}}{\bar{D}t} = \frac{\partial}{\partial t} + \langle v_1 \rangle \frac{\partial}{\partial x_1}, \tag{4.41}$$

and the viscous stresses and entropy changing effects (e.g. chemical heat release, shocks, etc.) have been discarded, as well.

Introducing the Reynolds decomposition (4.39) into the RHS of (4.40a) yields Phillips acoustic analogy applied to a two-dimensional sheared flow, which reads

$$\frac{\bar{D}^2\mathcal{P}}{\bar{D}^2 t} - c_{\mathrm{ref}}^2 \frac{\partial^2 \mathcal{P}}{\partial x_j^2} = 2\frac{\partial v_1}{\partial x_2}\frac{\partial v_2'}{\partial x_1} + \frac{\partial v_j'}{\partial x_i}\frac{\partial v_i'}{\partial x_j}. \tag{4.42}$$

To obtain once more a third order wave equation of Lilley's type, the material derivative (4.41) is applied to (4.42), yielding

$$\frac{\bar{D}}{\bar{D}t}\left[\frac{\bar{D}^2\mathcal{P}}{\bar{D}^2 t} - c_{\mathrm{ref}}^2 \frac{\partial^2 \mathcal{P}}{\partial x_j^2}\right] = 2\frac{\bar{D}}{\bar{D}t}\left[\frac{\partial\langle v_1\rangle}{\partial x_2}\frac{\partial v_2'}{\partial x_1}\right] + \frac{\bar{D}}{\bar{D}t}\left[\frac{\partial v_j'}{\partial x_i}\frac{\partial v_i'}{\partial x_j}\right]. \tag{4.43}$$

Expanding the term on the RHS of equation (4.43) yields

$$2\frac{\bar{D}}{\bar{D}t}\left[\frac{\partial\langle v_1\rangle}{\partial x_2}\frac{\partial v_2'}{\partial x_1}\right] = 2\frac{\partial\langle v_1\rangle}{\partial x_2}\frac{\bar{D}}{\bar{D}t}\frac{\partial v_2'}{\partial x_1} + 2\frac{\partial v_2'}{\partial x_1}\frac{\bar{D}}{\bar{D}t}\frac{\partial\langle v_1\rangle}{\partial x_2}. \tag{4.44}$$

Applying the derivative, with respect to x_1 to the transverse momentum equation generally given by (4.11), using the logarithmic pressure $\mathcal{P}$, and further applying the identity (4.13), the following expression is obtained

$$\begin{aligned} \frac{\partial}{\partial x_1}\frac{\bar{D}v_2'}{\bar{D}t} = \frac{\bar{D}}{\bar{D}t}\frac{\partial v_2'}{\partial x_1} + \frac{\partial v_j}{\partial x_1}\frac{\partial v_2'}{\partial x_j} &= -c_{\mathrm{ref}}^2\frac{\partial^2\mathcal{P}}{\partial x_1 \partial x_2} \\ \Rightarrow \frac{\bar{D}}{\bar{D}t}\frac{\partial v_2'}{\partial x_1} = -c_{\mathrm{ref}}^2\frac{\partial^2\mathcal{P}}{\partial x_1 \partial x_2} - \frac{\partial v_j}{\partial x_1}\frac{\partial v_2'}{\partial x_j}&. \end{aligned} \tag{4.45}$$

Introducing the above expressions into the third order wave equation (4.43) yields

$$\begin{aligned} \frac{\bar{D}}{\bar{D}t}\left[\frac{\bar{D}^2\mathcal{P}}{\bar{D}^2 t} - c_{\mathrm{ref}}^2 \frac{\partial^2 \mathcal{P}}{\partial x_j^2}\right] + 2c_{\mathrm{ref}}^2\frac{\partial\langle v_1\rangle}{\partial x_2}\frac{\partial^2\mathcal{P}}{\partial x_1\partial x_2} &= \\ \frac{\bar{D}}{\bar{D}t}\left[\frac{\partial v_j'}{\partial x_i}\frac{\partial v_i'}{\partial x_j}\right] + 2\frac{\partial v_2'}{\partial x_1}\frac{\bar{D}}{\bar{D}t}\frac{\partial\langle v_1\rangle}{\partial x_2} - 2\frac{\partial\langle v_1\rangle}{\partial x_2}\frac{\partial v_j}{\partial x_1}\frac{\partial v_2'}{\partial x_j}&. \end{aligned} \tag{4.46}$$

As expected the wave operator on the LHS of (4.46) is identical to the operator in the corresponding formulation for the acoustic analogy of Lilley (4.40b). The second term on the RHS side of (4.46) vanishes since

$$\frac{\bar{D}}{\bar{D}t}\frac{\partial\langle v_1\rangle}{\partial x_2} = \cancelto{=0}{\frac{\partial}{\partial t}\frac{\partial\langle v_1\rangle}{\partial x_2}} + \cancelto{=0}{\langle v_1\rangle\frac{\partial}{\partial x_1}\frac{\partial\langle v_1\rangle}{\partial x_2}} = 0. \tag{4.47}$$

Assuming that the fluctuating velocities are divergence free $\partial v_i'/\partial x_i = 0$, the

RHS of (4.46) can be transformed yielding

$$\frac{\bar{D}}{\bar{D}t}\left[\frac{\bar{D}^2\mathcal{P}}{\bar{D}^2t} - c_{\mathrm{ref}}^2\frac{\partial^2\mathcal{P}}{\partial x_j^2}\right] + 2c_{\mathrm{ref}}^2\frac{\partial\langle v_1\rangle}{\partial x_2}\frac{\partial^2\mathcal{P}}{\partial x_1\partial x_2} =$$
$$\frac{\bar{D}}{\bar{D}t}\left[\frac{\partial^2 v_i' v_j'}{\partial x_i\partial x_j}\right] - 2\frac{\partial\langle v_1\rangle}{\partial x_2}\frac{\partial^2 v_2' v_j'}{\partial x_1\partial x_j}. \tag{4.48}$$

Goldstein argued that these two terms on the RHS of equation (4.48) are the main aeroacoustic source terms for sheared flow configurations (e.g. free jets, mixing layer, etc.).

4.4.1 Application of the LEE to the two-dimensional shear flow

To show that the acoustic analogy based on the LEE (4.31) together with the main aeroacoustic source terms $\mathcal{S}_i$ (4.32b), derived in section 4.3, is equivalent to Lilley's acoustic analogy, a third order wave equation of Lilley's type is derived from the LEE and applied to the two-dimensional shear flow.

Considering the continuity equation of the LEE (4.31a) applied to the two-dimensional shear flow and rewritten as

$$\frac{1}{c_{\mathrm{ref}}^2}\frac{\partial p_{\mathrm{a}}}{\partial t} + \frac{1}{c_{\mathrm{ref}}^2}\frac{\partial p_{\mathrm{a}}\langle v_i\rangle}{\partial x_i} + \frac{\partial v_{\mathrm{a},i}}{\partial x_i} = 0, \tag{4.49}$$

where the acoustic density fluctuations ρ_{a} were replaced by the acoustic pressure fluctuations using $p_{\mathrm{a}} = c_{\mathrm{ref}}^2\rho_{\mathrm{a}}$. Applying the material derivative (4.41) to the continuity equation (4.49) leads to

$$\frac{1}{c_{\mathrm{ref}}^2}\frac{\bar{D}^2 p_{\mathrm{a}}}{\bar{D}t^2} + \frac{\bar{D}}{\bar{D}t}\frac{\partial\langle v_{\mathrm{a},i}\rangle\rho_{\mathrm{ref}}}{\partial x_i} = 0. \tag{4.50}$$

We recall the momentum equation of the LEE (4.31b), which shall be applied to two-dimensional shear flow and is accordingly rewritten as

$$\frac{\partial\rho_{\mathrm{ref}}v_{\mathrm{a},i}}{\partial t} + \frac{\partial\langle v_i\rangle\rho_{\mathrm{ref}}v_{\mathrm{a},i}}{\partial x_j} + \frac{\partial p_{\mathrm{a}}}{\partial x_i} = \rho_{\mathrm{ref}}\mathcal{S}_i, \tag{4.51}$$

where the aeroacoustic source term $\mathcal{S}_i$ appears as a priorly unknown term. Applying the divergence to (4.51) and rewriting the first two terms on the LHS using the material derivative leads to

$$\frac{\partial}{\partial x_i}\frac{\bar{D}\rho_{\mathrm{ref}}v_{\mathrm{a},i}}{\bar{D}t}+\frac{\partial^2 p_{\mathrm{a}}}{\partial x_i^2}=\rho_{\mathrm{ref}}\frac{\partial \mathcal{S}_i}{\partial x_i} \tag{4.52}$$

Subtracting equation (4.52) from equation (4.50) one obtains

$$\frac{1}{c_{\mathrm{ref}}^2}\frac{\bar{D}^2 p_{\mathrm{a}}}{\bar{D}t^2}-\frac{\partial^2 p_{\mathrm{a}}}{\partial x_i^2}+\frac{\bar{D}}{\bar{D}t}\frac{\partial\langle v_{\mathrm{a},i}\rangle\,\rho_{\mathrm{ref}}}{\partial x_i}-\frac{\partial}{\partial x_i}\frac{\bar{D}\rho_{\mathrm{ref}}v_{\mathrm{a},i}}{\bar{D}t}=-\rho_{\mathrm{ref}}\frac{\partial \mathcal{S}_i}{\partial x_i}. \tag{4.53}$$

Applying the identity (4.13) to two-dimensional shear flow, i.e.,

$$\frac{\partial}{\partial x_i}\frac{D}{Dt}\equiv\frac{D}{Dt}\frac{\partial}{\partial x_i}+\frac{\partial\langle v_1\rangle}{\partial x_2}\frac{\partial}{\partial x_1}, \tag{4.54}$$

the third term on the LHS in equation (4.53) can be rewritten as

$$\frac{\bar{D}}{\bar{D}t}\frac{\partial\langle v_{\mathrm{a},i}\rangle\,\rho_{\mathrm{ref}}}{\partial x_i}=\frac{\partial}{\partial x_i}\frac{\bar{D}\rho_{\mathrm{ref}}v_{\mathrm{a},i}}{\bar{D}t}-2\frac{\partial\langle v_1\rangle}{\partial x_2}\frac{\partial v_{\mathrm{a},i}\rho_{\mathrm{ref}}}{\partial x_1}. \tag{4.55}$$

Applying again the material derivative to (4.53), after substituting (4.55), leads to the third order wave equation

$$\frac{\bar{D}}{\bar{D}t}\left[\frac{1}{c_{\mathrm{ref}}^2}\frac{\bar{D}^2 p_{\mathrm{a}}}{\bar{D}t^2}-\frac{\partial^2 p_{\mathrm{a}}}{\partial x_i^2}\right]-2\frac{\bar{D}}{\bar{D}t}\frac{\partial\langle v_1\rangle}{\partial x_2}\frac{\partial v_{\mathrm{a},i}\rho_{\mathrm{ref}}}{\partial x_1}=-\frac{\bar{D}}{\bar{D}t}\rho_{\mathrm{ref}}\frac{\partial \mathcal{S}_i}{\partial x_i}. \tag{4.56}$$

Taking the derivative with respect to x_1 of the transverse momentum equation written as

$$\frac{\partial}{\partial x_1}\frac{\bar{D}\rho_{\mathrm{ref}}v_{\mathrm{a},2}}{\bar{D}t}+\frac{\partial^2 p_{\mathrm{a}}}{\partial x_1\partial x_2}=\rho_{\mathrm{ref}}\frac{\partial \mathcal{S}_2}{\partial x_1}, \tag{4.57}$$

the third order wave equation finally reads

$$\begin{aligned}\frac{\bar{D}}{\bar{D}t}\left[\frac{1}{c_{\mathrm{ref}}^2}\frac{\bar{D}^2 p_{\mathrm{a}}}{\bar{D}t^2}-\frac{\partial^2 p_{\mathrm{a}}}{\partial x_i^2}\right]-2\frac{\bar{D}}{\bar{D}t}\frac{\partial\langle v_1\rangle}{\partial x_2}\frac{\partial^2 p_{\mathrm{a}}}{\partial x_1\partial x_2}&=\\ -\frac{\bar{D}}{\bar{D}t}\rho_{\mathrm{ref}}\frac{\partial \mathcal{S}_i}{\partial x_i}-\frac{\partial\langle v_1\rangle}{\partial x_2}\rho_{\mathrm{ref}}\frac{\partial \mathcal{S}_2}{\partial x_1}&\quad.\end{aligned} \tag{4.58}$$

If the aeroacoustic source term $\mathcal{S}_i$ is chosen as

$$\mathcal{S}_i=-\frac{\partial v_j' v_i'}{\partial x_j} \tag{4.59}$$

the resulting third order wave equation and its aeroacoustic source term are equivalent to the formulation derived by Goldstein (4.48). This aeroacoustic source term represents the non-linear turbulent velocity fluctuations already identified as the main aeroacoustic source term in section 4.3.

4.5 Aeroacoustic sources from LES

In section 4.3 the aeroacoustic sources for the LEE were identified. In the present section the method for calculating the aeroacoustic sources from an incompressible LES simulation is discussed.

LES basically provides resolved instantaneous velocities $\tilde{v}_i$, pressure $\tilde{p}$, and, in case of a compressible LES, density $\tilde{\rho}$ fields down to the grid scale (see section 3.2). By subtracting the temporally averaged resolved flow quantities $\left\langle\tilde{\phi}\right\rangle$ from the resolved instantaneous flow quantities $\tilde{\phi}$ the resolved turbulent fluctuations $\tilde{\phi}'$ are obtained as

$$\tilde{\phi}' = \tilde{\phi} - \left\langle\tilde{\phi}\right\rangle . \tag{4.60}$$

The resolved turbulent contribution to the main aeroacoustic source term consistently reads

$$\tilde{\mathcal{S}}_{i,\mathrm{LES}} = \tilde{v}_j' \frac{\partial \tilde{v}_i'}{\partial x_j}. \tag{4.61}$$

The resolved cross-terms appearing in the momentum equation of the LEE (4.34), as used by FIRE™, rewritten as

$$\widetilde{\Lambda}_{i,\mathrm{LES}} = \tilde{v}_j' \frac{\partial\langle\tilde{v}_i\rangle}{\partial x_j} + \left\langle\tilde{v}_j\right\rangle \frac{\partial \tilde{v}_i'}{\partial x_j}, \quad \text{and} \tag{4.62a}$$

$$\widetilde{\Pi}_{\mathrm{LES}} = \tilde{v}_j' \frac{\partial\langle\tilde{p}\rangle}{\partial x_j}, \tag{4.62b}$$

can also be directly calculated from the resolved flow quantities.

4.5.1 Determination of aeroacoustic source term

The aeroacoustic source terms generated by the turbulent motion, as occurring on the RHS of the LEE (4.31) are basically constituted by the turbulent velocity fluctuations around the corresponding statistical average values (4.60). As such, these fluctuations cover the full range of turbulent scales from the largest to the smallest eddies. The contribution of the large low-frequency vortical structures, being thus included into the aeroacoustic source term, deserves special attend and is therefore further investigated in this Master's Thesis.

As shown in the derivation of the LEE, the subset of momentum equations to be solved for the mean (= Reynolds averaged) velocities $\langle v_i\rangle$, (4.30c), involves the divergence of the statistically averaged Reynolds stress tensor $\partial\left\langle v_j' v_i'\right\rangle/\partial x_j$. This term finally appears in the momentum aeroacoustic source term, where it effectively reduces the contribution of the non-averaged instantaneous counterpart $\partial v'_j v'_i / \partial x_j$. This important aspect was already addressed by Bogey [17]. In this Master's Thesis three different methods are investigated for computing this temporal average. The corresponding aeroacoustic source terms read

$$\widetilde{\Omega}'_{i,\mathrm{LES}} = \tilde{\mathcal{S}}_{i,\mathrm{LES}} - \left\langle \tilde{\mathcal{S}}_{i,\mathrm{LES}} \right\rangle , \tag{4.63a}$$

$$\widetilde{\Omega}'^{\mathrm{fa}}_{i,\mathrm{LES}} = \tilde{\mathcal{S}}_{i,\mathrm{LES}} - \left\langle \tilde{\mathcal{S}}_{i,\mathrm{LES}} \right\rangle_{\mathrm{fa}} , \tag{4.63b}$$

$$\widetilde{\Omega}'^{\mathrm{ma}}_{i,\mathrm{LES}} = \tilde{\mathcal{S}}_{i,\mathrm{LES}} - \left\langle \tilde{\mathcal{S}}_{i,\mathrm{LES}} \right\rangle_{\mathrm{ma}} , \tag{4.63c}$$

where the unsubscripted angular brackets $\langle \ \rangle$ indicate a standard statistical average, basically determined for an infinite averaging period $T_{\mathrm{TF}} \to \infty$. The two alternative methods indicated by the subscripted angular brackets $\langle \ \rangle_{\mathrm{ma}}$ and $\langle \ \rangle_{\mathrm{fa}}$ represent the moving time-frame averaging method (3.23) and the Fourier based averaging method (3.26), respectively. The moving average procedure temporally averages over an given finite time-period T_{TF} , whereas the Fourier average applies a low-pass filter, with the given cut-off frequency $\not{f}_{\mathrm{TF}} = 1/T_{\mathrm{TF}}$. The width of the moving time-frame and the temporal filter width are based on the different time-scales of the large low-frequency vortical structures, representing the turbulent time-scales presented in section 3.1.9. The present Master's Thesis compares the different averaging methods highlighting their efficiency in eliminating the influence of the large low-frequency vortical structures from the aeroacoustic source terms.

4.5.2 Influence of the SGS model

In the previous section the calculation of the aeroacoustic source terms from the resolved instantaneous flow quantities was presented. It was also mentioned that these resolved quantities only contain the turbulence scales down to the grid scale. Since the SGS only contains the small unresolved turbulence structures, thus representing high-frequency fluctuations which are supposed to act as effective sound sources, they should therefore be somehow considered in the aeroacoustic source terms. Since the SGS velocity fluctuations are not known in LES, a further SGS model (SGM) would be required for this purpose. The further discussion of such a model shall be based on incompressible flows and on the analysis of the SGS contribution to the aeroacoustic source term.

Since in incompressible flows the turbulent velocity fluctuations are divergence-free, $\partial v'_j / \partial x_j = 0$, the main aeroacoustic source term $\mathcal{S}_i$ (4.32b) can be rewritten as

$$\mathcal{S}_i = \frac{\partial v'_j v'_i}{\partial x_j}. \tag{4.64}$$

This term shall be investigated analogously to the study of Seror et al. [49, 50], who investigated the contribution of the SGS to the Lighthill stress tensor T_{ij}. Seror et al. assumed in his analysis isotropic turbulence and concluded that the SGS contribution might be negligible if the cut-off frequency of the applied LES filter is high enough. In consistence with the filtering based concept of LES, the instantaneous aeroacoustic source term can be split into

$$\mathcal{S}_i = \tilde{\mathcal{S}}_{i,\mathrm{LES}} + \tilde{\mathcal{S}}_{i,\mathrm{SGS}} \tag{4.65}$$

where, $\tilde{\mathcal{S}}_{i,\mathrm{LES}}$ is the resolved part, which can be directly computed from the resolved LES results

$$\tilde{\mathcal{S}}_{i,\mathrm{LES}} = \frac{\partial \tilde{v}'_j \tilde{v}'_i}{\partial x_j}, \tag{4.66}$$

and $\tilde{\mathcal{S}}_{i,\mathrm{SGS}}$ is the unresolved subgrid-scale contribution. The latter can be computed as the spatial derivation of the SGS tensor, as appearing in equation (3.58)

$$\tilde{\mathcal{S}}_{i,\mathrm{LES}} = \frac{\partial \tau_{ij,\mathrm{SGS}}}{\partial x_j}. \tag{4.67}$$

As such, this contribution can be obtained from the subgrid-scale model, which is actually applied for closing the filtered equations of motion.

Providing a high resolution of the computational grid will certainly help to keep the unresolved part as small as possible, increasing the computational cost though. The relative contribution of the SGM can be estimated by a comparison between the resolved and the modelled unresolved turbulence kinetic energy.

4.6 The CAA tool in FIRE™

4.6.1 Solution procedure of the acoustic field

The CAA tool in FIRE™ solves the LEE (4.34), based on a hybrid approach, using the aeroacoustic decomposition (4.33), where the aeroacoustic source terms, occurring in the vector $\vec{\mathcal{S}}$, are modeled with the UKSG from an RANS solution. The system of equations rewritten in vectorial notation reads [16, 17, 51]

$$\frac{\partial \vec{U}}{\partial t} + \frac{\partial \vec{F}_i}{\partial x_i} + \vec{H} = \vec{\mathcal{S}}, \tag{4.68}$$

where

$$\vec{U} = \left[\rho_\mathrm{a}, \langle\rho\rangle\, v_{\mathrm{a},i}, p_\mathrm{a}\right]^\mathrm{T}, \tag{4.69a}$$

$$\vec{F}_i = \begin{bmatrix} \rho_\mathrm{a}\langle v_i\rangle + \langle\rho\rangle\, v_{\mathrm{a},i} \\ \langle\rho\rangle\langle v_i\rangle\, v_{\mathrm{a},j} + p_\mathrm{a} \\ \langle v_i\rangle\, p_\mathrm{a} + \gamma\langle p\rangle\, v_{\mathrm{a},i} \end{bmatrix}, \tag{4.69b}$$

$$\vec{H} = \begin{bmatrix} 0 \\ (\langle\rho\rangle\, v_{\mathrm{a},i} + \rho_\mathrm{a}\langle v_i\rangle)\dfrac{\partial v_{0,j}}{\partial x_i} + (\bar{\rho} v_i' + \rho'\bar{v}_i)\dfrac{\partial \bar{v}_j}{\partial x_i} \\ (\gamma-1)p_\mathrm{a}\dfrac{\partial\langle v_i\rangle}{\partial x_i} - (\gamma-1)v_{\mathrm{a},i}\dfrac{\partial\langle p\rangle}{\partial x_i} \end{bmatrix}. \tag{4.69c}$$

(4.69d)

The vector $\vec{H}$ which only vanishes if the temporally averaged flow field is uniform [9, 11] is neglected. The remaining system of equations is solved by using a finite element method (FEM), applying the *Quadrature-Free Discontinuous Galerkin* [3–5] spatial discretization approach. Inside each finite element linear independent base-functions are defined, which approximate the spatial variation of the unknown dependent variables. These base-functions are often chosen as polynomials of degree $N_\mathrm{poly} = 3$ in case of FIRE™. Between the interfaces of the finite elements, the solution is discontinuous, therefore an additional *Riemann flux* has to be included.

4.6.2 Boundary conditions

Three different kinds of boundary conditions for the acoustic variables are available in the CAA module of FIRE™:

Reflecting boundaries for solid walls. These boundary conditions are easy to implement (similar as in CFD) and numerically not problematic.

Non reflecting boundaries for artificial far field boundaries. These are boundaries, where the acoustic energy exits completely the domain. Consistently, the applied numerical scheme should not introduce any kind of reflection.

Porous boundaries are basically internal boundaries which serve as a transitional surface between computational and analytic transport processes. Starting from these internal boundaries the acoustic field is propagated analytically based on the, e.g., Ffowcs Williams-Hawkings equations.

4.6.3 Spatial and temporal discretization

For the spatial discretization an unstructured grid based on tetrahedrons (see section 3.3) is used. It was already mentioned that CAA is very sensitive to numerical errors, thus the grid has to be of high quality. The CAA module within FIRE™ therefore suggests a stringent minimum volume-based aspect ratio (3.67) $\mathit{AR}_{\mathrm{V}} = 3.3$. The required CAA grid size Δx_{CAA} is estimated, based on the CFD grid size Δx_{CFD} and the Mach number $\mathcal{M}a$ as

$$\Delta x_{\mathrm{CAA}} \approx \frac{\Delta x_{\mathrm{CFD}}}{\mathcal{M}a}, \tag{4.70}$$

where both grid sizes can be estimated by $V_{\mathrm{C}}^{1/3}$, with V_{C} beeing the volume of the corresponding cell within the computational grid.

The CAA module of FIRE™ uses a *Runge-Kutta* time scheme of fourth or first order for the temporal integration. Due to the small CAA time-step the first order *Runge-Kutta* scheme might be often sufficiently accurate with the advantage of higher computational speed. The time-step for the CAA Δt_{CAA} is estimated by the CFL condition depending on the speed of sound and the mean velocity as

$$\mathit{CFL}_{\mathrm{CAA}} = \frac{(c + |v|)\Delta t_{\mathrm{CAA}}}{\Delta x_{\mathrm{CAA}}} \quad \Rightarrow \quad \Delta t_{\mathrm{CAA}} = \frac{\mathit{CFL}_{\mathrm{CAA}} \Delta x_{\mathrm{CAA}}}{(c + |v|)}. \tag{4.71}$$

Additionally, the target maximum resolved frequencies f_{high}, which should be resolved, might further decrease the permitted minimum time-step if $2\Delta t_{\mathrm{CAA}} > 1/f_{\mathrm{high}}$.

The time-step of the UKSG Δt_{UKSG} is estimated depending on the time-step of the CAA solver and the Mach number $\mathcal{M}a$ of the flow configuration:

$$\Delta t_{\text{UKSG}} \approx \left(1 + \frac{1}{\mathcal{M}a}\right) \Delta t_{\text{CAA}}. \tag{4.72}$$

The different time-steps and their approximated relation is presented in figure 4.1.

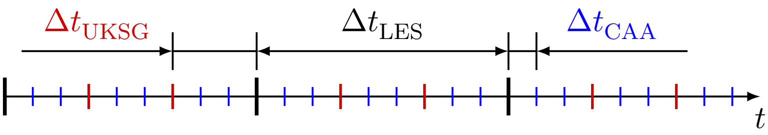

FIGURE 4.1: Different time-steps in hybrid CAA methods.

4.6.4 Generation of aeroacoustic sources

In this section the computational algorithm for calculating the aeroacoustic sources by the CAA tool of FIRE™ is presented. In general, these aeroacoustic sources generation methods are often referred to as “stochastic noise generation and radiation (SNGR)” methods, because they are generally based on a stochastic approach to mimic turbulence. Bailly & Juve [10], Bechara et al. [13] and Billson et al. [14] used a similar approach to generate aeroacoustic sources. In FIRE™ the module for calculating the aeroacoustic source terms is called a “unstructured kinematic source generator (UKSG)”.

The UKSG calculates the following aeroacoustic source terms as given by equations (4.35) and (4.36), being here rewritten as

$$\begin{aligned}\Lambda_i + \mathcal{S}_i &= v'_j \frac{\partial \langle v_i \rangle}{\partial x_j} + \langle v_j \rangle \frac{\partial v'_i}{\partial x_j} + v'_j \frac{\partial v'_i}{\partial x_j} \\ \Pi &= v'_j \frac{\partial \langle p \rangle}{\partial x_j}\end{aligned}$$

where the turbulent velocity fluctuations $v'_i = v'_{i,\text{UKSG}}$ are generated as pseudo stochastic turbulent fluctuations around the statistically averaged flow field obtained from a RANS simulation. As such, the UKSG uses the averaged quantities $\langle \rho \rangle$, $\langle v_i \rangle$, $\langle p \rangle$, $\langle \mathscr{k} \rangle$ and $\langle \varepsilon \rangle$, obtained from the preceding incompressible RANS simulation, as input for computing the three turbulent velocity fluctuations v'_i, occurring in the aeroacoustic source terms. The foundation of most source generation models, alike the UKSG in FIRE™, is the prescription of a certain turbulence kinetic energy spectrum, assuming isotropic turbulence. This implies that kinetic energy contained in the turbulence spectrum is statistically equally distributed among the three spatial components of the turbulent velocity fluctuations at all relevant scales of turbulence. Isotropic turbulence also implies divergence-free Reynolds stresses, so that the temporal average of the main aeroacoustic source term in the momentum equation $\langle \mathcal{S}_i \rangle = 0$.

In some cases the assumption of isotropic turbulence does not hold (e.g. in highly sheared flows), which basically requires anisotropic turbulence and SNGR models [15] and comes with higher computational costs.

Stochastic turbulent velocity model

The turbulent velocity fluctuations $v'_{i,\mathrm{UKSG}}$ are determined from an inverse Fourier transformation written as

$$v'_{i,\mathrm{UKSG}} = \int_{\kappa} \left[\hat{v}(\vec{\kappa}) e^{i \Xi_i(\vec{\kappa})} \vec{\sigma}_{\kappa} \right] e^{i \vec{\kappa} x_i} d\vec{\kappa}, \tag{4.74}$$

where $\vec{\kappa}$ is the wave vector, $\vec{\sigma}(\vec{\kappa})$ is the direction of the turbulent velocity vector and Ξ_i is a random phase for each reconstructed component, which is required to resemble the stochastic nature of turbulence. From the inverse Fourier transform only the real part is used, so that

$$v'_{i,\mathrm{UKSG}} = \int_{\kappa} \left[\hat{v}(\vec{\kappa}) \vec{\sigma}_{\kappa} \right] cos(\vec{\kappa} \cdot \vec{x} + \Xi_i(\vec{\kappa})) d\vec{\kappa}. \tag{4.75}$$

After discretization of the wave domain into N_κ modes, the following expression for the modeled turbulence velocity $v_{\mathrm{t},i,\mathrm{UKSG}}$ can be obtained

$$v'_{i,\mathrm{UKSG}} = 2 \sum_{\kappa=1}^{N_\kappa} \hat{v}_\kappa cos(\vec{\kappa} \cdot \vec{x} + \Xi_i) \vec{\sigma}_\kappa. \tag{4.76}$$

The parameter Ξ_i is a random phase in the range of $0 \leq \Xi_i \leq 2\pi$, and is independent of the position within the domain. As a result for each realization, the three components $v'_{i,\mathrm{UKSG}}$ are temporally different, but statistically isotropic, such that

$$\left\langle (v'_{x,\mathrm{UKSG}})^2 \right\rangle = \left\langle (v'_{y,\mathrm{UKSG}})^2 \right\rangle = \left\langle (v'_{z,\mathrm{UKSG}})^2 \right\rangle \tag{4.77}$$

The wave vector $\vec{\kappa}$ covers the appropriate wave number domain. The direction of the turbulent velocity $\vec{\sigma}_\kappa$ is chosen perpendicular to the wave vector $\vec{\kappa}$. The spectral turbulent velocity amplitude $\hat{v}_\kappa$ is dependent on the wave numbers κ, and is obtained from a presumed turbulence kinetic energy spectrum $\mathcal{E}(\kappa)$ as

$$\hat{v}_\kappa = \sqrt{\mathcal{E}(\kappa) d\kappa}. \tag{4.78}$$

Von Kármán spectrum

In case of FIRE™ a *Von Kármán spectrum* $\mathcal{E}_{\mathrm{VKS}}(\kappa)$ [13] is chosen as the presumed turbulence kinetic energy spectrum which reads

$$\mathcal{E}_{\mathrm{VKS}}(\kappa) = 1.453 \frac{\frac{2}{3}\mathscr{k}}{\kappa_e} \frac{\left(\frac{\kappa}{\kappa_e}\right)^4}{\left(1+\left(\frac{\kappa}{\kappa_e}\right)^2\right)^{17/6}} e^{-2\kappa^2/\kappa_\nu^2}. \tag{4.79}$$

The constants κ_e and κ_ν are given as

$$\kappa_e = \frac{0.747}{\lambda} \quad \text{and} \tag{4.80}$$

$$\kappa_\nu = \sqrt[4]{\frac{\varepsilon}{\nu^3}}, \tag{4.81}$$

and the parameter λ is calculated from

$$\lambda = \lambda_{\mathrm{UKSG}} \frac{\left(\frac{2}{3}\mathscr{k}\right)^{3/2}}{\varepsilon}, \tag{4.82}$$

where λ_{UKSG} is a model parameter to be specified in the UKSG. Note that the local turbulence kinetic energy $\mathscr{k}$ and turbulence dissipation rate ε effectively determine the strength of the turbulent velocity fluctuations, and hence, the strength of the aeroacoustic source term as well as the main turbulent time-scale $\mathscr{t}_{\mathscr{k}\varepsilon} = \mathscr{k}/\varepsilon$ of the spectrum.

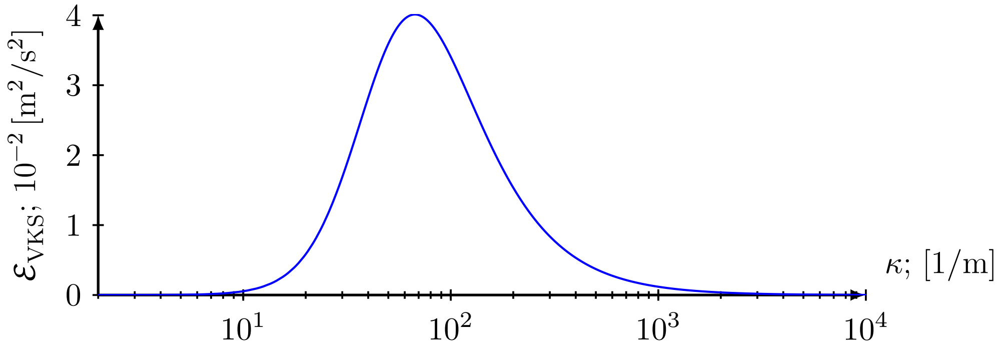

FIGURE 4.2: Von Kármán spectrum $\mathcal{E}_{\mathrm{VKS}}(\kappa)$ with $\mathscr{k} = 10\,\mathrm{m^2/s^2}$, $\varepsilon = 1000\,\mathrm{m^2/s^2}$ and $\nu_{\mathrm{ref}} = 1.5266\times10^{-5}\,\mathrm{m^2/s}$.

In figure 4.2 a Von Kármán spectrum is shown for arbitrarily selected values of $\mathscr{k} = 10\,\mathrm{m^2/s^2}$ and $\varepsilon = 1000\,\mathrm{m^2/s^3}$ as well as for the reference kinematic viscosity $\nu_{\mathrm{ref}} = 1.5266\times10^{-5}\,\mathrm{m^2/s}$. Using these values the eddy turnover time (3.15) $\mathscr{t}_{\mathscr{k}\varepsilon} = \mathscr{k}/\varepsilon = 0.01\,\mathrm{s}$ and the Kolmogorov time-scale (3.18a) $\mathscr{t}_{\mathcal{K}} = (\nu/\varepsilon)^{1/2} = 0.000\,12\,\mathrm{s}$

can be computed. From these time-scales their corresponding frequencies are $\mathscr{f}_{\mathscr{k}\varepsilon} = 100\,\mathrm{Hz}$, which corresponds to the high amplitude region, and $\mathscr{f}_{\mathcal{K}} = (\nu/\varepsilon)^{1/2} = 8333.33\,\mathrm{Hz}$, which corresponds to the smallest turbulent scales in the Von Kármán spectrum , respectively.

Convection of the turbulent velocity

The convection of the noise generating eddies with the mean flow needs to be consistently reflected by the aeroacoustic source terms. To this end the modeled turbulence velocity is convected using a simple convection scheme, which reads

$$\frac{\partial v'_{i,\mathrm{UKSG}}}{\partial t} + \langle v_j \rangle \frac{\partial v'_{i,\mathrm{UKSG}}}{\partial x_j} = 0. \tag{4.83}$$

To obtain the turbulent velocity at the current time-step $v'^{n}_{i,\mathrm{UKSG}}$ a Marcov chain is applied, which temporally correlates the convected turbulent velocity field $v'^{n-1}_{i,\mathrm{UKSG,conv}}$ from the preceding time-step with the new realisation of the turbulent velocity $v'^{n}_{i,\mathrm{UKSG,new}}$ at the current time-step as follows

$$v'^{n}_{i,\mathrm{UKSG}} = \alpha_{\mathrm{UKSG}} v'^{n-1}_{i,\mathrm{UKSG,conv}} + \sqrt{1-\alpha^2_{\mathrm{UKSG}}}\, v'^{n}_{i,\mathrm{UKSG,new}}, \quad \text{where} \tag{4.84a}$$

$$\alpha_{\mathrm{UKSG}} = e^{(-\Delta t_{\mathrm{CAA}}/\mathscr{t}_{\mathrm{UKSG}})}, \tag{4.84b}$$

and $\mathscr{t}_{\mathrm{UKSG}}$ is the time-scale $\mathscr{t}_{\mathscr{k}\varepsilon}$ corrected by the parameter λ_{UKSG}, such that

$$\mathscr{t}_{\mathrm{UKSG}} = \lambda_{\mathrm{UKSG}} \mathscr{t}_{\mathscr{k}\varepsilon} = \lambda_{\mathrm{UKSG}} \frac{\mathscr{k}}{\varepsilon}. \tag{4.85}$$

5 Task definition and applied methods

In the previous chapters the theoretical background of this Master's Thesis was discussed. In this chapter the particular tasks of this Master's Thesis and the method for reaching the goals of this Master's Thesis are presented. In section 5.1 the investigated geometry and the expected flow configuration is discussed. This is followed by the description of the computational domain and the grid generation process in section 5.2. After that, the applied simulations and involved tasks are presented in section 5.3. At the end of the chapter the setup of the performed simulations is presented.

5.1 Geometry and expected flow configuration

5.1.1 Geometry

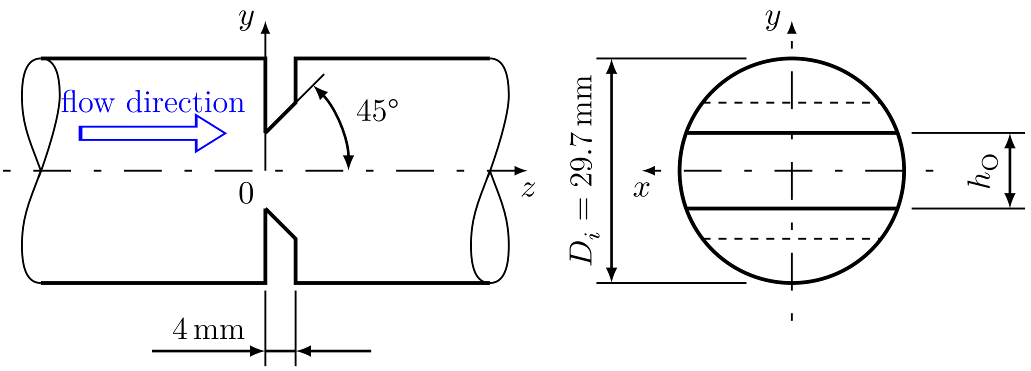

FIGURE 5.1: Key region of the considered flow geometry: a slot orifice inside a straight cylindrical pipe.

As already mentioned, the investigated flow configuration consists of a *straight cylindrical pipe* with a inner diameter of $D_\mathrm{I} = 29.7\,\mathrm{mm}$, which is abruptly constricted by a slot *orifice* with a *gap height* h_O at its entrance (see figure 5.1). The total axial length of the orifice is 4 mm. The upper and lower walls are inclined by an angle 45°, so that sharp backward facing corners appear at the entrance of the gap.

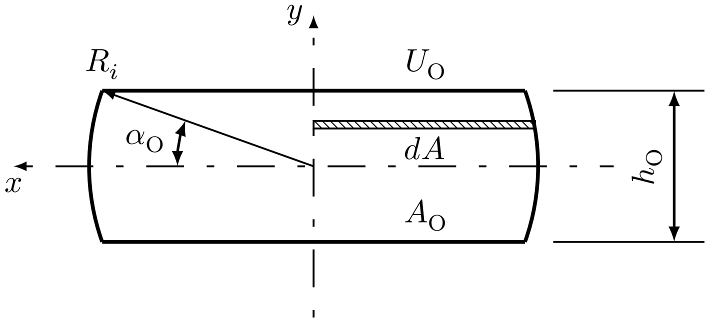

FIGURE 5.2: Geometrical relations of the entrance of the orifice.

The cross-sectional area of the entrance of the orifice A_O and its circumference U_O (see figure 5.2) can be calculated from the gap height h_O as

$$A_\mathrm{O} = 4\int_0^{h/2} \underbrace{\sqrt{R_\mathrm{I}^2 - y^2}dy}_{dA} = 4\left[\frac{R_\mathrm{I}^2}{2}\alpha_\mathrm{O}(h_\mathrm{O}) + \frac{h_\mathrm{O}}{4}\sqrt{R_\mathrm{I}^2 - \left(\frac{h_\mathrm{O}}{2}\right)^2}\right], \tag{5.1a}$$

$$U_\mathrm{O} = 4\sqrt{R_\mathrm{I}^2 - \left(\frac{h_\mathrm{O}}{2}\right)^2} + 4R_\mathrm{I}\alpha_\mathrm{O}(h_\mathrm{O}), \tag{5.1b}$$

where $R_\mathrm{I} = D_\mathrm{I}/2 = 14.85\,\mathrm{mm}$ is the inner radius of the pipe and $\alpha_\mathrm{O} = \arcsin(h_\mathrm{O}/2R_\mathrm{I})$. Using (5.1a) and (5.1b) the hydraulic diameter d_O of the entrance cross-section of the orifice opening is calculated from

$$d_\mathrm{O} = \frac{4A_\mathrm{O}}{U_\mathrm{O}},$$

according to the general definition of the hydraulic diameter (3.2).

In this Master's Thesis two entrance gap heights with $h_\mathrm{O} = h_5 = 5\,\mathrm{mm}$, and $h_\mathrm{O} = h_{10} = 10\,\mathrm{mm}$ are examined. The relevant geometrical parameters for the two different orifice configurations are listed in table 5.1.

TABLE 5.1: Geometrical parameters of the orifice and the pipe.

	symbol	value	[unit]
pipe:	D_I	29.700	[mm]
	R_I	14.850	
entrance gap of the orifice:	h_5	5	[mm]
	h_{10}	10	
cross-sectional area:	A_{D_I}	692.792	[mm^2]
	A_{h_5}	291.289	
	$A_{h_{10}}$	147.796	
constriction:	A_{D_I}/A_{h_5}	2.378	[–]
	$A_{D_\mathrm{I}}/A_{h_{10}}$	4.688	
circumference:	U_{D_I}	93.305	[mm]
	U_{h_5}	76.330	
	$U_{h_{10}}$	68.600	
hydraulic diameter:	$d_{D_\mathrm{I}} = D_i$	29.700	[mm]
	d_{h_5}	15.265	
	$d_{h_{10}}$	8.618	

5.1.2 Fluid properties

Air is chosen as the operating fluid, which is modeled as an ideal gas (2.27) at athomspheric conditions $\theta_\mathrm{ref} = 293.15\,\mathrm{K}$ and $p_\mathrm{ref} = 1\,\mathrm{bar}$. The reference density $\rho_\mathrm{ref} = 1.189\,\mathrm{kg/m^3}$ was determined by the thermal equation of state for an ideal gas (2.23) using the specific gas constant for air $\mathcal{R}_\mathrm{air} = 287\,\mathrm{J/(kg\,K)}$. The reference dynamic viscosity $\mu_\mathrm{ref} = 18.148\times10^{-6}\,\mathrm{Pa\,s}$ was determined by Sutherland's law (3.68) and the reference kinematic viscosity is calculated from $\nu_\mathrm{ref} =$

$\mu_\mathrm{ref}/\rho_\mathrm{ref} = 15.226\times10^{-6}\,\mathrm{Pa\,s}$. The given fluid properties are summarized in table 5.2.

Table 5.2: The chosen reference fluid properties of air at reference temperature $\theta_{ref} = 293.15\,\mathrm{K}$ and reference pressure $p_\mathrm{ref} = 1\,\mathrm{bar}$.

property	value	[unit]
θ_ref	293.15	[K]
p_ref	1	[bar]
$\mathcal{R}_\mathrm{air}$	287	[J/(kg K)]
ρ_ref	1.188 58	[kg/m^3]
μ_ref	18.145×10^{-6}	[Pa s]
ν_ref	15.266×10^{-6}	[m^2/s]

5.1.3 Operating conditions

Two cases with *bulk Reynolds numbers* $\mathcal{R}e_{D_\mathrm{I}} = 5300$ and 7400, based on the cylindrical pipe inflow conditions, were considered. From the definition of the Reynolds number (3.4) the corresponding *mean bulk velocity* $\bar{\boldsymbol{v}}_{\dot{V},D_\mathrm{I}}$ in the cylindrical pipes are calculated from

$$\bar{\boldsymbol{v}}_{\dot{V},D_\mathrm{I}} = \frac{\mathcal{R}e_{D_\mathrm{I}}\nu_\mathrm{ref}}{\boldsymbol{d}_{D_\mathrm{I}}}. \tag{5.2}$$

From the relation

$$\dot{m} = \rho_\mathrm{ref}\boldsymbol{v}_{\dot{V},D_\mathrm{I}}A_{D_\mathrm{I}} \tag{5.3}$$

the corresponding mass flow rates $\dot{m}$ are calculated. The mean volumetric velocity at the orifice entrance $\bar{\boldsymbol{v}}_{\dot{V},\mathrm{O}}$ is calculated from

$$\begin{aligned} \dot{V} = \bar{\boldsymbol{v}}A = \bar{\boldsymbol{v}}_{\dot{V},D_\mathrm{I}}A_{D_\mathrm{I}} &= \bar{\boldsymbol{v}}_{\dot{V},\mathrm{O}}A_\mathrm{O} \quad \Rightarrow \\ \bar{\boldsymbol{v}}_{\dot{V},\mathrm{O}} &= \bar{\boldsymbol{v}}_{\dot{V},D_\mathrm{I}}\frac{A_{D_\mathrm{I}}}{A_\mathrm{O}}. \end{aligned} \tag{5.4}$$

The resulting mean volumetric velocities and the mass flow corresponding to the two chosen Reynolds numbers $\mathcal{R}e_{D_\mathrm{I}} = 5300$ and 7400 are listed in table 5.3.

TABLE 5.3: The appearing mean volumetric velocities in the pipe and the orifice.

$\mathcal{Re}_{D_\mathrm{I}}$ [–]	$\bar{v}_{\dot{V},D_\mathrm{I}}$ [m/s]	$\bar{v}_{\dot{V},h_{10}}$ [m/s]	$\bar{v}_{\dot{V},h_5}$ [m/s]	$\dot{m}$ [kg/s]
5300	2.724	6.479	12.770	2.243×10^{-3}
7400	3.804	9.047		3.132×10^{-3}

The considered Reynolds numbers were actually chosen so that the simulations carried out for generating appropriate turbulent inflow conditions could be verified against data from existing DNS simulations provided by the ISW [32]. The DNS data used for validation were simulated assuming wall shear stress based Reynolds numbers (3.48) $\mathcal{Re}_{\tau_\mathrm{W}} = 360$ and 500, which is equivalent to bulk flow Reynolds numbers close to $\mathcal{Re}_{D_\mathrm{I}} = 5300$ and 7400, respectively.

5.1.4 Expected flow field

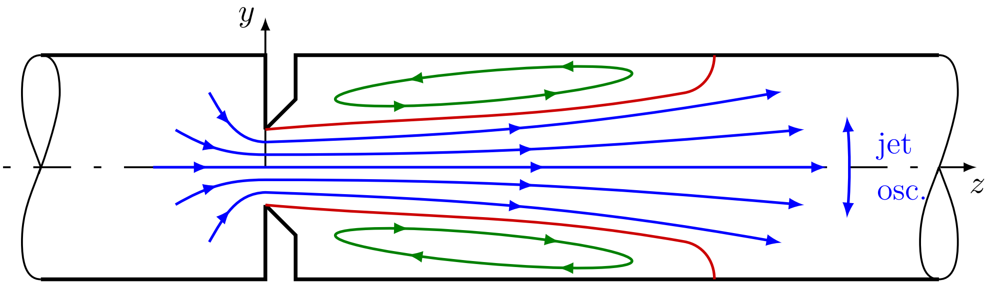

FIGURE 5.3: The expected flow field.

The basic structure of the expected flow field is shown in figure 5.3. Starting from hydraulically fully developed turbulent pipe flow as upstream condition, the fluid (air) approaches the orifice at moderate Reynolds numbers $\mathcal{Re}_{D_\mathrm{I}}$. Due to the constriction of the orifice, the fluid accelerates. The flow detaches at the sharp corners of the orifice entrance, so that a jet-like core flow emerges downstream of the orifice. Inside the outer region down to the reattachment of the flow, two recirculation zones appear. Between the recirculation zones and the jet two shear layers arise, which will enhance the production of turbulence due to the large velocity gradients. It is therefore also expected that the strongest aeroacoustic source terms are generated inside these shear layers. Additionally, large coherent vortical structures (eddies) might emerge from these shear layers, which are convected downstream until they decay.

It will be shown that, at the chosen Reynolds numbers, the jet-like core flow does not oscillate around the center line as indicated in figure 5.3, but rather attaches at one side of the wall so that the flow pattern becomes asymmetric. This phenomenon is called the *Coanda* effect. The Coanda effect associated with a so called *bifurcation*, where two possible flow configurations (attachment at the top or bottom of the pipe) statistically occur with the same probability for a certain range of flow conditions. Outside this range the flow pattern is unique again.

It is clear that the region downstream of the orifice represents the main region of interest for the generation of the aeroacoustic sources.

5.2 Computational domain and grid generation

5.2.1 Computational domain for LES

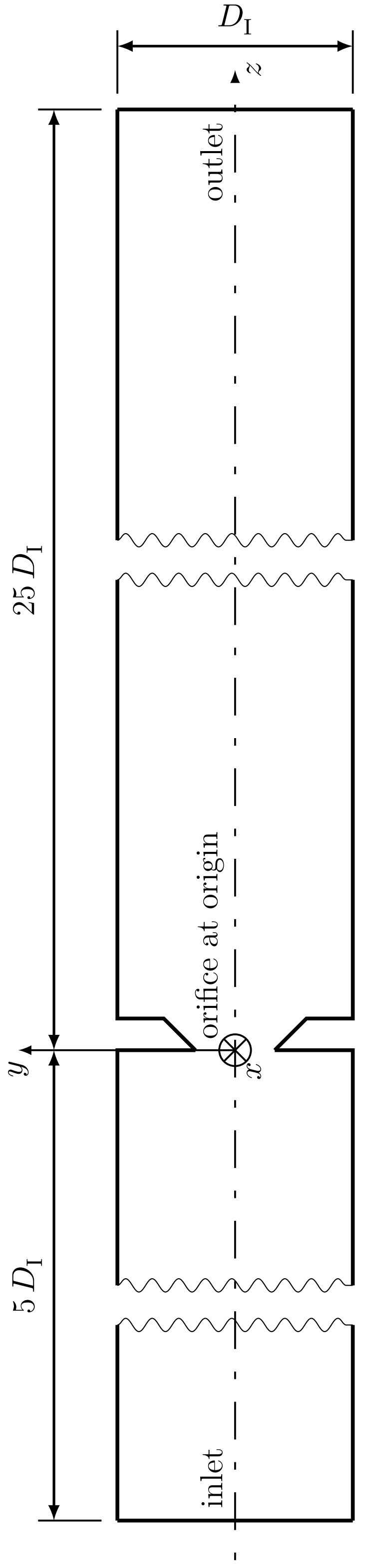

Figure 5.4: The computational domain.

The chosen computational domain, with the orifice positioned at the origin of the Cartesian coordinate system is shown in figure 5.4. The domain axially extends twenty-fife diameters downstream of the orifice, and fife diameters upstream. The actually assumed length of the domain downstream of the orifice ($25\,D_\mathrm{I}$) was supposed to be sufficient to cover the full region of relevant turbulent sound generation. The chosen length should further ensure, that the solution is not contaminated by any spurious perturbations triggered by the outlet boundary condition.

5.2.2 Grid generation for LES

The generation of the hex-based structured computational grids for the LES was divided into four main steps:

Subdomain: The grid generation process exploited the symmetries of the computational domain and the uniformity of the straight pipe generally, given at the inflow and ouflow sections. Therefore, some steps were only performed on a subdomain which covers only a quarter of the full cross-section. The so reduced subdomain is shown in figure 5.5. The required subdomain surface was generated with CATIA™[1]

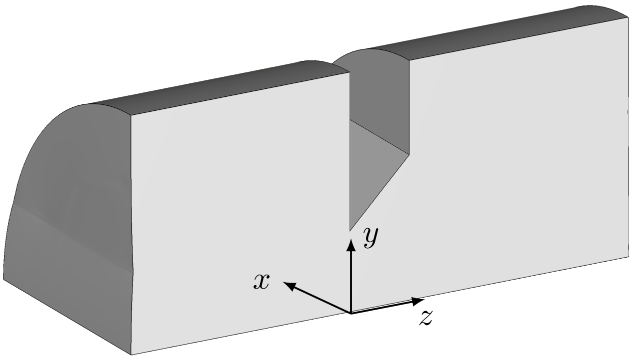

Figure 5.5: The subdomain for the grid generation process, with orifice $h_{10} = 10\,\mathrm{mm}$ as an example.

Features: The implementation of the main grid features using HyperMesh™[2], including e.g. a circumferential boundary layers around the cylindrical pipe.

Refinement: As the LES was supposed to resolve the turbulent BL, a refinement of the layers near to the walls of the pipe and the orifice down to $y^+ \approx 1$ was necessary. The radial grid size was clustered towards the wall to provide computationally feasible grid sizes. A section of the resulting computational subgrids near the orifice is exemplarily shown in figure 5.6 for different LES cases.

---

[1] Dessault Systems Catia

[2] Altair®HyperWorks®HyperMesh®

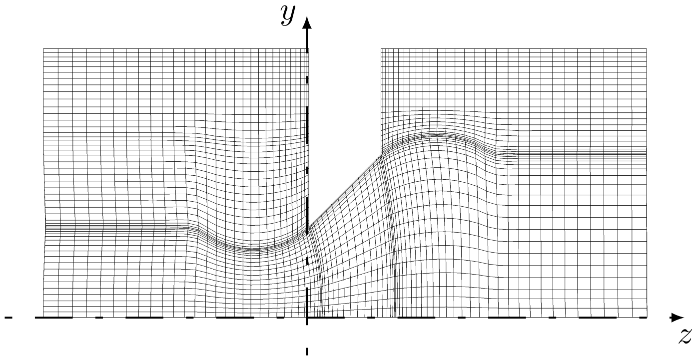

(a) Subgrid $h_{10} = 10\,\mathrm{mm}$ with refinement for $\mathit{Re}_{D_\mathrm{I}} = 5300$.

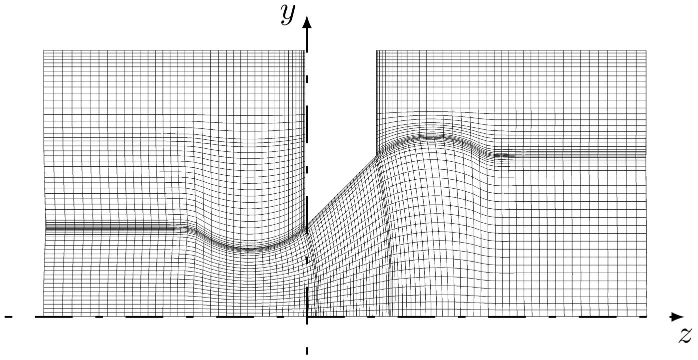

(b) Subgrid $h_{10} = 10\,\mathrm{mm}$ with refinement for $\mathit{Re}_{D_\mathrm{I}} = 7400$.

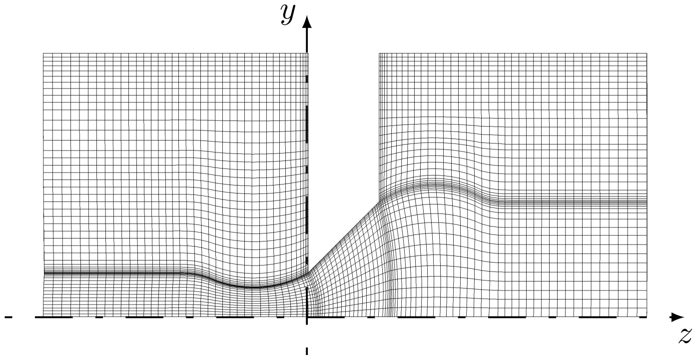

(c) Subgrid $h_5 = 5\,\mathrm{mm}$ with refinement for $\mathit{Re}_{D_\mathrm{I}} = 5300$.

FIGURE 5.6: The resulting subgrids for different orifice openings h_O and different flow configuration $\mathit{Re}_{D_\mathrm{I}}$.

Finalization: The full computational domain were finally meshed by mirroring the subdomain grids with respect to the x- and y- axis and by extending the surface meshes at the inlet and exit surface of the subdomain shown in figure 5.5 to the inflow and the outflow boundaries, respectively. The axial resolution was thereby coarsened keeping a maximum Aspect ratio $\mathit{AR} = 10$ as upper limit.

Auxiliary simulation grid

As already noted, the present LES prescribes the turbulent inflow boundary conditions, using the instantaneous flow field obtained from a separate auxiliary LES of fully developed turbulent pipe flows (periodic pipe flows). The computational grid applied in this precursor LES, serving here as inflow generator, has exactly the same spatial discretization into the cross-stream directions as the surface mesh at the inflow boundary. As a result, no spatial interpolation is required when mapping an instantaneous cross-sectional solution of the fully developed auxiliary (*periodic pipe*) LES onto the inlet BC for the main (*acoustic pipe*) LES. The total axial extension of the domain used for the fully developed periodic pipe flow LES is $10\,D_\mathrm{I}$, with a constant axial resolution $\Delta z_{\mathrm{PP,ref}} = \mathrm{const.}$

5.2.3 RANS and CAA grids

RANS typically require coarser grids than LES do. The RANS, which was presently carried out for comparison still used the same grid as the corresponding LES for simplicity.

For the CAA simulations a slightly shorter straight pipe outflow section was used. As already mentioned the CAA grid was generated by the VIRTUAL VEHICLE Research Center. The unstructured CAA grid was generated using FAME™ from AVL. In a second step the grid was improved using a so called *volume optimizer* so that an important restriction on the grid imposed by the CAA solver (volume based aspect ratio $\mathit{AR}_\mathrm{V} < 3.3$) is fulfilled. The section around the orifice of the CAA grid is presented in figure 5.7.

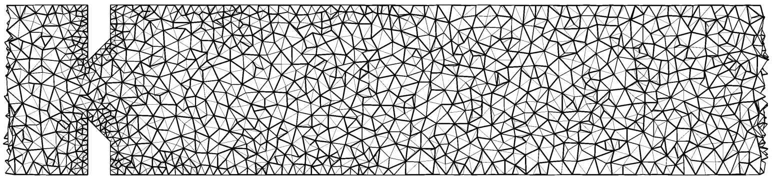

Figure 5.7: Meridional cut (x-cut) through the CAA grid near the orifice.

The total number of all computational grids used for LES, RANS and CAA, whith the resulting number of computational cells N_C, are listed in table 5.4. The abbreviations (Gpp_... and Gap_...), which are further used for reference are listed as well.

TABLE 5.4: The computational grids.

	h_O	$\mathcal{R}e_{D_i}$	N_C	Grid:
auxiliary grids: *periodic pipe*	h_{10}	5300	1 467 600	Gpp_h10
	h_{10}	7400	2 632 500	Gpp_h10F
	h_5	5300	1 736 400	Gpp_h5
main grids: *acoustic pipe*	h_{10}	5300	3 788 944	Gap_h10
	h_{10}	7400	7 050 132	Gap_h10F
	h_5	5300	4 559 480	Gap_h5
CAA	h_{10}	5300	339 368	Gap_h10T

Further details, concerning the computational grids, like selected local values of V_C and $\Delta \boldsymbol{x}_\mathrm{C}$ are listed in table A.1.

5.3 Applied simulations and tasks

As already stated in section 5.1, two different gap heights of the orifice $h_5 = 5\,\mathrm{mm}$ and $h_{10} = 10\,\mathrm{mm}$ are examined, assuming two different flow conditions $\mathcal{R}e_{D_i} = 5300$ and 7400. The higher Reynolds number $\mathcal{R}e_{D_i} = 7400$ is applied only to the orifice with the larger gap hight h_{10}. Additionally, the influence of the grid is examined, which adds another LES case considering the orifice with $h_{10} = 10\,\mathrm{mm}$ and $\mathcal{R}e_{D_i} = 5300$, but on a finer grid. The finer computational grid used for this simulation is simply taken from the LES carried out for the same orifice h_{10} prepared for the higher Reynolds number $\mathcal{R}e_{D_i} = 7400$.

For each main simulation (*acoustic pipe* LES) a separate auxiliary simulation (*periodic pipe* LEE) was performed to obtain the required transient instantaneous inflow boundary condition.

For a comparison of the aeroacoustic source terms from LES against the prediction of the UKSG, an additional RANS simulation and an additional CAA simulation was carried out for gap hight h_{10} at $\mathcal{R}e_{D_i} = 5300$. These simulations are also included into the summary of all performed simulations listed in table 5.5. The abbreviations (e.g. PP_... and AP_...) given in the last column will be used in all the further discussions, when referring to the individual simulation cases.

Table 5.5: All performed Simulations.

	h_O	$\mathcal{R}e_{D_i}$	Grid:	Case:
auxiliary simulations: *periodic pipe*	h_{10}	5300	GPP_h10	PP_h10Re5300
	h_{10}	5300	GPP_h10F	PP_h10Re5300F
	h_{10}	7400	GPP_h10F	PP_h10Re7400
	h_5	5300	GPP_h5	PP_h5Re5300
main simulations: *acoustic pipe*	h_{10}	5300	GAP_h10	AP_h10Re5300
	h_{10}	5300	GAP_h10F	AP_h10Re5300F
	h_{10}	7400	GAP_h10F	AP_h10Re7400
	h_5	5300	GAP_h5	AP_h5Re5300
hybrid CAA	h_{10}	5300	GAP_h10F	RANS_h10Re5300
	h_{10}	5300	GAP_h10T	CAA_h10Re5300

The LES were performed with the Coherent Structure Model (CSM) as the SGS model and the RANS simulation was performed with the k-ζ-f model as the used turbulence model, which were both introduced in section 3.2.

5.4 Boundary and initial conditions, temporal integration

5.4.1 Boundary conditions

Inflow boundary

In contrast to RANS simulations, which require BCs for the temporally averaged quantities $\langle\phi\rangle$, LES simulations require BCs for the instantaneous quantities v_i. For generating such instantaneous BCs some kind of statistical model might be used to artificially generate the turbulent velocity fluctuations. The present LES applies an alternative approach imposing the turbulent fluctuating velocities obtained from an instantaneous solution of an LES of a fully developed pipe flow. The instantaneous pipe flow solution is taken from a separate precursor *periodic pipe* LES (PP_...), which is simulated for the same Reynolds number using periodic boundary conditions in the axial direction. The cross-section, where the instantaneous velocities are taken from, is temporally advanced downstream, assuming the spatially axial fluctuations as equivalent to the temporal fluctuations. This concept requires only one instantaneous solution of the periodic pipe LES, and inherently relies on the statistical homogeneity of this flow in the axial direction z. The fluctuations in time and z-direction are assumed to be related through a mean convecting velocity, which is chosen as equal to the volume flow equivalent velocity $\bar{\boldsymbol{v}}_{\dot{V},D_\mathrm{I}}$. Accordingly, the cross-section providing the actual inflow data is successively advanced through the instantaneous pipe flow solution by an increment $\Delta z = \bar{\boldsymbol{v}}_{\dot{V},D_\mathrm{I}}\Delta t$, where Δt is the time-step used in the corresponding *acoustic pipe* LES (AP_...). Since the actual z-position of the advancing cross-section does not automatically coincide with the z-positions of the discretized periodic pipe flow solution, a linear interpolation between the nearest neighboring z-positions is used. The whole concept used for generating the inflow BC is schematically shown in figure 5.8

The prescription of axially periodic BC condition in the auxiliary LES implies, that the velocity field from the outlet boundary face is mapped onto the inlet boundary face. The periodic pipe LES therefore requires the prescription of the flow rate through the pipe or, equivalently, the prescription of a pressure difference between the inlet and the outlet. Since the mass flow through the pipe is known from the given volume flow equivalent velocity (5.3), depending on the Reynolds number (5.2), the first option was chosen. The prescribed mass flow rate is approached in an iterative procedure using an under-relaxation factor, which was chosen as $\alpha_{\dot{m}} = 0.4$.

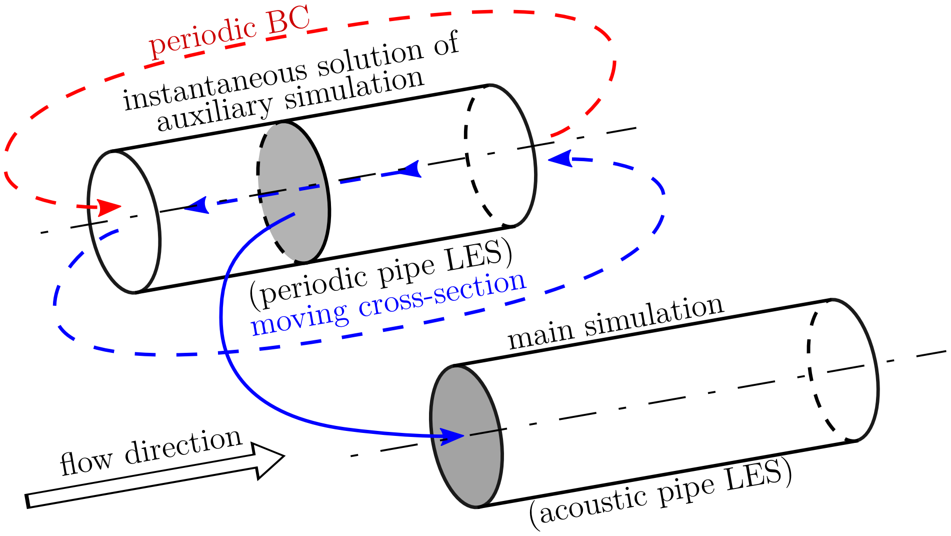

Figure 5.8: Concept for generating the transient instantaneous inlet boundary conditions.

Outflow boundary

As discussed in section 5.2 one factor, which decided the chosen length of the pipe downstream the orifice, was that no spurious perturbation introduced by the outflow BC contaminates the main source region. Simply setting a fixed constant pressure $p = p_{\mathrm{BC,outlet}} = p_{\mathrm{ref}} = \mathrm{const.}$ at the outlet boundary might lead to spurious perturbations. These would also nonphysically perturb the turbulent velocity field upstream. Therefore, the so called *averaged pressure* BC was applied at the outflow boundary, which reads

$$\bar{p}_{\mathrm{BC,outlet}} = \frac{1}{A_{\mathrm{BC,outlet}}} \int_{A_{\mathrm{BC,outlet}}} p dA = \mathrm{const.}, \tag{5.5}$$

where the pressure, averaged over the outflow face, is set constant $\bar{p}_{\mathrm{BC,outlet}} = p_{\mathrm{ref}} = \mathrm{const.}$, effectively allowing the pressure fluctuations in the turbulent flow to exit the domain.

Solid wall boundary

For all CFD simulations, the periodic pipe LES and the acoustic pipe LES, the *no-slip* condition $v_{i,\mathrm{W}} = 0$ was applied at solid walls.

5.4.2 Flow initialization

The solution for the auxiliary LES of the periodic pipe flow was initialized imposing an axial velocity v_z, which varies radially according to a *1/7-power law* written as

$$v_{z,\mathrm{PL}}(r) = v_{\mathrm{PL,max}} \left(1 - \frac{r}{R_i}\right)^{1/7} . \tag{5.6}$$

Additionally, a local disturbance was prescribed at two neighboring z-positions in the middle of the pipe, which should trigger the transition to a turbulent flow regime. The perturbation, which is added to the 1/7-power law

$$v_z(r) = v_{z,\mathrm{PL}}(r) + v_{z,\mathrm{pert}}, \tag{5.7}$$

was definded as:

$$v_{z,\mathrm{pert}} = v_{\mathrm{PL,max}} \underbrace{\lambda_{\mathrm{pert}}}_{=10} \left[\cos\left(\frac{4\pi x}{R_i}\right) \cos\left(\frac{4\pi y}{R_i}\right)\right] . \tag{5.8}$$

Contours of the resulting velocity distribution are presented in figure 5.9.

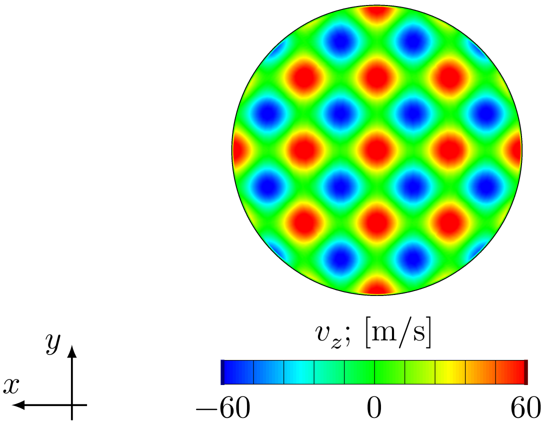

Figure 5.9: Perturbed velocity field $v_z = v_{\mathrm{PL},z} + v_{\mathrm{pert},z}$ [m/s] at selected cross-sections for case PP_h10Re5300.

In the acoustic pipe LES (AP_...), considering the pipe flow configuration with the sharp orifice, the flow field was uniformly initialized with $v_{i,\mathrm{init}} = 0$ and $p_{\mathrm{init}} = p_{\mathrm{ref}}$. Starting from this quiescent state, the mass flow was successively increased towards the prescribed target value imposing a temporally ramped 1/7-power law velocity distribution at the inflow boundary. The ramped profile reads

$$v_{z,\mathrm{PL,ramp}}(r) = \lambda_{\mathrm{ramp}}(t) v_{z,\mathrm{PL}}, \quad \text{where} \tag{5.9a}$$

$$\lambda_{\mathrm{ramp}}(t) = \begin{cases} \dfrac{t}{T_{\mathrm{ramp}}} & \text{if} \quad t < T_{\mathrm{ramp}} \\ 1 & \text{else} \end{cases}, \tag{5.9b}$$

where $T_{\mathrm{ramp}} = 0.01\,\mathrm{s}$. After the ramping phase the solution of the periodic pipe LES was used for specifying the instantaneous inflow BC, as explained in section 5.4.1.

To check the statistical convergence of the periodic pipe LES (PP_...) solution the wall shear stress τ_{W} averaged over the whole pipe wall, was monitored, where the flow has converged to a statistically fully developed state when the value of this monitored quantity reached a constant level.

5.4.3 Temporal integration

For the temporal integration over time an implicit method is used in FIRE™, where, due to the setting of the blending factor $\alpha_{\mathrm{B},t} = 1$, the second order marching scheme is applied. The time-steps for the periodic pipe LES (PP_...) and the acoustic pipe LES (AP_...) were chosen with respect to the CFL condition (3.69) with $CFL_{\mathrm{CFD}} \approx 0.5$. The time-step for the periodic pipe LES were based on the constant axial resolution $\Delta z_{\mathrm{PP,ref}}$ and the mean bulk velocity in the pipe $\bar{\boldsymbol{v}}_{\dot{V},D_{\mathrm{I}}}$(5.2)

$$\Delta t_{\mathrm{PP,ref}} = \frac{\Delta z_{\mathrm{PP,ref}} CFL_{\mathrm{CFD}}}{\bar{\boldsymbol{v}}_{\dot{V},D_{\mathrm{I}}}}. \tag{5.10}$$

The time-step for the acoustic pipe LES were based on a reference cell size $\Delta z_{\mathrm{AP,ref}}$, located at the center of the pipe one pipe diameter downstream of the orifice, and the mean volumetric velocity inside the orifice $\bar{\boldsymbol{v}}_{\dot{V},h}$ (5.4)

$$\Delta t_{\mathrm{AP,ref}} = \frac{\Delta z_{\mathrm{AP,ref}} CFL}{\bar{\boldsymbol{v}}_{\dot{V},h}}. \tag{5.11}$$

Choosing a time-step with reference to the smallest cell inside the orifice would have let to much smaller time-steps, due to the local refinements directly at the corners of the orifice extending into the center of the pipe, which would have increased the number of required time-steps enormously.

The total simulation times were chosen with reference to an approximated flow-through time (FTT), which is defined as the required time a particle, traveling with the mean volumetric velocity $\bar{\boldsymbol{v}}_{\dot{V},D_\mathrm{I}}$, would need to pass the computational domain once, which are $10\,D_\mathrm{I}$ for the periodic pipe LES and $25\,D_\mathrm{I}$, measured from the entrance of orifice to the outflow boundary, for the acoustic pipe LES. For the periodic pipe LES simulations approximately 26 flow-through times for the total simulation time and approximately 5 flow-through times for the time-frame for the sampling of the statistical results were chosen. For the acoustic pipe LES approximately 4 flow-through times for the total simulation time and approximately 1 flow-through time for the sampling of the statistical results and the monitoring of the aeroacoustic source terms were chosen. This led to the corresponding time-frames listed in table 5.6, where t_end is the total simulation time and $T_\mathrm{statistics} = t_\mathrm{end} - t_\mathrm{reset}$ is the time-frame for the sampling of the statistical results.

TABLE 5.6: The chosen time-steps, time-period and approximated flow-through times (FTT) for the applied LES.

Case:	Δt [s]	t_end [s]	≈FTT [−]	t_reset [s]	$T_\mathrm{statistic}$ [s]	≈FTT [−]
PP_h10Re5300	2×10^{-4}	2.8	26.7	2.2	0.6	5.5
PP_h10Re5300F						
PP_h5Re5300						
PP_h10Re7400	1×10^{-4}	2.0	26.6	1.6	0.4	5.1
AP_h10Re5300	5×10^{-5}	1.2	4.3	0.9	0.3	1.0
AP_h10Re5300F	2.5×10^{-5}					
AP_h5Re5300						
AP_h10Re7400		0.8	4.1	0.6	0.2	1.0

5.4.4 RANS and CAA simulation

RANS

The RANS simulation was initialized, similar to the LES simulations, imposing a uniform flow field with zero velocity $v_{i,\mathrm{init}} = 0$ and the reference pressure $p_\mathrm{init} = p_\mathrm{ref}$. The same initial ramping of the inflow using a 1/7-power law was applied to approach the desired mass flow rate.

At the outlet also the averaged pressure BC $\bar{p}_\mathrm{BC,outlet} = p_\mathrm{ref}$ was used for better comparison with the LES.

The RANS was carried out as a steady-state simulation, where a stationary solution is iterated until convergence.

CAA simulation

The results of the RANS simulation, the flow field $\langle v_i \rangle$, $\langle p \rangle$ and $\langle \rho \rangle = \rho_{\mathrm{ref}}$ and the turbulence quantities $\langle k \rangle$ and $\langle \varepsilon \rangle$, are mapped from the CFD grid onto the CAA grid. Within the mapping process the CAA module of FIRE™ estimates an optimum time-step for the CAA Δt_{CAA} depending on the CFL condition (3.69). Additionally, a time-step used by the UKSG Δt_{UKSG} method for computing the evolution of the aeroacoustic source terms is determined from equation (4.72), but can be modified by the user. In the CAA simulation the acoustic solution is integrated in time using a fourth order accurate *Runge-Kutta* temporal discretization scheme. Approximately one flow through time FTT was chosen for the total simulation time $T_{\mathrm{CAA}} = 0.1\,\mathrm{s}$. In table 5.7 the used CAA time-steps and the total simulation time are listed. At the inlet and outlet boundaries *non-reflecting*, and at the solid walls *reflecting* boundaries were applied.

Table 5.7: The used time-steps Δt and the simulation time T_{CAA} of the CAA in [s].

quantity	value	[unit]
Δt_{CAA}	1.15×10^{-7}	[s]
Δt_{UKSG}	5×10^{-6}	[s]
T_{CAA}	1×10^{-1}	[s]

6 Flow simulation results

In this chapter the results obtained from the incompressible flow simulations shall be discussed and analyzed. In section 6.1 the results obtained from the *periodic pipe* LES (PP_...) are presented, discussed and validated against DNS results available at the ISW. Finally, in section 6.2 the flow results from the *acoustic pipe* LES (AP_...) are presented and discussed.

6.1 Periodic pipe flow

6.1.1 Initial conditions to a fully developed turbulent state

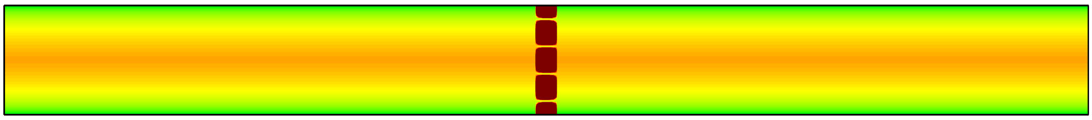

(a) $t = 0\,\mathrm{s}$

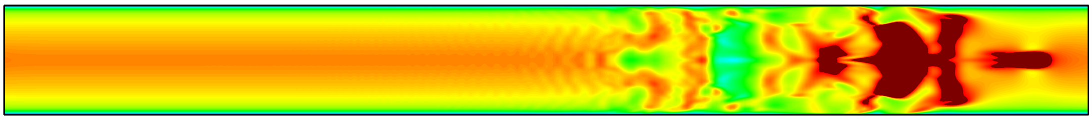

(b) $t = 0.03\,\mathrm{s}$

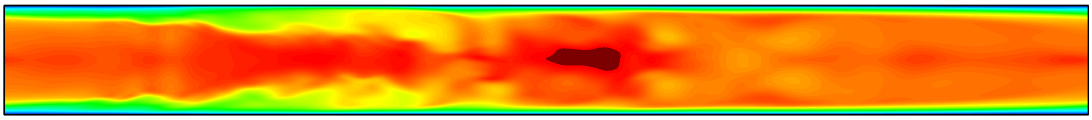

(c) $t = 0.2\,\mathrm{s}$

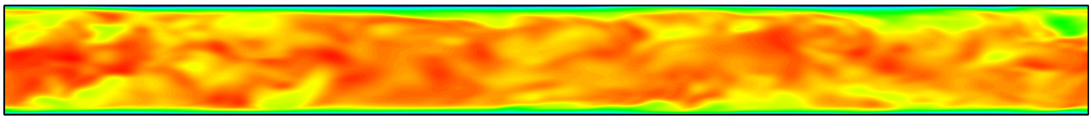

(d) $t = 0.4\,\mathrm{s}$

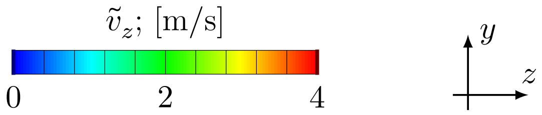

Figure 6.1: Turbulence transition presented as contours of the instantaneous velocity field $\tilde{v}_z$ [m/s] at different times t for case PP_h10Re5300.

Each *periodic pipe* LES (PP_...) was initialized with a perturbed velocity field based on equation (5.8) to trigger the transition to a fully developed turbulent state, which is presented for case PP_h10Re5300 in figure 6.1. Due to the initial perturbation at $t = 0\,\mathrm{s}$ (see figure 6.1a) a laminar high velocity structure appears which travels through the periodic pipe (see figure 6.1b). After some time this high velocity structure decays and it seems that this flow field might stay laminar and symmetric, however at $t = 0.2\,\mathrm{s}$, in the wake of the high velocity structure, the flow field becomes asymmetric and falls into a transition to a fully developed turbulent state. At $t = 0.4\,\mathrm{s}$ figure 6.1d the flow field appears to be fully turbulent.

6.1.2 The instantaneous vorticity fields

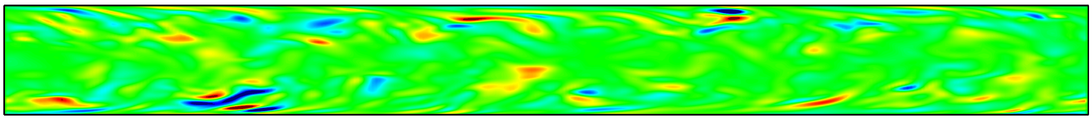

(a) Case PP_h10Re5300 with $\mathcal{R}e_{D_i} = 5300$ at $t_{\mathrm{end}} = 2.8\,\mathrm{s}$.

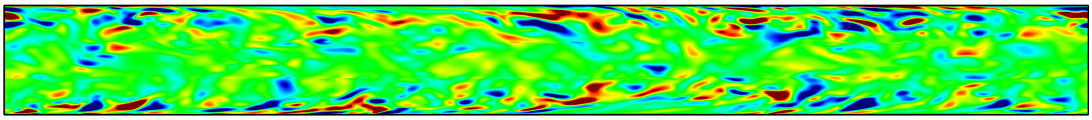

(b) Case PP_h10Re7400 with $\mathcal{R}e_{D_i} = 7400$ at $t_{\mathrm{end}} = 2.0\,\mathrm{s}$.

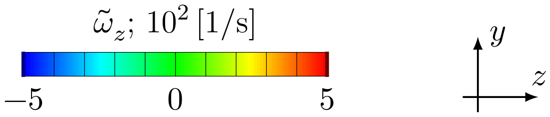

FIGURE 6.2: Comparison of conrours of the axial component of the instantaneous resolved vorticity $\tilde{\omega}_z$ [1/s] of different Reynolds numbers.

Figure 6.2 exemplarily shows instantaneous contours of the vorticity in the axial direction $\tilde{\omega}_z$ for the statistically converged cases PP_h10Re5300 and case PP_h10Re7400, in the longitudinal section plane $x = 0$. As expected, the higher Reynolds number case exhibits more small scale turbulent structures with generally higher intensity.

6.1.3 Convergence of the statistics

The history of the spatially averaged wall shear stress τ_W is exemplarily shown for the case PP_h10Re5300 and PP_h10Re7400 in figure 6.3. After about $t = 0.6\,\mathrm{s}$ the wall shear stress stays approximately constant. The starting point of the temporal averaging for sampling the flow statistics is at $t_\mathrm{reset} = 1.6\,\mathrm{s}$ for case PP_h10Re7400 and $t_\mathrm{reset} = 2.2\,\mathrm{s}$ for case PP_h10Re5300. The level of the statistical (= temporal averaged) value $\langle\tau_\mathrm{W}\rangle$ is indicated as well.

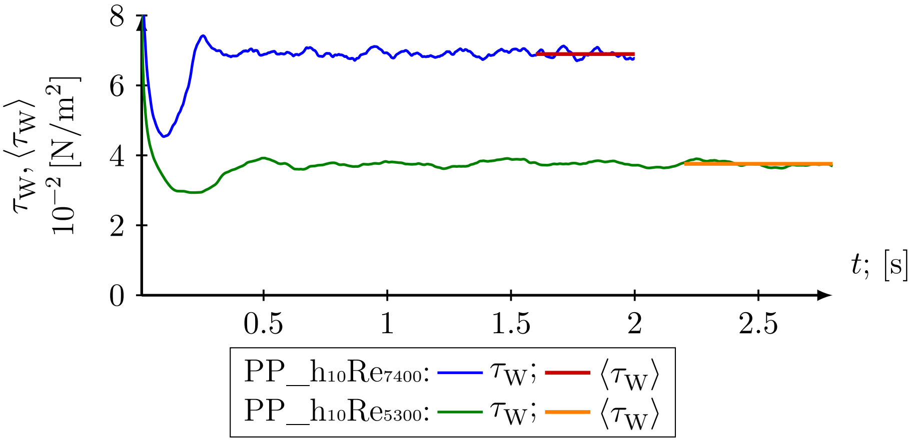

Figure 6.3: History of the wall shear stress τ_W [N/m^2] and its finally obtained temporal average $\langle\tau_\mathrm{W}\rangle$ [N/m^2] over time for the case PP_h10Re5300 and case PP_h10Re7400.

6.1.4 Validation

For validation the results of the periodic pipe LES (PP_...) are compared against DNS data obtained for the wall friction based Reynolds numbers $\mathcal{Re}_{\tau_\mathrm{W}} = 360$ and 500 available at the ISW.

The predicted wall friction based Reynolds numbers $\mathcal{Re}_{\tau_\mathrm{W}}$ of all periodic pipe LES are listed in table 6.1. One can see from the also shown near wall resolution in terms of y^+, that a refinement tends to produce a better agreement with the wall friction based Reynolds numbers $\mathcal{Re}_{\tau_\mathrm{W}}$ of the DNS. The smaller y^+ the closer the results are to the target values.

Table 6.1: The main flow quantities of the periodic pipe LES (PP_...) results.

Case:	$\mathcal{Re}_{\tau_\mathrm{W}}$ [−]	y^+ [−]
PP_h10Re5300	344.10	1.239
PP_h10Re5300F	349.37	0.882
PP_h5Re5300	346.52	1.167
PP_h10Re7400	466.17	1.177

The results presented in the following figures for validation are all non-dimensionalized, so that a comparison against DNS data is better possible. The dimensionless pipe radius r^*, denoted by the superscript * is normalized with the inner pipe radius $R_\mathrm{I} = 14.85\,\mathrm{mm}$, such that $1 - r^* = 0$ represents the pipe wall, and $1 - r^* = 1$ is at the center of the pipe. The wall friction velocity $\boldsymbol{v}_{\tau_\mathrm{W}}$ of the corresponding periodic pipe LES was used to non-dimensionalize the turbulent velocity fluctuations and Reynolds stresses, which are denoted with a superscript $^+$. The presented quantities are based on a cylindrical coordinate system with $i = ax, r, tg$ representing the axial, radial and tangential directions, respectively.

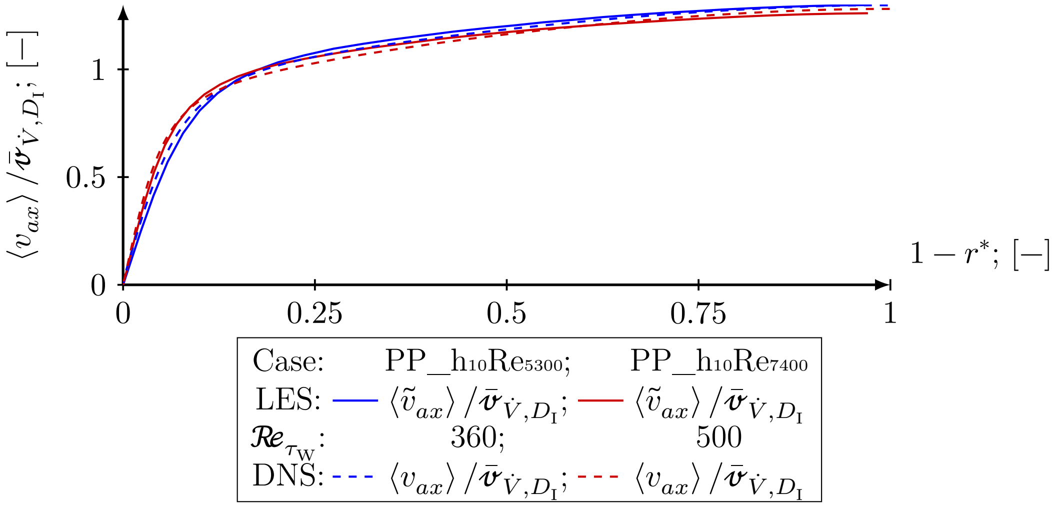

Figure 6.4: Comparison of the temporally averaged dimensionless velocity profiles in axial direction $\langle v_{ax} \rangle / \bar{\boldsymbol{v}}_{\dot{V},D_\mathrm{I}}$ [−] between LES and DNS for $\mathcal{Re}_{\tau_\mathrm{W}} = 360$ and 500.

Figure 6.4 shows the comparison of the radial variation of the mean axial velocity $\langle v_{ax} \rangle$ normalized by the volume flow equivalent velocity $\bar{\boldsymbol{v}}_{\dot{V},D_i}$ for the case PP_h10Re5300 and case PP_h10Re7400 to the DNS data. The higher Reynolds number leads to a higher velocity gradient close to the pipe wall $1 - r^* = 0$, which results in higher wall shear stress τ_W, also visible in figure 6.3, and a stronger pressure loss.

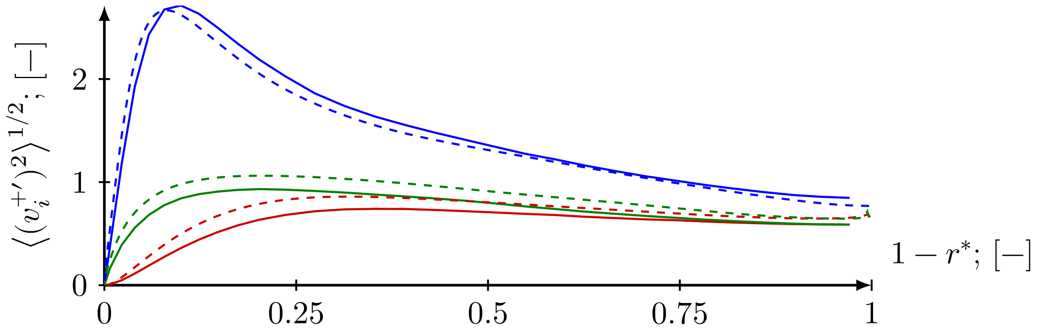

(a) Comparison of case PP_h10Re5300 with DNS for $\mathcal{Re}_{\tau_\mathrm{W}} = 360$.

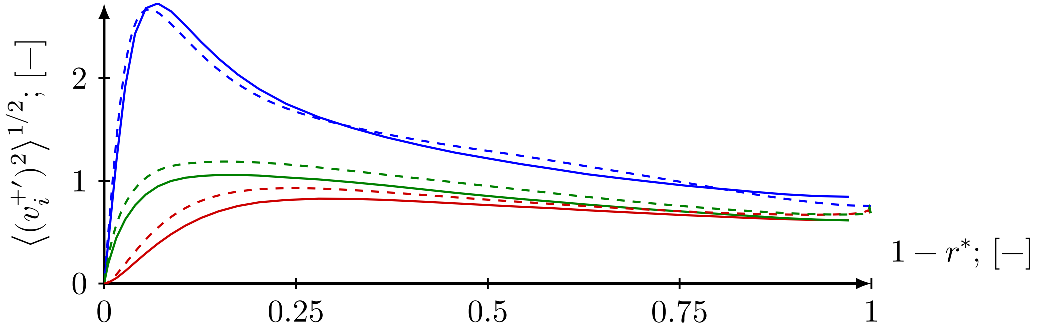

(b) Comparison of case PP_h10Re7400 with DNS for $\mathcal{Re}_{\tau_\mathrm{W}} = 500$.

LES: — $\left\langle (\tilde{v}_{ax}^{+\prime})^2\right\rangle^{1/2}$; — $\left\langle (\tilde{v}_{r}^{+\prime})^2\right\rangle^{1/2}$; — $\left\langle (\tilde{v}_{tg}^{+\prime})^2\right\rangle^{1/2}$
DNS: - - - $\left\langle (v_{ax}^{+\prime})^2\right\rangle^{1/2}$; - - - $\left\langle (v_{r}^{+\prime})^2\right\rangle^{1/2}$; - - - $\left\langle (v_{tg}^{+\prime})^2\right\rangle^{1/2}$

Figure 6.5: Comparison of the RMS of the turbulent fluctuations $\left\langle (\tilde{v}_i^{+\prime})^2\right\rangle^{1/2}$; [−] between LES and DNS for $\mathcal{Re}_{\tau_\mathrm{W}} = 360$ and 500 in axial, radial and tangential direction ($i = ax, r, tg$).

For validating the predicted second order statistics figure 6.5 shows the dimensionless temporally averaged turbulence velocity fluctuations in the axial $\left\langle (v_{ax}^{+\prime})^2\right\rangle^{1/2}$, radial $\left\langle (v_{r}^{+\prime})^2\right\rangle^{1/2}$, and tangential direction $\left\langle (v_{tg}^{+\prime})^2\right\rangle^{1/2}$ representing the RMS of the resolved turbulent normal stresses, generally defined as

$$\left\langle (\tilde{v}_i^{+\prime})^2\right\rangle^{1/2} = \left\langle (\tilde{v}_i^{+} - \langle \tilde{v}_i^{+}\rangle)^2\right\rangle^{1/2}. \tag{6.1}$$

As typically observed, the radial fluctuations are the smallest due to the damping effect of the pipe wall, while the less impeded axial fluctuations are the largest. For higher Reynolds numbers the peaks are evidently shifted towards the wall. The results from LES are in good agreement with DNS for the axial fluctuations, while the radial and tangential components are notably under-predicted.

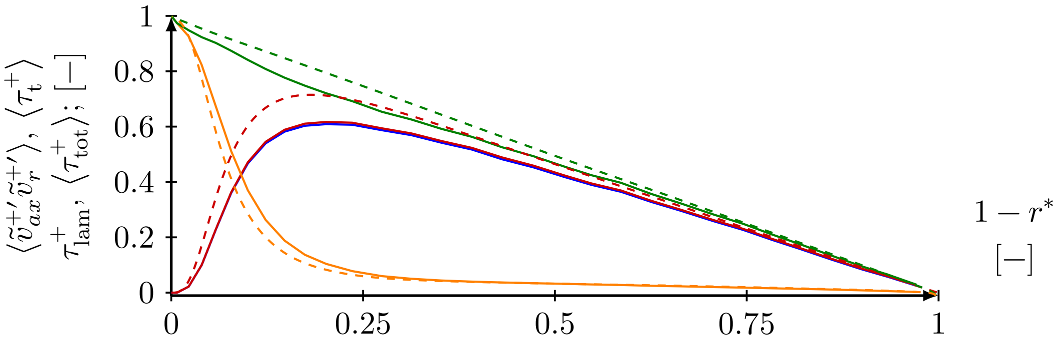

(a) Comparison of case PP_h10Re5300 with DNS for $\mathcal{Re}_{\tau_{\mathrm{W}}} = 360$.

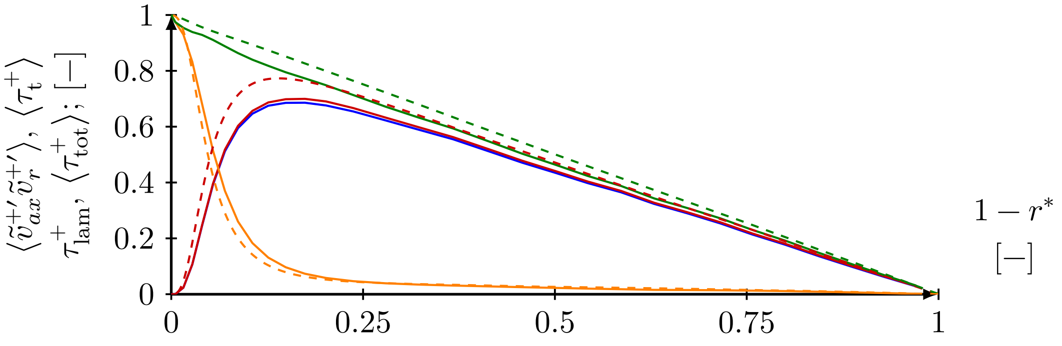

(b) Comparison of case PP_h10Re7400 with DNS for $\mathcal{Re}_{\tau_{\mathrm{W}}} = 500$.

LES: —— $\langle \tilde{v}_{ax}^{+\prime}\tilde{v}_r^{+\prime}\rangle$; —— $\langle \tilde{\tau}_{\mathrm{t}}^{+}\rangle$; —— $\langle \tilde{\tau}_{\mathrm{lam}}^{+}\rangle$; —— $\langle \tilde{\tau}_{\mathrm{tot}}^{+}\rangle$
DNS: - - - $\langle \tau_{\mathrm{t}}^{+}\rangle$; - - - $\langle \tau_{\mathrm{lam}}^{+}\rangle$; - - - $\langle \tau_{\mathrm{tot}}^{+}\rangle$

Figure 6.6: Comparison of the stresses between LES and DNS for $\mathcal{Re}_{\tau_{\mathrm{W}}} = 360$ and 500.

Figure 6.6 shows the dimensionless shear stresses dependent on the dimensionless radius r^* for the same cases with $\mathcal{Re}_{\tau_{\mathrm{W}}} = 360$ and 500. The total shear stress $\langle \tilde{\tau}_{\mathrm{tot}}^{+}\rangle$ is composed of the turbulent shear stresses $\langle \tilde{\tau}_{\mathrm{t}}^{+}\rangle$ and the laminar shear stress $\langle \tilde{\tau}_{\mathrm{lam}}^{+}\rangle$ rewritten as

$$\langle \tilde{\tau}_{\mathrm{tot}}^{+}\rangle = \langle \tilde{\tau}_{\mathrm{t}}^{+}\rangle + \langle \tilde{\tau}_{\mathrm{lam}}^{+}\rangle , \tag{6.2}$$

where

$$\langle \tilde{\tau}_{\mathrm{lam}}^{+}\rangle = -\,\nu_{\mathrm{ref}}^{+}\frac{\partial\langle \tilde{v}_{ax}^{+}\rangle}{\partial r^*} \tag{6.3}$$

and in case of LES the turbulent stresses are composed of the resolved and modeled turbulent stresses

$$\langle \tilde{\tau}_{\mathrm{t}}^{+}\rangle = \langle v_{ax}^{+\prime}v_r^{+\prime}\rangle - \nu_{\mathrm{SGS}}^{+}\frac{\partial\langle \tilde{v}_{ax}^{+}\rangle}{\partial r^*} \tag{6.4}$$

Since the stresses were made dimensionless with the wall friction velocity $\boldsymbol{v}_{\tau_{\mathrm{W}}}$, the total stresses are one $\langle \tilde{\tau}_{\mathrm{tot}}^{+}\rangle = 1$ at the wall. Due to the axial symmetry of the pipe flow all shear stresses are zero at the center of the pipe. As following from analytical considerations, it is mandatory for fully developed turbulent pipe flows that the total shear stress is linearly dependent on the radial coordinate r. The total turbulence stresses $\langle \tau_{\mathrm{t}}^{+} \rangle$ of the DNS are equal to $\langle v_{ax}^{+\prime} v_{r}^{+\prime} \rangle$ hence, including no modeled SGS contribution, because the whole turbulence spectrum is resolved. For both Reynolds number cases the LES evidently under-predicts the turbulent shear stresses. The unresolved gap to the DNS data is not fully compensated by the contribution of the SGS-model.

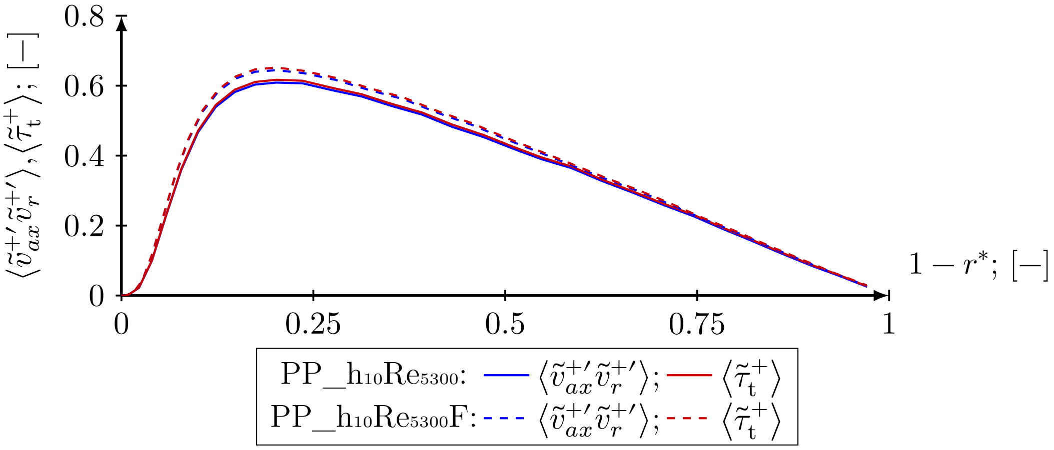

FIGURE 6.7: Comparison of the contribution of the subgrid-scale model (SGM) between case PP_h10Re5300 and case PP_h10Re5300F.

Figure 6.7 illustrates the influence of the spatial resolution comparing the LES results obtained with different computational grids, as applied in the cases PP_h10Re5300 and PP_h10Re5300F. Due to the higher grid resolution in case PP_h10Re5300F, the resolved stresses $\langle \tilde{v}_{ax}^{+\prime} \tilde{v}_{r}^{+\prime} \rangle$ are higher, whilst the contribution of the subgrid-scale model is smaller. This expected tendency is also demonstrated in table 6.2, comparing the temporally averaged turbulence kinetic energy $\langle \mathscr{k} \rangle$ averaged over the whole periodic pipe domain.

TABLE 6.2: The contribution of the SGM dependent on the grid resolution averaged over all cells N_{C} of the periodic pipe domain.

Case:	$\left\langle \widetilde{k}_{\mathrm{tot}} \right\rangle$	$\left\langle \widetilde{k}_{\mathrm{LES}} \right\rangle$		$\langle k_{\mathrm{SGS}} \rangle$	
	$[\mathrm{m}^2/\mathrm{s}^2]$	$[\mathrm{m}^2/\mathrm{s}^2]$	[%]	$[\mathrm{m}^2/\mathrm{s}^2]$	[%]
PP_h10Re5300	0.057 02	0.056 57	99.21	0.000 45	0.79
PP_h10Re5300F	0.059 81	0.059 46	99.41	0.000 35	0.59
PP_h5Re5300	0.057 14	0.056 71	99.24	0.000 44	0.76
PP_h10Re7400	0.110 11	0.108 94	98.94	0.001 17	1.06

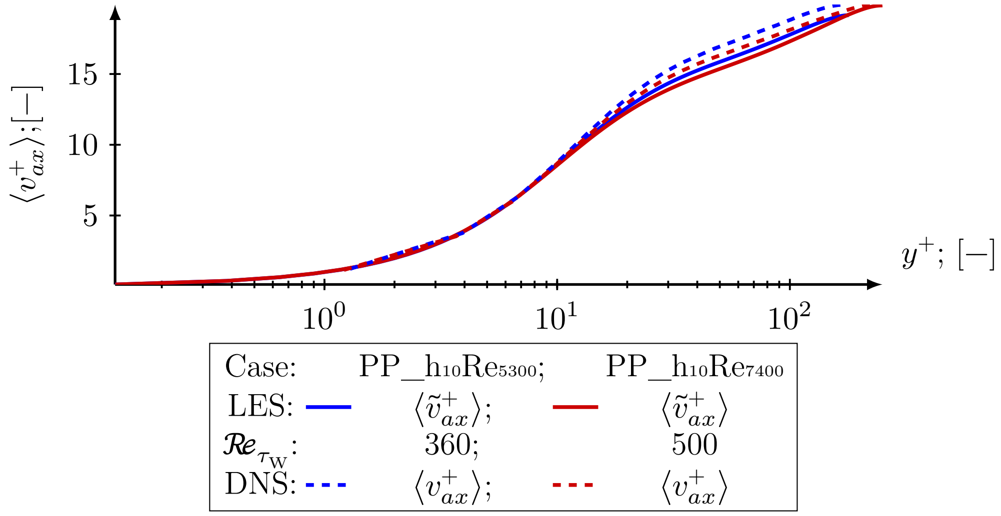

FIGURE 6.8: Comparison of the logarithmic law of the wall between LES and DNS for $\mathcal{Re}_{\tau_{\mathrm{W}}} = 360$ and 500.

Figure 6.8 shows the predicted axial velocity plotted over the non-dimensional wall distance y^+ for the cases PP_h10Re5300 and PP_h10Re7400. The viscous sublayer ($y^+ < 5$) is evidently well resolved and the predicted data are very close to the analytic function (compare to figure 3.6). In the core region beyond the buffer layer the solution approaches a logarithmic dependence on y^+, as indicated by the straight section of profiles.

Despite the deviations which were particularly observed for the second order statistics, the LES solution of the periodic pipe flows still represents a physically reliable basis for delivering turbulent fluctuating velocity distributions for use as inflow conditions in the acoustic pipe LES, where the pipe contains the orifice constriction.

6.1.5 Instantaneous flow field used for inflow boundary conditions

Figure 6.9 and 6.10 exemplarily show contours of the resolved instantaneous velocity components $\tilde{v}_i$ obtained from the LES for case PP_h10Re5300 at $t_{\mathrm{end}} = 2.8\,\mathrm{s}$, in longitudinal sectional and axial cross-sectional view, respectively. The resolved instantaneous velocity components $\tilde{v}_i$, which are exemplarily shown in figure 6.10 at a certain cross-section, are directly mapped onto the inflow boundary of the corresponding acoustic pipe LES.

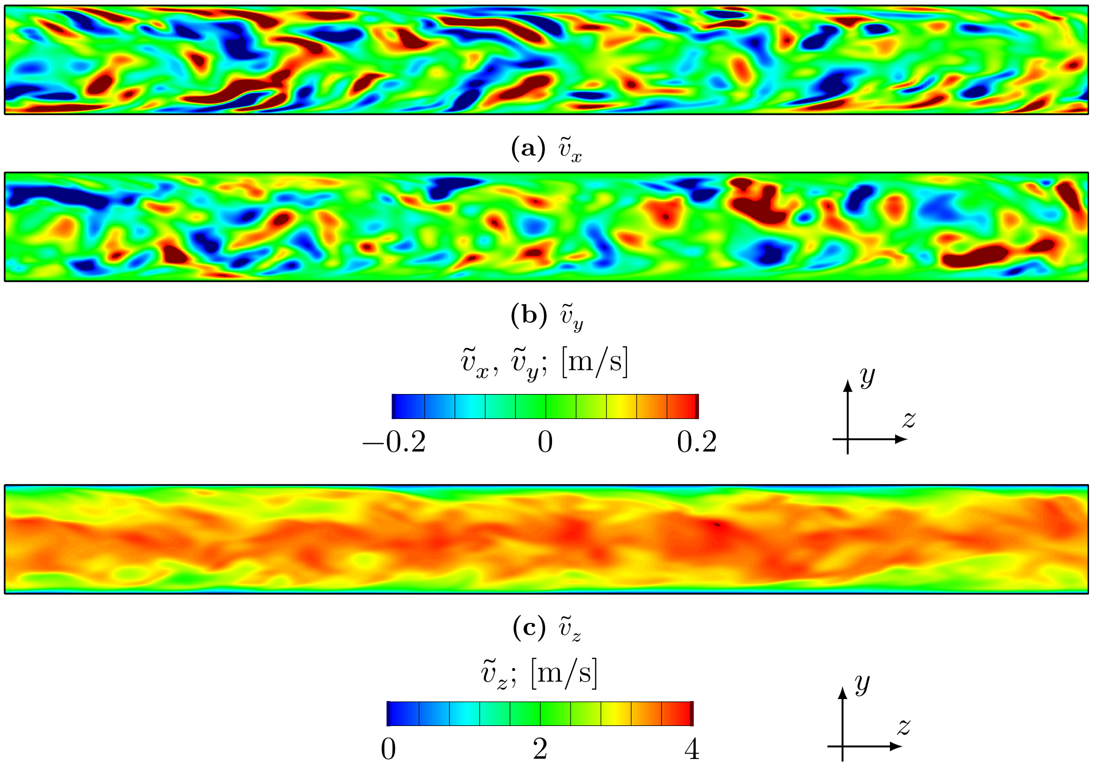
(a) $\tilde{v}_x$

(b) $\tilde{v}_y$

(c) $\tilde{v}_z$

Figure 6.9: Resolved instantaneous velocity components $\tilde{v}_i$ [m/s], presented as contours in longitudinal section, at $t_{\mathrm{end}} = 2.8\,\mathrm{s}$ for case PP_h10Re5300.

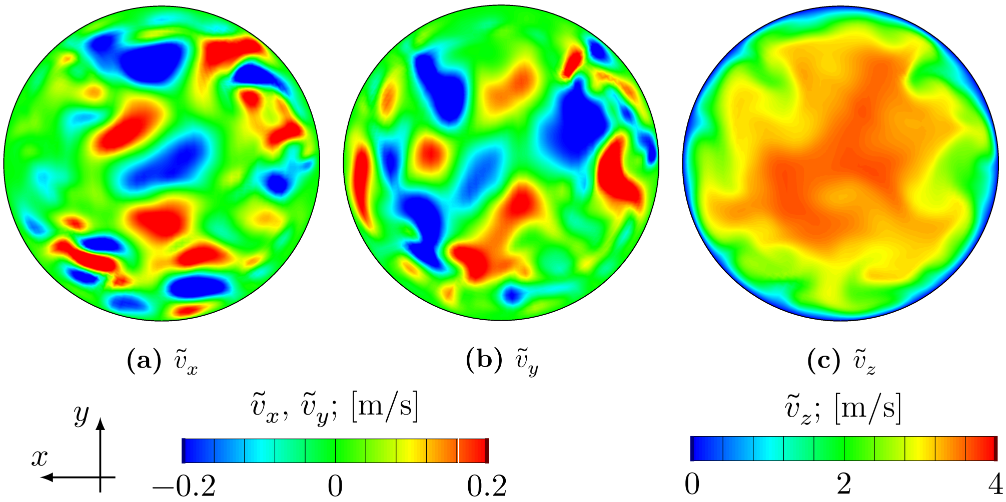

(a) $\tilde{v}_x$ (b) $\tilde{v}_y$ (c) $\tilde{v}_z$

Figure 6.10: Resolved instantaneous velocities $\tilde{v}_i$ [m/s], presented as contours in a cross-section at position $z = 0$ and at $t_{\text{end}} = 2.8\,\text{s}$ of case PP_h₁₀Re₅₃₀₀.

6.2 Acoustic pipe results

In this section the results of the acoustic pipe LES (AP_...), considering the pipe flow configuration associated with the sharp orifice constriction, are presented and discussed.

6.2.1 Flow conditions upstream the orifice

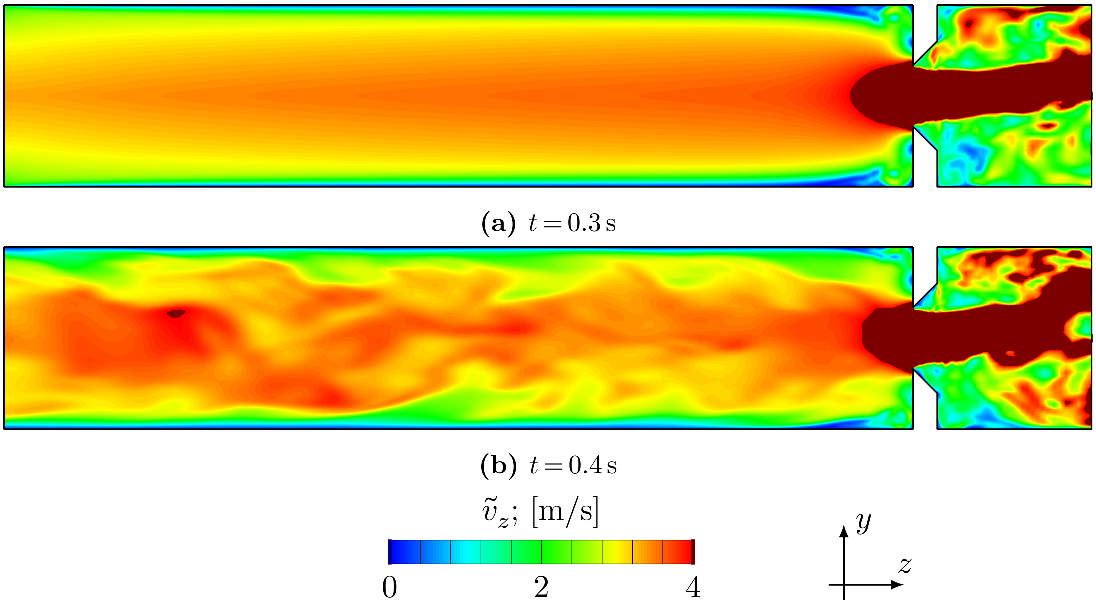

(a) $t = 0.3\,\mathrm{s}$

(b) $t = 0.4\,\mathrm{s}$

Figure 6.11: Contours of the instantaneous resolved velocity component $\tilde{v}_z$ [m/s] at the inflow pipe of case AP_h10Re5300 at $t = 0.3\,\mathrm{s}$ and $t = 0.4\,\mathrm{s}$.

Figure 6.11 gives a qualitative insight into the flow upstream of the orifice as obtained at two distinct instants of time, $t = 0.3\,\mathrm{s}$ and $0.4\,\mathrm{s}$. Figure 6.11a shows instantaneous contours of the axial velocity at $t = 0.3\,\mathrm{s}$. This corresponds to approximately one flow-through time, where a temporally ramped 1/7-power law was used as velocity inlet boundary condition. Immediately, thereafter the mapping procedure using the instantaneous velocity field from the corresponding periodic pipe LES was started. After a further time interval $T = 0.1\,\mathrm{s}$, imposing the turbulent fluctuating inflow boundary conditions, the flow field upstream of the orifice is evidently completely governed by irregular vortical structures very similar to the structures shown in figure 6.9 for the corresponding periodic pipe LES.

6.2.2 The instantaneous velocity field downstream of the orifice

Figure 6.12 shows contours of the resolved instantaneous velocity component in axial direction $\tilde{v}_z$, from the inlet of the acoustic pipe, located at $z = -5\,D_\mathrm{I}$ upstream the orifice until $z = 10\,D_\mathrm{I}$ downstream of the orifice, for all acoustic pipe LES, case AP_h$_{10}$Re$_{5300}$, case AP_h$_{10}$Re$_{5300}$F, case AP_h$_{5}$Re$_{5300}$ and case AP_h$_{10}$Re$_{7400}$. The irregular vortical structures upstream the orifice, as well as the unsteady asymmetrical jet-like core flow downstream the orifice are clearly visible. Additionally, it is clearly visible, that the instantaneous flow field is strongly influenced by the orifice even ten diameters downstream of the orifice, resulting in smaller turbulent vortical structures in comparison to the larger turbulent vortical structures upstream of the orifice.

Also note that the jet-like core flow is attached at different sides of the pipe wall, representing the bifurcation characteristics of the Coanda effect. In previous publications considering similar geometries [8, 12, 19, 24, 40] the Coanda effect also appeared, leading to an asymetric jet-like core flow.

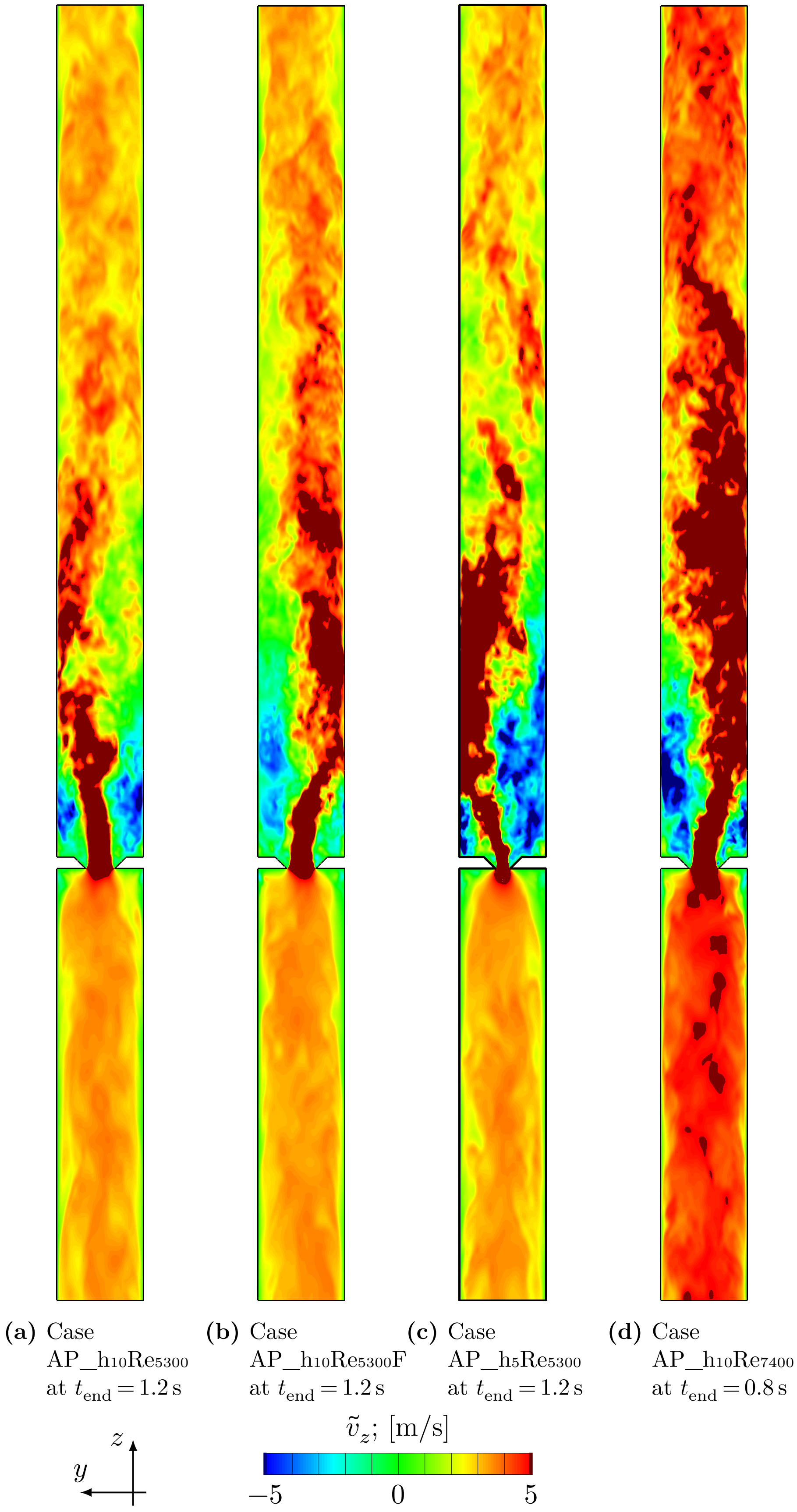

(a) Case AP_h10Re5300 at $t_{\mathrm{end}} = 1.2\,\mathrm{s}$

(b) Case AP_h10Re5300F at $t_{\mathrm{end}} = 1.2\,\mathrm{s}$

(c) Case AP_h5Re5300 at $t_{\mathrm{end}} = 1.2\,\mathrm{s}$

(d) Case AP_h10Re7400 at $t_{\mathrm{end}} = 0.8\,\mathrm{s}$

FIGURE 6.12: Contours of the resolved instantaneous velocity component in axial direction $\tilde{v}_z$ [m/s] at $t = t_{\mathrm{end}}$ in a longitudinal section of the acoustic pipe.

6.2.3 The temporally averaged flow field downstream of the orifice

In this section the temporal averaged velocity and pressure fields are presented and discussed. For each acoustic pipe LES (AP_...) approximately one flow-through time (FTT) was used for sampling the statistically averaged values, as listed in table 5.6.

Temporally averaged velocity field

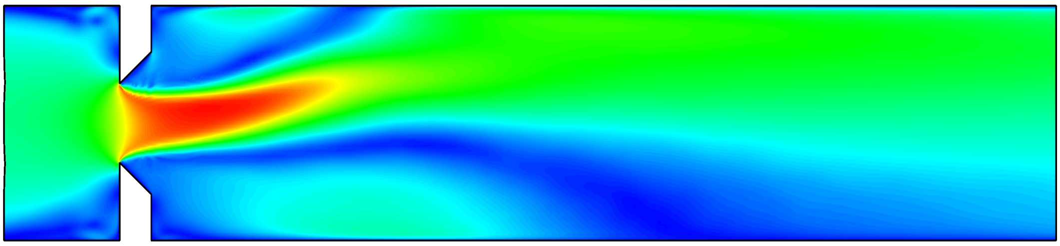

(a) $\langle|\tilde{v}|\rangle$ of case AP_h10Re5300

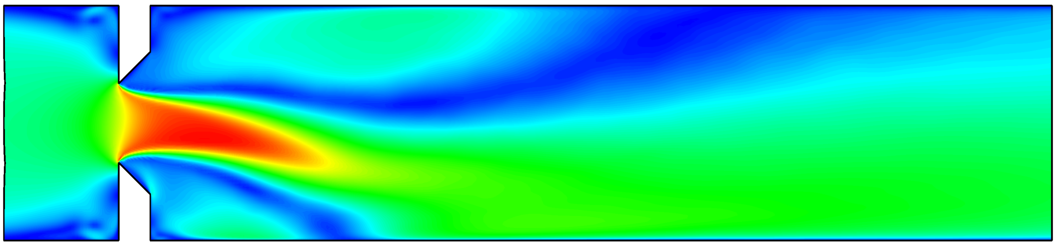

(b) $\langle|\tilde{v}|\rangle$ of case AP_h10Re5300F

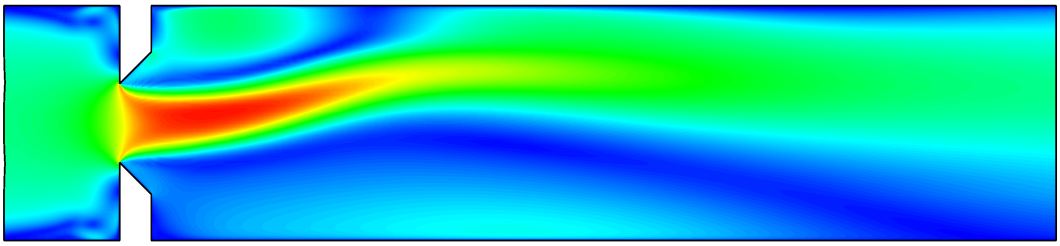

(c) $\langle|v|\rangle$ of case RANS_h10Re5300

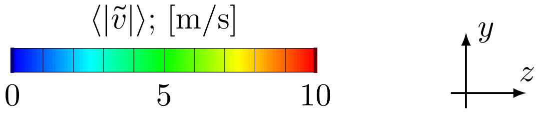

Figure 6.13: Comparison of contours of the temporally averaged velocity magnitude $\langle|\tilde{v}|\rangle$ [m/s] between acoustic pipe LES and RANS for $\mathcal{Re}_{D_\mathrm{I}} = 5300$.

Figure 6.13 presents contours of the averaged velocity magnitude $\langle|v|\rangle$ for the acoustic pipe LES cases with gap height h_{10} and $\mathcal{Re}_{D_\mathrm{I}} = 5300$, as well as for the corresponding case computed with RANS. Due to the so called Coanda effect, the emerging jet is evidently attached to the top ($y > 0$) or bottom ($y < 0$) side of the acoustic pipe. The LES results of the cases AP_h10Re5300 and AP_h10Re5300F, which only differ in the applied spatial resolution of the computational grid, GAP_h10 and GAP_h10F, respectively, are practically identical, as indicated by the very good agreement on the reattachment points of the jet downstream the orifice. The RANS simulation RANS_h10Re5300 is close to the LES. However, the reattachment point is predicted further downstream in comparison to the LES results.

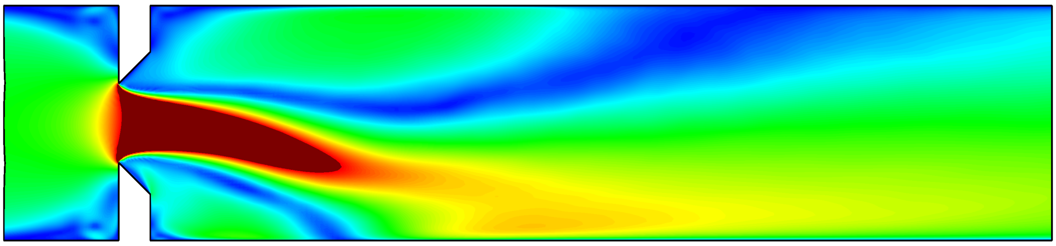

(a) $\langle|\tilde{v}|\rangle$ of case AP_h10Re7400

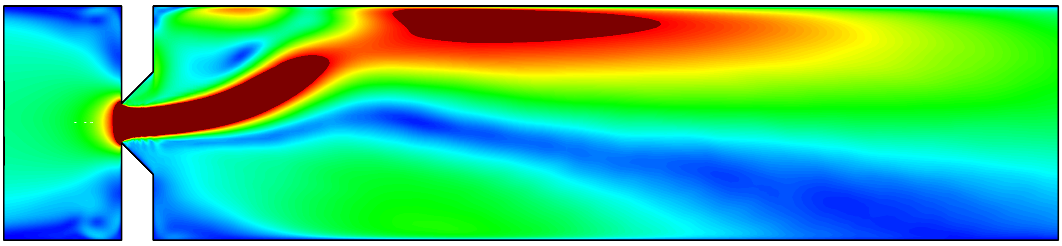

(b) $\langle|\tilde{v}|\rangle$ of case AP_h5Re5300

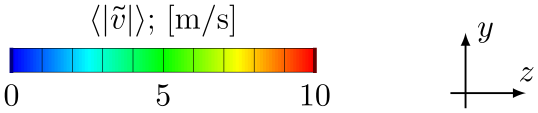

Figure 6.14: Comparison of contours of the temporally averaged velocity magnitude $\langle|\tilde{v}|\rangle$ [m/s] between acoustic pipe LES at $\mathcal{R}e_{D_\mathrm{I}} = 7400$ AP_h10Re7400 and $h_\mathrm{O} = h_5 = 5\,\mathrm{mm}$ AP_h5Re5300.

Figure 6.14 presents contours of the averaged velocity magnitude $\langle|v|\rangle$ for the LES cases AP_h10Re7400 and AP_h5Re5300. The increase of the Reynolds number from $\mathcal{R}e_{D_\mathrm{I}} = 5300$ to $\mathcal{R}e_{D_\mathrm{I}} = 7400$ has apparently only a small impact as compared to the reduction of the gap height h_O from $h_{10} = 10\,\mathrm{mm}$ to $h_5 = 5\,\mathrm{mm}$ of the orifice. The Coanda effect also appears in the case of AP_h5Re5300. Due to the stronger constriction, the deflected jet has evidently much higher axial momentum, which is preserved also downstream of the reattachment point, as indicated by the high velocity region near the upper wall ($y > 0$) in figure 6.14b.

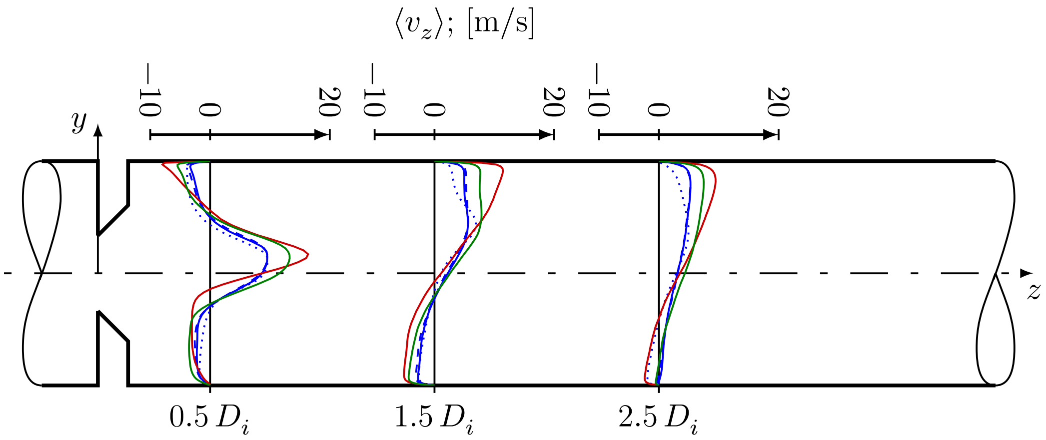

(a) (z-) positions: $0.5\,D_i$, $1.5\,D_i$ and $2.5\,D_i$

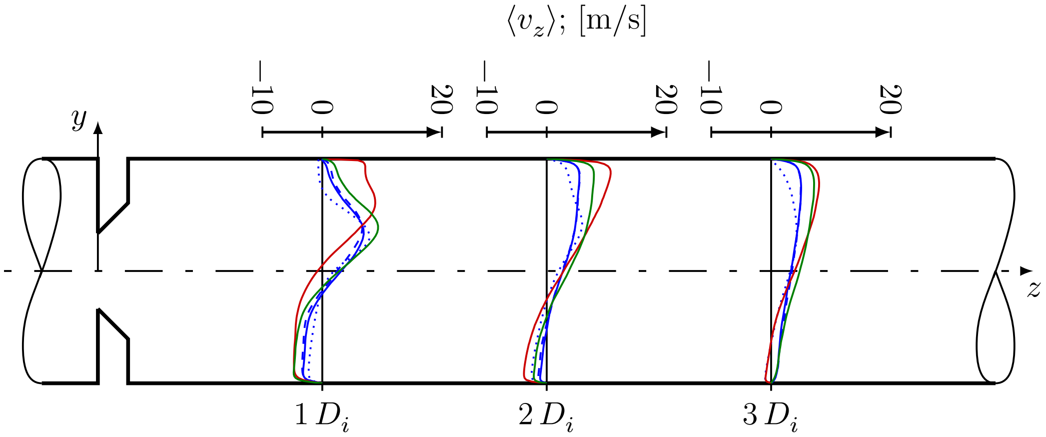

(b) (z-) positions: $1\,D_i$, $2\,D_i$ and $3\,D_i$

AP_h10Re5300; AP_h10Re5300F; RANS_h10Re5300
AP_h10Re7400; AP_h5Re5300

FIGURE 6.15: Comparison of the temporally averaged velocity component $\langle v_z \rangle$ [m/s] between LES and RANS along the vertical coordinate y at selected downstream (z-) positions.

Figure 6.15 shows the temporal average velocity component $\langle v_z \rangle$ along the vertical coordinate y at selected downstream z-positions in the central symmetry plane ($x = 0$) for all acoustic pipe LES. One can observe that case AP_h5Re5300 exhibits the highest velocities, followed by case AP_h10Re7400. Case AP_h10Re5300 and case AP_h10Re5300F, where only the computational grids are different GAP_h10 and GAP_h10F, show a good agreement at all positions. Note that the velocity profile of the RANS simulation is very different to the corresponding LES cases AP_h10Re5300 and AP_h10Re5300F, especially close to the reatachement point of the jet-like core flow.

Temporally averaged pressure field

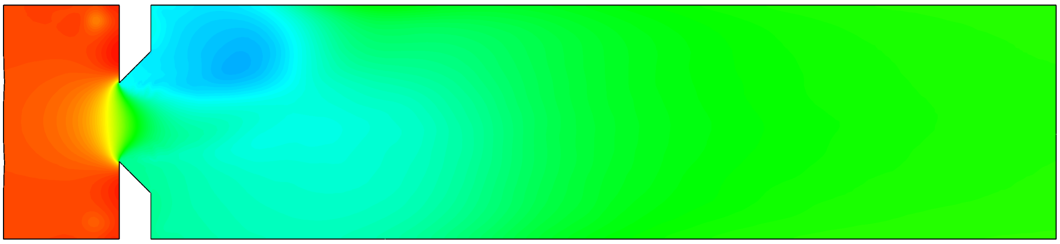

(a) $\langle \tilde{p} \rangle - p_{\text{ref}}$ of case AP_h10Re5300

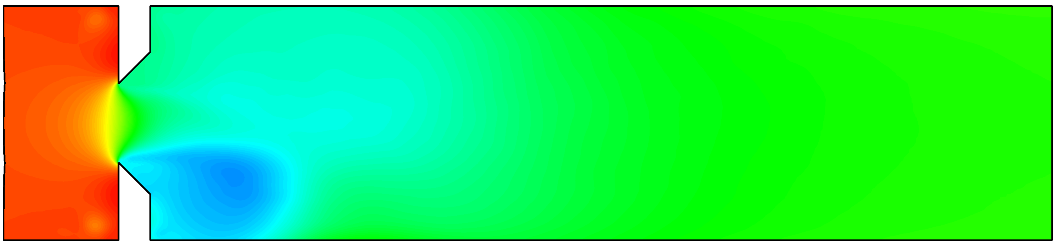

(b) $\langle \tilde{p} \rangle - p_{\text{ref}}$ of case AP_h10Re5300F

(c) $\langle p \rangle - p_{\text{ref}}$ of case RANS_h10Re5300

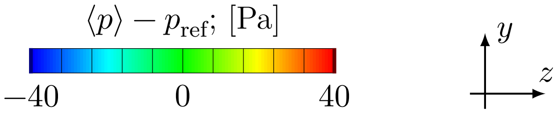

Figure 6.16: Comparison of contours of the temporally averaged pressure field $\langle p \rangle - p_{\text{ref}}$ [Pa] between acoustic pipe LES and RANS at $\mathcal{Re}_{D_\text{I}} = 5300$.

Figure 6.16 shows contours of the temporally averaged pressure field $\langle p \rangle - p_{\text{ref}}$ for the acoustic pipe LES and RANS for $\mathcal{Re}_{D_\text{I}} = 5300$. The LES solutions of cases AP_h10Re5300 and AP_h10Re5300F are in general well comparable to the result of the RANS based results of case RANS_h10Re5300, showing a similar structure of the contours. However, inside the recirculation zone the local pressure drops much more in case of the LES compared to RANS. Due to higher pressure gradients in the LES case in this subregion, the resulting pressure source term from LES will be much more intense here.

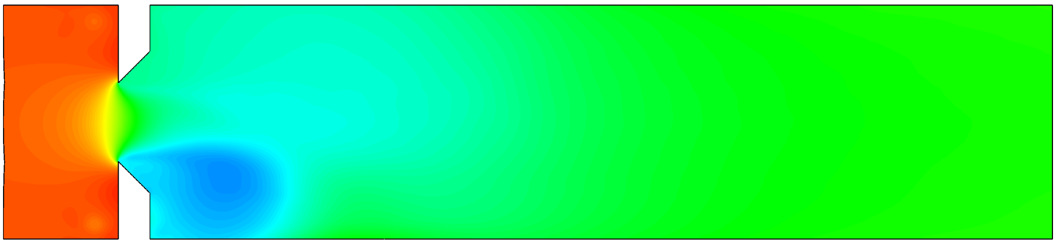

(a) $\langle\tilde{p}\rangle - p_{\mathrm{ref}}$ of case AP_h10Re7400

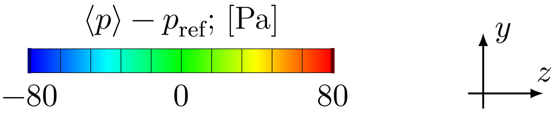

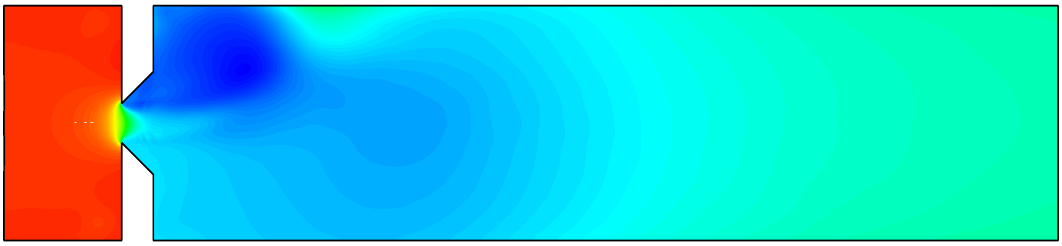

(b) $\langle\tilde{p}\rangle - p_{\mathrm{ref}}$ of case AP_h5Re5300

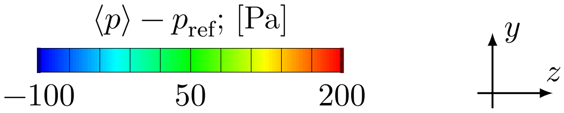

FIGURE 6.17: Comparison of contours of the temporally averaged pressure field $\langle p\rangle - p_{\mathrm{ref}}$ [Pa] between acoustic pipe LES at $\mathcal{R}e_{D_{\mathrm{I}}} = 7400$ AP_h10Re7400 and $h_{\mathrm{O}} = h_5 = 5\,\mathrm{mm}$ AP_h5Re5300.

Figure 6.17 shows contours of the temporally averaged pressure field $\langle p\rangle - p_{\mathrm{ref}}$ for the LES cases AP_h10Re7400 and AP_h5Re5300. The temporally averaged pressure field of case AP_h10Re7400 for $\mathcal{R}e_{D_{\mathrm{I}}} = 7400$ is comparible to the cases AP_h10Re5300 and AP_h10Re5300F presented in figure 6.16 for $\mathcal{R}e_{D_{\mathrm{I}}} = 5300$, showing similar contours. Only the pressure loss is greater in the higher Reynolds number case. The temporally averaged pressure field of case AP_h5Re5300 is quite different to the other cases, which is especially seen in the much higher pressure loss due to the small gap height of the orifice. Due to the impingement of the deflected core jet-flow on the upper pipe wall, resulting in high linear deformation in the reattachement subregion, the local pressure increases.

The high pressure gradients around the sharp corners of the orifice are well visible in each acoustic pipe simulation.

6.2.4 The temporally averaged turbulence kinetic energy field downstream of the orifice

Since the flow-induced noise is mainly generated by the turbulent motion, the turbulence kinetic energy produced by the orifice represents a highly relevant key parameter for the aeroacoustic sources.

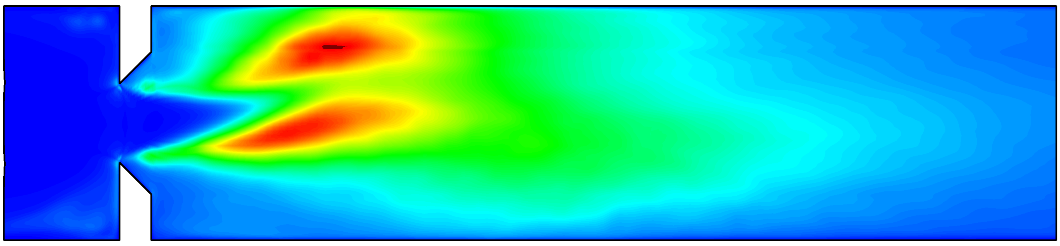

(a) $\left\langle \widetilde{k}_{\mathrm{tot}} \right\rangle$ of case AP_h10Re5300

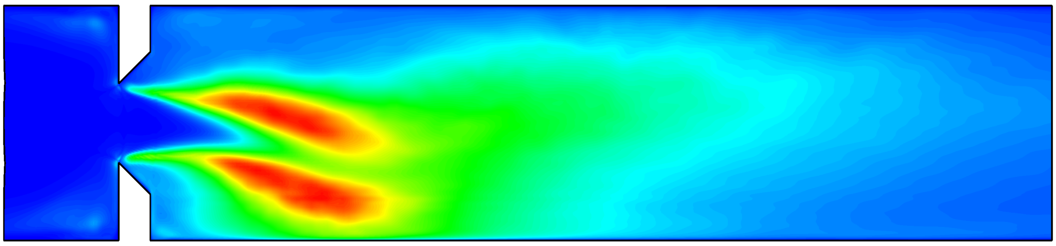

(b) $\left\langle \widetilde{k}_{\mathrm{tot}} \right\rangle$ of case AP_h10Re5300F

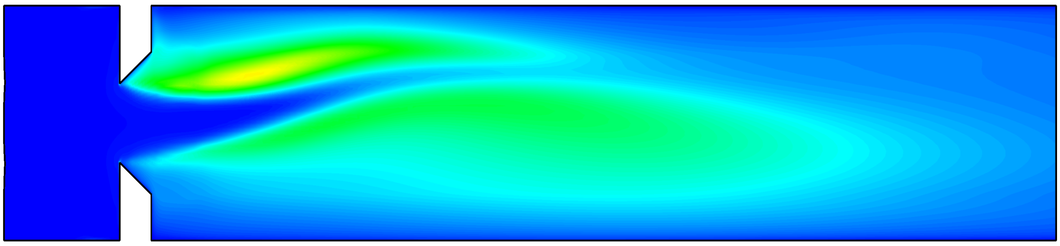

(c) $\langle k_{\mathrm{tot}} \rangle$ of case RANS_h10Re5300

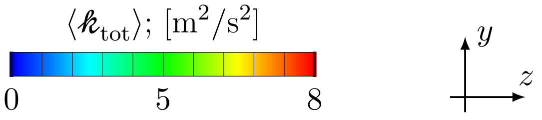

Figure 6.18: Comparison of contours of the temporally averaged total turbulence kinetic energy field $\langle k_{\mathrm{tot}} \rangle$ [m^2/s^2] between LES and RANS at $\mathcal{R}e_{D_i} = 5300$.

In figure 6.18 contours of the temporally averaged total turbulence kinetic energy $\left\langle \widetilde{k}_{\mathrm{tot}} \right\rangle$ for the LES cases AP_h10Re5300, AP_h10Re5300F, and the corresponding RANS simulation RANS_h10Re5300 for $\mathcal{R}e_{D_{\mathrm{I}}} = 5300$ are presented. In the LES cases, the resulting temporally averaged turbulence kinetic energy is the sum of the resolved und modeled SGS part $\left\langle \widetilde{k}_{\mathrm{tot}} \right\rangle = \left\langle \widetilde{k}_{\mathrm{LES}} \right\rangle + \left\langle \widetilde{k}_{\mathrm{SGS}} \right\rangle$. The results, of the two LES cases are quite similar. The case AP_h10Re5300F computed with the finer computational grid (Gap_h10F) should basically resolve a larger fraction of turbulence kinetic energy, so that it should predict a slightly higher level of turbulence kinetic energy. This expected feature can be seen here in particular close to the sharp edges of the orifice, where the turbulence kinetic energy for case AP_h10Re5300F is higher in comparison to the case AP_h10Re5300. Comparing the RANS simulation to the LES cases, the averaged turbulence kinetic energy field is very different. The present RANS simulation predicts a significantly lower turbulence kinetic energy in both shear layers emerging downstream of the orifice. The applied turbulence model (k-ζ-f) produces evidently substantially less turbulence kinetic energy inside those highly sheared regions. Using this considerably lower averaged turbulence kinetic energy $\langle k \rangle$ as input, the UKSG is expected to deliver much weaker aeroacoustic source terms as compared to the LES.

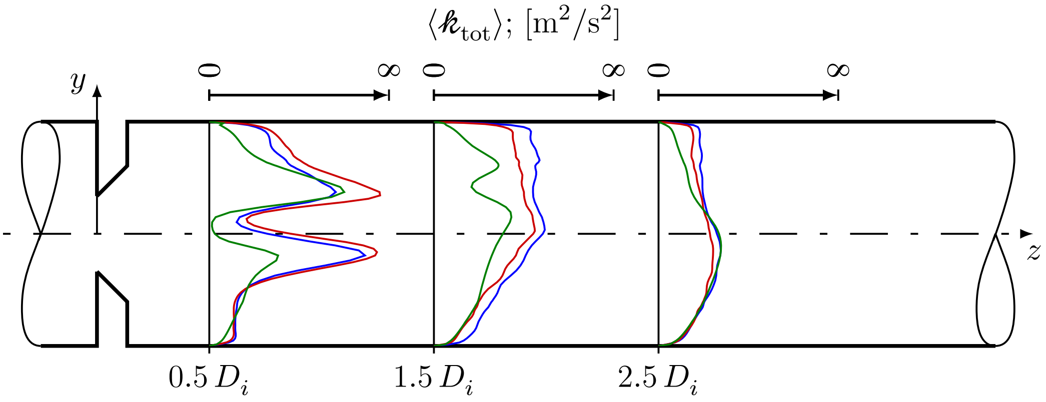

(a) (z-) positions: $0.5\,D_i$, $1.5\,D_i$ and $2.5\,D_i$

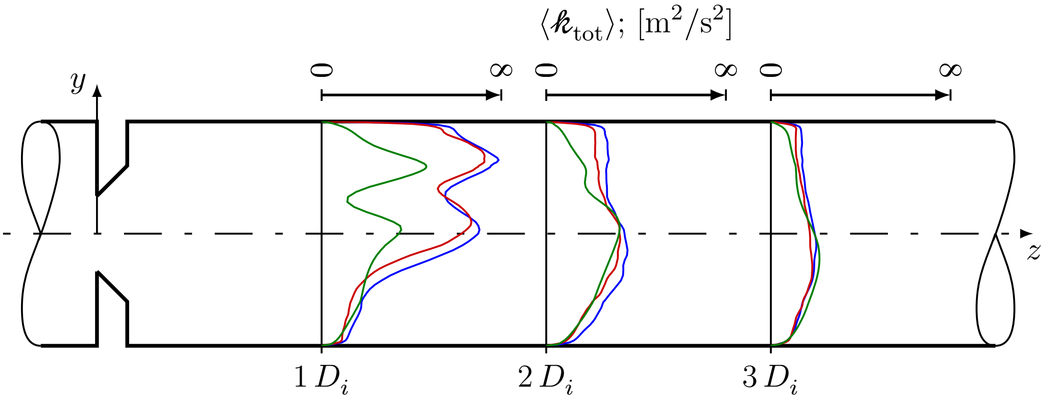

(b) (z-) positions: $1\,D_i$, $2\,D_i$ and $3\,D_i$

— AP_h10Re5300 — AP_h10Re5300F — RANS_h10Re5300

FIGURE 6.19: Comparison of the temporally averaged total turbulence kinetic energy $\langle k_{\mathrm{tot}} \rangle$ [m^2/s^2] along the vertical coordinate y at selected downstream (z-) positions between LES and RANS at $\mathcal{R}e_{D_\mathrm{I}} = 5300$.

Figure 6.19 shows, the temporally averaged total turbulence kinetic energy $\langle k_{\mathrm{tot}} \rangle$ along the vertical coordinate y at different (z-) positions for the cases

AP_h10Re5300, AP_h10Re5300F and RANS_h10Re5300. The profiles essentially show the trends in more detail as already observed for the corresponding contours presented in figure 6.18. Concerning the effect of the refined computational grid the observations somewhat differ downstream of position $z = 1\,D_\mathrm{I}$. The case AP_h10Re5300F (GAP_h10F) exhibits lower turbulence kinetic energy than the case with the coarser computational grid AP_h10Re5300 (GAP_h10). The rather unexpected tendency might be due to the fact, that a refined resolution also leads to an inherently more accurate description of the turbulence dissipation rate. The dissipative loss might be effectively higher, reducing the intensity of the resolved turbulent motion.

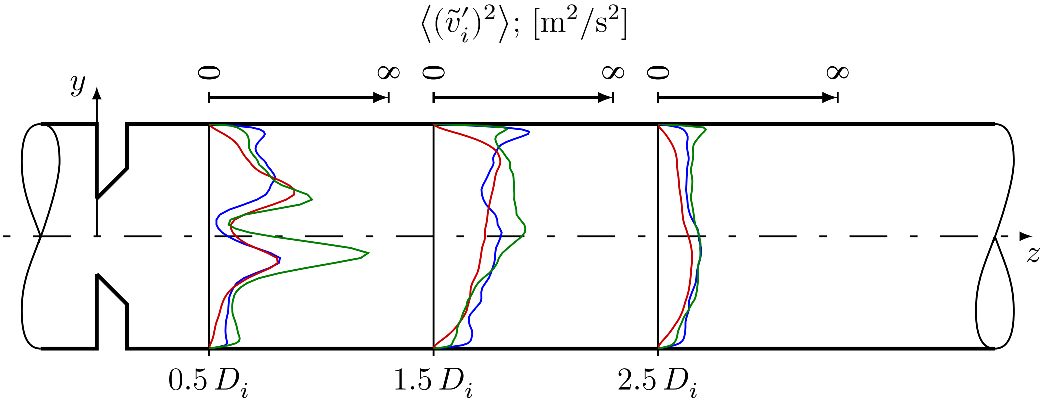

(a) (z-) positions: $0.5\,D_i$, $1.5\,D_i$ and $2.5\,D_i$

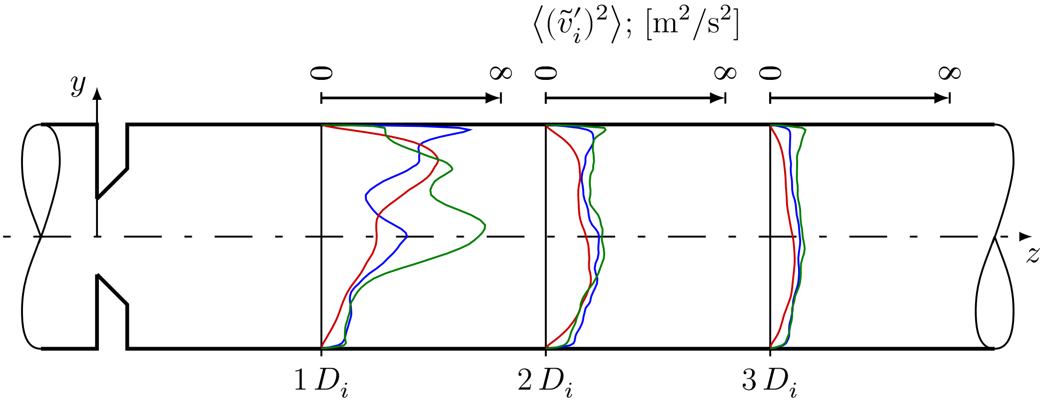

(b) (z-) positions: $1\,D_i$, $2\,D_i$ and $3\,D_i$

— $\langle(\tilde{v}_x')^2\rangle$; — $\langle(\tilde{v}_y')^2\rangle$; — $\langle(\tilde{v}_z')^2\rangle$

Figure 6.20: Comparison of the three components of temporally averaged turbulence velocity fluctuations $\langle(\tilde{v}_i')^2\rangle$ [m^2/s^2] of the case AP_h10Re5300 along the vertical coordinate y at selected downstream (z-) positions.

Figure 6.20 shows the three components of the temporally averaged velocity fluctuations $\langle(\tilde{v}_x')^2\rangle$, $\langle(\tilde{v}_y')^2\rangle$ and $\langle(\tilde{v}_z')^2\rangle$ along the vertical coordinate y at different (z-) positions. The z-component $\langle(\tilde{v}_z')^2\rangle$ of the temporally averaged velocity fluctuations is mostly the largest. Only near the reattachement point of the deflected core jet, the x-component $\left\langle (\widetilde{v}'_x)^2 \right\rangle$ exhibits a larger value close to the wall ($y \rightarrow R_i$). The here observed significant difference of the individual turbulence intensities indicates that the turbulence is quite anisotropic, especially close to the orifice.

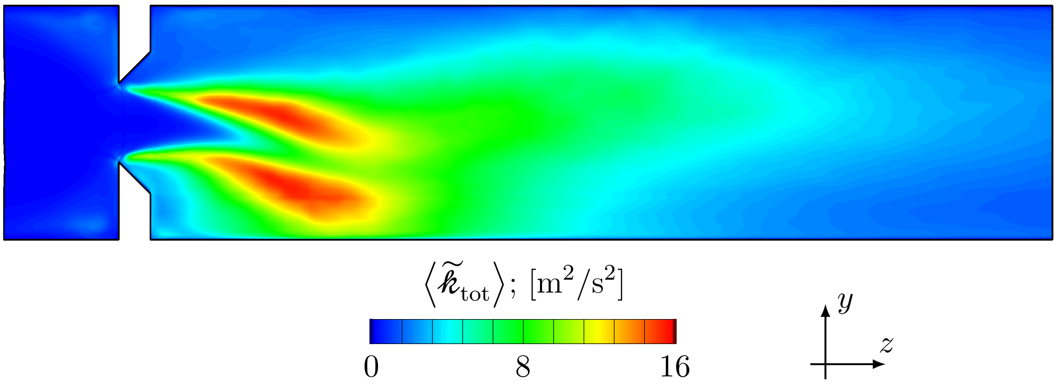

(a) $\left\langle \widetilde{k}_{\mathrm{tot}} \right\rangle$ of case AP_h10Re7400

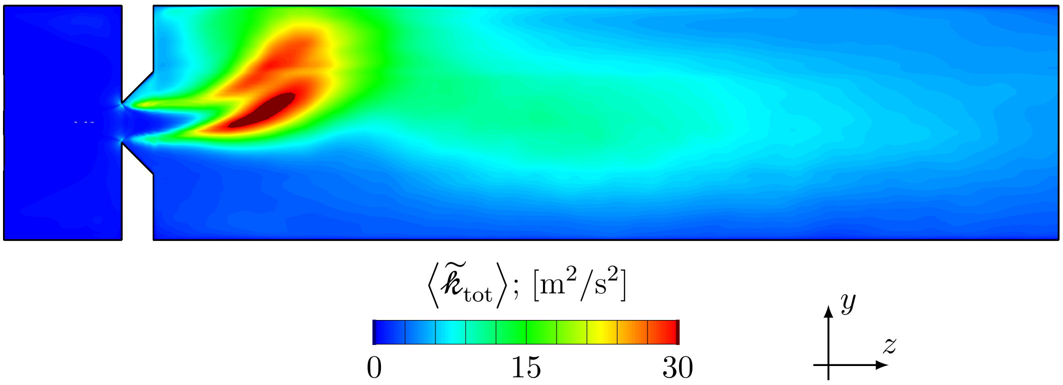

(b) $\left\langle \widetilde{k}_{\mathrm{tot}} \right\rangle$ of case AP_h5Re5300

FIGURE 6.21: Comparison of contours of the temporally averaged total turbulence kinetic energy field $\left\langle \widetilde{k}_{\mathrm{tot}} \right\rangle$ [m^2/s^2] between acoustic pipe LES at $\mathcal{Re}_{D_\mathrm{I}} = 7400$ AP_h10Re7400 and $h_\mathrm{O} = h_5 = 5\,\mathrm{mm}$ AP_h5Re5300.

Figure 6.21 compares the contours of the temporally averaged total turbulence kinetic energy $\left\langle \widetilde{k}_{\mathrm{tot}} \right\rangle$ for the cases AP_h10Re7400 and AP_h5Re5300 to examine the effects of the increased Reynolds number to $\mathcal{Re}_{D_\mathrm{I}} = 7400$ and the reduction of the gap height h_O to $h_5 = 5\,\mathrm{mm}$ of the orifice, respectively. In both cases, the turbulence increases significantly, especially for the case AP_h5Re5300, associated with the reduced gap hight h_O of the orifice. Based on this observation, one might certainly expect that the case AP_h5Re5300 should deliver the most intense aeroacoustic source term, followed in second place by the case AP_h10Re7400, associated with the increase in the Reynolds number. Case AP_h10Re5300F might deliver slightly higher aeroacoustic sources, as compared to AP_h10Re5300, due to the finer grid resolution. The weakest aeroacoustic sources should be delivered by the UKSG based on case RANS_h10Re5300, which always predicted the lowest levels of turbulence kinetic energy.

Further detailed results for selected local values of the temporally averaged total turbulence kinetic energy $\langle k_{\mathrm{tot}} \rangle$ for all acoustic pipe LES and the RANS simulation are listed in table A.2. For the cases AP_h10Re5300 and AP_h10Re5300F local values of the temporally averaged total turbulence kinetic energy $\left\langle \widetilde{k}_{\mathrm{tot}} \right\rangle$, split into the resolved turbulence kinetic energy $\left\langle \widetilde{k}_{\mathrm{LES}} \right\rangle$ and the modeled turbulence kinetic energy $\left\langle \widetilde{k}_{\mathrm{SGS}} \right\rangle$ are listed in table A.3.

6.2.5 The instantaneous vorticity field downstream the orifice

Alike the turbulence kinetic energy the resolved vorticity might be used as a suitable indicator for identifying the regions of intense generation of flow induced sound.

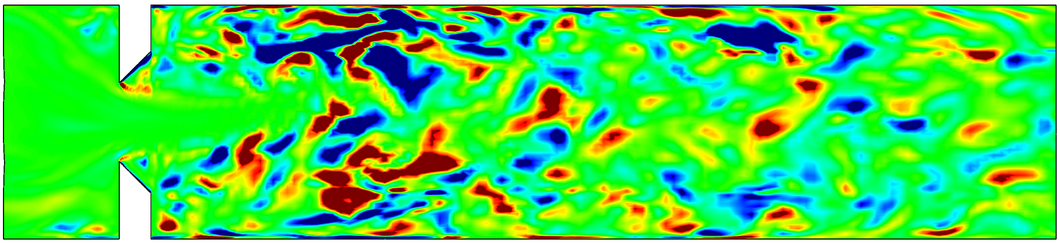

(a) Case AP_h10Re5300 at $t_{\mathrm{end}} = 1.2\,\mathrm{s}$

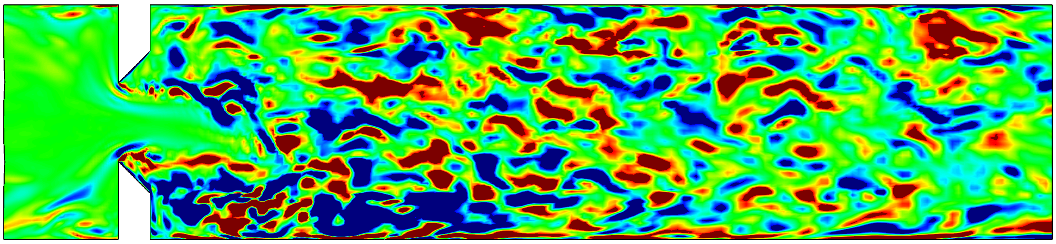

(b) Case AP_h10Re7400 at $t_{\mathrm{end}} = 0.8\,\mathrm{s}$

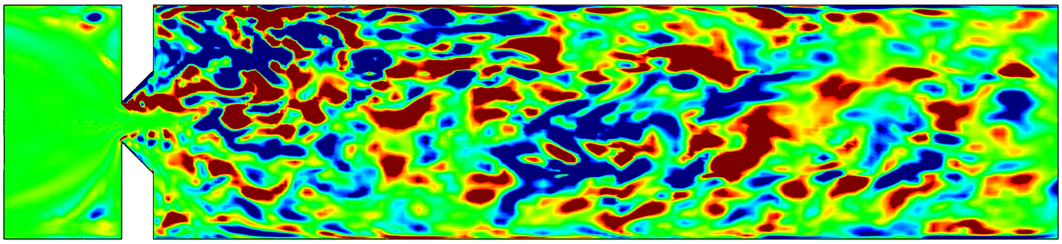

(c) Case AP_h5Re5300 at $t_{\mathrm{end}} = 1.2\,\mathrm{s}$

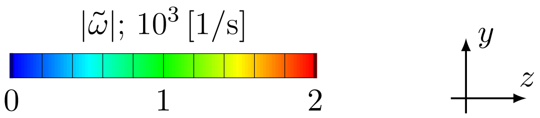

Figure 6.22: Comparison of contours of the instantaneous vorticity field $|\tilde{\omega}|$ [1/s] of the acoustic pipe LES at $t = t_{\mathrm{end}}$.

Figure 6.22 shows instantaneous contours of the magnitude of the instantaneous vorticity $|\tilde{\omega}|$ for the LES cases AP_h10Re5300, AP_h10Re7400 and AP_h5Re5300. Close to the orifice, confined high- vorticity regions emerge, which can be considered as the main aeroacoustic sources region. Eddies emerging from these highly sheared layers are further convected downstream, and merging to larger structures, or decaying. These low-frequency vortical structures convected downstream might not contribute a lot to the aeroacoustic source terms, but might still noticeably affect the propagation of sound waves. In comparison to the case AP_h10Re5300 the emerging eddies seem to be much smaller in case AP_h10Re7400 due to the higher Reynolds number, which might also influence the structure of the aeroacoustic source terms.

6.2.6 Investigation of aeroacoustic key quantities in the time and frequency domain

To investigate aeroacoustic key quantities (like the aeroacoustic source term $\tilde{\mathcal{S}}_i$) in the time (or frequency) domain, these quantities were stored at every time-step of the LES simulations over one flow-through time at 49 points positioned in a 7×7 rectangular grid pattern covering the main source region for every acoustic pipe LES, as shown in figure 6.23. Whenever referring to these selected individual points in the following sections or chapters, they are always referred to as "GP(col/row)", indicating their column and row numbers as defined in figure 6.23.

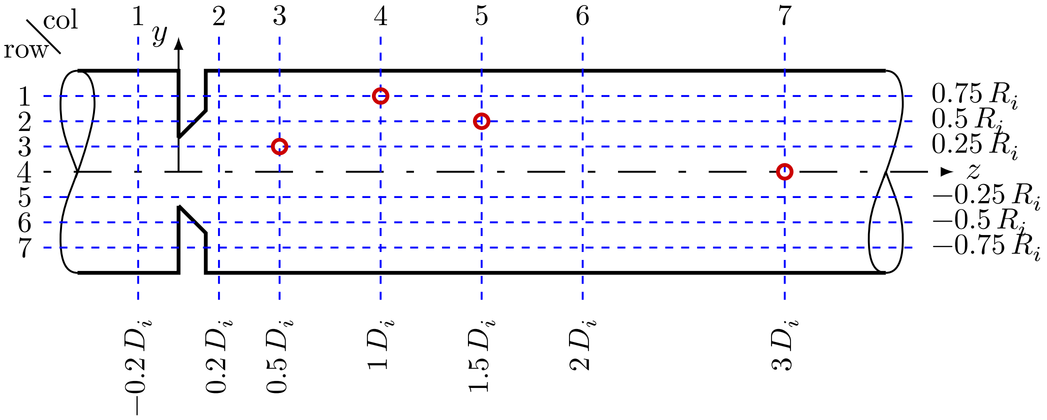

Figure 6.23: The 7×7 grid pattern defining the positions of the selected points.

As already mentioned, the jet-like core flow is always deflected towards one side of the pipe, leading to an asymmetric flow field. Therefore, when comparing acoustic pipe LES, where the jet-like core flow attaches at the upper or lower sides of the pipe, the row numbers in the case with the jet attaching at the bottom side ($y < 0$) are flipped. E.g. the results from cell at column 4 and row 2 GP(4/2) form case X (with a jet attached at the top ($y > 0$)) is compared to the data from the cell at column 4 and row 6 GP(4/6) of case Y (with a jet attached at the bottom ($y < 0$)), using always the notation GP(4/2). This ensures that only points with equivalent underlying flow characteristics are compared. In the tables in appendix A the data for the simulations with the core jet-flow attaching at the bottom ($y < 0$) are consistently flipped.

For further detailed discussions, four special grid points downstream of the orifice were chosen from the 7×7 grid pattern. They are highlighted in figure 6.23. These particular positions were chosen for following reasons.

- GP(3/3) is located inside the core jet-flow between the shear layers with high anisotropic turbulence 0.5 diameter downstream of the orifice,
- GP(4/1) is close to the reattachment point of the core jet-flow with high deformation and high anisotropic turbulence, as observed one diameter downstream of the orifice,
- GP(5/2) is further downstream of the orifice with still anisotropic turbulence but already inside the less sheared region 1.5 diameters downstream of the orifice,
- GP(7/4) is at the center of the acoustic pipe three diameters downstream of the orifice with less turbulence kinetic energy and almost isotropic turbulence.

6.2.7 Turbulence time-scales

In this section, the results of the computed turbulence time-scales, introduced in section 3.1.9, are presented. These three investigated turbulence time-scales, rewritten here as

$$\begin{aligned} t_{\mathrm{ST}} &= || \left\langle S_{ij} \right\rangle ||^{-1}, \\ t_{k\varepsilon} &= \frac{k}{\varepsilon}, \\ t_{\mathrm{SW}} &= \frac{\ell_{\mathrm{E}}}{\left\langle v'_{\mathrm{iso}} \right\rangle}, \end{aligned}$$

were computed at all selected points defined by the 7×7 grid pattern, but only the results of the acoustic pipe LES case AP_h10Re5300 in the four selected grid positions GP(3/3), GP(4/1), GP(5/2) and GP(7/4) shall be discussed in detail, which are highlighted in figure 6.23. Results in all 7×7 grid positions are listed in table A.4.

Time-scale: t_{ST}

The time-scale based on the inverse norm of the rate of strain tensor t_{ST} (3.27) was computed with a FIRE™ *Formula*, where the spatial derivatives were computed from the temporally averaged velocity field $\partial \langle \tilde{v}_i \rangle / \partial x_j$ to assemble the temporally averaged rate of strain tensor as

$$\left\langle \tilde{S}_{ij} \right\rangle = \frac{1}{2} \left(\frac{\partial \langle \tilde{v}_i \rangle}{\partial x_j} - \frac{\partial \langle \tilde{v}_j \rangle}{\partial x_i} \right). \tag{6.6}$$

Its norm was then calculated as

$$|| \left\langle \tilde{S}_{ij} \right\rangle || = \sqrt{2 \left\langle \tilde{S}_{ij} \right\rangle \left\langle \tilde{S}_{ij} \right\rangle}, \tag{6.7}$$

so that the resulting time-scale was computed as

$$t_{\mathrm{ST}} = || \left\langle \tilde{S}_{ij} \right\rangle ||^{-1}. \tag{6.8}$$

Time-scale: $t_{k\varepsilon}$

The eddy-turnover time (3.15) was computed from the temporally averaged resolved turbulence kinetic energy $\left\langle \widetilde{k}_{\mathrm{LES}} \right\rangle$ and the resolved turbulence dissipation rate $\tilde{\varepsilon}_{\mathrm{LES}}$ (3.11), which were both computed from the resolved instantaneous velocity fluctuations $\partial v_i' / \partial x_j$ and their derivatives as

$$\left\langle \widetilde{k}_{\mathrm{LES}} \right\rangle = \frac{1}{2} \left(\langle (\tilde{v}_x')^2 \rangle + \langle (\tilde{v}_y')^2 \rangle + \langle (\tilde{v}_z')^2 \rangle \right) \quad \text{and} \tag{6.9a}$$

$$\tilde{\varepsilon}_{\mathrm{LES}} = \nu_{\mathrm{ref}} \left\langle \frac{\partial \tilde{v}_i'}{\partial x_k} \frac{\partial \tilde{v}_i'}{\partial x_k} \right\rangle, \tag{6.9b}$$

and the resulting eddy-turnover time was computed as

$$t_{k\varepsilon} = \frac{\left\langle \widetilde{k}_{\mathrm{LES}} \right\rangle}{\tilde{\varepsilon}_{\mathrm{LES}}} \tag{6.10}$$

The instantaneous resolved velocity fluctuations $\tilde{v}_i'$ were computed directly during the simulation by subtracting the ensemble average (3.70) $\langle \tilde{v}_i \rangle_{\mathrm{ea}}$ from the instantaneous resolved velocities $\tilde{v}_i$

$$\tilde{v}_i' = \tilde{v}_i - \langle \tilde{v}_i \rangle$$

Time-scale: t_{SW}

The sweeping time t_{SW} (3.29) was computed from the temporally averaged resolved turbulence kinetic energy $\left\langle \widetilde{k}_{\mathrm{LES}} \right\rangle$ (6.9a)

$$\left\langle \tilde{v}'_{\mathrm{iso}} \right\rangle = \left(\frac{2}{3} \left\langle \widetilde{k}_{\mathrm{LES}} \right\rangle \right)^{1/2}, \tag{6.11}$$

assuming isotropic turbulence, and using the gap height h_{O} of the orifice as the characteristic length-scale $\ell_{\mathrm{E}} = h_{10} = 10\,\mathrm{mm}$, such that

$$t_{\mathrm{SW}} = \frac{h_{10}}{\left\langle \tilde{v}'_{\mathrm{iso}} \right\rangle}. \tag{6.12}$$

Time-scales: results and comparison

Table 6.3: The resulting time-scales t and corresponding frequencies f_t of case AP_h₁₀Re₅₃₀₀ at four selected grid positions in the 7×7 pattern (see figure 6.23).

col	row	t_{ST} [s]	$t_{k\varepsilon}$ [s]	t_{SW} [s]	f_{ST} [Hz]	$f_{k\varepsilon}$ [Hz]	f_{SW} [Hz]
3	3	3.95×10^{-4}	2.29×10^{-2}	6.22×10^{-3}	2534.55	43.60	160.85
4	1	9.98×10^{-4}	2.24×10^{-3}	4.51×10^{-3}	1001.59	447.40	221.62
5	2	4.23×10^{-3}	1.40×10^{-3}	5.69×10^{-3}	236.38	714.73	175.89
7	4	4.01×10^{-3}	7.12×10^{-3}	8.73×10^{-3}	249.35	140.38	114.54

From the obtained results, listed in table 6.3 the following conclustions are obtained. As expected, the time-scale based on the averaged rate of strain tensor t_{ST}, which should generally deliver the largest time-scales, are the smallest since the gradients of the temporally averaged velocity field close to the shear layers produced by the orifice are indeed very high, especially at the points GP(3/3) and GP(4/1), thus resulting in high frequencies f_{ST} at this grid positions. As a result, applying temporal filters with the time-scale t_{ST} would remove not only large low-frequency vortical structures, but also high frequency content, thus removing highly relevant contributions to the aeroacoustic sources.

Comparing the eddy turnover time $t_{k\varepsilon}$ to the sweeping time t_{SW} at the four selected grid positions, the eddy turnover time delivers smaller time-scales in almost every grid point except GP(3/3). Thus, when the temporal filters are applied, the eddy turnover time $t_{k\varepsilon}$ would cut-off also higher frequencies.

Since the target of applying temporal filters to the aeroacoustic source terms is to remove large low-frequency vortical structures the sweeping time t_{SW} was chosen as the most suitable time-scale, since it delivered generally the largest time-scales in the whole source region downstream of the orifice (also see table A.4). Note that the hearing range of humans starts at approximately $f_{\mathrm{low}} \approx 20\,\mathrm{Hz}$ (see section 2.1), thus with the applied time-scale at approximatelly $f_{\mathrm{SW}} \approx 200\,\mathrm{Hz}$ also hearable frequencies are cut-off from the aeroacoustic source term, which might indicate that the sweeping time is also not the ideal time-scale. Furthermore, isotropic turbulence was assumed for the sweeping time, which is close to the orifice not fulfilled, as already observed and discussed (see figure 6.20).

Time-scale: $t_{\mathcal{K}}$

Using the resolved turbulence dissipation rate also the Kolmogorov time-scale (3.18a), rewritten as

$$t_{\mathcal{K}} = \left(\frac{\nu_{\mathrm{ref}}}{\tilde{\varepsilon}} \right)^{1/2}, \tag{6.13}$$

was computed, where the results for the four selected points are listed in table 6.4. Note that the obtained frequencies $f_{\mathcal{K}} = 1/t_{\mathcal{K}}$ are, as mandatory, higher then the turbulence time-scales listed in table 6.3, since the Kolmogorov scales represent the smalles scales of turbulence.

TABLE 6.4: The resulting Kolmogorov time-scale $t_{\mathcal{K}}$ and the corresponding frequencies $f_{\mathcal{K}}$ of case AP_h10Re5300 at four points selected from the 7×7 grid pattern (see figure 6.23).

col	row	$t_{\mathcal{K}}$ [s]	$f_{\mathcal{K}}$ [Hz]
3	3	3.53×10^{-4}	2831.88
4	1	1.94×10^{-4}	5145.97
5	2	3.01×10^{-4}	3324.23
7	4	5.77×10^{-4}	1732.73

6.2.8 Turbulence kinetic energy spectrum

Figure 6.24 shows the turbulence kinetic energy spectrum $|\Psi_{f}| = |\mathcal{F}(\widetilde{k}(t)))|$, obtained from a fourier analysis of the instantaneous resolved turbulence kinetic energy $\widetilde{k}_{\mathrm{LES}}(t)$ of case AP_h10Re5300 computed as

$$\widetilde{k}_{\mathrm{LES}}(t) = \frac{1}{2}\left((\tilde{v}'_x(t))^2 + (\tilde{v}'_y(t))^2 + (\tilde{v}'_z(t))^2\right). \tag{6.14}$$

Additionally, the turbulent time-scales $t_{k\varepsilon}$ (3.15), t_{SW} (3.29) taken from table 6.3 and $t_{\mathcal{K}}$ (6.13) from table 6.4 are marked. The shown time-scales are consitent with the turbulence kinetic energy spectrum $|\Psi_{f}| = |\mathcal{F}(\widetilde{k}_{\mathrm{LES}}(t)))|$, where the Kolmogorov time-scale $t_{\mathcal{K}}$ evidently represents the highest resolved frequencies and the eddy turnover time $t_{k\varepsilon}$ as well as the sweeping time t_{SW} obviously represent the regions with high amplitudes. Further note that the present turbulence kinetic energy spectra contains large low-frequency contributions with high amplitudes, which implies that the turbulence field contains vortical structures, which are convected downstream the orifice.

Altough the time-step $\Delta t = 5\times10^{-4}$ s of the acoustic pipe LES allows resolving frequencies up to $f_{\mathrm{H}} = 10\,\mathrm{kHz}$, limited by the Nyquist criterion (see section 2.1), only frequencies up to the Kolmogorov scales were resolved, due to the incompressible flow model used for solving the governing Navier-Stokes equations equations. As a result the whole turbulence kinetic energy spectrum was at least temporally fully resolved but no acoustic content is included. Consequently, the aeroacoustic source terms obtained from the incompressible LES should therefore not contain a contribution from frequencies above the Kolmogorov time-scale $t_{\mathcal{K}}$.

Basically, the SGS model has the task to dissipate the smallest resolved scales down to the Kolmogorov scale. If the contribution of the SGS model is too small, then small turbulent scales are not dissipated but remain. Considering that small turbulent scale are correlated with high frequencies this might result in high amplitudes of the remaining, not dissipated, frequencies close to Kolmogorov time-scale $f \approx f_{\mathcal{K}}$. Such a shortcoming is not observed in the present spectra.

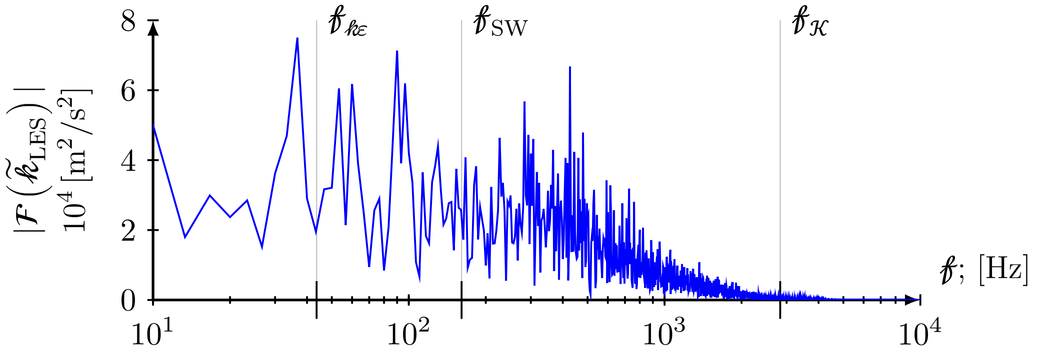

(a) GP(3/3)

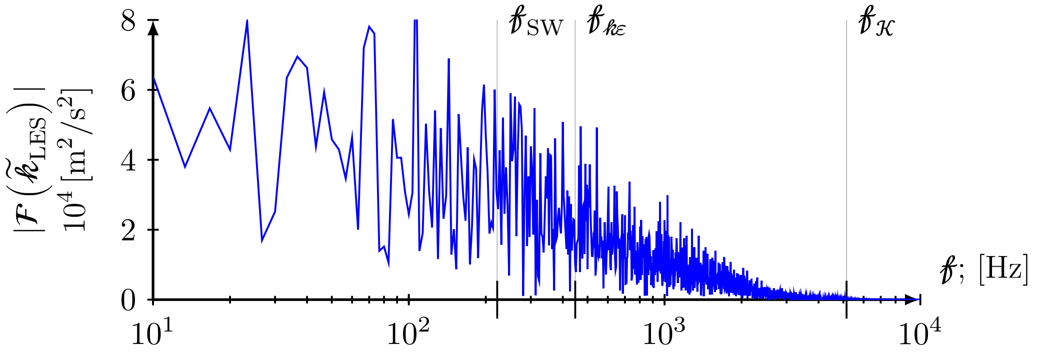

(b) GP(4/1)

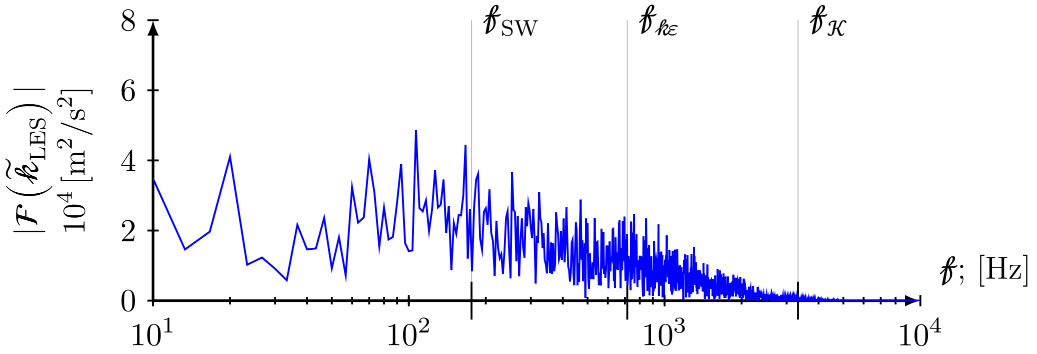

(c) GP(5/2)

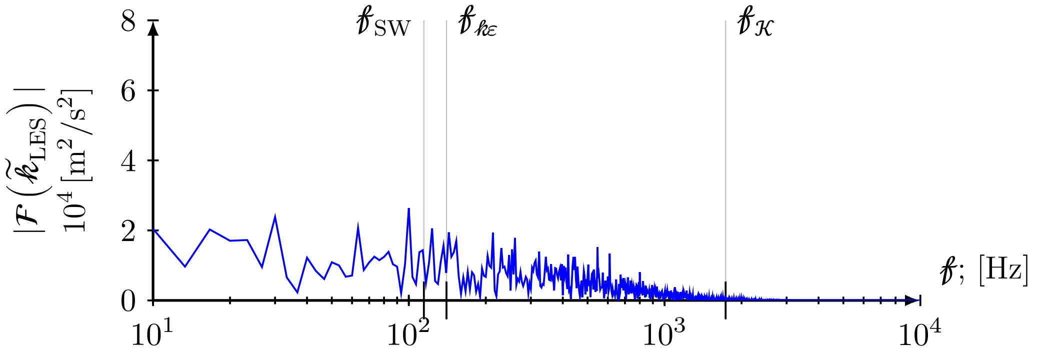

(d) GP(7/4)

FIGURE 6.24: Comparison of the resolved turbulence kinetic energy spectrum $|\Psi_f| = |\mathcal{F}(\widetilde{k}_{\mathrm{LES}})|$ $[\mathrm{m^2/s^2}]$ of case AP_h10Re5300 at the four selected grid positions (see figure 6.23).

7 Aeroacoustic sources

In the previous chapter 6, the solutions of the incompressible CFD simulations, the basis of the aeroacoustic source terms, was presented. Using these simulated flow fields, the aeroacoustic source terms, as derived in chapter 4, were computed as field variables and stored at the 7×7 grid positions, defined in section 6.2.6 (see figure 6.23), over the period of one flow-through time. From these 7×7 available grid positions the results of four specially selected grid positions, GP(3/3), GP(4/1), GP(5/2) and GP(7/4), circled in figure 6.23, being well representative for the main flow features of the flow field downstream of the orifice (see section 6.2.6), are examined in further detail.

In section 7.1 the results of the main aeroacoustic source terms for the momentum equation of the LEE $\mathcal{S}_i$ and Ω_i is presented and discussed. The approaches to exclude the contribution of large low-frequency vortical structures, will be examined as well. Finally, the cross-terms, which appear as additional aeroacoustic source terms in the momentum equation of the LEE Λ_i, which are considered in the CAA module of FIRE™, are discussed. In section 7.2 the cross-term appearing in the energy equation of the LEE Π_i computed from the LES solution is compared to the equivalent cross-term generated by the UKSG within the RANS-based CAA tool of FIRE™.

7.1 The aeroacoustic source terms computed from LES

The representation of the main aeroacoustic source term appearing on the RHS of the LEE formulation equation (4.31) shall be considered first. Using the resolved LES results the main aeroacoustic source term is rewritten as

$$\widetilde{\Omega}'_{i,\mathrm{LES}} = \underbrace{\tilde{v}'_j \frac{\partial \tilde{v}'_i}{\partial x_j}}_{\tilde{\mathcal{S}}_{i,\mathrm{LES}}} - \underbrace{\left\langle \tilde{v}'_j \frac{\partial \tilde{v}'_i}{\partial x_j} \right\rangle}_{\left\langle \tilde{\mathcal{S}}_{i,\mathrm{LES}} \right\rangle} . \tag{7.1}$$

We recall at this point, that the subtraction of the mean $\left\langle \tilde{\mathcal{S}}_{i,\mathrm{LES}} \right\rangle$ basically follows from the rigorous derivation of the LEE. The full formulation of the LEE (4.31) contains the Reynolds averaged momentum equations as subset, introducing the divergence of the Reynolds stresses represented by $\left\langle \tilde{\mathcal{S}}_{i,\mathrm{LES}} \right\rangle$. Other authors interpreted this term rather as an important modification of the instantaneous representation, which effectively centers the signal, so that its statistical average becomes identically zero $\left\langle \widetilde{\Omega}'_{i,\mathrm{LES}} \right\rangle = 0$. Bogey et al. [17] argued that this centering avoids the generation of non-physical large-amplitude signals, which might, especially, when reflected at solid boundaries, seriously contaminate the acoustic sound field. The present analysis of the LES-based aeroacoustic source terms addresses this particular aspect as well, discussing first the contributions of the instantaneous components $\tilde{\mathcal{S}}_{i,\mathrm{LES}}$, thereafter demonstrating the effect of the modification with the mean value.

7.1.1 Instantaneous aeroacoustic source terms $\tilde{\mathcal{S}}_{i,\mathsf{LES}}$ for momentum

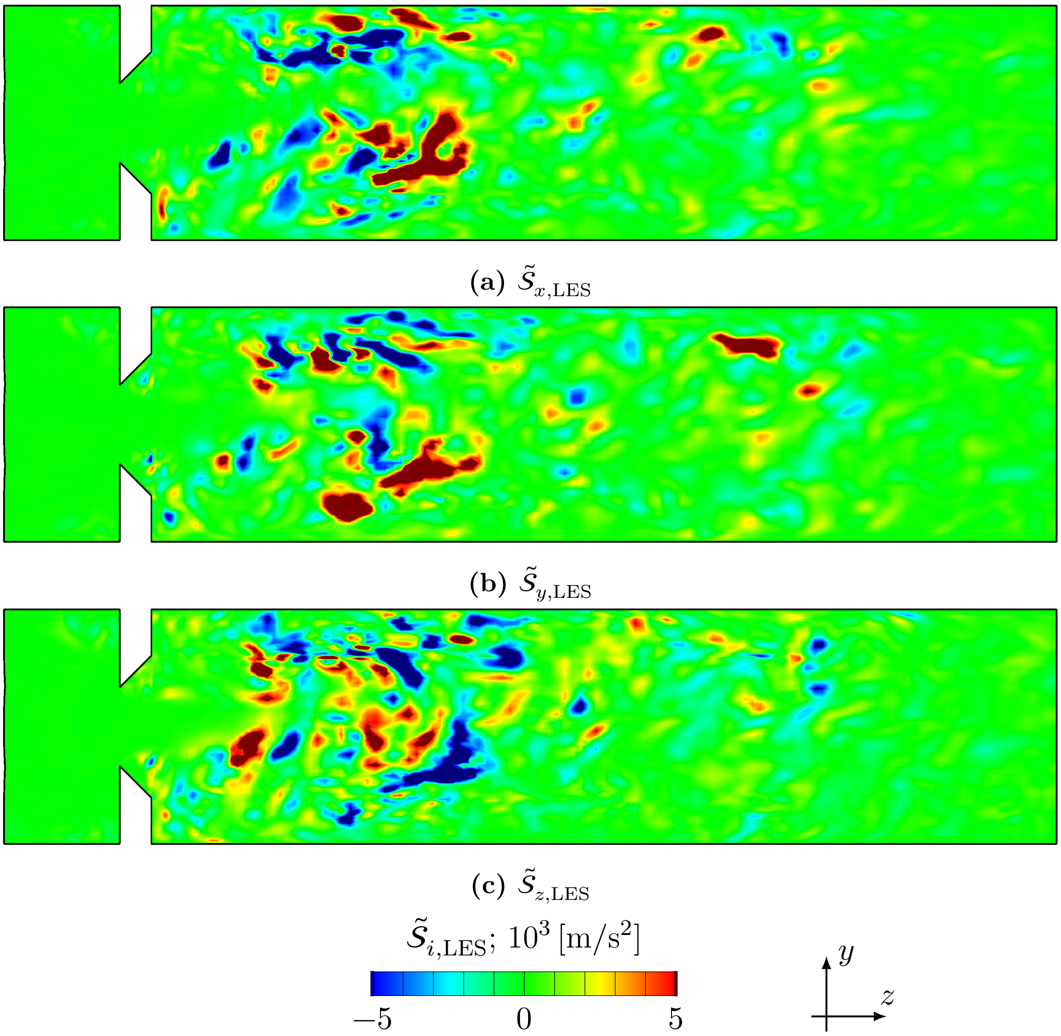
(a) $\tilde{\mathcal{S}}_{x,\mathrm{LES}}$

(b) $\tilde{\mathcal{S}}_{y,\mathrm{LES}}$

(c) $\tilde{\mathcal{S}}_{z,\mathrm{LES}}$

Figure 7.1: Contours of the three instantaneous aeroacoustic source term components $\tilde{\mathcal{S}}_{i,\mathrm{LES}}$ [m/s^2] of case AP_h10Re5300 at $t_{\mathrm{end}} = 1.2$ s.

Figure 7.1 exemplarily shows contours of the three components of the aeroacoustic source term $\tilde{\mathcal{S}}_{i,\mathrm{LES}}$ for the case AP_h10Re5300 at $t_{\mathrm{end}} = 1.2$ s.

Each component basically consists of three terms, written as

$$\mathcal{S}_x = \tilde{v}'_x \frac{\partial \tilde{v}'_x}{\partial x} + \tilde{v}'_y \frac{\partial \tilde{v}'_x}{\partial y} + \tilde{v}'_z \frac{\partial \tilde{v}'_x}{\partial z}, \tag{7.2a}$$

$$\mathcal{S}_y = \tilde{v}'_x \frac{\partial \tilde{v}'_y}{\partial x} + \tilde{v}'_y \frac{\partial \tilde{v}'_y}{\partial y} + \tilde{v}'_z \frac{\partial \tilde{v}'_y}{\partial z} \quad \text{and} \tag{7.2b}$$

$$\mathcal{S}_z = \tilde{v}'_x \frac{\partial \tilde{v}'_z}{\partial x} + \tilde{v}'_y \frac{\partial \tilde{v}'_z}{\partial y} + \tilde{v}'_z \frac{\partial \tilde{v}'_z}{\partial z}, \tag{7.2c}$$

using the resolved turbulent velocity fluctuations $\tilde{v}'_i$, as generally defined by (4.60)

None of the three components seem to be dominant and all of them appear in the same region downstream of the orifice. As one might expect, very intense aeroacoustic sources are mainly generated inside the highly sheared boundary layer between the inner core jet emerging from the orifice and the two separated flow regions in the wake of the upper and lower wall of the orifice.

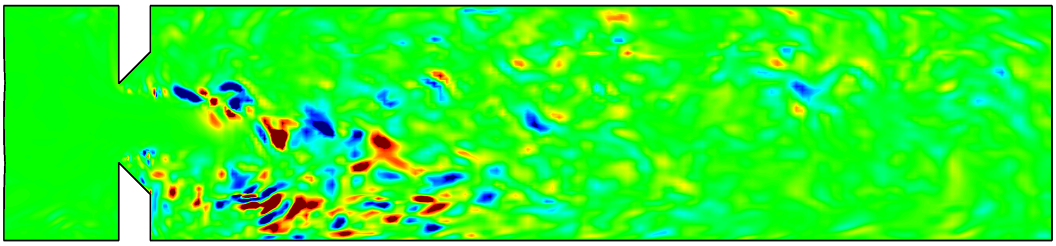

(a) $\tilde{\mathcal{S}}_{x,\mathrm{LES}}$

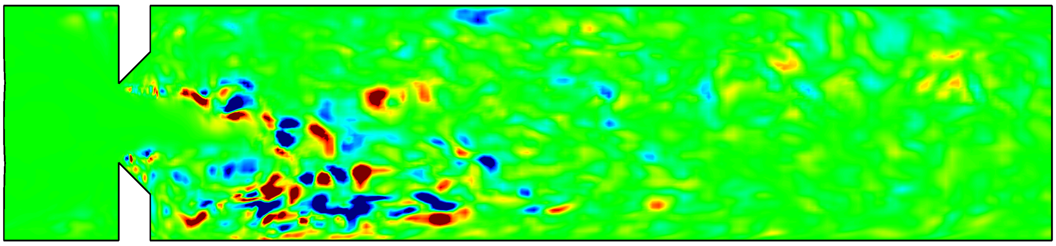

(b) $\tilde{\mathcal{S}}_{y,\mathrm{LES}}$

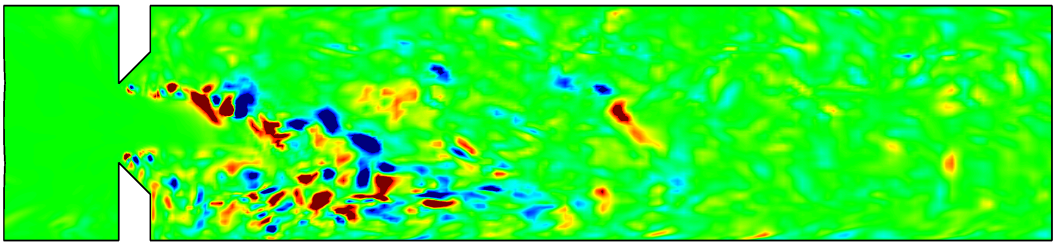

(c) $\tilde{\mathcal{S}}_{z,\mathrm{LES}}$

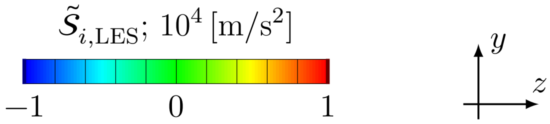

FIGURE 7.2: Contours of the three instantaneous aeroacoustic source term components $\tilde{\mathcal{S}}_{i,\mathrm{LES}}$ [m/s^2] of case AP_h10Re7400 at $t_{\mathrm{end}} = 1.2$ [s].

Figure 7.2 shows the contours of the aeroacoustic source term components $\tilde{\mathcal{S}}_{i,\mathrm{LES}}$ for case AP_h10Re7400, representing the case with higher Reynolds number $\mathcal{Re}_{D_i} = 7400$. Note that the magnitude of the aeroacoustic source terms is significantly higher then for the case with the lower Reynolds number shown in figure 7.1. Furthermore, the structures seem to be much finer in the case AP_h10Re7400 than in AP_h10Re5300, which corresponds to the predicted vorticity fields already discussed in section 6.2.5.

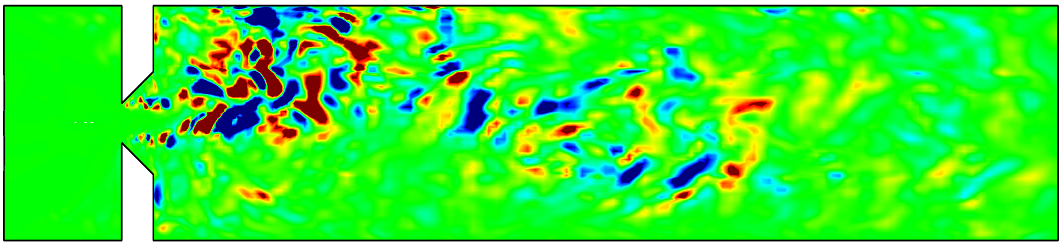

(a) $\tilde{S}_{x,\mathrm{LES}}$

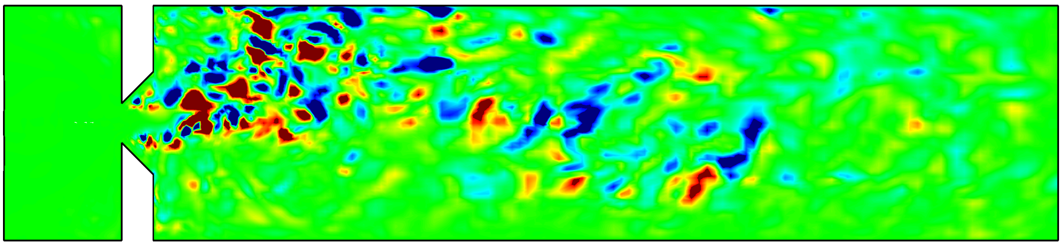

(b) $\tilde{S}_{y,\mathrm{LES}}$

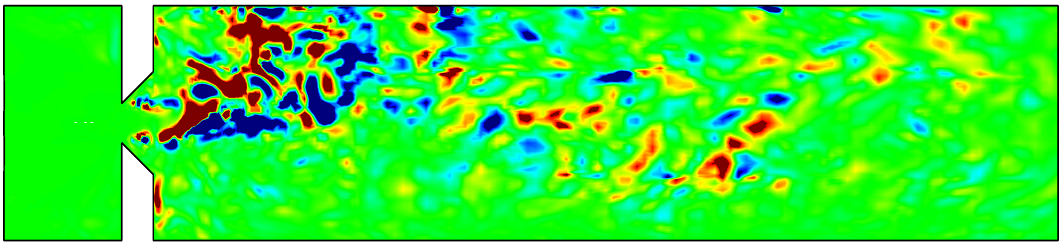

(c) $\tilde{S}_{z,\mathrm{LES}}$

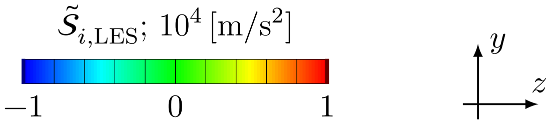

Figure 7.3: Contours of the three instantaneous aeroacoustic source term components $\tilde{\boldsymbol{S}}_{i,\mathrm{LES}}$ [m/s^2] of case AP_h₅Re₅₃₀₀ at $t_{\mathrm{end}} = 0.8$ [s].

The aeroacoustic source terms of the case AP_h₅Re₅₃₀₀, presented in figure 7.3, are obviously much more intense than the aeroacoustic source terms of the cases AP_h₁₀Re₅₃₀₀ and AP_h₁₀Re₇₄₀₀. This is due to the markedly higher shear rate induced by the high velocity $\bar{\boldsymbol{v}}_{\dot{V},h_5}$ of the core jet-flow, emerging from the constriction with the gap height reduced to $h_5 = 5\,\mathrm{mm}$ in case AP_h₅Re₅₃₀₀.

The instantaneous aeroacoustic source terms represent by definition strongly turbulent fluctuating quantities. The intensity of these fluctuations can be statistically quantified by the RMS values, written as

$$\widetilde{\Omega}'_{i,\mathrm{LES,RMS}} = \left\langle \left(\tilde{\boldsymbol{S}}_{i,\mathrm{LES}} - \left\langle \tilde{\boldsymbol{S}}_{i,\mathrm{LES}} \right\rangle \right)^2 \right\rangle^{1/2} . \tag{7.3}$$

Regions with high fluctuation intensities are expectedly zones with intense aeroacoustic sound generation.

Table 7.1: Comparison of the intensity of the centered aeroacoustic source term components $\widetilde{\Omega}'_{i,\mathrm{LES,RMS}}$ [m/s^2] and the temporally averaged total turbulence kinetic energy $\left\langle \widetilde{k}_{\mathrm{tot}} \right\rangle$ at four selected grid positions for cases AP_h10Re5300, AP_h5Re5300 and AP_h10Re7400.

Case:	col	row	$\widetilde{\Omega}'_{x,\mathrm{LES,RMS}}$ [m/s^2]	$\widetilde{\Omega}'_{y,\mathrm{LES,RMS}}$ [m/s^2]	$\widetilde{\Omega}'_{z,\mathrm{LES,RMS}}$ [m/s^2]	$\left\langle \widetilde{k}_{\mathrm{tot}} \right\rangle$ [m^2/s^2]
AP_h10Re5300	3	3	2594.80	2626.20	3042.14	3.88
	4	1	6636.81	6061.40	6180.30	7.37
	5	2	2678.67	2777.82	3353.35	4.64
	7	4	1026.92	954.01	1192.09	1.97
AP_h10Re7400	3	3	7595.34	8302.53	9125.54	8.07
	4	1	13 347.20	12 389.10	12 728.60	13.27
	5	2	5237.87	5187.77	6639.22	7.35
	7	4	2500.52	2292.19	2478.74	3.80
AP_h5Re5300	3	3	19 814.30	20 197.50	22 252.20	26.25
	4	1	16 162.10	15 482.40	15 278.70	18.86
	5	2	6822.64	6929.33	8442.23	9.30
	7	4	3932.42	3678.70	4291.81	6.83

The resulting intensities obtained at the investigated four grid positions for the cases AP_h10Re5300, AP_h10Re7400 and AP_h5Re5300 are listed in table 7.1. At some grid positions the level of RMS-values of case AP_h5Re5300 is more than double the level of case AP_h10Re7400, and more then five times larger than the corresponding level of the case AP_h10Re5300. Also notice that for any case very high intensities occur at grid position GP(4/1) close to the reattachement point of the core jet-flow followed by the the grid position GP(3/3) close to the shear layers. The intensity strongly decreases further downstream of the orifice, as also the temporally averaged turbulence kinetic energy $\left\langle \widetilde{k}_{\mathrm{LES}} \right\rangle$ decreases, as already presented in section 6.2.4. For all 7×7 grid positions and all acoustic pipe LES, the intensity levels are listed in table A.5 and table A.6 in the appendix.

7.1.2 Modification of the aeroacoustic source term for momentum with statistical averages or temporal filtering

The presently discussed statistical averages are always obtained from averaging the resolved instantaneous data over a full flow-through time (FTT), as listed in table 5.6.

Centering with statistical averages

Assuming incompressible flow allows to rewrite the statistical average appearing in equation (7.1) in terms of the divergence of the resolved Reynolds stresses

$$\left\langle \tilde{\mathcal{S}}_{i,\mathrm{LES}} \right\rangle = \frac{\partial \left\langle \tilde{v}_j' \tilde{v}_i' \right\rangle}{\partial x_j}. \tag{7.4}$$

As such, this quantity would vanish in the case of statistically homogeneous turbulent flows. On the other hand, it is expected to be very large in highly sheared or strongly linearly deformed regions.

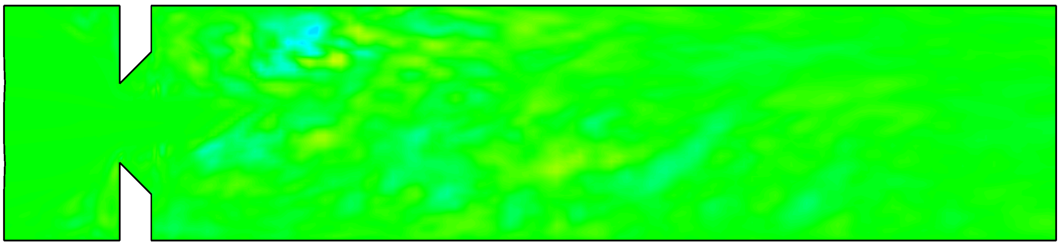

(a) $\left\langle \tilde{\mathcal{S}}_{x,\mathrm{LES}} \right\rangle$

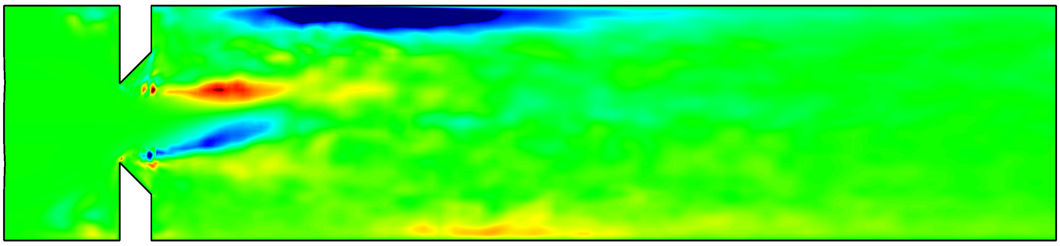

(b) $\left\langle \tilde{\mathcal{S}}_{y,\mathrm{LES}} \right\rangle$

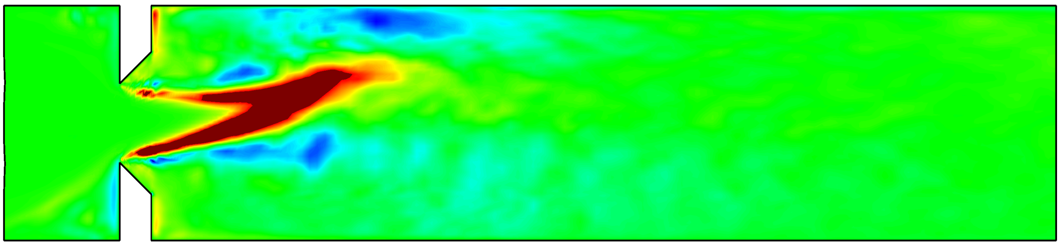

(c) $\left\langle \tilde{\mathcal{S}}_{z,\mathrm{LES}} \right\rangle$

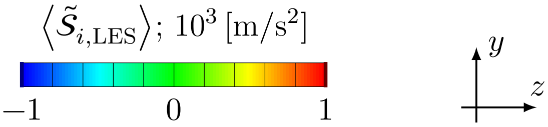

FIGURE 7.4: Contours of the statistical averages of the aeroacoustic source term components $\left\langle \tilde{\mathcal{S}}_{i,\mathrm{LES}} \right\rangle$ for case AP_h10Re5300.

This is clearly seen in figure 7.4, showing contours of the statistically averaged aeroacoustic source term components $\left\langle \tilde{\mathcal{S}}_{i,\mathrm{LES}} \right\rangle$ for the case AP_h10Re5300. The components $\left\langle \tilde{\mathcal{S}}_{y,\mathrm{LES}} \right\rangle$ and $\left\langle \tilde{\mathcal{S}}_{z,\mathrm{LES}} \right\rangle$ exhibit large magnitudes in the shear layers downstream of the two sharp corners of the orifice, and the region near the reattachment point of the core jet-flow. The z-component plays a dominant role, especially in the core jet-flow region. The x-component $\left\langle \tilde{\mathcal{S}}_{x,\mathrm{LES}} \right\rangle$ is in comparison negligibly small, because there is no significant deformation of the base flow into the spanwise direction x.

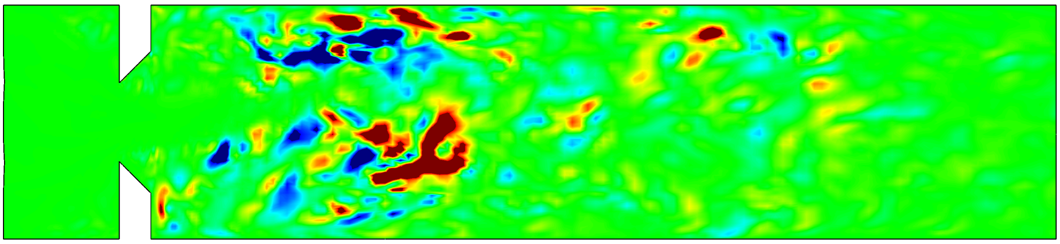

(a) $\widetilde{\Omega}'_{x,\mathrm{LES}}$

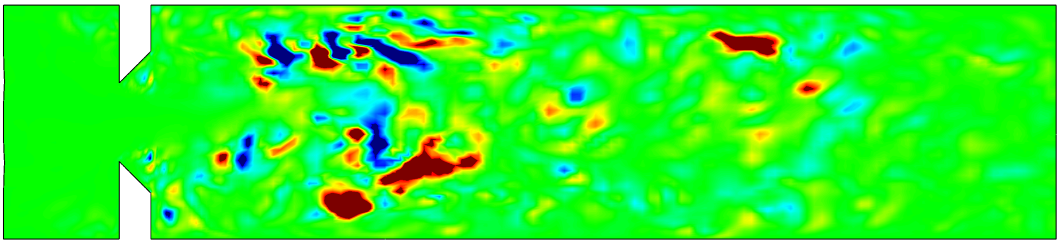

(b) $\widetilde{\Omega}'_{y,\mathrm{LES}}$

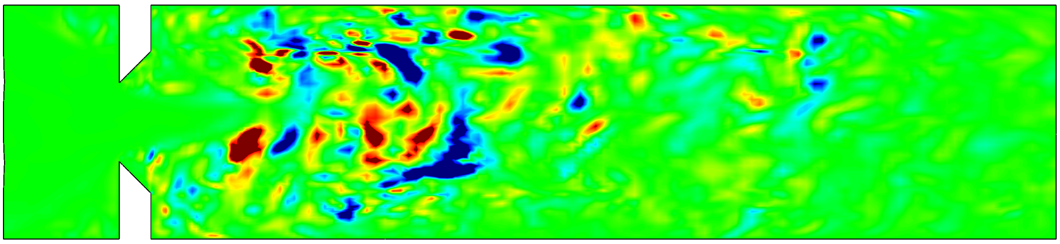

(c) $\widetilde{\Omega}'_{z,\mathrm{LES}}$

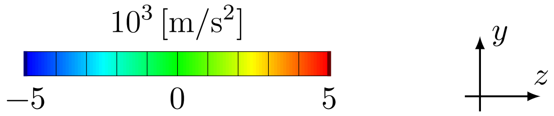

FIGURE 7.5: Contours of the centered instantaneous aeroacoustic source term components $\widetilde{\Omega}'_{i,\mathrm{LES}}$ from case AP_h10Re5300 at $t_{\mathrm{end}} = 1.2\,\mathrm{s}$.

Figure 7.5 shows contours of the centered instantaneous aeroacoustic source term components $\widetilde{\Omega}'_{i,\mathrm{LES}}$, where only in the regions near the core jet-flow and the reattachement point some very small differences are noticeable in comparison to the non-centered instantaneous aeroacoustic source term components $\tilde{\mathcal{S}}_{i,\mathrm{LES}}$ presented in figure 7.1. This is due to the fact that local instantaneous peaks of the aeroacoustic source terms $\tilde{\mathcal{S}}'_{i,\mathrm{LES}}$ are generally significantly higher than their statistical averages $\left\langle \tilde{\mathcal{S}}_{i,\mathrm{LES}} \right\rangle$.

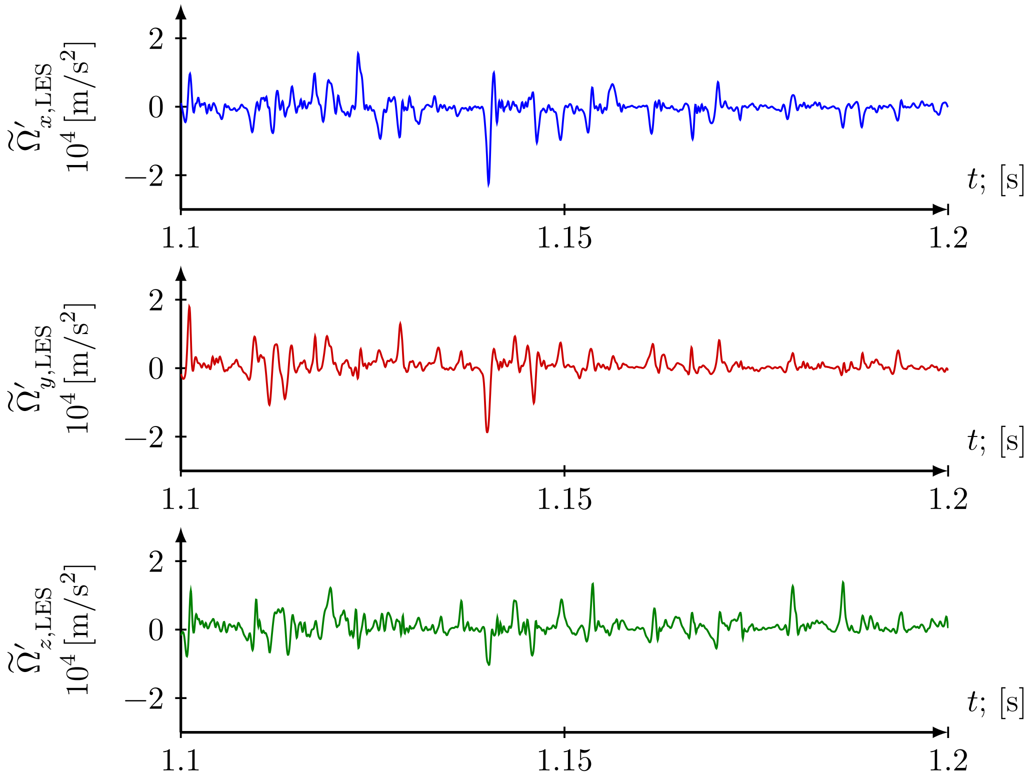

(a) GP(3/3)

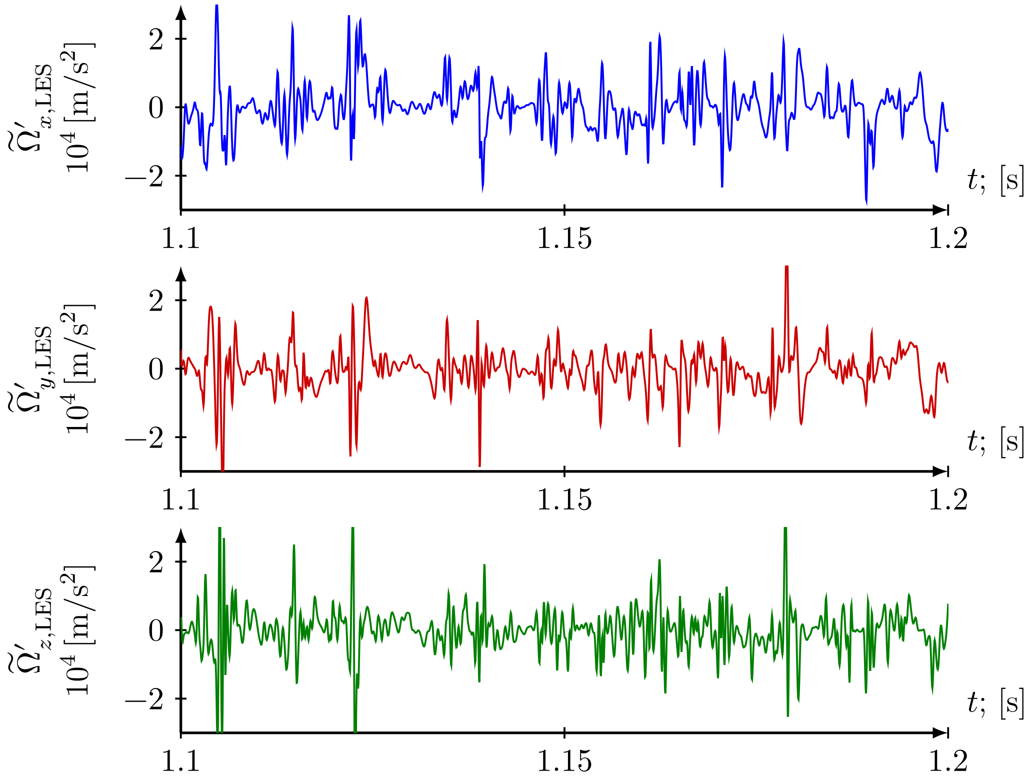

(b) GP(4/1)

FIGURE 7.6: Figure continued and caption on right page.

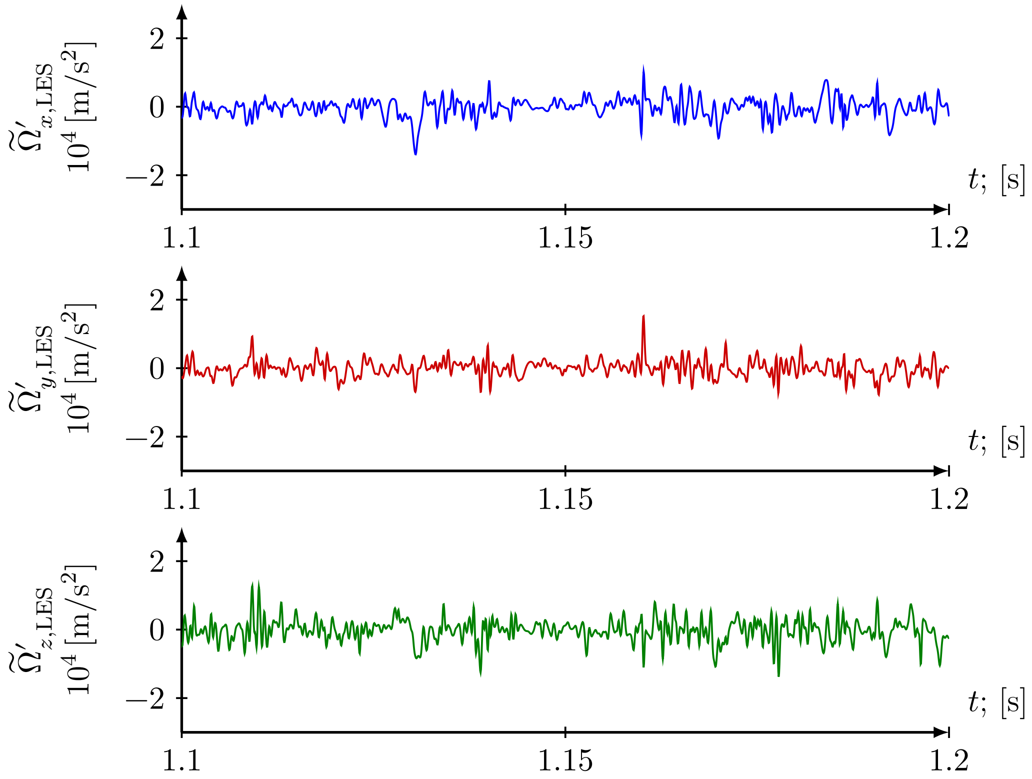

(c) GP(5/2)

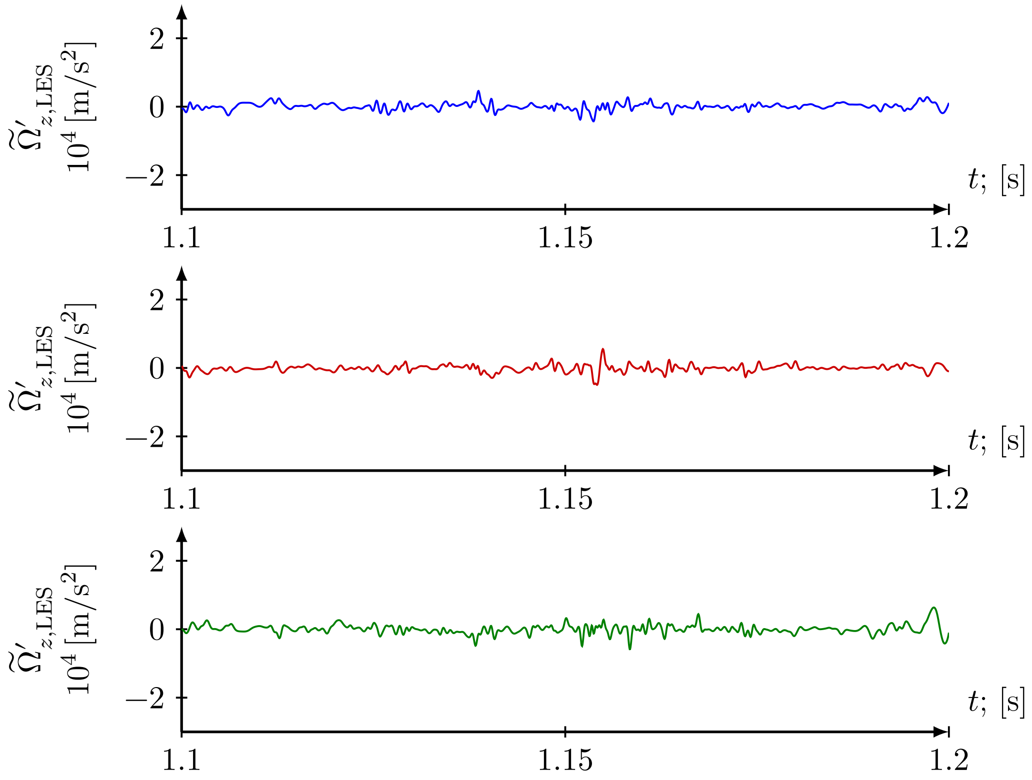

(d) GP(7/4)

Figure 7.6: Histories of centered instantaneous aeroacoustic source term components $\widetilde{\Omega}'_{i,\mathrm{LES}}$ $[\mathrm{m/s^2}]$ at the four selected grid positions for case AP_h10Re5300.

Figure 7.6 shows the history of the aeroacoustic source term components $\widetilde{\Omega}'_{i,\mathrm{LES}}$ over a time-period $T = 0.1\,\mathrm{s}$ at the four selected grid positions. Note the high intensity of the aeroacoustic source terms close to the reattachement point at GP(4/1) due to the large deformation. Also, as already observed from the instantaneous contours in the previous section, none of the three spatial components seem to be dominant and as indicated by the RMS-values in table 7.1. Furthermore, as seen from figure 7.6d the intensity strongly decreases far downstream of the orifice.

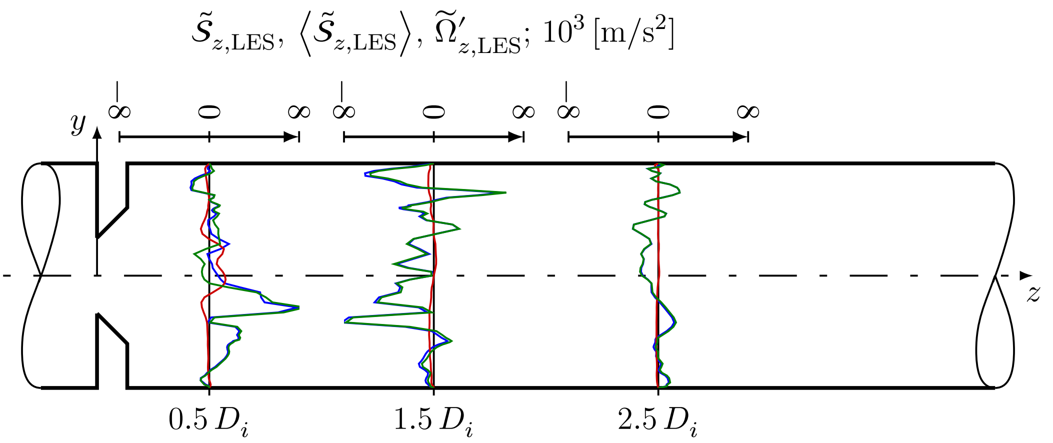

(a) (z-) positions: $0.5\,D_i$, $1.5\,D_i$ and $2.5\,D_i$

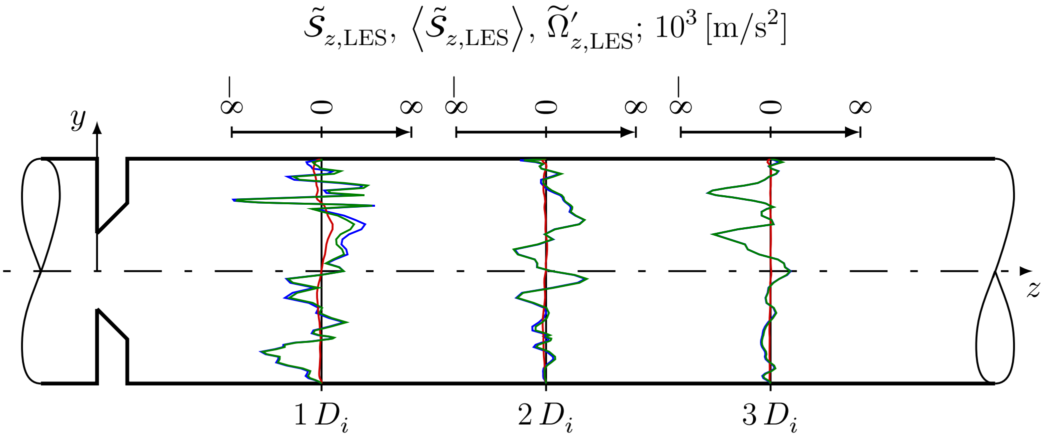

(b) (z-) positions: $1\,D_i$, $2\,D_i$ and $3\,D_i$

— $\tilde{\mathcal{S}}_{z,\mathrm{LES}}$; — $\left\langle \tilde{\mathcal{S}}_{z,\mathrm{LES}} \right\rangle$; — $\widetilde{\Omega}'_{z,\mathrm{LES}}$

Figure 7.7: Comparison of the non-centered $\tilde{\mathcal{S}}_{z,\mathrm{LES}}$, temporal averaged $\left\langle \tilde{\mathcal{S}}_{z,\mathrm{LES}} \right\rangle$ and centered $\widetilde{\Omega}'_{z,\mathrm{LES}}$ aeroacoustic source term z-component along the vertical coordinate y at selected (z-) positions of case AP_h$_{10}$Re$_{5300}$ at $t_{\mathrm{end}} = 1.2\,\mathrm{s}$.

Subtracting the temporal average $\left\langle \tilde{\mathcal{S}}_{i,\mathrm{LES}} \right\rangle$ from the instantaneous representation $\tilde{\mathcal{S}}_{i,\mathrm{LES}}$ effectively centers the total aeroacoustic source terms. The effect on the obtained signal is quantitatively demonstrated in figure 7.7, showing particular profiles of the instantaneous non-centered component $\tilde{\mathcal{S}}_{z,\mathrm{LES}}$, its statistical average $\left\langle \tilde{\mathcal{S}}_{z,\mathrm{LES}} \right\rangle$ as well as the centered component $\widetilde{\Omega}'_{z,\mathrm{LES}}$ for the case AP_h10Re5300, plotted over the vertical coordinate y in the center symmetry plane $x = 0$ at selected downstream (z-) positions. At (z-) positions close to the orifice ($z = 0.5\,\mathrm{D_I}$) the influence of the shear layers bounding the core jet-flow is clearly visible. Also in the region with high linear deformation, close to the upper wall ($y > 0$) at the (z-) positions $z = 1\,\mathrm{D_I}$ and $z = 1.5\,\mathrm{D_I}$ the influence of the centering is noticeable. Further downstream of the orifice the centering effect is much smaller, since the flow is more homogenous, already discussed in section 6.2.4.

Centering with temporal filtering

In the case of free turbulent shear flow, involving large low-frequency vortical structures (e.g. shed in separated flow regions), the absence of strong mean deformation rates typically leads to very small statistical averages $\left\langle \tilde{\mathcal{S}}_{i,\mathrm{LES}} \right\rangle$. The centering, therefore, does not effectively modify the instantaneous component $\tilde{\mathcal{S}}_{i,\mathrm{LES}}$. To investigate the possible contribution of large low-frequency vortical structures to the aeroacoustic source terms the alternative temporal filtering approaches are applied to exclude these structures from the statistics. In contrast to the standard statistical averaging approach these alternative methods might also effectively eliminate low-frequency vortical structures further downstream of the orifice.

The first alternative approach simply subtracts time averages $\left\langle \tilde{\mathcal{S}}_{i,\mathrm{LES}} \right\rangle_{\mathrm{ma}}$ which are computed as moving box averages (see section 3.1.8) over a suitably defined sampling time-frame T_{TF}, according to equation (3.23) .

The second approach applies a spectral filter (see section 3.1.8) to the instantaneous Fourier-transformed components $\Psi_{\mathscr{f}} = \mathcal{F}(\tilde{\mathcal{S}}_{i,\mathrm{LES}})$, using a cut-off frequency $\mathscr{f}_{\mathrm{TF}} = 1/T_{\mathrm{TF}}$, according to equation (3.26). Assuming the sweeping time $\mathscr{t}_{\mathrm{SW}}$ as relevant time-scale of the large low-frequency vortical structures (see section 3.1.9) both approaches are supposed to reduce or even eliminate contributions from large low-frequency vortical sturctures associated with the sweeping time $\mathscr{t}_{\mathrm{SW}}$ and beyond in the transient signal $\tilde{\mathcal{S}}_{i,\mathrm{LES}}$.

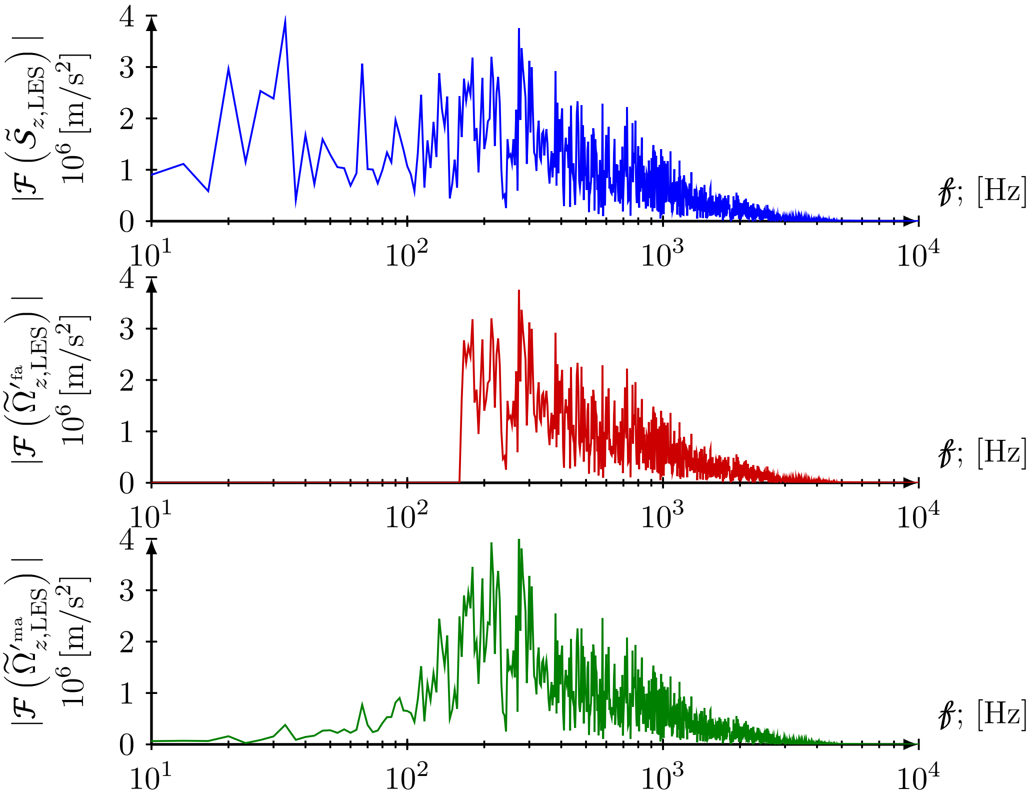

(a) GP(3/3) : $\not{f}_{\mathrm{SW}} = 160.85\,\mathrm{Hz}$

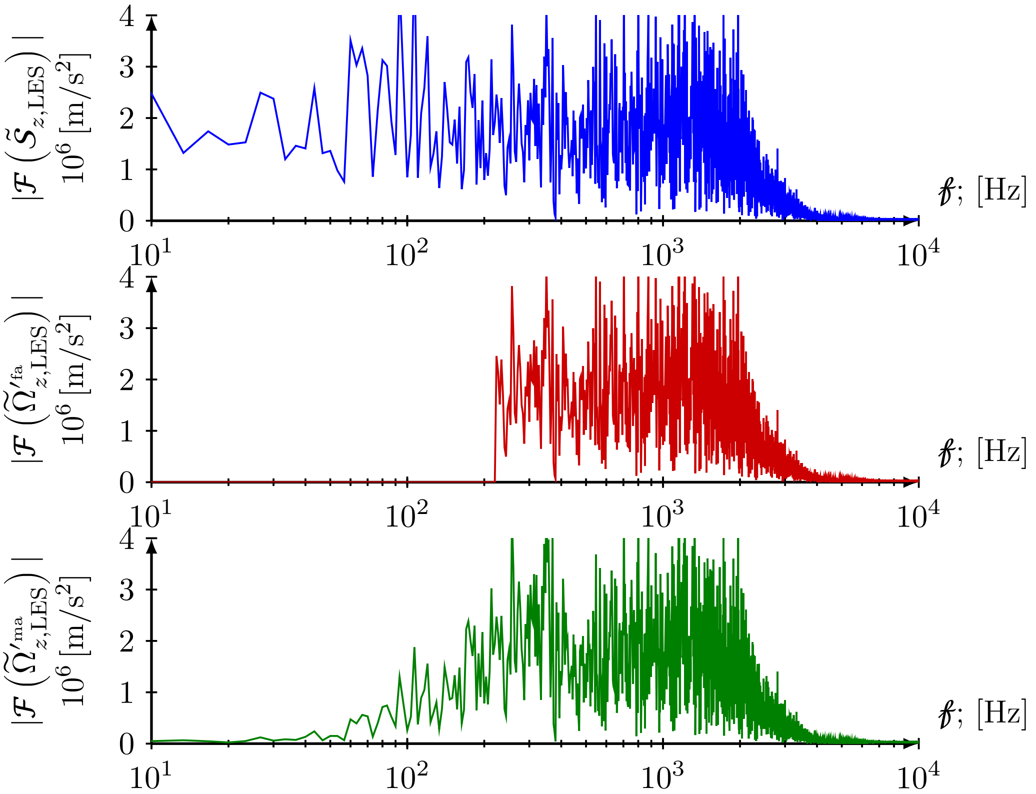

(b) GP(4/1): $\not{f}_{\mathrm{SW}} = 221.62\,\mathrm{Hz}$

Figure 7.8: Figure continued and caption on right page.

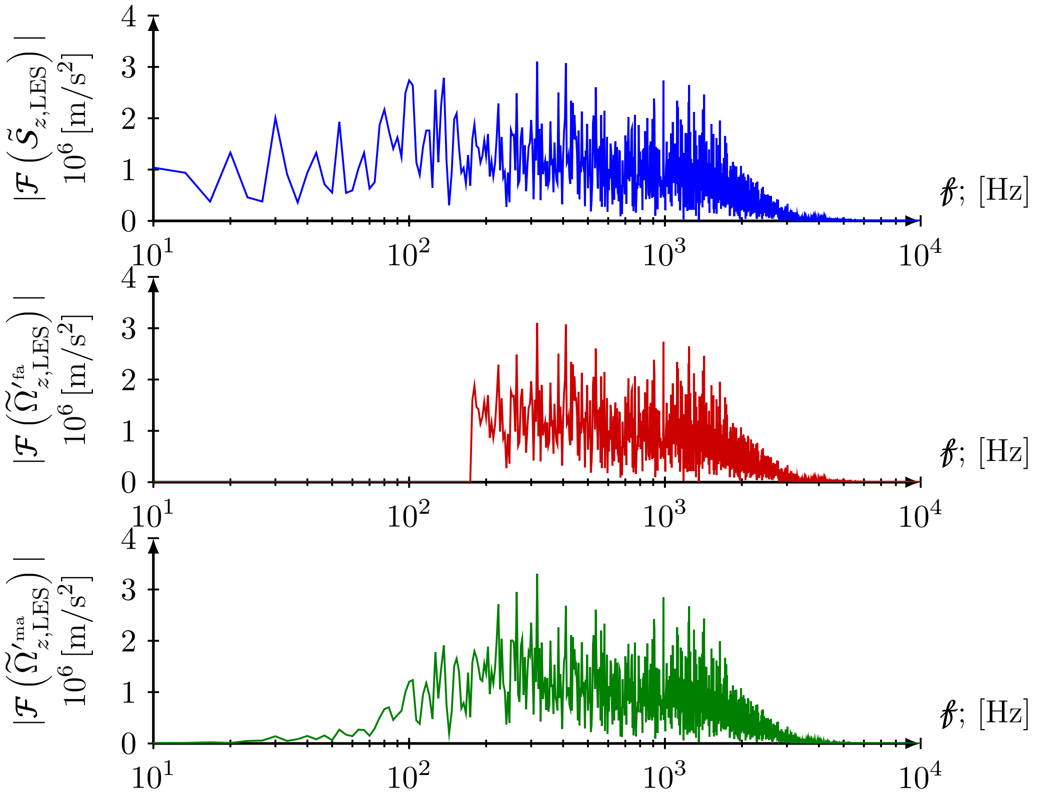

(c) GP(5/2): $\not{f}_{\mathrm{SW}} = 175.89\,\mathrm{Hz}$

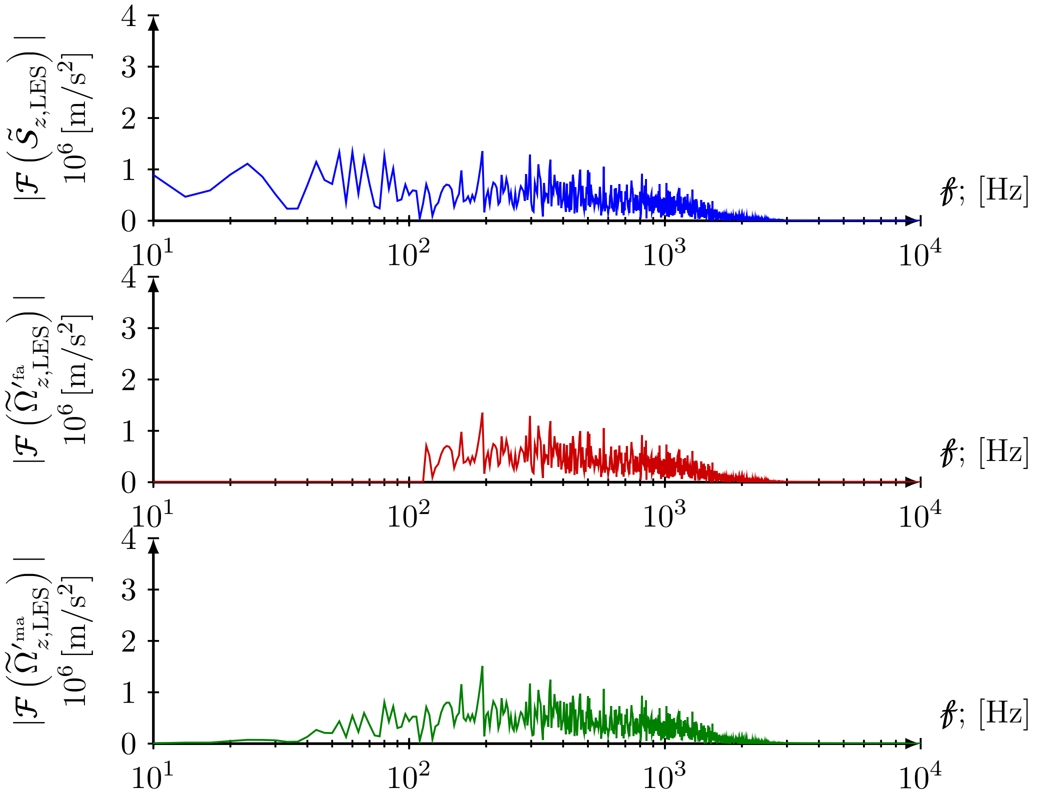

(d) GP(7/4): $\not{f}_{\mathrm{SW}} = 114.54\,\mathrm{Hz}$

Figure 7.8: Spectral density of source terms $|\Psi_{\not{f}}| = |\mathcal{F}(\phi)|$ before and after applying temporal filters based on the *sweeping time* $\boldsymbol{t}_{\mathrm{SW}}$ at the selected grid positions of case AP_h10Re5300.

The effect of the alternative temporal filtering approaches on the spectral-distribution is exemplarily shown in figure 7.8, considering a time sequence of instantaneous signals obtained from LES at the four selected grid positions GP(3/3), GP(4/1), GP(5/2) and GP(7/4) for the case AP_h10Re5300. The spectral temporal filter based on the FFT sharply cuts off all amplitudes below the cut-off frequency determined by the chosen time-scale $\mathscr{f}_{\mathrm{SW}} = 1/\mathscr{t}_{\mathrm{SW}}$. In contrast, the temporal filter based on the moving box average does not rigorously eliminate the content below $\mathscr{f}_{\mathrm{SW}}$, while completely preserving the content beyond. As a result, some low-frequency content remains and, therefore, the reduction in the strength of the aeroacoustic source term is slightly smaller.

Note the low-frequency content $|\mathcal{F}\left(\tilde{\mathcal{S}}_{z,\mathrm{LES}}\right)|$ for $\mathscr{f}_{\mathrm{SW}} < \mathscr{t}_{\mathrm{SW}}$, included in the non-centered aeroacoustic source terms $\tilde{\mathcal{S}}_{z,\mathrm{LES}}$, which remains in case of centering with statistical averages also further downstream of the orifice.

Figure 7.9 shows the evolution of the averages obtained from the different temporal filtering approaches in the time domain, shown at the selected grid positions for the case AP_h10Re5300 exemplarily for the z-component of the aeroacoustic source term $\tilde{\mathcal{S}}_{i,LES}$. For each grid position the averaged quantity $\left\langle\tilde{\mathcal{S}}_{z,\mathrm{LES}}\right\rangle$ and the averages based on the temporal filters $\left\langle\tilde{\mathcal{S}}_{z,\mathrm{LES}}\right\rangle_{\mathrm{fa}}$ and $\left\langle\tilde{\mathcal{S}}_{z,\mathrm{LES}}\right\rangle_{\mathrm{ma}}$ are presented. Note that the averages based on the moving time-frame approach $\left\langle\tilde{\mathcal{S}}_{z,\mathrm{LES}}\right\rangle_{\mathrm{ma}}$, as already presumed, show in general less intense variations compared to the fourier-based spectral cut-off averages $\left\langle\tilde{\mathcal{S}}_{z,\mathrm{LES}}\right\rangle_{\mathrm{fa}}$.

As already discussed the influence of the centering with statistical averages decreases further downstream of the orifice, while the alternative temporal filters still effectively remove low-frequency content above the chosen time-scale.

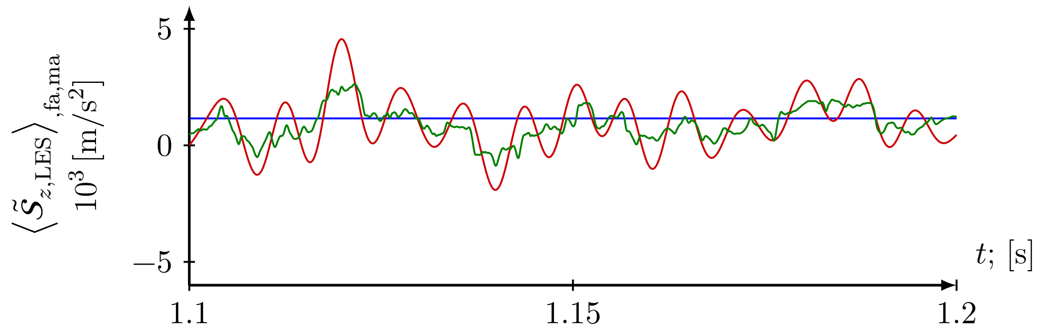

(a) GP(3/3): $\boldsymbol{t}_{\mathrm{SW}} = 160.85\,\mathrm{Hz}$

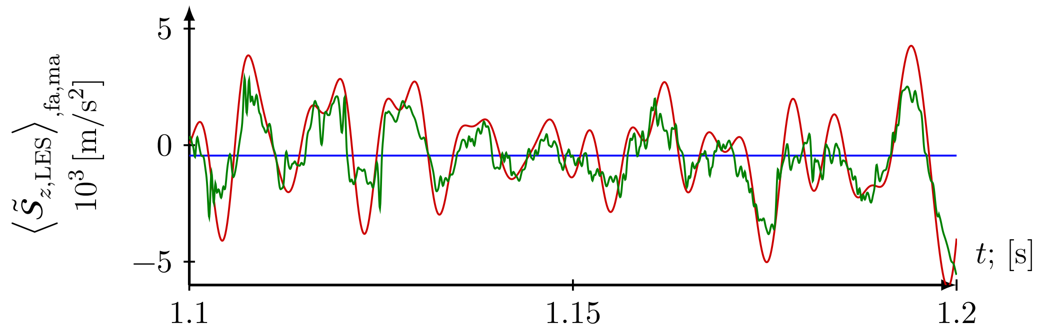

(b) GP(4/1): $\boldsymbol{t}_{\mathrm{SW}} = 221.62\,\mathrm{Hz}$

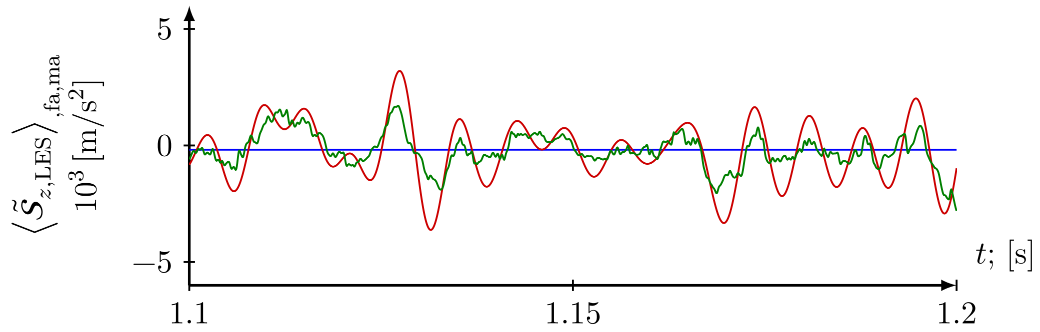

(c) GP(5/2): $\boldsymbol{t}_{\mathrm{SW}} = 175.89\,\mathrm{Hz}$

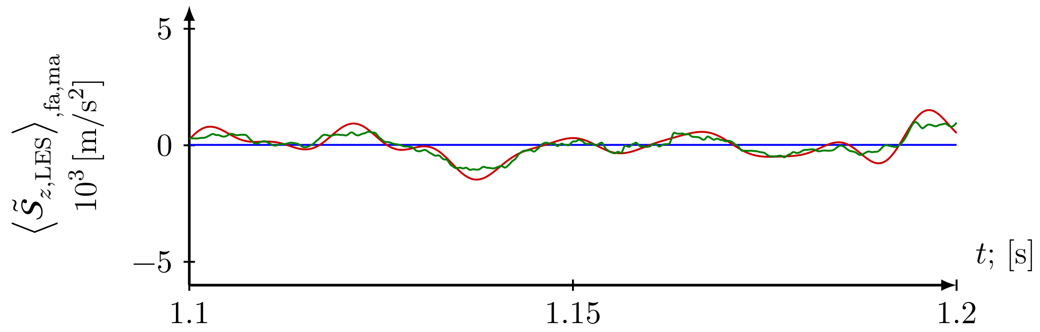

(d) GP(7/4): $\boldsymbol{t}_{\mathrm{SW}} = 114.54\,\mathrm{Hz}$

— $\left\langle \tilde{\mathcal{S}}_{z,\mathrm{LES}} \right\rangle$ — $\left\langle \tilde{\mathcal{S}}_{z,\mathrm{LES}} \right\rangle_{\mathrm{fa}}$ — $\left\langle \tilde{\mathcal{S}}_{z} \right\rangle_{\mathrm{ma}}$

FIGURE 7.9: Evolution of the averages of the aeroacoustic source term component $\tilde{\mathcal{S}}_{z,\mathrm{LES}}$ [m/s^2] at the four selected grid positions of case AP_h10Re5300. Temporally filtered averages are based on the shown sweeping time $\boldsymbol{t}_{\mathrm{SW}}$.

Table 7.2: Intensity of the temporally filtered aeroacoustic source term components $\widetilde{\Omega}'^{\text{fa,ma}}_{i,\text{LES,RMS}}$ [m/s^2] at the four selected grid positions for the case AP_h10Re5300.

	col	row	$\widetilde{\Omega}'^{\text{fa,ma}}_{x,\text{LES,RMS}}$ [m/s^2]	$\widetilde{\Omega}'^{\text{fa,ma}}_{y,\text{LES,RMS}}$ [m/s^2]	$\widetilde{\Omega}'^{\text{fa,ma}}_{z,\text{LES,RMS}}$ [m/s^2]
Fourier average	3	3	2343.79	2376.13	2726.16
	4	1	5763.10	5361.43	5812.86
	5	2	2421.36	2503.81	3120.29
	7	4	850.03	862.28	1073.24
moving average	3	3	2457.37	2485.65	2930.71
	4	1	6180.91	5780.26	6005.58
	5	2	2551.26	2627.30	3220.56
	7	4	922.66	904.65	1116.07

Using the alternatively obtained temporal averages $\langle\ \rangle_{\text{fa}}$ or $\langle\ \rangle_{\text{ma}}$ significantly reduces the RMS-values of the respective aeroacoustic source term variations as well. Applying the time-dependent averages $\langle\ \rangle_{\text{fa}}$ or $\langle\ \rangle_{\text{ma}}$ instead of the statistical average $\langle\ \rangle$ in (7.3) produces evidently markedly less intense fluctuations, as seen from the values $\widetilde{\Omega}'^{\text{fa}}_{i,\text{LES}}$ and $\widetilde{\Omega}'^{\text{ma}}_{i,\text{LES}}$ listed in table 7.2 for the investigated grid positions of case AP_h10Re5300. As compared to the very small impact of the standard statistical average based centering method on the intensity of the aeroacoustic source terms (see table 7.1) the effectivity of the two alternative temporal filtering methods can be still observed also further downstream of the orifice GP(7/4), where the mean flow gradients are small and the flow field is more homogeneous compared to the grid positions close to the shear layers at GP(3/3).

Summing up, applying the presented alternative temporal filtering approaches, can evidently eliminate some low-frequency content from the aeroacoustic source term. This aspect might become important, when dealing with persistent large low-frequency vortical structures, which are not dissipated even far away from the regions associated with intense aeroacoustic sources. Assuming that the remaining high-frequency content remaining from the filtering is more isotropic, the temporally filtered aeroacoustic source terms should essentially contain only the isotropic fraction of the turbulence kinetic energy.

It was also shown, as expected, that the obtained aeroacoustic source terms are strongly connected with the observed instantaneous vorticity of the turbulent flow field. Therefore, a reliable prediction of the instantaneous turbulent flow field is essential for a good prediction of the aeroacoustic source terms.

7.1.3 Aeroacoustic sources of momentum in LEE generated by cross-terms.

The LEE for momentum (4.34b) used in the CAA tool of FIRE™ and [13], consideres in addition to the non-linear momentum exchange between the turbulent fluctuating components, $v'_j \partial v'_i / \partial x_j$, also the contribution of the cross-terms between the mean and the fluctuating components, such that the total momentum source term reads

$$\Lambda_i + \mathcal{S}_i = \langle v_j \rangle \frac{\partial v'_i}{\partial x_j} + v'_j \frac{\partial \langle v_i \rangle}{\partial x_j} + v'_j \frac{\partial v'_i}{\partial x_j}. \tag{7.5}$$

As such, the cross-terms Λ_i represent the sound generation caused by interaction of the mean $\langle v_i \rangle$ and the turbulent v'_i flow field.

In the context of RANS the statistically averaged velocities $\langle v_i \rangle$ are known from the CFD solution of the RANS equations, while the fluctuating components v'_i have to be provided by a sub-model, like the UKSG. Having available instead the resolved turbulent fluctuating velocity field obtained from the LES, the cross-term contribution to the aeroacoustic source term $\widetilde{\Lambda}_{i,\mathrm{LES}}$ can be directly computed as

$$\widetilde{\Lambda}_{i,\mathrm{LES}} = \langle \tilde{v}_j \rangle \frac{\partial \tilde{v}'_i}{\partial x_j} + \tilde{v}'_j \frac{\partial \langle \tilde{v}_i \rangle}{\partial x_j}. \tag{7.6}$$

The evolution of this term was monitored at the 7×7 grid positions shown in figure 6.23. The results for a subset of the four specially selected grid position shall be discussed here in detail.

Figure 7.10 shows the histories of the cross-term contribution $\widetilde{\Lambda}_{i,\mathrm{LES}}$ over time-period $T = 0.1\,\mathrm{s}$ at the four selected grid positions for case AP_h10Re5300. Similar to the aeroacoustic source terms $\tilde{\mathcal{S}}'_{i,\mathrm{LES}}$ none of the components i seem to be dominant, while their intensity decreases further downstream of the orifice. In contrast to the aeroacoustic source term $\tilde{\mathcal{S}}'_{i,\mathrm{LES}}$, which is generally most intense at GP(4/1), the intensity of $\widetilde{\Lambda}_{i,\mathrm{LES}}$ is generally highest at the grid points GP(3/3) and GP(5/2). One might conclude that the highly sheared layers bounding the core jet-flow produce higher cross-terms compared to the region close to the reattachment point with mainly linear deformation.

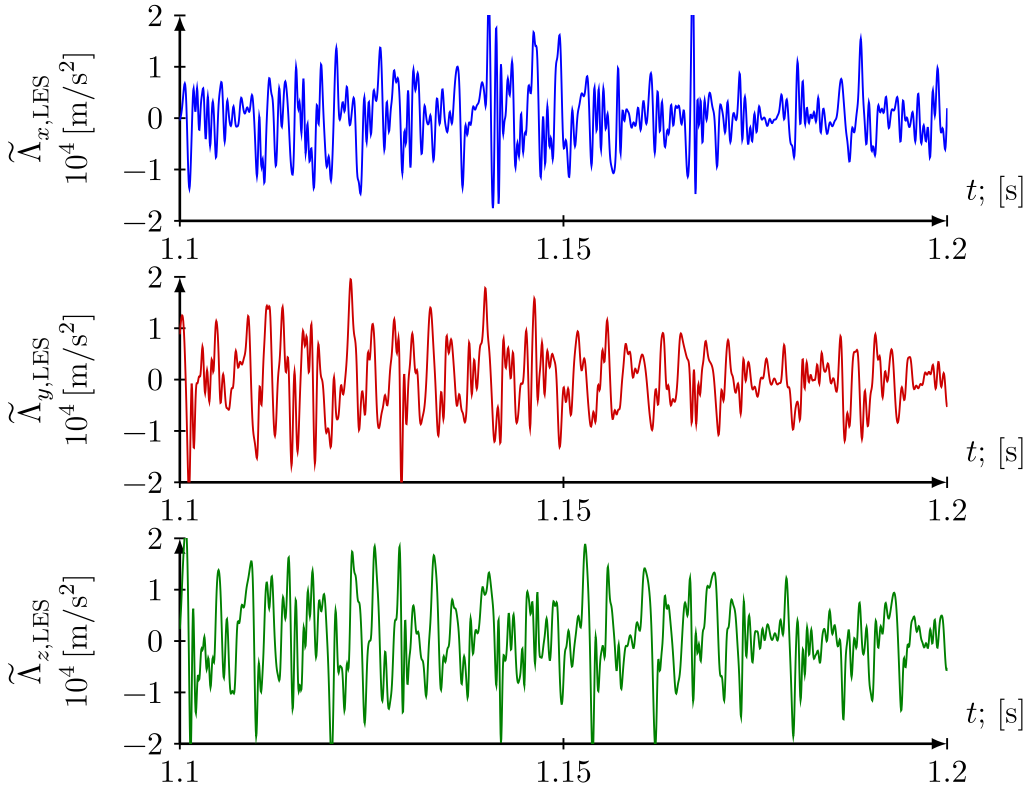

(a) GP(3/3)

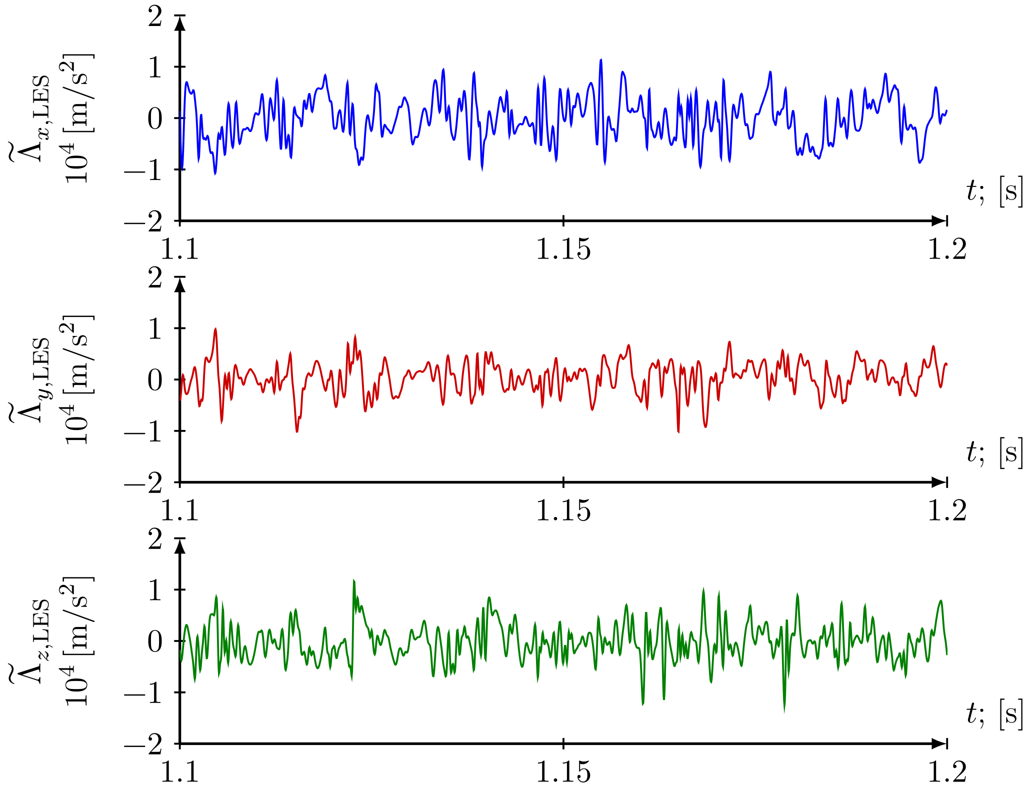

(b) GP(4/1)

Figure 7.10: Figure continued and caption on right page.

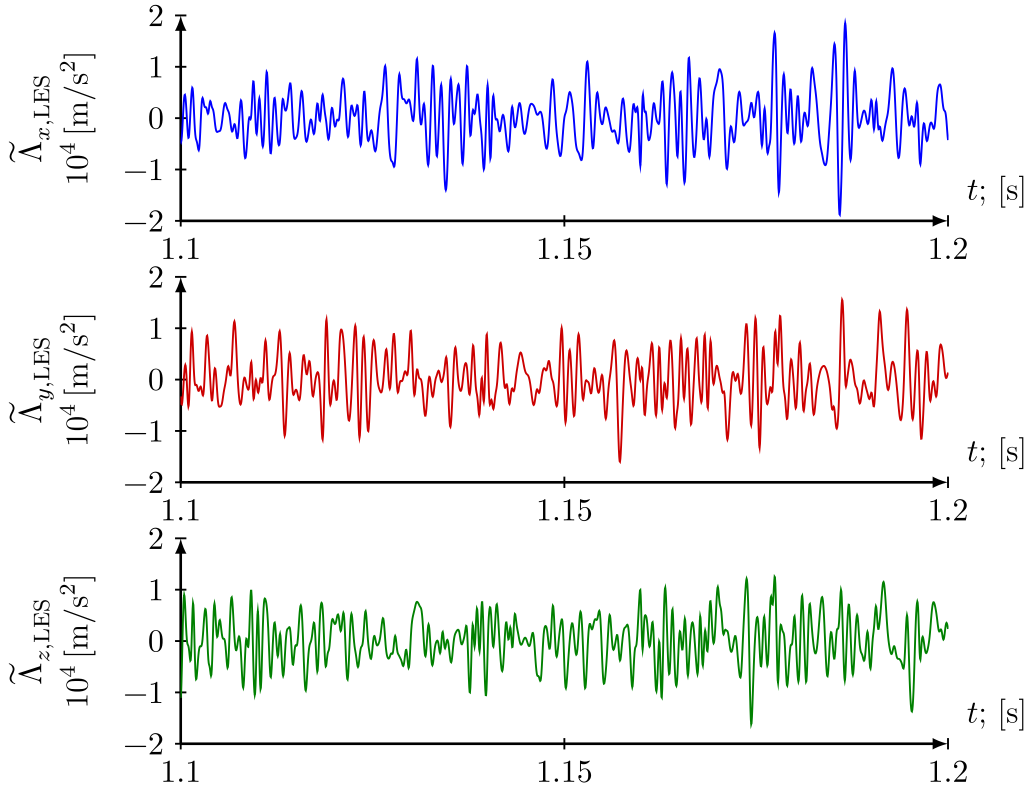

(c) GP(5/2)

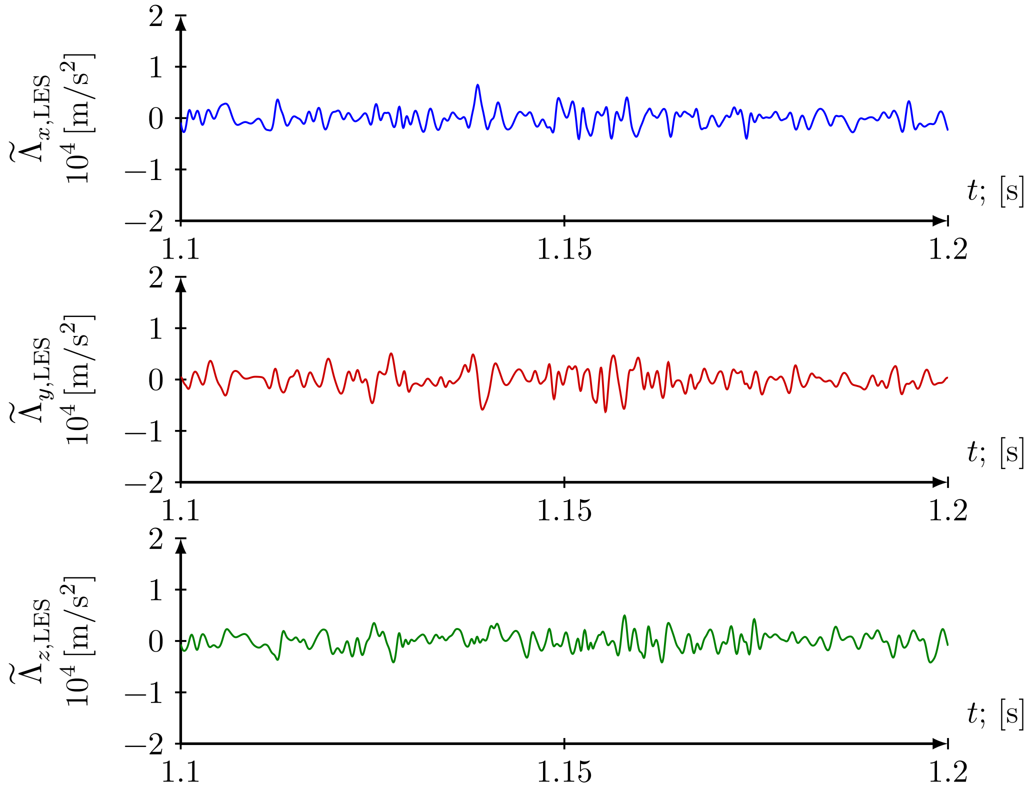

(d) GP(7/4)

Figure 7.10: Histories of instantaneous cross-term contributions $\widetilde{\Lambda}_{i,\mathrm{LES}}$ $[\mathrm{m/s^2}]$ at the four selected grid positions for case AP_h$_{10}$Re$_{5300}$.

TABLE 7.3: RMS-values of the cross-term components $\widetilde{\Lambda}_{i,\mathrm{LES,RMS}}$ [m/s^2] at the investigated grid positions for case AP_h10Re5300.

col	row	$\widetilde{\Lambda}_{x,\mathrm{LES,RMS}}$ [m/s^2]	$\widetilde{\Lambda}_{y,\mathrm{LES,RMS}}$ [m/s^2]	$\widetilde{\Lambda}_{z,\mathrm{LES,RMS}}$ [m/s^2]
3	3	5180.17	5866.88	6958.04
4	1	3938.20	2898.90	3185.21
5	2	4700.23	4796.40	4590.55
7	4	1566.68	1540.62	1422.29

The corresponding intensities of $\widetilde{\Lambda}_{i,\mathrm{LES}}$, quantified by the RMS-values $\widetilde{\Lambda}_{i,\mathrm{LES,RMS}}$, at the four examined grid positions of case AP_h10Re5300 are listed in table 7.3. The intensities of all cross-terms at the 7×7 grid positions of case AP_h10Re5300 are listed in the appendix in table A.8.

In general, at any grid position the resulting intensities of the cross-terms are comparable in magnitude to the intensities of the aeroacoustic source term $\tilde{\mathcal{S}}_{i,\mathrm{LES}}$, discussed in the previous sections and listed in table 7.2.

As already noted in section 4.3, the contribution of the cross-terms is often neglected. In most literature, where similar geometries were investigated (see [8, 12, 19, 24, 40]), the LEE consider only the aeroacoustic source term Ω_i', arising from the turbulent-turbulent interaction. Some authors like Bechara et al. [13] still included the cross-terms contributions into the aeroacoustic source terms. The influence of including these cross-terms on the finally predicted acoustic field should be certainly further debated and specially investigated.

It is noted, that the presently implemented CAA tool in FIRE™ does not provide access to the momentum sources, which are actually used for solving the LEE. Therefore, neither the RANS-based data for Ω_i, nor for Λ_i are available for a comparison against the present LES-based data. However, the CAA tool does provide access to the aeroacoustic source term Π, defined by (4.36) appearing in the energy equation of the LEE (4.34c). The following section is therefore particularly dedicated to the comparison of the RANS-based results, obtained with the UKSG, against the LES-based results, where the aeroacoustic source term $\widetilde{\Pi}$ is computed directly from the resolved instantaneous turbulent flow field.

7.2 The aeroacoustic source term for energy computed from UKSG and the LES

Recalling the aeroacoustic source term for the energy equation of the LEE (4.34c) used by the CAA tool in FIRE™

$$\Pi = v_j' \frac{\partial \langle p \rangle}{\partial x_j},$$

makes evident that this term basically represents the interaction between the temporally averaged pressure gradients and the turbulent velocity fluctuations. In RANS-based CFD, these instantaneous fluctuations have to be provided by a dedicated sub-model. For the present comparison, the RANS-based aeroacoustic source term Π was computed using the UKSG within the CAA tool of FIRE™ as sub-model for the case CAA_h10Re5300. The corresponding LES results for $\widetilde{\Pi}$ were computed from an instantaneous resolved flow field for the equivalent LES case AP_h10Re5300.

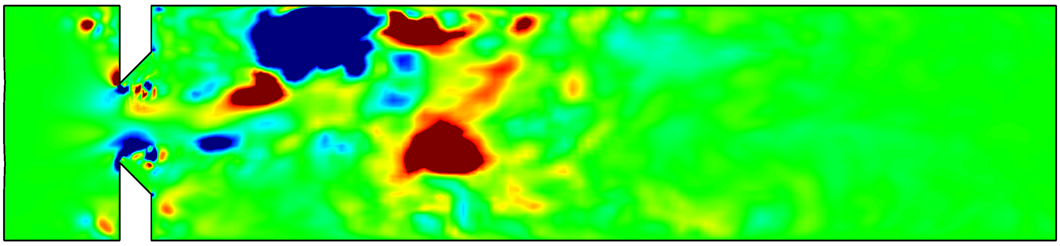

(a) $\widetilde{\Pi}_{\mathrm{LES}}$ of case AP_h10Re5300 at $t_{\mathrm{end}} = 1.2\,\mathrm{s}$

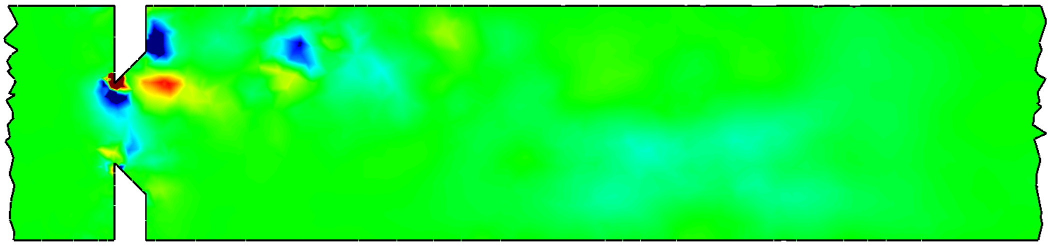

(b) Π_{UKSG} of case RANS_h10Re5300 at $t_{\mathrm{end}} = 0.1\,\mathrm{s}$

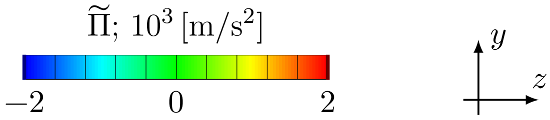

FIGURE 7.11: Comparison of contours of the instantaneous energy source Π [Pa/s] for LES case AP_h10Re5300 and the UKSG for RANS case CAA_h10Re5300 at $t = t_{\mathrm{end}}$.

Figure 7.11 shows the instantaneous contours of the aeroacoustic source term for energy as predicted from the UKSG, Π_{UKSG} ,and the LES, $\widetilde{\Pi}_{\mathrm{LES}}$, at a certain instance of time. In contrast to the UKSG, the LES produces also very intense aeroacoustic source terms further downstream of the orifice and also in the region near the upper wall, where the deflected jet-like core flow reattaches. In comparison to the instantaneous aeroacoustic source terms for momentum presented in figure 7.1, additional sub-regions with significant levels of aeroacoustic energy source terms Π appear near the sharp corners of the orifice, which is due to the local high mean pressure gradients occurring in this zone (see figure 6.16).

TABLE 7.4: Turbulent fluctuation intensities of the aeroacoustic energy source term Π_{RMS} [Pa/s] for LES and the UKSG, and the temporal averaged total turbulence kinetic energy $\langle \mathscr{k}_{\mathrm{tot}} \rangle$ [m^2/s^2] between case AP_h10Re5300 and case CAA_h10Re5300, at the selected grid positions.

Case:	col	row	Π_{RMS} [Pa/s]	$\langle \mathscr{k}_{\mathrm{tot}} \rangle$ [m^2/s^2]
AP_h10Re5300	3	3	3353.96	3.88
	4	1	2685.12	7.37
	5	2	1074.12	4.64
	7	4	87.07	1.97
CAA_h10Re5300	3	3	1302.66	3.30
	4	1	1776.75	2.78
	5	2	456.02	2.19
	7	4	240.36	1.92

The turbulent fluctuation intensity of the energy source term measured in terms of the RMS-values Π_{RMS} are presented in table 7.4 at the four selected grid positions of case AP_h10Re5300 and CAA_h10Re5300, together with the corresponding temporally averaged total turbulence kinetic energy $\langle \mathscr{k}_{\mathrm{tot}} \rangle$. The intensities of Π_{RMS} obtained from the LES are much higher close to the orifice at GP(3/3), GP(4/1) and GP(5/2), while being much smaller further downstream of the orifice at GP(7/4) in comparison to the intensities obtained from the UKSG.

In figure 7.12 the histories of the aeroacoustic energy source term $\Pi(t)$, predicted from the UKSG for the RANS case CAA_h10Re5300 and for the equivalent LES case AP_h10Re5300 are presented. The shown results were obtained at the four selected grid positions indicated in figure 6.23, covering a time-period $T = 0.1\,\mathrm{s}$. Note that at the grid position GP(5/2) and GP(7/4) the order of magnitude is significantly lower in comparison to the other grid positions GP(3/3) and GP(4/1), so that a different scaling for the ordinate was chosen.

Additionally figure 7.13 shows the spectral distribution of the aeroacoustic energy source term $|\mathcal{F}(\Pi)|$, obtained from a fast Fourier transform. We note again that at the grid position GP(7/4) the amplitudes are one order of magnitude smaller ($\sim 10^5$[Pa]) in comparison to the other grid positions ($\sim 10^6$[Pa]).

Both figures 7.12 and 7.13 clearly show the high frequency content ($\not{f} >3000\,\mathrm{Hz}$) appearing in the energy source term predicted from the UKSG. The amplitudes of these high frequency components are small though, compared to the amplitudes of the lower frequencies and therefore might be negligible. The capability of tracking much higher frequencies as compared to the highest frequencies appearing in the LES based source term, is due to the methodology of the UKSG, where the phase Ξ (see section 4.6.4) of the reconstructed turbulence velocity is chosen randomly advancing in very small time-steps Δt_{UKSG}. Since these time-steps are significantly smaller in size to the acoustic time-step size Δt_{CAA} (see table 5.7), the evaluated turbulent fluctuations inherently include very high frequency content, which cannot be captured by the incompressible LES using a much longer only flow-determined time-step size Δt_{LES}. Therefore, the energy source term predicted from such sub-models can also contain acoustic frequencies well beyond the inverse flow related time-scales, altough the modeling is based on an incompressible RANS solution. Additionally, the randomly chosen phase Ξ between every time-step might produce small discontinuities in time, which might also contribute some random high-frequency content.

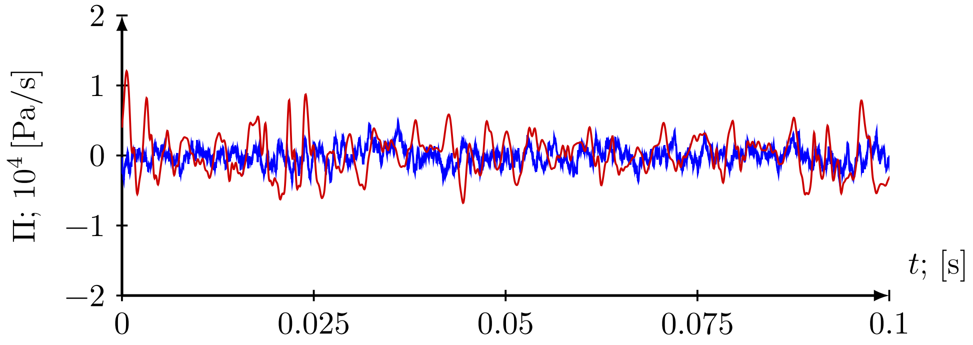

(a) GP(3/3)

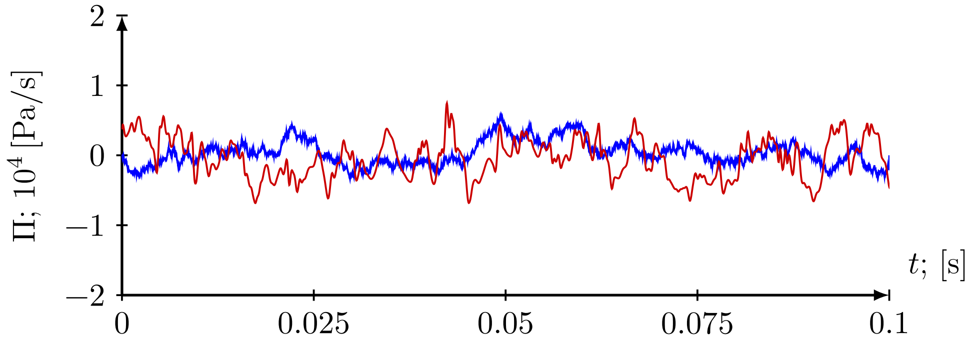

(b) GP(4/1)

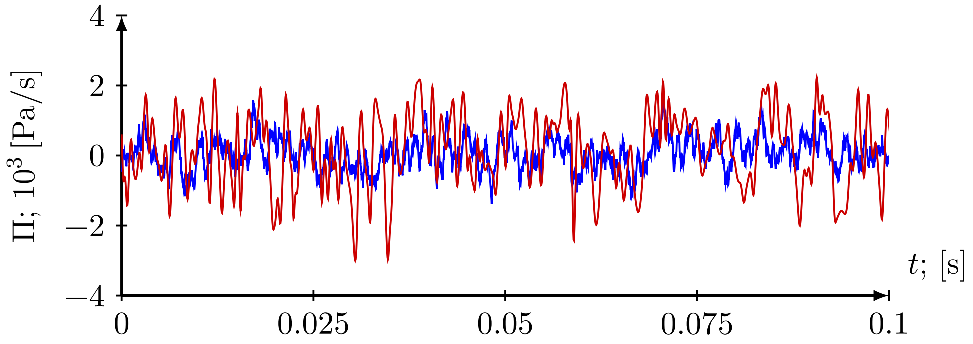

(c) GP(5/2)

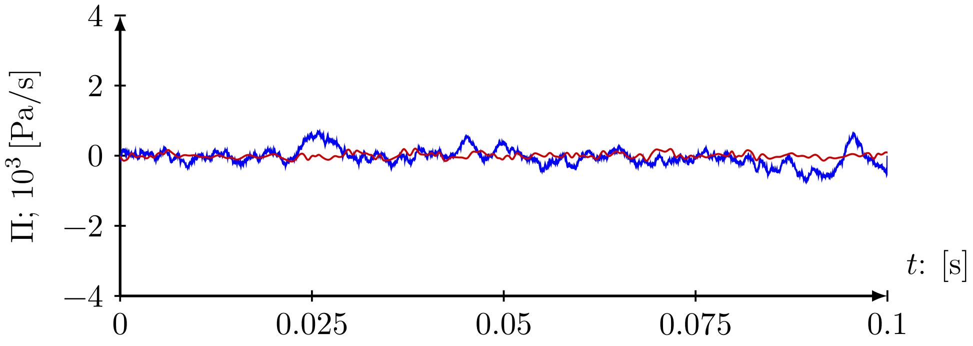

(d) GP(7/4)

Figure 7.12: Histories of the aeroacoustic energy source term $\widetilde{\Pi}_{\mathrm{LES}}$ [Pa/s] for the LES case AP_h10Re5300 and Π_{UKSG} [Pa/s] for the equivalent RANS case CAA_h10Re5300 obtained from the UKSG at the investigated grid positions.

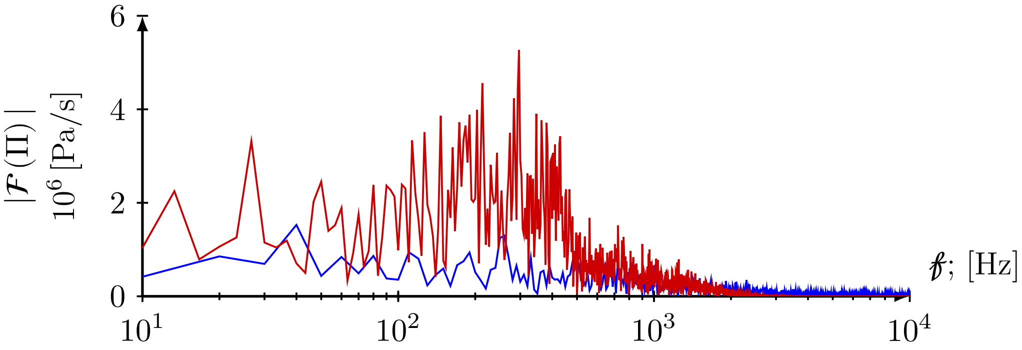

(a) GP(3/3)

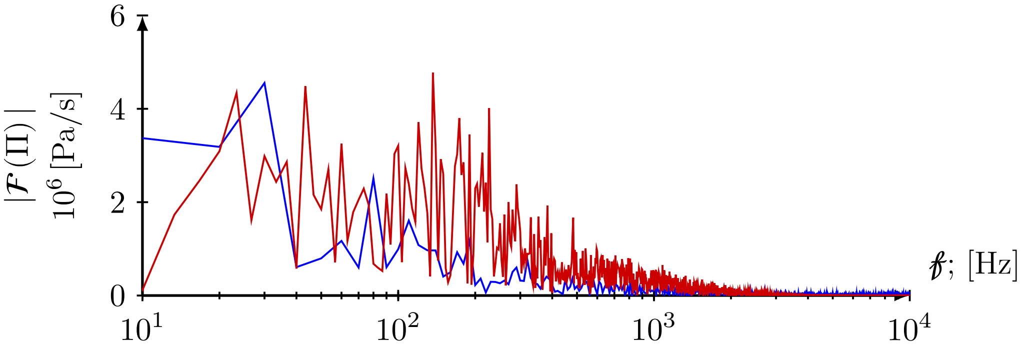

(b) GP(4/1)

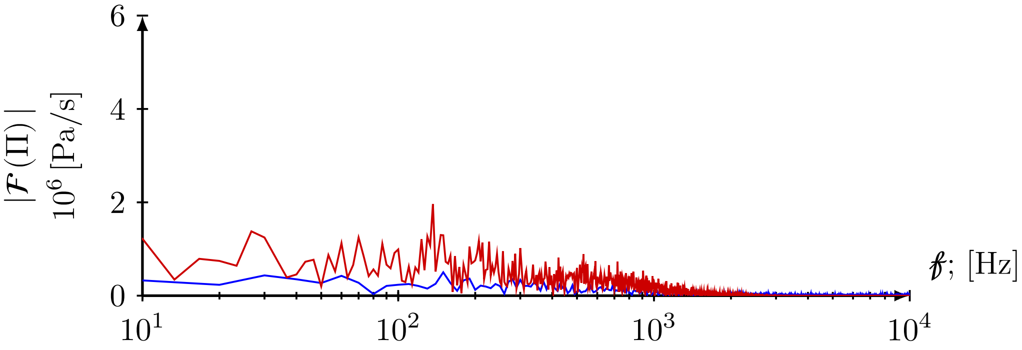

(c) GP(5/2)

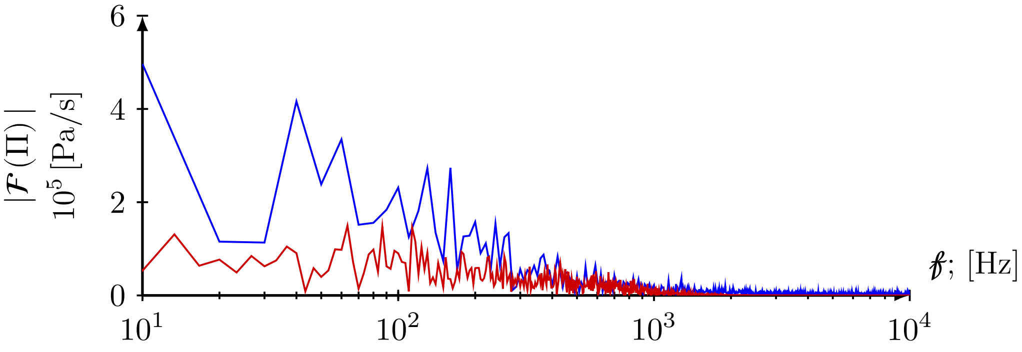

(d) GP(7/4)

— $|\mathcal{F}(\Pi_{\mathrm{UKSG}})|$; — $|\mathcal{F}(\widetilde{\Pi}_{\mathrm{LES}})|$

FIGURE 7.13: Spectral distribution of the aeroacoustic energy source term $|\Psi_{f}| = |\mathcal{F}(\Pi)|$ [Pa/s] for LES case AP_h10Re5300 and the equivalent RANS case CAA_h10Re5300 obtained from the UKSG at the investigated grid positions.

In general the magnitude of the aeroacoustic energy source terms obtained from the UKSG Π_{UKSG} is well below the predictions of the LES in the regions close to the shear layers at GP(3/3), GP(4/1) and GP(5/2), while it is above in the region further downstream of the orifice at GP(7/4).

The pressure source term at GP(4/1) contains more low-frequency ($f < 100\,\mathrm{Hz}$) content, in comparison to GP(3/3), which was similarily predicted by the LES and the UKSG, which is also indicated by the spectral densities of the turbulence kinetic energy in figure 6.24. At both grid positions the UKSG produces much less mid-frequency ($100 < f < 100\,\mathrm{Hz}$) content, due to the underpredicted total temporally averaged turbulence kinetic energy $\langle k_{\mathrm{tot}} \rangle$ in the RANS solution (see figure 6.18). At GP(5/2) the source term of the UKSG remains below the LES results over the whole range of frequencies. The opposite behavior is observed at GP(7/4), where the amplitudes are generally much lower, though.

To sum up the aeroacoustic energy source term predicted from the UKSG are in general markedly less intense than their counterparts obtained from LES. The observed difference can be to a great extent to an underpredicted turbulence kinetic energy, which is used by the UKSG model as key input parameter from the RANS solution. In turn, introducing the considerably higher predicted source terms from LES into the LEE will expectedly intensify the generation of sound especially in the near-field of the orifice.

8 Summary, conclusions and outlook

This Master's Thesis was carried out in cooperation with AVL LIST GmbH and the Institute of Fluid Mechanics and Heat Transfer (ISW) of the Graz University of Technology (TU Graz). Its primary aim was the numerical investigation of aeroacoustic sources produced by an orifice within a straight cylindrical pipe. The flow through the orifice was investigated using computational fluid dynamics (CFD) based on the numerical solution of the Reynolds averaged Navier-Stokes (RANS) equations and the Large-Eddy Simulation (LES).

After introducing the fundamentals of acoustics and fluid mechanics, the foundation of aeroacoustics, *Lighthill's acoustic analogy*, was derived and discussed. For the present task a more advanced acoustic analogy had to be found. For that *Lilley's acoustic analogy* was derived, which is difficult to solve due to its complex wave operator. After introducing the *aeroacoustic decomposition*, which is the foundation of every hybrid computational aeroacoustics (CAA) approach, the acoustic analogy based on the linearized Euler equations (LEE) was derived, which is a widely used acoustic analogy, because it is easier to solve due to its linearity, but also because it can describe some wave propagation effects. By applying Lilley's acoustic analogy and the acoustic analogy based on the LEE to a two-dimensional sheared flow, it was shown that both acoustic analogies are equivalent, because the same wave operator and aeroacoustic source term remain. As a result, the most relevant target aeroacoustic source term was identified, originating from the turbulent-turbulent velocity fluctuations. Additional cross-terms for the momentum and energy equation of the LEE, constituted of the mean flow field and the turbulent velocity fluctuations, were identified and investigated as well. Thereafter, the concept of computing the aeroacoustic source terms from the resolved LES quantities was described. Finally, the solution procedure of the CAA tool implemented in FIRE™ was introduced. This tool solves LEE, where the required aeroacoustic source term are artificially generated by the "unstructured kinematic source generator (UKSG)".

The accuracy of the LES solution obtained from the periodic pipe LES, which provided instantaneous inflow conditions for the acoustic pipe LES cases, was validated against DNS data. Comparing the first and second order statistics of the obtained results against direct numerical simulation (DNS), it was shown that the periodic pipe LES results were in fairly good agreement with the DNS data. The applied subgrid-scale model (SGM), the Coherent Structure Model, could not fully compensate the unresolved gap between the resolved LES and the DNS data. Summing up, the periodic pipe LES, delivered a reliable basis for the turbulent inflow BC.

The results of the acoustic pipe LES were also analyzed in much detail. The focus was first on the instantaneous resolved flow field, extending between the instantaneous inflow BC and the turbulent core jet-flow appearing downstream of the orifice. Due to the Coanda effect the core jet-flow attached at the top or bottom wall of the pipe, which had a strong influence on the basic structure of the turbulent flow field. At the higher Reynolds number and for the reduced gap height of the orifice a significantly enhanced turbulent motion downstream of the orifice was observed. It was additionally shown that the turbulence field is highly anisotropic in the shear layers of the core jet-flow and near the reattachment point with high linear deformation.

Comparing the temporally averaged flow fields of the LES solution with the RANS solution, it was shown that the structure of the flow field was quite similar, showing an asymmetrical flow field due to the Coanda effect. The RANS simulation predicted the reattachment point of the core jet-flow further downstream in comparison to the LES solution. The turbulence kinetic energy fields were quite different, where the RANS solution significantly underpredicted the turbulence kinetic energy especially close to the shear layers of the core jet-flow and the reattachment point.

By investigating the vorticity fields, one could observe that intense vortical structures are emerging from the shear layers of the core jet-flow. Some of these vortical structures might contain low-frequency content which might be convected even far downstream of the orifice, and therefore might strongly influence the propagation of sound waves.

The history of a selected number of acoustically relevant quantities was additionally stored at 49 points of each LES case, determined by a 7×7 rectangular grid pattern covering the main source region. From these 7×7 grid points four points were selected for further detailed discussions, which are representative for the different flow regions downstream of the orifice.

From the three introduced turbulent time-scales, the sweeping time delivered the most promising results for extracting large low-frequency vortical structures from the aeroacoustic sources.

In the final chapter 7, the results of the obtained aeroacoustic sources from the LES are presented. First the main aeroacoustic source term, appearing in the momentum equation, was discussed. Analogous to the turbulence kinetic energy field the obtained source field was intense close to the shear layers and the reattachment region of the core jet-flow. Further downstream of the orifice the intensity decreased fast. Therefore, the vortical structures, which were observed in the vorticity fields and are convected downstream of the orifice, might not contribute a lot to the aeroacoustic source term. Also, it seems that none of the three components of the aeroacoustic source term is dominant, although the turbulence is highly anisotropic.

Comparing the different flow configurations, the obtained source term intensities of the case with the reduced orifice gap height were the highest, followed by the case with the higher Reynolds number, which is in accordance with the obtained turbulence kinetic energy fields.

The centering of the aeroacoustic source term, obtained by subtracting its temporal average, effectively reduces the aeroacoustic source term in regions with high mean deformation rates, occurring in the shear layers and close to the reattachment point of the core jet-flow. The large low-frequency vortical structures are not affected. The axial (z) and vertical (y) components of the temporally averaged aeroacoustic source term are dominant close to the shear layers and the reattachment point of the core jet-flow. The spanwise (x) component seems to be negligible, since no significant deformation appears.

Applying temporal filters to the aeroacoustic source terms effectively subtracts all low-frequency content below the chosen turbulent time-scales, therefore excluding large low-frequency vortical structures. While the spectral method based on the Fourier transform sharply cuts off content below the cut-off frequency, the moving averaging method does not remove all low-frequency content. In contrast to the standard centering method also low-frequency content further downstream of the orifice are effectively removed.

Following from a rigorous derivation of the LEE, additional cross-terms, constituted of the mean and turbulent flow field, appear as aeroacoustic sources. In most literature these are neglected. In this Master's Thesis also the cross-terms appearing in the momentum equation were investigated. It is shown that they are equally intense near the sheared region and the reattachment point of the core jet-flow as the main turbulence-turbulence aeroacoustic source term. Therefore, it is mandatory to investigate the influence of these cross-terms on the acoustic field.

The CAA tool in FIRE™ accounts for the cross-terms in the momentum, together with the non-centered aeroacoustic source term, and the energy equation of the LEE. Since the CAA tool is based on an incompressible RANS based hybrid approach, the aeroacoustic source terms have to be modeled, which is performed by the UKSG. Since only the output of the energy source term is available, this energy source term was also computed from the acoustic pipe LES solution for comparison. The UKSG mostly underpredicted the energy source term, since the turbulence kinetic energy field of the RANS solution was predicted less intense than the turbulence kinetic energy fields of the LES solution, especially in regions close to the shear layers and the reattachment point of the core jet-flow. By investigating the spectra of the energy source terms, it was observed that the energy source term from the UKSG contains contributions of high-frequencies above the time-scale, which could be resolved by the incompressible LES.

The next future steps following this Master's Thesis could be to modify the CAA module in FIRE™ in a way so that the aeroacoustic source terms obtained from the LES can be used as input data. This would allow the investigation of the different acoustic fields obtained from differently generated aeroacoustic source terms.

Since, in the current hybrid CAA approach different computational grids are used for the CFD and CAA simulation, also the influence of the mapping procedure of the aeroacoustic source terms between the computational grids on the aeroacoustic source terms could be investigated. Since the CAA grids are much coarser, some parts of the finer spatial resolution of the aeroacoustic source terms obtained from LES might be lost.

One major problem though of aeroacoustics in confined flow configurations is that the interest lies in the acoustic field outside of the pipe, at some observers position, and not within the pipe. If the technical application does not have some kind of exhaust (e.g. in closed coolant systems), where the acoustic field can emerge, somehow the transfer path through the surrounding walls have to be described so that the acoustic field outside can be obtained. Since the vibrations of solids and their sound radiation is well understood, the difficult part is extracting the required boundary conditions from the internal turbulent flow field.

List of Figures

List of Tables

Bibliography

[1] Y. Addad, D. Laurence, C. Talotte & M. Jacob (2003) Large eddy simulation of a forward–backward facing step for acoustic source identification. *International Journal of Heat and Fluid Flow* **24**.4 (2003), 562–571.

[2] B. Andersson, R. Andersson, L. Hakansson, M. Mortensen, R. Sudiyo & B. Wachem (2017) Computational Fluid Dynamics for Engineers. Cambridge University Press, 2017.

[3] H. Atkins (1997) “Continued development of the discontinuous Galerkin method for computational aeroacoustic applications”. In *3rd AIAA/CEAS Aeroacoustics Conference*. 1997, p. 1581.

[4] H. Atkins & D. Lockard (1999) “A high-order method using unstructured grids for the aeroacoustic analysis of realistic aircraft configurations”. In *5th AIAA/CEAS Aeroacoustics Conference and Exhibit*. 1999, p. 1945.

[5] H. Atkins & C.-W. Shu (1998) Quadrature-free implementation of discontinuous Galerkin method for hyperbolic equations. *AIAA journal* **36**.5 (1998), 775–782.

[6] AVL (2017) *FIRE™CAA Solver*. Version 2017.1. AVL List GmbH, Advanced Simulation Technologies. Graz, Austria, 2017.

[7] AVL (2017) *FIRE™CFD Solver*. Version 2017.1. AVL List GmbH, Advanced Simulation Technologies. Graz, Austria, 2017.

[8] C. Bailly, P. Lafon & S. Candel (1996) Computation of noise generation and propagation for free and confined turbulent flows. *AIAA Paper* **1732** (1996).

[9] C. Bailly & D. Juve (2000) Numerical solution of acoustic propagation problems using linearized Euler equations. *AIAA journal* **38**.1 (2000), 22–29.

[10] C. Bailly & D. Juves (1999) A stochastic approach to compute subsonic-noise using linearized euler’s equations (1999).

[11] C. Bailly & D. Juves (1998) *Numerical solution of acoustic propagation problems using linearized Euler’s equations. AIAA Paper*. Tech. rep. AIAA-98-2267, 1998.

[12] M. Bayati & M. Tadjfar (2015) High Helmholtz Sound Prediction Generated by Confined Flows and Propagation within Ducts. *Editor’s Space* (2015), 47.

[13] W. Bechara, C. Bailly, P. Lafon & S. M. Candel (1994) Stochastic approach to noise modeling for free turbulent flows. *AIAA journal* **32**.3 (1994), 455–463.

[14] M. Billson, L.-E. Eriksson & L. Davidson (2002) Acoustic source terms for the linear Euler equations on conservative form. *AIAA paper* **2582**.8 (2002).

[15] M. Billson, L.-E. Eriksson & L. Davidson (2004) "Jet noise modeling using synthetic anisotropic turbulence". In *10th AIAA/CEAS Aeroacoustics Conference*. 2004, p. 3028.

[16] C. Blom, B. Verhaar, J. van der Heijden & B. Soemarwoto (2001) "A linearized Euler method based prediction of turbulence induced noise using time-averaged flow properties". In *39th Aerospace Sciences Meeting and Exhibit*. 2001, p. 1100.

[17] C. Bogey, C. Bailly, D. Juvé, *et al.* (2002) Computation of flow noise using source terms in linearized Euler's equations. *AIAA journal* **40**.2 (2002), 235–243.

[18] T. Colonius, S. K. Lele & P. Moin (1997) Sound generation in a mixing layer. *Journal of Fluid Mechanics* **330** (1997), 375–409.

[19] F. Crouzet, P. Lafon, T. Buchal & D. Laurence (2002) "Aerodynamic noise prediction in internal flows using LES and linear Euler equations". In *8th AIAA/CEAS Aeroacoustics Conference & Exhibit*. 2002, p. 2568.

[20] N. Curle (1955) "The influence of solid boundaries upon aerodynamic sound". In *Proceedings of the Royal Society of London A: Mathematical, Physical and Engineering Sciences*. Vol. 231. 1187. The Royal Society. 1955, pp. 505–514.

[21] P. Davidson (2009) Turbulence, An introduction for scientists and engineers. Oxford University Press, 2009.

[22] P. Doak (1972) Analysis of internally generated sound in continuous materials: 2. a critical review of the conceptual adequacy and physical scope of existing theories of aerodynamic noise, with special reference to supersonic jet noise. *Journal of Sound and Vibration* **25**.2 (1972), 263–335.

[23] J. Fröhlich (2006) Large eddy simulation turbulenter Strömungen. Springer, 2006.

[24] X. Gloerfelt & P. Lafon (2008) Direct computation of the noise induced by a turbulent flow through a diaphragm in a duct at low Mach number. *Computers & fluids* **37**.4 (2008), 388–401.

[25] M. E. Goldstein (2003) A generalized acoustic analogy. *Journal of Fluid Mechanics* **488** (2003), 315–333.

[26] M. E. Goldstein (1976) Aeroacoustics. 1976.

[27] H. Guowei, R. Rubinstein & W. Lian-Ping (2001) Effects of eddy viscosity on time correlations in large eddy simulation (2001).

[28] K. Hanjalić, M. Popovac & M. Hadžiabdić (2004) A robust near-wall elliptic-relaxation eddy-viscosity turbulence model for CFD. *International Journal of Heat and Fluid Flow* **25**.6 (2004), 1047–1051.

[29] G. C. J. Hofmans (1998) Vortex sound in confined flows. PhD thesis. Technische Universiteit Eindhofen, 1998.

[30] M. Howe (1975) Contributions to the theory of aerodynamic sound, with application to excess jet noise and the theory of the flute. *Journal of Fluid Mechanics* **71**.4 (1975), 625–673.

[31] A. F. Hussain (1986) Coherent structures and turbulence. *Journal of Fluid Mechanics* **173** (1986), 303–356.

[32] C. Irrenfried & H. Steiner (2017) DNS based analytical P-function model for RANS with heat transfer at high Prandtl numbers. *International Journal of Heat and Fluid Flow* **66** (2017), 217–225.

[33] H. Kobayashi, F. Ham & X. Wu (2008) Application of a local SGS model based on coherent structures to complex geometries. *International Journal of Heat and Fluid Flow* **29**.3 (2008), 640–653.

[34] H. Kobayashi (2005) The subgrid-scale models based on coherent structures for rotating homogeneous turbulence and turbulent channel flow. *Physics of Fluids* **17**.4 (2005), 045104.

[35] S. Lele (1997) "Computational aeroacoustics-A review". In *35th Aerospace Sciences Meeting and Exhibit*. 1997, p. 18.

[36] M. J. Lighthill (1952) "On sound generated aerodynamically. I. General theory". In *Proceedings of the Royal Society of London A: Mathematical, Physical and Engineering Sciences*. Vol. 211. 1107. The Royal Society. 1952, pp. 564–587.

[37] M. J. Lighthill (1954) "On sound generated aerodynamically. II. Turbulence as a source of sound". In *Proceedings of the Royal Society of London A: Mathematical, Physical and Engineering Sciences*. Vol. 222. 1148. The Royal Society. 1954, pp. 1–32.

[38] G. M. Lilley (1974) On the noise from jets. *Noise Mechanism* **AGARD-CP-131** (1974), 13.1–13.12.

[39] G. M. Lilley (2003) The source of aerodynamic noise. *International Journal of Aeroacoustics* **2**.3 (2003), 241–253.

[40] E. Longatte, P. Lafon & S. Candel (1998) "Computation of noise generation by turbulence in internal flows". In *4th AIAA/CEAS Aeroacoustics Conference*. 1998, p. 2332.

[41] J. M. McDonough (2007) Introductory Lectures on Turbulence: Physics, Mathematics and Modeling. University of Kentucky, Department of Mechanical Engineering and Mathematics, 2007.

[42] O. M. Phillips (1960) On the generation of sound by supersonic turbulent shear layers. *Journal of Fluid Mechanics* **9**.1 (1960), 1–28.

[43] M. Popovac & K. Hanjalic (2007) Compound wall treatment for RANS computation of complex turbulent flows and heat transfer. *Flow, turbulence and combustion* **78**.2 (2007), 177.

[44] A. Powell (1964) Theory of vortex sound. *The journal of the acoustical society of America* **36**.1 (1964), 177–195.

[45] L. F. Richardson (1922) Weather prediction by numerical process (1922).

[46] S. Rienstra & A. Hirschberg (2017) An Introduction to Acoustics. Eindhoven University of Technology, 2017.

[47] P. J. Roache (1998) Fundamentals of computational fluid dynamics. Albuquerque, New Mexico: Hermosa Publishers, 1998.

[48] H. Schlichting & K. Gersten (2006) Grenzschicht-theorie. Springer-Verlag, 2006.

[49] C. Seror, P. Sagaut, C. Bailly & D. Juvé (2001) On the radiated noise computed by large-eddy simulation. *Physics of Fluids* **13**.2 (2001), 476–487.

[50] C. Seror, P. Sagaut, C. Bailly & D. Juvé (2000) Subgrid-scale contribution to noise production in decaying isotropic turbulence. *AIAA journal* **38**.10 (2000), 1795–1803.

[51] M. Snellen, L. van Lier, C. Rops, M. Janssens, J. Heck & G. Strumolo (2002) “Flow-induced noise around the A-pillar of an idealized car greenhouse”. In *8th AIAA/CEAS Aeroacoustics Conference & Exhibit.* 2002, p. 2548.

[52] J. H. Spurk & N. Aksel (2007) Strömungslehre: Einführung in die Theorie der Strömungen. 7th ed. Berlin Heidelberg: Springer, 2007.

[53] W. Sutherland (1893) LII. The viscosity of gases and molecular force. *The London, Edinburgh, and Dublin Philosophical Magazine and Journal of Science* **36**.223 (1893), 507–531.

[54] P. G. Tucker (2016) Advanced Computational Fluid and Aerodynamics. Cambridge University Press, 2016.

[55] H. K. Versteeg & W. Malalasekera (2007) An introduction to computational fluid dynamics: the finite volume method. Pearson Education, 2007.

[56] C. Wagner, T. Hüttl & P. Sagaut (2007) Large-eddy simulation for acoustics. Cambridge University Press, 2007.

[57] J. F. Williams & D. L. Hawkings (1969) Sound generation by turbulence and surfaces in arbitrary motion. *Philosophical Transactions of the Royal Society of London A: Mathematical, Physical and Engineering Sciences* **264**.1151 (1969), 321–342.

A Appendix

In the following tables the presented data corresponds to the 7×7 grid points, which were defined in section 6.2.6 and are shown again in figure A.1. In this Master's Thesis four selected grid points GP(3/3), GP(4/1), GP(5/2) and GP(7/4) are investigated in more detail and are circled in figure A.1.

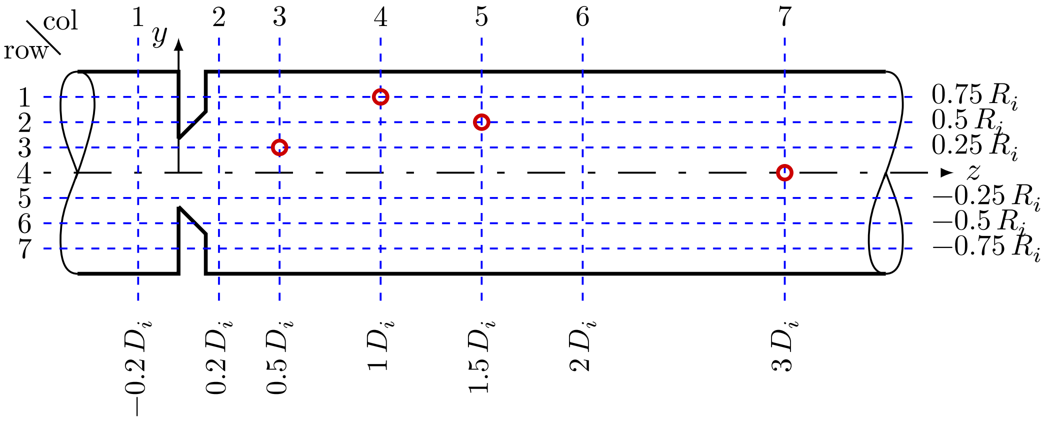

FIGURE A.1: The 7×7 grid of the evaluated cells.

As already mentioned in chapter 6, the jet-like core flow is always deflected towards one side of the pipe, leading to an asymmetric flow field. Therefore, when comparing acoustic pipe LES, where the jet-like core flow attaches at the upper or lower sides of the pipe, the row numbers in the case with the jet attaching at the bottom side ($y < 0$) are flipped. E.g. the results from cell at column 4 and row 2 GP(4/2) form case X (with a jet attached at the top ($y > 0$)) is compared to the data from the cell at column 4 and row 6 GP(4/6) of case Y (with a jet attached at the bottom ($y < 0$)), using always the notation GP(4/2). This ensures that only points with equivalent underlying flow characteristics are compared. In the following tables the data for the simulations with the core jet-flow attaching at the bottom ($y < 0$) are consistently flipped.

Table A.1: The cell volumes V_{C} and characteristic cell lengths $\Delta \boldsymbol{x}_{\mathrm{C}} = V_{\mathrm{C}}^{1/3}$ of the computational grids at the 7×7 grid positions.

grid pos.		GAP_h10		GAP_h10F		GAP_h5		GAP_h10T	
		V_{C}	Δx_{C}	V_{C}	Δx_{C}	V_{C}	Δx_{C}	V_{C}	Δx_{C}
col	row	$10^{-12}\,[\mathrm{m}^3]$	$10^{-4}\,[\mathrm{m}^3]$	$10^{-12}\,[\mathrm{m}^3]$	$10^{-4}\,[\mathrm{m}^3]$	$10^{-12}\,[\mathrm{m}^3]$	$10^{-4}\,[\mathrm{m}^3]$	$10^{-12}\,[\mathrm{m}^3]$	$10^{-4}\,[\mathrm{m}^3]$
1	1	10.18	4.67	7.5	4.22	11.55	4.87	121.01	10.66
	2	9.85	4.62	6.04	3.92	7.62	4.24	142.77	11.26
	3	8.4	4.38	4.7	3.61	8.15	4.34	141.85	11.24
	4	9.74	4.6	5.31	3.76	3.34	3.22	179.9	12.16
	5	8.4	4.38	4.7	3.61	8.15	4.34	199.73	12.59
	6	9.85	4.62	6.04	3.92	7.62	4.24	258.38	13.72
	7	10.18	4.67	7.5	4.22	11.55	4.87	147.18	11.37
2	1	2.66	2.98	2.14	2.78	6.1	3.94	25.95	6.38
	2	9.25	4.52	5.41	3.78	0.97	2.13	100.49	10.02
	3	11.08	4.8	5.46	3.79	8.47	4.39	145.67	11.34
	4	8.38	4.38	5.06	3.7	8	4.31	233.95	13.28
	5	11.08	4.8	5.46	3.79	8.47	4.39	119.17	10.6
	6	9.25	4.52	5.41	3.78	0.97	2.13	39.98	7.37
	7	2.66	2.98	2.14	2.78	6.1	3.94	46.59	7.75
3	1	8.94	4.47	5.42	3.78	10.16	4.67	113.74	10.44
	2	15.12	5.33	8.77	4.44	8.99	4.48	189.66	12.38
	3	24.26	6.24	9.78	4.61	11.66	4.89	102.02	10.07
	4	19.89	5.84	8.47	4.39	11.73	4.9	147.39	11.38
	5	24.26	6.24	9.78	4.61	11.66	4.89	195.02	12.49
	6	15.12	5.33	8.77	4.44	8.99	4.48	164.46	11.8
	7	8.94	4.47	5.42	3.78	10.16	4.67	40.47	7.4
4	1	14	5.19	8.24	4.35	15.44	5.37	95.73	9.86
	2	23.69	6.19	13.34	5.11	13.67	5.15	152.94	11.52
	3	38.01	7.24	14.87	5.3	17.73	5.62	212.16	12.85
	4	31.17	6.78	12.88	5.05	17.84	5.63	187.01	12.32
	5	38.01	7.24	14.87	5.3	17.73	5.62	145.29	11.33
	6	23.69	6.19	13.34	5.11	13.67	5.15	198.5	12.57
	7	14	5.19	8.24	4.35	15.44	5.37	57.45	8.31
5	1	12.69	5.03	9.05	4.49	21.32	5.97	213.71	12.88
	2	21.46	5.99	14.66	5.27	18.87	5.74	230.2	13.2
	3	34.47	7.01	16.37	5.47	24.48	6.26	103.18	10.1
	4	28.31	6.57	14.2	5.22	24.62	6.27	246.33	13.51
	5	34.47	7.01	16.37	5.47	24.48	6.26	76.68	9.15
	6	21.46	5.99	14.66	5.27	18.87	5.74	216.01	12.93
	7	12.69	5.03	9.05	4.49	21.32	5.97	148.28	11.4
6	1	12.69	5.03	9.05	4.49	21.32	5.97	248.01	13.54
	2	21.46	5.99	14.66	5.27	18.87	5.74	227.17	13.15
	3	34.47	7.01	16.37	5.47	24.48	6.26	118.71	10.59
	4	28.31	6.57	14.2	5.22	24.62	6.27	195.2	12.5
	5	34.47	7.01	16.37	5.47	24.48	6.26	352.29	15.22
	6	21.46	5.99	14.66	5.27	18.87	5.74	193.37	12.46
	7	12.69	5.03	9.05	4.49	21.32	5.97	209.99	12.81
7	1	12.69	5.03	9.05	4.49	21.32	5.97	84.16	9.44
	2	21.46	5.99	14.66	5.27	18.87	5.74	209.58	12.8
	3	34.47	7.01	16.37	5.47	24.48	6.26	157.96	11.65
	4	28.31	6.57	14.2	5.22	24.62	6.27	118.74	10.59
	5	34.47	7.01	16.37	5.47	24.48	6.26	147.84	11.39
	6	21.46	5.99	14.66	5.27	18.87	5.74	157.92	11.65
	7	12.69	5.03	9.05	4.49	21.32	5.97	178.7	12.13

Table A.2: The temporal averaged total turbulence kinetic energy $\langle k_{\mathrm{tot}} \rangle$ [$\mathrm{m^2/s^2}$] at the 7×7 grid positions of the acoustic pipe simulations.

grid pos. col	row	AP_h10Re5300 $\langle \widetilde{k}_{\mathrm{tot}} \rangle$ [$\mathrm{m^2/s^2}$]	AP_h10Re5300F $\langle \widetilde{k}_{\mathrm{tot}} \rangle$ [$\mathrm{m^2/s^2}$]	AP_h5Re5300 $\langle \widetilde{k}_{\mathrm{tot}} \rangle$ [$\mathrm{m^2/s^2}$]	AP_h10Re7400 $\langle \widetilde{k}_{\mathrm{tot}} \rangle$ [$\mathrm{m^2/s^2}$]	RANS_h10Re5300 $\langle k_{\mathrm{tot}} \rangle$ [$\mathrm{m^2/s^2}$]
1	1	0.16	0.63	0.67	0.68	3.93×10^{-2}
	2	5.81×10^{-2}	0.15	9.46×10^{-2}	0.13	2.1×10^{-2}
	3	3.24×10^{-2}	3.12×10^{-2}	6.15×10^{-2}	6.67×10^{-2}	1.88×10^{-2}
	4	2.58×10^{-2}	2.68×10^{-2}	3.97×10^{-2}	5.14×10^{-2}	1.68×10^{-2}
	5	3.19×10^{-2}	3.8×10^{-2}	6.27×10^{-2}	8.98×10^{-2}	1.88×10^{-2}
	6	0.12	5.37×10^{-2}	0.28	0.34	2.1×10^{-2}
	7	0.61	0.41	0.46	1.25	3.98×10^{-2}
2	1	1.1	1.2	5.75	2.56	1.36
	2	1.3	1.38	5.34	3.3	2.69
	3	1.09	4.5	8.71	10.04	1.79
	4	8.15×10^{-2}	0.12	1.95	0.24	0.1
	5	3.7	4.96	2.37	9.47	1.07
	6	0.85	0.85	1.81	1.42	1.26
	7	0.75	0.83	1.88	1.58	0.96
3	1	2.71	3.47	14.21	6.93	1.63
	2	4.33	5.61	18.28	11.67	4.32
	3	3.88	3.9	26.25	8.07	3.3
	4	1.94	3.93	31.28	8.07	0.16
	5	5.83	6.63	5.59	12	2.82
	6	1.49	1.43	2.49	2.21	1.63
	7	1.18	1.09	2.66	1.89	1.12
4	1	7.37	7.13	18.86	13.27	2.78
	2	6.71	6.03	19.37	11.96	3.8
	3	5.65	6.17	16.98	12.13	1.22
	4	7.04	6.13	9.88	11.54	3.53
	5	4.5	3.4	4.87	6.95	2.24
	6	2.08	1.48	3.76	3.21	1.83
	7	1.58	1.12	3.18	2.28	1.33
5	1	4.63	3.62	8.51	7.24	2
	2	4.64	3.98	9.3	7.35	2.19
	3	4.63	4.16	10.51	8.28	3.05
	4	4.97	4.4	10.15	8.68	3.11
	5	3.98	3.46	7.84	7.16	2.44
	6	2.81	2.34	6.04	4.53	2.07
	7	2.08	1.63	3.9	2.99	1.52
6	1	2.77	2.17	6.09	4.15	1.21
	2	2.72	2.3	7.45	4.54	1.78
	3	2.9	2.7	9.12	5.79	2.61
	4	3.53	3.25	10.19	6.37	3.27
	5	3.45	3.15	9.03	6.43	2.77
	6	3	2.47	7.26	5.46	2.26
	7	2.2	1.54	4.71	3.58	1.63
7	1	1.38	1.11	4.7	2.1	0.91
	2	1.5	1.31	5.52	2.57	1.13
	3	1.7	1.52	6.57	3.17	1.37
	4	1.97	1.75	6.83	3.8	1.92
	5	1.94	1.84	6.41	3.83	2.18
	6	1.67	1.63	5.29	3.15	1.88
	7	1.27	1.12	3.53	2.48	1.42

Table A.3: The temporal averaged resolved turbulence kinetic energy $\left\langle \widetilde{k}_{\text{LES}} \right\rangle$ [m^2/s^2] and the temporal averaged SGS turbulence kinetic energy $\langle k_{\text{SGS}} \rangle$ [m^2/s^2] at the 7×7 grid positions of case AP_h10Re5300 and case AP_h10Re5300F.

grid pos.		AP_h10Re5300			AP_h10Re5300F		
col	row	$\langle \widetilde{k}_{\text{LES}} \rangle$ [m^2/s^2]	$\langle k_{\text{SGS}} \rangle$ [m^2/s^2]	$\langle k_{\text{SGS}} \rangle / \langle \widetilde{k}_{\text{tot}} \rangle$ [%]	$\langle \widetilde{k}_{\text{LES}} \rangle$ [m^2/s^2]	$\langle k_{\text{SGS}} \rangle$ [m^2/s^2]	$\langle k_{\text{SGS}} \rangle / \langle \widetilde{k}_{\text{tot}} \rangle$ [%]
1	1	0.15	9.38×10^{-3}	5.95	0.61	1.74×10^{-2}	2.78
	2	5.35×10^{-2}	4.6×10^{-3}	7.9	0.14	5.72×10^{-3}	3.9
	3	2.39×10^{-2}	8.54×10^{-3}	26.34	2.49×10^{-2}	6.3×10^{-3}	20.16
	4	1.54×10^{-2}	1.04×10^{-2}	40.4	2.06×10^{-2}	6.22×10^{-3}	23.19
	5	2.3×10^{-2}	8.92×10^{-3}	27.95	3.27×10^{-2}	5.22×10^{-3}	13.74
	6	0.11	7.9×10^{-3}	6.58	5.05×10^{-2}	3.14×10^{-3}	5.86
	7	0.59	2.11×10^{-2}	3.47	0.4	1.22×10^{-2}	2.97
2	1	1.07	2.79×10^{-2}	2.55	1.16	3.92×10^{-2}	3.26
	2	1.25	5.22×10^{-2}	4.02	1.33	4.83×10^{-2}	3.51
	3	1.04	5.63×10^{-2}	5.14	4.17	0.32	7.17
	4	6.66×10^{-2}	1.5×10^{-2}	18.36	0.1	1.44×10^{-2}	12.44
	5	3.46	0.24	6.42	4.57	0.38	7.69
	6	0.81	3.4×10^{-2}	4.01	0.82	2.74×10^{-2}	3.22
	7	0.74	1.49×10^{-2}	1.97	0.81	1.66×10^{-2}	1.99
3	1	2.6	0.11	3.94	3.34	0.13	3.67
	2	4.12	0.2	4.74	5.38	0.23	4.17
	3	3.71	0.17	4.41	3.68	0.22	5.55
	4	1.78	0.16	8.06	3.71	0.21	5.46
	5	5.48	0.35	5.97	6.28	0.35	5.27
	6	1.43	5.75×10^{-2}	3.87	1.38	5.52×10^{-2}	3.85
	7	1.15	2.92×10^{-2}	2.48	1.07	1.99×10^{-2}	1.82
4	1	6.97	0.4	5.36	6.75	0.38	5.36
	2	6.37	0.33	4.99	5.7	0.33	5.42
	3	5.35	0.29	5.19	5.9	0.26	4.25
	4	6.69	0.34	4.87	5.89	0.24	3.96
	5	4.26	0.25	5.47	3.24	0.16	4.73
	6	1.98	9.59×10^{-2}	4.61	1.41	7.15×10^{-2}	4.81
	7	1.54	4.33×10^{-2}	2.74	1.08	3.56×10^{-2}	3.18
5	1	4.44	0.19	4.06	3.45	0.16	4.53
	2	4.41	0.23	4.87	3.78	0.2	4.94
	3	4.36	0.26	5.72	3.97	0.19	4.58
	4	4.73	0.23	4.72	4.23	0.17	3.93
	5	3.78	0.2	4.97	3.31	0.15	4.45
	6	2.7	0.11	3.79	2.22	0.11	4.84
	7	1.99	8.35×10^{-2}	4.02	1.56	6.3×10^{-2}	3.87
6	1	2.68	9.46×10^{-2}	3.41	2.08	8.45×10^{-2}	3.9
	2	2.59	0.13	4.77	2.19	0.11	4.71
	3	2.74	0.16	5.67	2.57	0.12	4.54
	4	3.37	0.16	4.64	3.13	0.13	3.86
	5	3.29	0.16	4.59	3.02	0.13	4.01
	6	2.87	0.12	4.16	2.37	0.1	4.19
	7	2.12	7.82×10^{-2}	3.56	1.47	6.62×10^{-2}	4.31
7	1	1.34	4.15×10^{-2}	3.02	1.08	3.32×10^{-2}	2.98
	2	1.43	5.97×10^{-2}	3.99	1.25	5.55×10^{-2}	4.24
	3	1.63	7.51×10^{-2}	4.41	1.46	5.54×10^{-2}	3.66
	4	1.89	7.4×10^{-2}	3.76	1.69	5.7×10^{-2}	3.26
	5	1.87	6.82×10^{-2}	3.52	1.77	6.49×10^{-2}	3.53
	6	1.63	4.65×10^{-2}	2.78	1.58	5.75×10^{-2}	3.52
	7	1.23	3.49×10^{-2}	2.76	1.09	3.11×10^{-2}	2.77

Table A.4: The resulting time-scales $\boldsymbol{t}$ [s] and corresponding frequencies $\boldsymbol{f}$ [Hz] at the 7×7 grid positions of case AP_h10Re5300.

grid pos.		time-scales				frequencies			
col	row	t_{ST} [s]	$t_{k\varepsilon}$ [s]	t_{SW} [s]	$t_{\mathcal{K}}$ [s]	f_{ST} [Hz]	$f_{k\varepsilon}$ [Hz]	f_{SW} [Hz]	$f_{\mathcal{K}}$ [Hz]
1	1	1.69×10^{-3}	6.92×10^{-2}	3.08×10^{-2}	1.49×10^{-3}	591.76	14.46	32.43	673.28
	2	2.75×10^{-3}	0.14	5.08×10^{-2}	3.14×10^{-3}	364.06	7.16	19.69	318.86
	3	2.22×10^{-3}	0.12	6.8×10^{-2}	5.4×10^{-3}	449.54	8.15	14.71	185.24
	4	2.3×10^{-3}	0.11	7.63×10^{-2}	7.07×10^{-3}	435.32	9.29	13.11	141.38
	5	2.22×10^{-3}	9.9×10^{-2}	6.86×10^{-2}	5.04×10^{-3}	451.39	10.1	14.58	198.42
	6	2.11×10^{-3}	6.06×10^{-2}	3.54×10^{-2}	1.64×10^{-3}	473.77	16.5	28.28	609.74
	7	1.56×10^{-3}	3.12×10^{-2}	1.57×10^{-2}	7.23×10^{-4}	640.65	32	63.72	1 382.52
2	1	1.62×10^{-3}	1.72×10^{-2}	1.17×10^{-2}	4.67×10^{-4}	616.28	58.16	85.5	2 143.61
	2	2.48×10^{-3}	7.9×10^{-3}	1.07×10^{-2}	4.95×10^{-4}	402.98	126.57	93.09	2 020.63
	3	2.23×10^{-4}	8.86×10^{-2}	1.17×10^{-2}	5.66×10^{-4}	4 480.35	11.28	85.4	1 766.79
	4	2.29×10^{-3}	8.91×10^{-2}	4.29×10^{-2}	3.7×10^{-3}	436.18	11.22	23.32	270.04
	5	1.92×10^{-4}	1.97×10^{-2}	6.37×10^{-3}	2.79×10^{-4}	5 206.81	50.65	157.03	3 588.81
	6	2.96×10^{-3}	1.02×10^{-2}	1.33×10^{-2}	6.13×10^{-4}	337.64	98.33	75.2	1 632.4
	7	2.03×10^{-3}	3.42×10^{-2}	1.41×10^{-2}	6.46×10^{-4}	493.13	29.2	70.87	1 547.43
3	1	2.52×10^{-3}	3.15×10^{-3}	7.44×10^{-3}	3.12×10^{-4}	396.08	317.88	134.43	3 205.92
	2	9.41×10^{-4}	6.1×10^{-3}	5.89×10^{-3}	2.92×10^{-4}	1 062.5	164.03	169.83	3 425.95
	3	3.95×10^{-4}	2.29×10^{-2}	6.22×10^{-3}	3.53×10^{-4}	2 534.55	43.6	160.85	2 831.88
	4	1.07×10^{-3}	9.14×10^{-3}	8.79×10^{-3}	5.06×10^{-4}	933.47	109.38	113.75	1 975.36
	5	5.5×10^{-4}	7.82×10^{-3}	5.07×10^{-3}	2.86×10^{-4}	1 817.97	127.94	197.12	3 501.38
	6	5.88×10^{-3}	4.86×10^{-3}	1×10^{-2}	5.86×10^{-4}	170.13	205.57	99.59	1 706.75
	7	4.94×10^{-3}	1×10^{-2}	1.13×10^{-2}	6.13×10^{-4}	202.28	99.86	88.53	1 630.14
4	1	9.98×10^{-4}	2.24×10^{-3}	4.51×10^{-3}	1.94×10^{-4}	1 001.59	447.4	221.62	5 145.97
	2	7.99×10^{-4}	5.45×10^{-3}	4.73×10^{-3}	2.61×10^{-4}	1 251.35	183.52	211.44	3 824.78
	3	1.84×10^{-3}	3.2×10^{-3}	5.15×10^{-3}	3.1×10^{-4}	544.78	312.07	194.05	3 224.8
	4	8.92×10^{-4}	5.85×10^{-3}	4.62×10^{-3}	2.82×10^{-4}	1 121.57	170.88	216.59	3 542.26
	5	1.27×10^{-3}	5.75×10^{-3}	5.77×10^{-3}	3.55×10^{-4}	786.31	173.9	173.27	2 813.68
	6	5.25×10^{-3}	2.75×10^{-3}	8.49×10^{-3}	4.57×10^{-4}	190.59	363.09	117.74	2 189.66
	7	6.47×10^{-3}	5.68×10^{-3}	9.74×10^{-3}	5.56×10^{-4}	154.68	176.04	102.64	1 798.18
5	1	3.96×10^{-3}	1.48×10^{-3}	5.69×10^{-3}	2.73×10^{-4}	252.52	674.29	175.71	3 668.98
	2	4.23×10^{-3}	1.4×10^{-3}	5.69×10^{-3}	3.01×10^{-4}	236.38	714.73	175.89	3 324.23
	3	2.08×10^{-3}	3.04×10^{-3}	5.69×10^{-3}	3.39×10^{-4}	479.82	329.41	175.66	2 952.53
	4	1.44×10^{-3}	4.92×10^{-3}	5.49×10^{-3}	3.24×10^{-4}	694.09	203.3	182.05	3 088.27
	5	1.87×10^{-3}	5.04×10^{-3}	6.14×10^{-3}	3.84×10^{-4}	533.85	198.58	162.88	2 606.49
	6	3.73×10^{-3}	3.49×10^{-3}	7.31×10^{-3}	3.91×10^{-4}	267.89	286.5	136.82	2 555.91
	7	3.89×10^{-3}	3.37×10^{-3}	8.5×10^{-3}	4.05×10^{-4}	256.78	296.79	117.67	2 467.95
6	1	4.31×10^{-3}	2.8×10^{-3}	7.35×10^{-3}	3.57×10^{-4}	231.92	357.07	135.97	2 802.19
	2	5.85×10^{-3}	1.78×10^{-3}	7.43×10^{-3}	3.94×10^{-4}	170.92	562.97	134.64	2 536.71
	3	2.86×10^{-3}	3.51×10^{-3}	7.19×10^{-3}	4.25×10^{-4}	349.55	284.62	139.12	2 354.08
	4	2.07×10^{-3}	5.09×10^{-3}	6.52×10^{-3}	3.91×10^{-4}	483.7	196.44	153.46	2 558.51
	5	2.1×10^{-3}	5.92×10^{-3}	6.59×10^{-3}	4.23×10^{-4}	475.16	169.05	151.65	2 364.44
	6	3.29×10^{-3}	4.4×10^{-3}	7.08×10^{-3}	4.34×10^{-4}	303.81	227.19	141.34	2 306.77
	7	3.73×10^{-3}	4.62×10^{-3}	8.26×10^{-3}	4.36×10^{-4}	268.14	216.28	121.09	2 295.21
7	1	1.02×10^{-2}	3.17×10^{-3}	1.04×10^{-2}	5.47×10^{-4}	98.42	315.01	95.83	1 827.18
	2	5.8×10^{-3}	5.1×10^{-3}	1×10^{-2}	6.07×10^{-4}	172.31	196	99.84	1 648.54
	3	4.62×10^{-3}	6.27×10^{-3}	9.39×10^{-3}	6.32×10^{-4}	216.3	159.49	106.54	1 582.58
	4	4.01×10^{-3}	7.12×10^{-3}	8.73×10^{-3}	5.77×10^{-4}	249.35	140.38	114.54	1 732.73
	5	4.84×10^{-3}	7.99×10^{-3}	8.8×10^{-3}	6.49×10^{-4}	206.78	125.17	113.6	1 541.19
	6	4.71×10^{-3}	1.39×10^{-2}	9.47×10^{-3}	7.47×10^{-4}	212.11	72.19	105.63	1 339.4
	7	8.4×10^{-3}	6.87×10^{-3}	1.09×10^{-2}	6.99×10^{-4}	118.99	145.61	91.87	1 429.86

Table A.5: The intensity of the centered aeroacoustic source terms $\widetilde{\Omega}'_{i,\mathrm{RMS}}$ [m/s^2] at the 7×7 grid positions of case AP_h$_{10}$Re$_{5300}$ and case AP_h$_{10}$Re$_{5300}$F.

grid pos.		AP_h10Re5300			AP_h10Re5300F		
col	row	$\widetilde{\Omega}'_{x,\mathrm{RMS}}$ [m/s^2]	$\widetilde{\Omega}'_{y,\mathrm{RMS}}$ [m/s^2]	$\widetilde{\Omega}'_{z,\mathrm{RMS}}$ [m/s^2]	$\widetilde{\Omega}'_{x,\mathrm{RMS}}$ [m/s^2]	$\widetilde{\Omega}'_{y,\mathrm{RMS}}$ [m/s^2]	$\widetilde{\Omega}'_{z,\mathrm{RMS}}$ [m/s^2]
1	1	159.46	85.18	158.88	481.76	260.49	330.73
	2	29.85	20.07	47.74	115.41	89	285.96
	3	16.35	12.83	14.44	15.6	10.79	16.88
	4	7.11	8.96	9.4	9.99	8.05	9.82
	5	19.39	12.66	13.42	20.68	14.01	14.52
	6	142.6	71.54	282.33	41.83	25.67	67.33
	7	741.69	386.38	521.94	374.56	241.15	329.89
2	1	930.95	860.62	1 026	1 312.93	1 257.98	1 376.76
	2	911.97	989.35	980.93	1 231.61	1 315.79	1 306.94
	3	817.49	549.48	1 231.51	5 227.1	4 690.38	5 780.91
	4	33.82	53.21	50.92	68.15	130.2	116.06
	5	4 966.26	3 481.9	4 721.93	5 443.08	5 499.87	6 462.71
	6	608.77	730.58	743.89	730.64	824.25	867.86
	7	633.39	552.93	736.8	771.37	704.63	890.54
3	1	2 463.17	2 146.01	2 433.99	3 233.16	3 202.59	3 589.46
	2	3 475.55	3 003.16	3 132.1	5 625.18	5 209.88	5 443.85
	3	2 594.8	2 626.2	3 042.14	3 859.64	3 755.92	5 264.32
	4	1 996.62	1 571.71	3 189.46	5 152.08	4 051.62	6 104.06
	5	3 925.39	3 332.22	4 265.02	6 411.36	4 673.94	5 488.55
	6	1 335.96	1 066.2	1 343.02	1 454.58	1 508.25	1 405.13
	7	773.67	729.13	947.42	706.84	667.79	873.52
4	1	6 636.81	6 061.4	6 180.3	6 432.99	6 169.91	6 512.94
	2	4 149.57	3 957.47	4 531.61	4 672.46	4 848.98	5 869.56
	3	2 942.61	2 744.35	4 344.53	4 004.44	3 978.74	5 063.42
	4	4 136.84	3 436.18	4 672.74	5 283.87	4 087.44	5 008.07
	5	2 937.09	2 137.13	3 360	2 853.15	2 801.05	3 331.36
	6	1 388.79	1 340.82	1 799.9	1 153.85	1 152.83	1 296.31
	7	1 198.04	1 135.43	1 329.92	794.65	833.5	965.5
5	1	3 331.38	3 406.65	3 484.26	2 757.48	2 981.02	3 206.02
	2	2 678.67	2 777.82	3 353.35	2 743.93	2 676.55	3 400.41
	3	2 553.65	2 415.06	3 277.45	2 853.82	2 640.98	3 553.44
	4	3 301.78	2 714.49	3 355.3	3 587.39	3 064.12	3 660.94
	5	2 348.25	2 345.21	2 737.03	2 987.87	2 670.28	2 750.55
	6	1 847.18	1 879.55	2 149.61	1 808.29	1 731.73	1 715.41
	7	1 616.72	1 509.46	1 925.46	1 649.34	1 513.32	1 585.28
6	1	1 847.27	1 741.01	2 186.18	1 515.11	1 456.96	1 892.03
	2	1 881.23	1 695.85	2 102.11	1 709.5	1 603.7	1 886.19
	3	1 713.06	1 588.98	2 039.52	1 811.59	1 845.45	2 057.73
	4	1 972.29	1 715.41	2 303.57	1 992.96	2 005.63	2 362.65
	5	1 970.02	1 913.05	1 884.06	2 190.31	2 051.88	2 191.22
	6	1 632.06	1 804.22	1 823.59	1 723.15	2 085.91	1 848.17
	7	1 400.94	1 549.62	1 431.3	1 589.49	1 706.78	1 560.03
7	1	781.81	746.77	1 082.82	764.15	716.66	845.75
	2	825.86	826.33	908.11	836.35	879.03	955.28
	3	865.07	935.74	1 025.56	897.19	797.89	932.64
	4	1 026.92	954.01	1 192.09	1 039.04	959.51	1 121.71
	5	915.46	959.76	996.3	1 041.36	1 026.39	1 046.67
	6	748.13	738.27	754.91	911.17	1 025.69	988.26
	7	717.01	736.76	814.07	744.37	707.21	826.81

Table A.6: The intensity of the centered aeroacoustic source terms $\widetilde{\Omega}'_{i,\mathrm{RMS}}$ [m/s^2] at the 7×7 grid positions of case AP_h10Re7400 and case AP_h5Re5300.

grid pos.		AP_h10Re7400			AP_h5Re5300		
col	row	$\widetilde{\Omega}'_{x,\mathrm{RMS}}$ [m/s^2]	$\widetilde{\Omega}'_{y,\mathrm{RMS}}$ [m/s^2]	$\widetilde{\Omega}'_{z,\mathrm{RMS}}$ [m/s^2]	$\widetilde{\Omega}'_{x,\mathrm{RMS}}$ [m/s^2]	$\widetilde{\Omega}'_{y,\mathrm{RMS}}$ [m/s^2]	$\widetilde{\Omega}'_{z,\mathrm{RMS}}$ [m/s^2]
1	1	835.41	643.26	701.81	555.11	517.27	504.51
	2	105.34	88.74	113.88	138.68	74.79	103.66
	3	46.42	49.96	52.78	27.39	18.27	24.88
	4	18.19	20.27	22.79	12.7	13.99	18.66
	5	51.49	40.74	46.04	23.94	19.56	34.73
	6	456.99	462.31	645.22	269.17	185.24	210.17
	7	1 264.93	1 020.64	1 348.81	408.24	285.58	648.88
2	1	3 008.57	2 972.71	3 300.15	6 330.86	5 500.27	6 793.06
	2	2 588.16	3 043.72	2 880.52	6 025.82	5 555.29	6 507.33
	3	11 254.5	9 671.92	12 712.6	7 206.53	10 666.3	8 271.67
	4	179.93	304.2	194.95	1 272.03	2 636.86	2 877.61
	5	12 387.2	9 838.07	12 511.9	1 992.83	2 663.39	2 380.89
	6	1 023.62	1 070.1	1 235.28	1 364.66	1 386.24	1 542.72
	7	1 211.43	1 312.12	1 556.49	1 449.43	1 532.81	1 884.74
3	1	7 459.79	7 239.03	7 891.72	12 189.9	12 084.5	12 152
	2	11 324	10 567.2	9 898.5	16 718.2	17 054.7	15 336.8
	3	7 595.34	8 302.53	9 125.54	19 814.3	20 197.5	22 252.2
	4	8 846.06	7 097.17	10 852.4	25 681.9	21 218.1	29 925.4
	5	11 971.7	10 270.8	12 398.9	5 891.28	6 296.56	7 623.98
	6	1 922.12	2 062.09	2 364.89	1 801.12	1 948.54	2 015.85
	7	1 404.87	1 356.04	1 714.67	1 803.82	1 680.48	2 294.15
4	1	13 347.2	12 389.1	12 728.6	16 162.1	15 482.4	15 278.7
	2	8 995.25	9 214.17	10 982.1	14 459.2	14 039.9	18 315.5
	3	7 980.58	7 091.04	10 031.5	12 127.8	11 493.1	14 335.8
	4	8 698.98	7 817.35	9 440.58	8 526.26	7 985.56	9 414.8
	5	5 310.76	5 090.82	6 497.84	3 429.34	3 328.12	4 363.51
	6	2 439.39	2 691.76	3 053.44	2 479.56	2 573.89	2 753.93
	7	1 467.42	1 781.09	2 058.78	2 014.55	2 048.98	2 189.33
5	1	5 966.86	5 620.07	6 808.16	6 440.27	6 278.77	6 962.07
	2	5 237.87	5 187.77	6 639.22	6 822.64	6 929.33	8 442.23
	3	6 023.43	5 168.63	6 719.24	8 084	7 240.26	8 287.17
	4	6 121.83	5 351.33	6 673.69	7 177.85	7 142.18	8 274.23
	5	5 370.1	4 905.89	5 228.81	5 021.14	4 854.62	5 365.02
	6	2 730.75	3 186.78	3 402.21	4 507.79	4 532.75	5 032.71
	7	2 032.04	2 338.18	2 386.89	2 729.7	2 852	3 398.33
6	1	3 384.81	3 526.2	3 904.68	4 326.48	4 217.76	5 211.16
	2	3 262.93	3 434.5	4 330.58	5 054.52	4 934.54	6 305.6
	3	4 111.69	3 971.12	4 982.72	6 223.62	5 882.36	7 390.1
	4	4 442.51	4 286.93	4 362.18	7 120.82	6 270.04	7 261.66
	5	4 172.52	4 408.37	4 092.35	6 171.27	5 619.01	6 056.83
	6	3 776.41	4 019.18	3 825.11	5 439.34	5 318.65	5 729.09
	7	2 450.61	2 340.46	2 480.69	3 311.43	3 241.42	3 340.36
7	1	1 573.01	1 646.57	2 177.89	2 697.89	2 532.87	3 520.18
	2	1 639.53	1 658.08	2 066.11	3 324.22	3 412.11	3 872.39
	3	2 115.22	2 147.58	2 284.53	3 419.48	3 613.28	4 240.95
	4	2 500.52	2 292.19	2 478.74	3 932.42	3 678.7	4 291.81
	5	2 714.49	2 404.79	2 817.33	3 528.11	3 378.9	3 875.55
	6	1 998.28	1 980.33	1 910.83	3 072.76	3 071.43	3 055.03
	7	1 684.03	1 657.88	1 927.26	2 399.14	2 047.65	2 362.02

Table A.7: The intensity of the centered aeroacoustic source terms $\widetilde{\Omega}'^{\text{fa,ma}}_{i,\text{LES,RMS}}$ [m/s^2] at the 7×7 grid positions of case AP_h10Re5300.

grid pos.		moving average			Fourier average		
col	row	$\widetilde{\Omega}'^{\text{ma}}_{x,\text{LES,RMS}}$ [m/s^2]	$\widetilde{\Omega}'^{\text{ma}}_{y,\text{LES,RMS}}$ [m/s^2]	$\widetilde{\Omega}'^{\text{ma}}_{z,\text{LES,RMS}}$ [m/s^2]	$\widetilde{\Omega}'^{\text{fa}}_{x,\text{LES,RMS}}$ [m/s^2]	$\widetilde{\Omega}'^{\text{fa}}_{y,\text{LES,RMS}}$ [m/s^2]	$\widetilde{\Omega}'^{\text{fa}}_{z,\text{LES,RMS}}$ [m/s^2]
1	1	157.62	80.56	158.3	153.3	78.36	151.19
	2	29.66	20.06	48.35	28.74	19.91	46.98
	3	16.39	12.82	14.38	16.21	12.74	14.33
	4	7.11	9.06	9.33	7.06	8.95	9.19
	5	18.79	12.69	13.14	18.56	12.48	13.07
	6	137.37	70.96	271.63	132.86	69.58	261.45
	7	540.27	337.16	395.93	449.15	309.94	342.99
2	1	898.73	807.5	984.63	865.49	778.44	952.41
	2	857.57	953.86	940.95	827.84	914.43	899.51
	3	762.03	507.75	1 135.98	735.74	488.1	1 090.05
	4	33.68	51.2	48.72	33.27	50.09	47.7
	5	4 663.84	3 027.61	4 295.09	4 424.53	2 746.63	3 908.49
	6	563.31	693.48	703.94	539.55	653.18	676.21
	7	612.25	536.87	692.32	585.82	512.95	671.32
3	1	2 309.05	2 078.43	2 347.36	2 208.39	1 949.06	2 281.59
	2	3 402.83	2 911.55	2 934.24	3 284.47	2 772.46	2 821.75
	3	2 457.37	2 485.65	2 930.71	2 343.79	2 376.13	2 726.16
	4	1 913.88	1 500.46	3 078.58	1 819.68	1 441.83	2 876.54
	5	3 709.51	3 030.91	4 099.12	3 491.08	2 780.29	3 871.62
	6	1 019.04	1 018.38	1 196.85	883.1	972.15	1 125.27
	7	681.3	691	897	640.86	658.42	867.46
4	1	6 180.91	5 780.26	6 005.58	5 763.1	5 361.43	5 812.86
	2	3 903.23	3 639.71	4 397.18	3 577.47	3 376.37	4 211.97
	3	2 712.57	2 558.34	4 138.84	2 520.57	2 398.07	3 912.88
	4	3 910.77	3 220.79	4 431.29	3 632.15	3 022.31	4 155.49
	5	2 802.96	2 029.17	3 293.2	2 574.07	1 934.49	3 140.84
	6	1 259.83	1 257.3	1 726.8	1 193.55	1 184.92	1 611.41
	7	1 140.42	1 088.13	1 287.09	1 094.73	1 047.11	1 245.92
5	1	3 159.13	3 267.17	3 397.89	3 014.49	3 149.83	3 315.68
	2	2 551.26	2 627.3	3 220.56	2 421.36	2 503.81	3 120.29
	3	2 382.65	2 305.17	3 128.31	2 231.51	2 191.02	3 020.32
	4	2 983.72	2 560.3	3 229.91	2 840.53	2 439.28	3 106.71
	5	2 198.73	2 191.58	2 604	2 049.71	2 049.17	2 472.18
	6	1 651.98	1 748.41	2 012.22	1 552.52	1 673.83	1 960.78
	7	1 473.25	1 421.91	1 859.81	1 410.99	1 346.9	1 814.3
6	1	1 798.81	1 686.38	2 121.76	1 726.44	1 620.47	2 062.8
	2	1 800.4	1 637.58	2 069.64	1 725.87	1 589.04	2 022.29
	3	1 641.59	1 517.75	1 973.33	1 549.89	1 446.26	1 884.83
	4	1 815.55	1 634.99	2 152.01	1 712.41	1 540.98	2 069.6
	5	1 742.23	1 761.35	1 764.27	1 585.03	1 645.46	1 650.14
	6	1 516.73	1 632.04	1 699.95	1 407.93	1 480.88	1 604.29
	7	1 328.22	1 402.75	1 347.89	1 249.77	1 267.19	1 277.93
7	1	767.59	718.27	1 058.47	748.91	705.47	1 035.66
	2	797.4	812.4	887.27	776.51	786.61	871.54
	3	818.61	893.82	992.96	783.52	866.11	972.54
	4	922.66	904.65	1 116.07	850.03	862.28	1 073.24
	5	857.88	893.95	935.59	816.75	849.34	898.94
	6	655.9	702.56	719.55	617.7	680	693.15
	7	664.21	704.18	776.07	625.58	674.88	754

TABLE A.8: The intensity of the cross-terms $\widetilde{\Lambda}_{i,\mathrm{RMS}}$ [m/s^2] at the 7×7 grid positions of case AP_h$_{10}$Re$_{5300}$.

grid pos.		AP_h10Re5300		
col	row	$\widetilde{\Lambda}_{x,\mathrm{RMS}}$ [m/s^2]	$\widetilde{\Lambda}_{y,\mathrm{RMS}}$ [m/s^2]	$\widetilde{\Lambda}_{z,\mathrm{RMS}}$ [m/s^2]
1	1	270.19	241.73	372
	2	147.84	152.98	201.14
	3	109.92	170.49	147.25
	4	100.8	137.31	113.27
	5	135.83	133.69	127.29
	6	319.23	240.08	319.03
	7	334.79	287.17	625.1
2	1	1 271.29	1 110.09	1 091.08
	2	974.8	824.73	986.08
	3	2 284.96	3 543.16	4 431.31
	4	338.27	869.1	877.15
	5	5 503.47	4 020.76	7 566.51
	6	827.66	883.15	766.79
	7	678.75	625.85	617.72
3	1	2 181	1 755	1 850.57
	2	1 295.91	1 014.95	1 836.57
	3	5 180.17	5 866.88	6 958.04
	4	4 091.18	4 699.44	4 684.4
	5	910.47	859.01	2 746.89
	6	1 295.87	1 108	1 037.18
	7	1 228.33	1 046.51	1 079.02
4	1	3 938.2	2 898.9	3 185.21
	2	5 730.49	5 698.93	5 413.45
	3	5 124.08	5 617.08	6 158.38
	4	3 322.81	2 731.48	3 695.93
	5	762.16	577.06	1 527.73
	6	1 610.35	1 182.02	1 457.65
	7	1 450.97	1 172.05	1 284.91
5	1	4 010.36	3 850.26	3 932.26
	2	4 700.23	4 796.4	4 590.55
	3	4 327.63	4 136.22	4 132.73
	4	2 368.22	1 904.56	2 338.26
	5	300.71	387.67	806.8
	6	1 347.21	1 155.46	1 053
	7	1 499.79	1 332.08	1 442.23
6	1	3 549.25	3 149.53	3 184.45
	2	3 444.15	3 179.73	3 139.55
	3	3 102.95	2 727.04	2 693.83
	4	2 039.9	1 754.54	1 925.41
	5	841.97	563.12	786.38
	6	215.34	289.88	420.2
	7	599.97	482.32	434.54
7	1	2 130.27	2 053.14	2 158.87
	2	2 058.19	1 869.08	1 761.53
	3	1 909.38	1 628.13	1 670.92
	4	1 566.68	1 540.62	1 422.29
	5	1 011.62	971.16	821.95
	6	549.47	600.01	481.92
	7	511.6	402.23	372.43

TABLE A.9: The intensity of the aeroacoustic sources Π_{RMS} [Pa/s] at the 7×7 grid positions of case AP_h10Re5300, case AP_h10Re5300F and case CAA_h10Re5300.

grid pos. col	grid pos. row	AP_h10Re5300 $\widetilde{\Pi}_{\mathrm{RMS}}$ [Pa/s]	CAA_h10Re5300 Π_{RMS} [Pa/s]
1	1	49.14	42.71
	2	101.52	18.23
	3	87.65	81.88
	4	114.12	87.58
	5	94.55	57.18
	6	106.37	30.76
	7	104.42	55.52
2	1	766.62	1 832.68
	2	472.15	370.94
	3	1 776.05	1 473.41
	4	393.81	228.32
	5	2 514.09	453.5
	6	360.72	325.09
	7	461.46	191.96
3	1	646.78	564.38
	2	457.63	982.49
	3	3 353.96	1 302.66
	4	447.51	257.46
	5	540.97	91.05
	6	233.09	30.32
	7	222.77	3.91
4	1	2 685.12	1 776.75
	2	2 627.27	1 077.21
	3	1 081.09	356.27
	4	602.95	377.57
	5	399.22	33.11
	6	234.83	25.54
	7	322.39	23.97
5	1	1 261.26	404.76
	2	1 074.12	456.02
	3	1 118.01	468.16
	4	999.09	178.29
	5	1 029.9	161.26
	6	910.2	120.27
	7	828.59	95.78
6	1	592.51	119.73
	2	481.86	172.03
	3	494.24	313.49
	4	526.17	368.28
	5	563.2	323.16
	6	590.02	394.08
	7	609.07	293.13
7	1	102.2	112.3
	2	79.08	131.89
	3	68.77	179.55
	4	87.07	240.36
	5	133.89	281.76
	6	201.17	297.57
	7	181.64	218.46